UNIVERSITY OF CALIFORNIA

Santa Barbara

Understanding the thermodynamics and kinetic processes of transmembrane protein incorporation in nanostructured silica

A dissertation submitted in partial satisfaction of the

requirements for the degree Doctor of Philosophy

in Chemical Engineering

by

Maxwell Woodcock Berkow

Committee in charge:

Professor Bradley F. Chmelka, Chair

Professor Songi Han

Professor Michael J. Gordon

Professor Lior Sepunaru

September 2023

The dissertation of Maxwell Woodcock Berkow is approved.

Songi Han

Michael J. Gordon

Lior Sepunaru

Bradley F. Chmelka, Committee Chair

August 2023

Understanding the thermodynamics and kinetic processes of transmembrane protein incorporation in nanostructured silica

by

Maxwell Woodcock Berkow

ACKNOWLEDGEMENTS

Completion of my dissertation would not have been possible without the personal and research-related support of many people in Santa Barbara and back home in New York. I would like to thank my collaborators for teaching and assisting me, the Chmelka group for guiding and learning with me, my friends and family for their extensive support and distractions in between experiments, and especially my girlfriend Dr. Shona Becwar for all of the above and more.

VITA OF MAXWELL WOODCOCK BERKOW
August 2023

DOCTORAL CANDIDATE IN CHEMICAL ENGINEERING

Experienced In Academic & Industrial Research In Biotechnology
Excellent Problem-Solving & Technical Communication Skills
Well-Versed In Chemical/Material Syntheses, Material Characterizations, Thermodynamic & Kinetic Self-Assembly Physics

---

EDUCATION

Doctor of Philosophy in Chemical Engineering 2017 – current
University of California, Santa Barbara, CA, USA - graduating October 2023
Adviser: Bradley F. Chmelka, PhD
Mentor for Summer Applied Biotechnology Research Experience
Mentor for first year graduate student
UCSB club soccer player

Bachelor of Science in Engineering in Chemical Engineering 2013 – 2017
City College New York, New York, New York
Grove School of Engineering & Macaulay Honors College
Chemical engineering honors society
Macaulay Honors College undergraduate research grant
NCAA men's soccer team, captain

RELEVANT WORK EXPERIENCE

ACADEMIC RESEARCH

Graduate Research – University of California, Santa Barbara
Department of Chemical Engineering, Santa Barbara, CA 2017 – current
Thesis: *Understanding the kinetic processes and thermodynamic driving forces to incorporate transmembrane proteins in inorganic/organic hybrid materials*
Expertise in both chemical/material synthesis and characterization methods on the atomic, mesoscopic, and macroscopic length scales on self-assembled organic-inorganic silica hosts of transmembrane proteins for solar to electrochemical energy conversion. Research emphasis on elucidating the complicated and closely coupled relationships among the compositions, structures, and dynamics of proteins in the nanostructured composite films. Knowledgeable in protein expression and characterization, advanced solid-state atomic characterization techniques, self-assembly physics, x-ray characterization, and cleanroom nanofabrication. Extensive experience in technical and broad-level communication.

Undergraduate Research, Honors College Thesis Project – City College of New York
Department of Chemical Engineering, New York, NY 2014 – 2017
Thesis: *Measuring Movement and Self-Assembly of 2D-Staggered Janus Particles and Chains*

Observed and modelled self-assembly kinetics of iron-coated Janus particle chains. Characterized and modelled movement of platinum-coated Janus particles in the presence of hydrogen peroxide.

Undergraduate Research, International Research Experiences for Students – KTH Royal Institute of Technology
Department of Chemical Engineering, Stockholm, Sweden Summer 2016
Thesis: *Reaction Optimization for the Production of Biofuels through Heterogenous Catalysis*
Characterized the structure and composition of catalysts used in the conversion of babassu oil to biofuels. Optimized synthesis conditions to increase yields for biofuel conversion. Presented research twice to engineering faculty, students, and public at CCNY and KTH Student Symposiums.

INDUSTRIAL INTERNSHIPS

Engineering Operations & Gas Engineering Co-op Intern – Con Edison
Con Edison Gas Engineering, Bronx – New York, NY Winter & Spring 2016
Worked with engineers and mechanics to prepare for gas engineering emergencies. Drafted and oversaw the planning of new projects.

PUBLICATIONS

1. Berkow, Chmelka, Han, et al., Lipid Membrane Mimetics and Oligomerization Tune Functional Properties of Proteorhodopsin. *Biophysical Journal*. **2022**.
2. Berkow, Chmelka, et al. Co-assembly of functionally-active proteorhodopsin membrane protein molecules in mesostructured silica-surfactant films. *Under review.* **2023**.
3. Jahnke, Kim, Wildemuth, Nolla, Berkow, Chmelka, et al., Mesostructured Materials with Controllable Long-Range Orientational Ordering and Anisotropic Properties. *Submitted*. **2023**.

PRESENTATIONS

1. American Institute of Chemical Engineers Annual Conference, Phoenix, Arizona. *Controlling the properties of the light-responsive transmembrane protein proteorhodopsin in mesostructured silica-surfactant hybrid materials*. November 8, 2022.
2. UCSB – Chalmers Colloquium on Materials Science and Engineering, Santa Barbara, California. *Incorporating light-responsive transmembrane protein molecules in mesostructured silica-surfactant hybrid materials*. January 31, 2023.
3. 15th Annual Clorox-Amgen Graduate Student Symposium, Santa Barbara, California. *Understanding the kinetic processes and thermodynamic driving forces to incorporate transmembrane proteins in inorganic/organic hybrid materials.* September 15, 2022.
4. UCSB – Stockholm University Advanced Characterization Techniques for Biological Applications. *Incorporating transmembrane proteins in inorganic/organic hybrid materials.* November 10, 2021.
5. UCSB 1st year Research Presentations Symposium, Santa Barbara, California. *Understanding kinetic processes incorporating transmembrane proteins in inorganic/organic hybrid materials.* September 26, 2018.

ABSTRACT

Understanding the thermodynamics and kinetic processes of transmembrane protein incorporation in nanostructured silica

by

Maxwell Woodcock Berkow

The desirable physicochemical properties and functions of membrane proteins (such as catalysis, biosensing, and ion transport) have generated interest for guest protein moieties in abiotic host systems for technological applications. Specifically, I have used a self-assembled nanostructured silica material host system to exploit the functionality of the light-activated H^+ ion-pump proteorhodopsin outside of its native cell membrane. Incorporated into a device, this protein is promising for applications as a sustainable bio-based alternative for solar-to-electrochemical energy conversion. Traditionally, the inclusion of membrane proteins into non-native inorganic materials has been challenging, in part because the surfactants, polymers, organic solvents, and synthesis conditions used to create well-ordered nanostructures often cause the protein to denature, whereas the biocompatible surfactants that are capable of stabilizing membrane proteins often do not produce the well-ordered nanostructures required of devices. Judicious selection and combination of structure-directing and protein-stabilizing short-chain nonionic surfactants and charged phospholipids has allowed us to stabilize membrane proteins in the cylindrical hydrophobic regions of

surfactants within silica-surfactant materials with high extents of mesostructural order. Furthermore, by optimizing the composition of the host film, I have achieved a record high 44 wt% concentration of functionally active guest membrane proteorhodopsin, which improve the prospects for macroscopic proton transport in devices.

Techniques were drawn from multiple fields of study to characterize and understand how these non-native host materials self-assemble, and how they impact the photocycle kinetics of proteorhodopsin guest molecules. These techniques include small-angle X-ray scattering (SAXS) to determine the mesoscale structure of the silica film, solid-state nuclear magnetic resonance (NMR) spectroscopy to analyze the atomic-scale composition and structure at the surfactant-silica interface, nanofabrication processes to alter substrates and direct self-assembly at the film-substrate interface, cryo-electron microscopy (cryo-EM) to determine the structure and intermolecular interactions of proteorhodopsin in precursor micellar assemblies, and time-resolved UV-visible light spectroscopy to quantify differences in the photocycle of proteorhodopsin due to differences in local host environments. Critically, these nanostructured protein-surfactant-silica films are well-ordered and display promising protein loading, mechanical and thermal robustness, and protein stabilizing effects necessary to exploit the highly desirable functions of membrane proteins. A novel and interdisciplinary approach to characterization, understanding, and subsequent optimization of proteorhodopsin and nanostructured silica films has enabled the preparation of robust abiotic inorganic-organic host materials with record high concentrations of functionally active guest membrane proteins, a significant step towards the integration of membrane proteins into devices.

TABLE OF CONTENTS

Chapter 1. Introduction and Background Information

1.1 General Motivation, Challenges, and Research Objectives

Located at cell boundaries, membrane proteins perform many important functions such as catalysis,[1,2] biosensing,[3] and passive or active ion transport.[4–6] For example, transmembrane proteins such as bacterial rhodopsins behave as light-induced ion pumps capable of solar-to-electrochemical energy conversion;[7] similarly, aquaporin facilitates highly selective water transport and has promising applications in water purification membranes.[8] The function specificity and selectivity exhibited by membrane proteins has been optimized over countless generations as a result of evolutionary biology, often making them superior to current human-designed systems in functions such as biosensing and signal transduction.[9,10] These desirable physiochemical properties have generated interest[11] as guest species in synthetic media for technological applications, potentially circumventing expensive financial and labor costs needed to engineer materials and devices with similar characteristics. Taking advantage of these benefits, my research focuses on understanding the interactions and processes by which membrane proteins can be stabilized and incorporated into non-native host materials in an effort to harness their diverse functions. This is a challenging pursuit due to the complex array of interactions between protein and host material which can disturb both protein stability and function, and in addition can disrupt the formation of a host material with desirable physical and chemical properties.

Membrane proteins are difficult to study in native hosts because cell membranes contain many different proteins that may be sensitive to similar techniques and thereby disrupt data collection. Protein-specific expression and purification techniques have therefore been

developed to isolate the desired membrane protein in synthetic lipid bilayer or micellar hosts. The products of these methods often feature amphiphilic detergent surfactants and lipids that solubilize water-insoluble membrane proteins in aqueous solutions; generally, hydrophobic hydrocarbon chains of surfactants stabilize outward-facing hydrophobic regions of the membrane protein while hydrophilic headgroups of surfactants favorably interact with surrounding water molecules. However, membrane protein stability alone is not indicative of native-like function or dynamics. Changes in the pH, surrounding charges, salt concentrations, or the structure of the host environment (liposomes versus detergent micelles) have been observed to significantly impact functionality of guest membrane proteins (Chapter 2).[12–14] Thus, understanding the influences that host environments have on guest membrane proteins may enable future protein-stabilizing surfactant selections that favorably tune protein function and dynamics. These results can then inform syntheses of highly complex co-assembled protein-containing mesostructured silica-surfactant host materials, which similarly utilize amphiphilic surfactants to stabilize hydrophobic membrane proteins within a hydrophilic robust silica matrix (Chapter 3).[15,16] This silica host matrix improves the mechanical robustness of the host and thermal stability of guest protein moieties when compared with soft synthetic host materials such as synthetic lipid bilayers,[17,18] hydrogels,[19,20] and block copolymers,[20,21] greatly improving the potential to harness the function of these proteins in technological applications. Importantly, solid host-materials are more easily integrated into technical devices as compared to (protein-containing) solutions, and they also adapt membrane proteins from the single protein ~10 nm length scale of a cell membrane, or lipid bilayer, to the macroscopic dimensions necessary to harness the functionalities of membrane proteins in device applications.

My research detailed in this thesis focuses on the incorporation of the transmembrane protein proteorhodopsin (PR), a light-activated proton pump, into these promising mesostructured protein-containing silica-surfactant host materials, with an emphasis on improving the characteristics that I hypothesize are necessary for device integration (Chapter 3). This synthesis utilizes intermolecular interactions similar to synthetic lipid bilayers and micelles, and is generally applicable to transmembrane proteins of similar sizes. These other proteins can have distinct or cooperative functions, which when incorporated into a host film expand the applications of this research to a variety of technologically-relevant functions. For the integration of ion transport proteins such as PR, I hypothesize that a successful material will require (1) significant loadings of stable guest protein moieties, (2) high extents of anisotropic mesostructural order (such as rectangular or hexagonal), and (3) orientational alignment of protein guests and mesochannels. Previous efforts have studied stabilization of PR in the channels of similar mesostructured silica films, however, they displayed limited application viability because of low protein loadings and relatively isotropic mesostructural and orientational ordering.[16] Achieving desirable material properties is challenging because of countervailing material synthesis conditions such as surfactant structure and charge distributions, pH, and organic versus aqueous solvents, which promote either protein stability or the co-assembly of a well-ordered mesostructured silica host. Other focuses of my research are to better understand the kinetic and thermodynamic processes during co-assembly related to PR (Chapter 4) and the host matrix (Chapter 5) to optimize synthesis compositions and conditions to improve mesostructural order and orientational alignment. As a result, I have been able to successfully develop and optimize PR-containing mesostructured silica-surfactant host materials that simultaneously exhibit high protein loadings and high extents of

mesostructural order, and also made significant progress towards achieving orientational mesostructure alignment, getting several steps closer to harnessing diverse membrane protein functions in devices.

1.2 Background

Proteorhodopsin

Proteorhodopsin (PR) is a transmembrane protein found ubiquitously in marine bacteria that acts as a light-activated proton pump, assisting in the supply of adenosine triphosphate (ATP), a source of cellular energy, to organisms such as picoplankton. These organisms are found in the ocean and therefore have native functionality at a pH around 8.2. This functionality involves undergoing a series of conformational changes resulting in the transport of an H^+ ion across the transmembrane region of PR. Under native pH conditions, the D97 residue of PR is deprotonated, necessary for the native photocycle to proceed. At lower pH, such as the film synthesis pH of 4.0, this residue is protonated, restricting transition through the native photocycle and forcing an alternate series of conformations; it is currently debated whether it pumps protons at all under these conditions.[22,23] This means that maintaining a function-capable pH during film synthesis, or returning PR to a function-capable pH after synthesis, is important to developing proton transport in films.

Proteorhodopsin is readily expressed in heterologous systems and known to form functional oligomers (primarily pentamers and hexamers) in a wide variety of membrane mimetic environments, including micellar,[13] bicellar,[24–26] and nanodisc systems.[27] It can also be expressed primarily as monomers, utilizing an E50Q point mutation that disrupts the formation of the oligomer complex but does not impact its optical properties.[28] These

monomers can be approximated as cylinders ~4 nm long and ~3 nm across, making them suitable guests for DDM+POPC+DOTAP-structure-directed mesostructured silica host materials that have center-to-center mesochannel distances of ~4 nm.[15] The functional properties of PR can be measured as a function of systematic modulation of the extent of oligomerization[29] or the makeup of the biomimetic environment.[13,24–26] The minimal functional unit of PR is a polypeptide chain that transverses the bacterial plasma membrane seven times, and that binds a retinal chromophore. Photoactivated PR undergoes a series of conformational changes that perturb the local environment around the retinal chromophore, changing its light-absorbent properties which can thereby be measured as a function of both wavelength and time. PR's proton transport capacity can therefore be conveniently assessed by optical absorption of the embedded retinal to evaluate (1) the rate of proton transport and (2) the population of PR molecules in a photo-active state. The rate of proton transport of PR is measured by the time-resolved change in optical absorbance after excitation with a pulsed green laser.[30–32] These characteristics of proteorhodopsin, as well as its relative high stability compared to other, even more fragile, membrane proteins,[33] make it a model membrane protein candidate for incorporation into mesostructured silica host materials.

Protein host materials

A variety of synthetic host materials have been developed to study membrane proteins better; many of which aim to achieve the most native-like environment, but this can be difficult to define.[34–36] Synthetic lipid bilayers are often used to probe the properties and function of specific membrane proteins, as their central hydrocarbons provide a stable, low dielectric environment with low water content, that strengthens intramolecular hydrogen bonding and structural integrity of the protein.[34] In fatty-acid-based lipid bilayers of

liposomes, hydrophobic lipid chains stabilize the α-helices of the membrane protein, whereas the charged and hydrophilic lipid headgroups at the cytoplasmic and extracellular interfaces stabilize the protein.[37] Similarly, micellar environments stabilize membrane proteins in aqueous environments with amphiphilic detergent molecules that mediate unfavorable interactions between hydrophobic α-helices and water. However, these bilayers and micelles, native or synthetic, exhibit poor mechanical and thermal stabilities and also are not easily processable into macroscopic material morphologies. Amphiphilic block copolymers similarly provide both hydrophilic and hydrophobic regions that offer suitable synthetic environments to stabilize membrane proteins with better mechanical and chemical stabilities, as well as local orientational order.[18,21,38] These wholly organic-amphiphile-based synthetic hosts accommodate modest bulk amounts of membrane proteins, with still relatively poor mechanical properties when compared to solid materials.

In order to improve these properties, protein guest molecules can be incorporated into more robust non-native abiotic hosts, such as polymers, glasses, and mesostructured hybrid materials, with diverse macroscopic morphologies, including particles, fibers, films, or monoliths to improve the mechanical or thermal stabilities of the protein-host system.[15,16] For example, globular proteins can be post-synthetically adsorbed onto the surface of porous materials[39–42] through hydrogen bonding, electrostatic forces, or hydrophobic effects; however, these interactions are generally transient or weak, and leaching of the catalyst can result in a loss of activity.[43] Alternatively, biologically-enabled materials can be made through the co-assembly and subsequent cross-linking of polymeric or inorganic oxide matrices around protein moieties, producing uniform distributions of stable and functionally-active guest molecules. While useful for relatively hydrophilic globular proteins,[44] hydrophilic host

environments such as silica tend to be incompatible with transmembrane proteins that are particularly challenging to incorporate into non-native host environments, due in part to their heterogeneous amphiphilic character. Nevertheless, as a host material for proteins, silica-surfactant films are a good candidate, because they are mechanically and thermally robust and can be synthesized under relatively mild conditions with structure-directing surfactants that create hydrophobic pockets that can accommodate stable membrane proteins.[15,16] These mesostructured silica-surfactant films display promising characteristics with the potential to harness varied membrane protein functions, and are the primary focus of this thesis.

Thermodynamic and kinetic effects on self-assembly

The self-assembly of any solution is governed in part by thermodynamics, and therefore a system's propensity is to reach its lowest possible Gibbs free energy state. If given infinite time to assemble, the solution will reach thermodynamic equilibrium, maximizing favorable and minimizing unfavorable interactions. In the case of proteorhodopsin-containing mesostructured silica-surfactant materials, this means that hydrophilic silica will associate with hydrophilic surfactant headgroups and hydrophobic surfactant tail groups will associate with each other as well as the predominantly hydrophobic proteorhodopsin moieties.[15] To achieve self-assembly into the lowest possible energy state, periodic mesophases form (such as hexagonal, lamellar, or cubic) dependent on the ratio and properties of the self-assembling components. The binary phase diagram of *n*-dodecyl-*β*-*D*-maltoside (DDM) and water shows that at temperatures greater than 15 °C, liquid crystals of DDM and water will form micelles below 49 wt% DDM and hexagonal phases from 49 wt% to 75 wt% DDM.[45] Similarly, the ternary phase diagram of DDM, water, and Cetyltrimethylammonium bromide (CTAB, an amphiphilic organic surfactant with a relatively long 16 chain carbon hydrophobic tail group)

at 50 °C displays a transition from the micellar to hexagonal phase when DDM+CTAB content reaches approximately 40 wt% and extends until 75 wt%.[46] While promising for the selection of mesostructured film compositions, these surfactant ranges cannot be strictly applied to mesostructured silica films because the presence of silica alters the thermodynamically preferred phase and importantly, because phase diagrams assume equilibrium conditions.

In the case of the evaporation-induced self-assembly of mesostructured silica materials, thermodynamic equilibrium is often never achieved because water evaporation alters which phase is thermodynamically favored, which can be seen as the composition shifts across the phase diagram, and silica polymerization increases solution viscosity thus disrupting the rearrangement of co-assembling molecules. Syntheses of these materials under non-equilibrium conditions are governed by (1) the thermodynamics of co-assembly and interactions between the protein, surfactant, solvent, and silica species, and (2) the kinetic processes associated with the rates of solvent evaporation, co-assembly of the component species, and polymerization of the silica into a robust cross-linked matrix. Mesostructured silica materials have been synthesized with high extents of mesostructural ordering utilizing very high or low pH or with high concentrations of organic solvents in order to slow (or temporarily stop) the rate of silica polymerization until a well-ordered mesophase has formed. However, these conditions generally denature membrane proteins. This means that other methods must be found to achieve high extents of mesostructural ordering in proteorhodopsin-containing mesostructured silica host materials.

1.3 Dissertation Outline

This dissertation covers the work that I have done to understand and synthesize mesostructured silica-surfactant membrane protein host materials and is organized into chapters differentiated by primary focus. Each chapter has been written as a modular exposition and includes an abstract, introduction to relevant information, presentation and discussion of relevant results that I have collected, conclusions, discussion of future work, and references lists. When relevant, chapters also include supporting information. Brief summaries of each chapter are presented below.

Chapter 2: Lipid membrane mimetics and oligomerization tune functional properties of proteorhodopsin. Transmembrane proteins play critical roles in a wide array of biological processes at the interface between the cell and its surrounding environment. The functional properties of these proteins have been shown to heavily depend on their oligomeric distributions and the membrane mimetic environment in which they are encapsulated. This study seeks to distinguish and compare the impacts of these two factors on the functional properties of a model transmembrane protein, the bacterial proteorhodopsin (PR). The findings from this study demonstrate the different mechanisms by which oligomerization and biomimetic composition modulate PR functions, emphasizing the importance of investigating the structure-function relationship of transmembrane proteins, while controlling for oligomerization and in different membrane mimetics.

Chapter 3: Co-assembly of functionally-active proteorhodopsin membrane protein molecules in mesostructured silica-surfactant films. While membrane proteins perform many varied industrially-relevant functions in cells, they lack stability and the

macroscopic framework needed to be integrated into instruments. Co-assembled mesostructured silica-surfactant composites provide a means to harness these highly selective and efficient capabilities. However, this dynamic multicomponent synthesis process is further complicated by countervailing synthesis conditions that promote either high and stable protein loadings or the formation of a suitable host film with significant mesostructural ordering, both of which are required characteristics of a functional protein-host film. A combination of small-angle X-ray scattering, UV-visible light spectroscopy, and solid-state NMR provide detailed insights on how these non-native host materials co-assemble, and how they impact the photocycle kinetics of the hosted proteorhodopsin guests. This novel and interdisciplinary approach to characterizing and understanding the structure-function relationships between proteorhodopsin, surfactants, and silica species has enabled the incorporation of up to a record 44 wt% proteorhodopsin into robust mesostructured silica-surfactant films.

Chapter 4: Cryo-electron microscopy analyses of oligomeric proteorhodopsin in micellar DDM solutions. Three-dimensional structures have only been solved for a small fraction of transmembrane proteins (and less than 6% of all solved protein structures) due in part to the highly complex relationship between the membrane protein and stabilizing-surfactants. Membrane proteins make up 50-60% of all drug targets and the interface between the protein and membrane is a common pathway for pharmaceutical drugs to reach key binding sites. While important to understand, many membrane proteins are extremely difficult to crystallize for X-ray crystallography and too large to study by NMR, the two traditional methods of protein-structure determination. Recent advances in instrumentation and computation have made cryogenic electron microscopy (cryo-EM) the new leading technique

to investigate these industrially and medically relevant molecules. This chapter covers my research into the structure of proteorhodopsin oligomers in surfactant micelles.

Chapter 5: Orientationally ordered mesostructured silica-surfactant protein-host films. To exploit the properties of proteins outside of native cell membranes, straight, parallel paths are desired because they provide a cohesive direct path for large-scale molecule or ion transport. One method of achieving macroscopic orientational alignment of cylindrical mesochannels is through the use of a micropatterned semipermeable stamp that facilitates solvent evaporation pathways and induces nucleation at desired interfaces. However, the processes which enable this are not well understood or immediately transferable to other film compositions such as the film that I have optimized for high proteorhodopsin loadings, in which new intermolecular interactions join the already complex transient co-assembly observed in freestanding films. This chapter focuses on my efforts to macroscopically orient protein-containing silica-surfactant films, on what I've learned, and on future steps to be taken which I believe can finally achieve this goal.

1.4 References

(1) Shieh, F.-K.; Wang, S.-C.; Yen, C.-I.; Wu, C.-C.; Dutta, S.; Chou, L.-Y.; Morabito, J. V.; Hu, P.; Hsu, M.-H.; Wu, K. C.-W.; Tsung, C.-K. Imparting Functionality to Biocatalysts via Embedding Enzymes into Nanoporous Materials by a *de Novo* Approach: Size-Selective Sheltering of Catalase in Metal–Organic Framework Microcrystals. *J. Am. Chem. Soc.* **2015**, *137* (13), 4276–4279. https://doi.org/10.1021/ja513058h.

(2) Hudson, S.; Cooney, J.; Magner, E. Proteins in Mesoporous Silicates. *Angew. Chem. Int. Ed.* **2008**, *47* (45), 8582–8594. https://doi.org/10.1002/anie.200705238.

(3) Swift, B. J. F.; Shadish, J. A.; DeForest, C. A.; Baneyx, F. Streamlined Synthesis and Assembly of a Hybrid Sensing Architecture with Solid Binding Proteins and Click Chemistry. *J. Am. Chem. Soc.* **2017**, *139* (11), 3958–3961. https://doi.org/10.1021/jacs.7b00519.

(4) Wang, M.; Wang, Z.; Wang, X.; Wang, S.; Ding, W.; Gao, C. Layer-by-Layer Assembly of Aquaporin Z-Incorporated Biomimetic Membranes for Water Purification. *Environ. Sci. Technol.* **2015**, *49* (6), 3761–3768. https://doi.org/10.1021/es5056337.

(5) Fane, A. G.; Wang, R.; Hu, M. X. Synthetic Membranes for Water Purification: Status and Future. *Angew. Chem. Int. Ed.* **2015**, *54* (11), 3368–3386. https://doi.org/10.1002/anie.201409783.

(6) Oda, I.; Hirata, K.; Watanabe, S.; Shibata, Y.; Kajino, T.; Fukushima, Y.; Iwai, S.; Itoh, S. Function of Membrane Protein in Silica Nanopores: Incorporation of Photosynthetic Light-Harvesting Protein LH2 into FSM. *J. Phys. Chem. B* **2006**, *110* (3), 1114–1120. https://doi.org/10.1021/jp0540860.

(7) Béjà, O.; Lanyi, J. K. Nature's Toolkit for Microbial Rhodopsin Ion Pumps. *Proc. Natl. Acad. Sci. U.S.A.* **2014**, *111* (18), 6538–6539. https://doi.org/10.1073/pnas.1405093111.

(8) Camilleri-Rumbau, M. S.; Soler-Cabezas, J. L.; Christensen, K. V.; Norddahl, B.; Mendoza-Roca, J. A.; Vincent-Vela, M. C. Application of Aquaporin-Based Forward Osmosis Membranes for Processing of Digestate Liquid Fractions. *Chemical Engineering Journal* **2019**, *371*, 583–592. https://doi.org/10.1016/j.cej.2019.02.029.

(9) Misawa, N.; Osaki, T.; Takeuchi, S. Membrane Protein-Based Biosensors. *J. R. Soc. Interface.* **2018**, *15* (141), 20170952. https://doi.org/10.1098/rsif.2017.0952.

(10) Misra, N.; Martinez, J. A.; Huang, S.-C. J.; Wang, Y.; Stroeve, P.; Grigoropoulos, C. P.; Noy, A. Bioelectronic Silicon Nanowire Devices Using Functional Membrane Proteins. *Proc. Natl. Acad. Sci. U.S.A.* **2009**, *106* (33), 13780–13784. https://doi.org/10.1073/pnas.0904850106.

(11) Fischer, F.; Wolters, D.; Rögner, M.; Poetsch, A. Toward the Complete Membrane Proteome. *Molecular & Cellular Proteomics* **2006**, *5* (3), 444–453. https://doi.org/10.1074/mcp.M500234-MCP200.

(12) Han, C.-T.; Nguyen, K. D. Q.; Berkow, M. W.; Hussain, S.; Kiani, A.; Kinnebrew, M.; Idso, M. N.; Baxter, N.; Chang, E.; Aye, E.; Winslow, E.; Rahman, M.; Seppälä, S.; O'Malley, M. A.; Chmelka, B. F.; Mertz, B.; Han, S. Lipid Membrane Mimetics and Oligomerization Tune Functional Properties of Proteorhodopsin. *Biophysical Journal* **2023**, *122* (1), 168–179. https://doi.org/10.1016/j.bpj.2022.11.012.

(13) Idso, M. N.; Baxter, N. R.; Narayanan, S.; Chang, E.; Fisher, J.; Chmelka, B. F.; Han, S. Proteorhodopsin Function Is Primarily Mediated by Oligomerization in Different Micellar Surfactant Solutions. *J. Phys. Chem. B* **2019**, *123* (19), 4180–4192. https://doi.org/10.1021/acs.jpcb.9b00922.

(14) Han, C.-T.; Song, J.; Chan, T.; Pruett, C.; Han, S. Electrostatic Environment of Proteorhodopsin Affects the PKa of Its Buried Primary Proton Acceptor. *Biophysical Journal* **2020**, *118* (8), 1838–1849. https://doi.org/10.1016/j.bpj.2020.02.027.

(15) Berkow, M. W.; Gwak, H.; Idso, M. N.; Schmithorst, M. B.; Rhodes, B.; Price, B.; Gianola, D. S.; Han, S.; Chmelka, B. F. Co-Assembly of Functionally-Active Proteorhodopsin Membrane Protein Molecules in Mesostructured Silica-Surfactant Films. *Chemistry of Materials* **2023**, under review.

(16) Jahnke, J. P.; Idso, M. N.; Hussain, S.; Junk, M. J. N.; Fisher, J. M.; Phan, D. D.; Han, S.; Chmelka, B. F. Functionally Active Membrane Proteins Incorporated in Mesostructured Silica Films. *J. Am. Chem. Soc.* **2018**, *140* (11), 3892–3906. https://doi.org/10.1021/jacs.7b06863.

(17) Janshoff, A.; Steinem, C. Transport across Artificial Membranes–an Analytical Perspective. *Anal Bioanal Chem* **2006**, *385* (3), 433–451. https://doi.org/10.1007/s00216-006-0305-9.

(18) Liang, H.; Whited, G.; Nguyen, C.; Stucky, G. D. The Directed Cooperative Assembly of Proteorhodopsin into 2D and 3D Polarized Arrays. *Proc. Natl. Acad. Sci. U.S.A.* **2007**, *104* (20), 8212–8217. https://doi.org/10.1073/pnas.0702336104.

(19) Jeon, T.-J.; Malmstadt, N.; Schmidt, J. J. Hydrogel-Encapsulated Lipid Membranes. *J. Am. Chem. Soc.* **2006**, *128* (1), 42–43. https://doi.org/10.1021/ja056901v.

(20) Ma, D.; Zhao, Y.; Wu, J.; Cui, T.; Ding, J. A Block-Copolymer Hydrogel Encapsulates Bacteriorhodopsin and Produces the Longest Photochromic Response of the Membrane Protein under High Water Content Conditions. *Soft Matter* **2009**, *5* (23), 4635. https://doi.org/10.1039/b917438a.

(21) Hua, D.; Kuang, L.; Liang, H. Self-Directed Reconstitution of Proteorhodopsin with Amphiphilic Block Copolymers Induces the Formation of Hierarchically Ordered Proteopolymer Membrane Arrays. *J. Am. Chem. Soc.* **2011**, *133* (8), 2354–2357. https://doi.org/10.1021/ja109796x.

(22) Friedrich, T.; Geibel, S.; Kalmbach, R.; Chizhov, I.; Ataka, K.; Heberle, J.; Engelhard, M.; Bamberg, E. S0272884200001103.Pdf. **2002**, 821–838. https://doi.org/10.1016/S0022283602006964.

(23) Wang, W. W.; Sineshchekov, O. A.; Spudich, E. N.; Spudich, J. L. Spectroscopic and Photochemical Characterization of a Deep Ocean Proteorhodopsin. *Journal of Biological Chemistry* **2003**, *278* (36), 33985–33991. https://doi.org/10.1074/jbc.M305716200.

(24) Tunuguntla, R.; Bangar, M.; Kim, K.; Stroeve, P.; Ajo-Franklin, C. M.; Noy, A. Lipid Bilayer Composition Can Influence the Orientation of Proteorhodopsin in Artificial Membranes. *Biophysical Journal* **2013**, *105* (6), 1388–1396. https://doi.org/10.1016/j.bpj.2013.07.043.

(25) Lindholm, L.; Ariöz, C.; Jawurek, M.; Liebau, J.; Mäler, L.; Wieslander, Å.; Von Ballmoos, C.; Barth, A. Effect of Lipid Bilayer Properties on the Photocycle of Green Proteorhodopsin. *Biochimica et Biophysica Acta (BBA) - Bioenergetics* **2015**, *1847* (8), 698–708. https://doi.org/10.1016/j.bbabio.2015.04.011.

(26) Han, C.-T.; Song, J.; Chan, T.; Pruett, C.; Han, S. Electrostatic Environment of Proteorhodopsin Affects the PKa of Its Buried Primary Proton Acceptor. *Biophysical Journal* **2020**, *118* (8), 1838–1849. https://doi.org/10.1016/j.bpj.2020.02.027.

(27) Ranaghan, M. J.; Schwall, C. T.; Alder, N. N.; Birge, R. R. Green Proteorhodopsin Reconstituted into Nanoscale Phospholipid Bilayers (Nanodiscs) as Photoactive Monomers. *J. Am. Chem. Soc.* **2011**, *133* (45), 18318–18327. https://doi.org/10.1021/ja2070957.

(28) Maciejko, J.; Mehler, M.; Kaur, J.; Lieblein, T.; Morgner, N.; Ouari, O.; Tordo, P.; Becker-Baldus, J.; Glaubitz, C. Visualizing Specific Cross-Protomer Interactions in the Homo-Oligomeric Membrane Protein Proteorhodopsin by Dynamic-Nuclear-Polarization-Enhanced Solid-State NMR. *J. Am. Chem. Soc.* **2015**, *137* (28), 9032–9043. https://doi.org/10.1021/jacs.5b03606.

(29) Hussain, S.; Kinnebrew, M.; Schonenbach, N. S.; Aye, E.; Han, S. Functional Consequences of the Oligomeric Assembly of Proteorhodopsin. *Journal of Molecular Biology* **2015**, *427* (6), 1278–1290. https://doi.org/10.1016/j.jmb.2015.01.004.

(30) Váró, G.; Lanyi, J. K. Distortions in the Photocycle of Bacteriorhodopsin at Moderate Dehydration. *Biophysical Journal* **1991**, *59* (2), 313–322. https://doi.org/10.1016/S0006-3495(91)82225-1.

(31) Váró, G.; Brown, L. S.; Lakatos, M.; Lanyi, J. K. Characterization of the Photochemical Reaction Cycle of Proteorhodopsin. *Biophysical Journal* **2003**, *84* (2), 1202–1207. https://doi.org/10.1016/S0006-3495(03)74934-0.

(32) Dioumaev, A. K.; Brown, L. S.; Shih, J.; Spudich, E. N.; Spudich, J. L.; Lanyi, J. K. Proton Transfers in the Photochemical Reaction Cycle of Proteorhodopsin. *Biochemistry* **2002**, *41* (17), 5348–5358. https://doi.org/10.1021/bi025563x.

(33) Gourdon, P.; Alfredsson, A.; Pedersen, A.; Malmerberg, E.; Nyblom, M.; Widell, M.; Berntsson, R.; Pinhassi, J.; Braiman, M.; Hansson, Ö.; Bonander, N.; Karlsson, G.; Neutze, R. Optimized in Vitro and in Vivo Expression of Proteorhodopsin: A Seven-

Transmembrane Proton Pump. *Protein Expression and Purification* **2008**, *58* (1), 103–113. https://doi.org/10.1016/j.pep.2007.10.017.

(34) Page, R. C.; Li, C.; Hu, J.; Gao, F. P.; Cross, T. A. Lipid Bilayers: An Essential Environment for the Understanding of Membrane Proteins. *Magn. Reson. Chem.* **2007**, *45* (S1), S2–S11. https://doi.org/10.1002/mrc.2077.

(35) Ratkeviciute, G.; Cooper, B. F.; Knowles, T. J. Methods for the Solubilisation of Membrane Proteins: The Micelle-Aneous World of Membrane Protein Solubilisation. *Biochemical Society Transactions* **2021**, *49* (4), 1763–1777. https://doi.org/10.1042/BST20210181.

(36) Khan, M.; Dosoky, N.; Williams, J. Engineering Lipid Bilayer Membranes for Protein Studies. *IJMS* **2013**, *14* (11), 21561–21597. https://doi.org/10.3390/ijms141121561.

(37) Bogdanov, M.; Dowhan, W.; Vitrac, H. Lipids and Topological Rules Governing Membrane Protein Assembly. *Biochimica et Biophysica Acta (BBA) - Molecular Cell Research* **2014**, *1843* (8), 1475–1488. https://doi.org/10.1016/j.bbamcr.2013.12.007.

(38) Liang, H.; Whited, G.; Nguyen, C.; Okerlund, A.; Stucky, G. D. Inherently Tunable Electrostatic Assembly of Membrane Proteins. *Nano Lett.* **2008**, *8* (1), 333–339. https://doi.org/10.1021/nl0729173.

(39) Kalantari, M.; Yu, M.; Yang, Y.; Strounina, E.; Gu, Z.; Huang, X.; Zhang, J.; Song, H.; Yu, C. Tailoring Mesoporous-Silica Nanoparticles for Robust Immobilization of Lipase and Biocatalysis. *Nano Res.* **2017**, *10* (2), 605–617. https://doi.org/10.1007/s12274-016-1320-6.

(40) Deodhar, G. V.; Adams, M. L.; Trewyn, B. G. Controlled Release and Intracellular Protein Delivery from Mesoporous Silica Nanoparticles. *Biotechnol. J.* **2017**, *12* (1), 1600408. https://doi.org/10.1002/biot.201600408.

(41) Cha, B. G.; Jeong, J. H.; Kim, J. Extra-Large Pore Mesoporous Silica Nanoparticles Enabling Co-Delivery of High Amounts of Protein Antigen and Toll-like Receptor 9

Agonist for Enhanced Cancer Vaccine Efficacy. *ACS Cent. Sci.* **2018**, *4* (4), 484–492. https://doi.org/10.1021/acscentsci.8b00035.

(42) Juère, E.; Caillard, R.; Marko, D.; Del Favero, G.; Kleitz, F. Smart Protein-Based Formulation of Dendritic Mesoporous Silica Nanoparticles: Toward Oral Delivery of Insulin. *Chem. Eur. J.* **2020**, *26* (23), 5195–5199. https://doi.org/10.1002/chem.202000773.

(43) Califano, V.; Costantini, A. Immobilization of Cellulolytic Enzymes in Mesostructured Silica Materials. *Catalysts* **2020**, *10* (6), 706. https://doi.org/10.3390/catal10060706.

(44) Blin, J. L.; Gérardin, C.; Carteret, C.; Rodehüser, L.; Selve, C.; Stébé, M. J. Direct One-Step Immobilization of Glucose Oxidase in Well-Ordered Mesostructured Silica Using a Nonionic Fluorinated Surfactant. *Chem. Mater.* **2005**, *17* (6), 1479–1486. https://doi.org/10.1021/cm048033r.

(45) Auvray, X.; Petipas, C.; Anthore, R.; Rico-Lattes, I.; Lattes, A. X-Ray Diffraction Study of the Ordered Lyotropic Phases Formed by Sugar-Based Surfactants. *Langmuir* **1995**, *11* (2), 433–439. https://doi.org/10.1021/la00002a012.

(46) Rahman, M. S.; Rankin, S. E. Predictive Synthesis of Ordered Mesoporous Silica with Maltoside and Cationic Surfactants Based on Aqueous Lyotropic Phase Behavior. *Journal of Colloid and Interface Science* **2010**, *342* (1), 33–42. https://doi.org/10.1016/j.jcis.2009.10.021.

Chapter 2. Lipid membrane mimetics and oligomerization tune functional properties of proteorhodopsin

---

This chapter is adapted from a published paper. I am co-first author on this paper and my contributions include time-resolved UV-visible light spectroscopy and analyses, the preparation and analyses of proteorhodopsin in SMA lipid nanodiscs, sample preparation and analyses of micellar proteorhodopsin via cryo-electron microscopy, and writing/editing.

Paper: *Biophysical Journal* **2023** *122* (1), 168-179

Authors: Chung-Ta Han*, Khanh Dinh Quoc Nguyen*, Maxwell W. Berkow*, Sunyia Hussain, Ahmad Kiani, Maia Kinnebrew, Matthew N. Idso, Naomi Baxter, Evelyn Chang, Emily Aye, Elsa Winslow, Mohammad Rahman, Susanna Seppälä, Michelle A. O'Malley, Bradley F. Chmelka, Blake Mertz, and Songi Han

* *Each of these authors contributed equally to the work*

DOI: 10.1016/j.bpj.2022.11.012

2.1 Abstract

The functional properties of proteorhodopsin (PR) have been found to be strongly modulated by oligomeric distributions and lipid membrane mimetics. This study aims to distinguish and explain their effects by investigating how oligomer formation impacts PR's function of proton transport in lipid-based membrane mimetic environments. We find that PR forms stable hexamers and pentamers in both *E. coli* membrane and synthetic liposomes. Compared with the monomers, the photocycle kinetics of PR oligomers is ~2 and ~4.5 times slower for transitions between the *K* and *M* and the *M* and *N* photo-intermediates, respectively, indicating that oligomerization significantly slows PR's rate constant of proton transport in liposomes. In contrast, the apparent pKa of the key proton acceptor residue D97 (pKa_{D97}) of liposome-embedded PR persists at 6.2–6.6, regardless of cross-protomer modulation of D97, suggesting that the liposome environment helps maintain PR's functional activity at neutral pH. By comparison, when extracted directly from *E. coli* membranes into styrene-maleic acid lipid particles (SMALPs), the pKa_{D97} of monomer-enriched E50Q PR drastically increases to 8.9, implying that there is a very low active PR population at neutral pH to engage in PR's photocycle. These findings demonstrate that oligomerization impacts PR's photocycle kinetics, while lipid-based membrane mimetics strongly affect PR's active population via different mechanisms.

2.2 Introduction

Transmembrane proteins are biomacromolecules that serve a multitude of crucial roles at the interface between the cell and its environment, including sensing[1], catalysis[2,3], and transport[4–6]. These proteins have extensive hydrophobic regions, which facilitate inter-protein interactions and require encapsulation in membrane mimetics, the former resulting in oligomerization[7–10]. Both oligomer formation[9–17] and the choice of the membrane mimetic environment[18–25] can exert significant impact on the functional properties of these proteins. Since these two factors are often interdependent[11,13,21], few studies have distinguished and compared their effects on transmembrane protein function. We hypothesized that the effect of these factors can be delineated by studying proteorhodopsin (PR), a model transmembrane proton pump whose functional properties can be measured as a function of systematic modulation of the extent of oligomerization[11] or the makeup of the biomimetic environment[18–21].

PR is a light-driven proton pump that is found in a variety of marine bacteria. The minimal functional unit of PR is a polypeptide chain that transverses the bacterial plasma membrane seven times, and that binds a retinal chromophore. PR is readily expressed in heterologous systems and known to form functional oligomers (primarily pentamers and hexamers) in a wide variety of membrane mimetic environments, including micellar[21], bicellar[18–20], and nanodisc systems[26]. PR's proton transport capacity is conveniently assessed by optical absorption of the embedded retinal to evaluate: i) the rate of proton transport and ii) the population of PR's active state. i) The rate of proton transport of PR is measured by the time-resolved change in optical absorbance after excitation with a pulsed green laser[27–29]. Photoactivated PR undergoes a series of conformational changes that perturb the local

environment of the retinal chromophore, resulting in photo-intermediate that constitute the photochemical reaction cycle. The transient conformational states, sequentially labeled as *K*, M_1/M_2, *N*, and *PR*', contribute to the overall optical absorbance spectrum, with partially resolved absorbances centered respectively at 555 nm, 410 nm, 560 nm, and 520 nm. ii) The activity of PR depends on the protonation state of its primary proton acceptor residue D97, *i.e.* pKa_{D97}[29–32]. Light-induced isomerization of the embedded retinal enables proton transfer to residue D97, requiring the aspartic acid to be deprotonated in the ground state[31]. The active form of PR, when residue D97 is deprotonated, absorbs maximally at around 518 nm, exhibiting a pink color. Conversely, when D97 is protonated and therefore unavailable to accept protons, PR absorbs maximally at around 535 nm, exhibiting a purple color. Given this pH-dependent color transition, the pKa_{D97} of PR, i.e. the active state of PR, can be readily observed via optical absorption spectroscopy as a function of bulk solution pH, followed by determination of the isosbestic point at 570 nm[29,32,33].

Using these well-established approaches, previous studies found that detergent-solubilized PR is affected more strongly by oligomeric distribution than by detergent micelle composition[10,11,21]. For example, PR's photocycle kinetics in detergent micelles is only subtly modulated by varying micelle composition, but it is significantly slowed down by oligomerization[21]. Further, oligomerization is critical for maintaining the population of active PR at neutral pH, given that the pKa_{D97} of PR oligomers (6.5–6.7) is much lower than that of its monomeric form (7.4–7.8) regardless of detergent type[11]. In contrast, it has been found that liposome composition strongly influences PR's proton transport properties. Specifically, the apparent pKa_{D97} of PR in positively charged POPC/DOTAP liposomes (with 5.6) has been shown to be much lower than in the negatively charged POPC/POPG counterpart (with

7.6), while in the presence of 150 mM NaCl concentration, these differences are smaller.[20] Clearly, both oligomer distribution and lipid-based mimetic composition can impact PR's proton transport activity. However, it is unclear which factor plays a stronger role and by what mechanism.

It is clear that the cross-protomer W34–H75 hydrogen bond electrostatically stabilizes the protonated state of residue D97, even though it remains unclear how oligomerization affects the overall proton transport function of PR.[34–37] The functional role of PR oligomerization can be investigated by disrupting cross-protomer interactions and observing changes in PR's proton transport properties. PR oligomers can be disrupted and separated by aminio acid substitutions or by size-exclusion chromatography (SEC). The W34D substitution disrupts the cross-protomer hydrogen bond while maintaining the PR oligomer assemblies, and leads to a substantially increased pKa_{D97}[34,36]. The E50Q substitution also disrupts the cross-protomer interaction, but by destabilizing the PR oligomers given that residue E50 is among the key residues at the oligomeric interface of PR[36]. Lastly, SEC can be used to isolate the smaller oligomeric species of PR wild-type (WT) that coexist with the larger (pentamer and hexamer) oligomer populations.

In this study, we characterized the functional roles of PR oligomerization in different lipid-based membrane mimetic platforms, including synthetic POPC/POPG liposomes and styrene maleic acid (SMA) lipid particles (SMALPs). The oligomeric distributions of PR in *E. coli* membranes and liposomes were investigated by chemical crosslinking and gel electrophoresis, electron paramagnetic resonance (EPR) spectroscopy, and molecular dynamics (MD) simulations. The proton transport function of the W34D mutant, E50Q mutant, and various SEC-separated oligomeric species of PR WT was evaluated via

measurements of pKa_{D97} and photocycle kinetics. The novel findings from this study highlight the substantial impact of oligomeric distribution and lipid-based membrane mimetics on the function of PR.

2.3 Materials and Methods

PR expression, purification, and separation of oligomers

Cysteine-free green-light absorbing PR with a C-terminal 6x His tag, both with and without the E50Q mutant that increased the population of monomeric PR[36] and the W34D mutant that disrupted the cross-protomer interaction[34], were expressed and purified using the protocol described in our previous studies[10,11]. Briefly, site-directed mutagenesis with a two-stage polymerase chain reaction (PCR) technique[38] was applied here to introduce desired single mutations at residues mentioned above. The PR gene template with desired mutations was then cloned into a pET26b (+) vector (Novagen) for expression in BL21(DE3). After PR was expressed and then purified by first isolating membranes using centrifugation, solubilizing membrane proteins in 2 wt% DDM, and then using Ni-NTA resin (Thermo Scientific) in batch mode to pull down His-tagged PR, the protein was buffer exchanged into a 150 mM potassium chloride, 50 mM potassium phosphate dibasic buffer (pH 8.2) with 0.05 wt% DDM using a PD-10 desalting column contains Sephadex G-25 resin (GE Healthcare) for storage and characterization purposes.

The removal of His-tag was done by a tobacco etch virus (TEV) protease (Sigma Aldrich), which recognize and cleave the sequence ENLYFQS in between the C-terminus of PR and the His-tag. His-tag removal reaction was done by first buffer exchanging PR into a 50 mM Tris-HCl buffer (pH 8) with 0.5 μM EDTA, 1 mM DTT and 0.05 wt% DDM after its

elution from Ni-NTA resin. Next, TEV protease was added to the PR solution at a protein-to-protein ratio of 1:100 (w/w) and incubated overnight at 4°C with gently mixing. The reacted solution was then buffer exchanged into the 50 mM potassium phosphate dibasic buffer (pH = 8.2) with 150 mM potassium chloride and 0.05 wt% DDM using the PD-10 desalting column for removing the EDTA, and then combined with the Ni-NTA resin. The mixture was mixed for 5 hours at 4°C to remove the unreacted PR that still has His-tag and residual TEV protease from the solution. The collected solution with Ni-NTA resin removed was the PR product with its His-tag removed.

Certain samples with enriched monomer or specific oligomeric species of PR were achieved by separation with a size exclusion column (SEC) after previous purification steps, as in other studies[10,11]. PR was loaded on a HiLoad™ 16/600 Superdex™ 200 pg (GE Healthcare) connected to a BioRad Duoflow FPLC and was then run through the column by applying the 150 mM potassium chloride, 50 mM potassium phosphate dibasic buffer (pH 8.2) with 0.05 % DDM at 0.5 mL/min. The collected protein fractions were concentrated using Amicon Ultra-15 Centrifuge Filter units with a 50 kDa cutoff limit (Millipore) and the oligomeric state of each concentrated PR sample was later confirmed by gel electrophoresis measurements.

Preparation of PR-containing liposomes

Large unilamellar vesicles with desired composition were prepared by a lipid extrusion method. Lipid stocks dissolved in chloroform were purchased from Avanti Polar Lipids and mixed to achieve a desired molar ratio between different lipid species. The lipid mixture was then dried under a nitrogen stream and further desiccated under vacuum overnight to ensure the removal of residue chloroform. The dried lipids were reconstituted

with a HEPES buffer (10 mM HEPES, 150 mM NaCl, pH 6.7), and lipid vesicles were extruded through the Avanti mini-extruder for 19 times using filters with 200 nm pore size. The prepared lipid vesicles were then mixed with DDM surfactant solution to achieve a final DDM concentration 2 times the DDM critical micelle concentration (0.0088 w/v %). The mixture was gently shaken for 1 hr to form lipid-surfactant complexes, and the desired type of PR was then added to the mixture with a 1:50 PR-to-lipid molar ratio. The DDM surfactants in PR-lipid-DDM complex were then removed by using six vials of ~160 mg polystyrene BioBeads SM2 (Bio-Rad) to drive the formation of PR liposomes.

SMA solubilization of PR

SMALP30010P was purchased from Orbiscope (Netherlands). PR-expressing *E. coli* membranes, at a final concentration of 40 mg/mL, were incubated in 50 mM Tris-HCl, 10% glycerol, 300 mM NaCl, 2.5% w/v SMA, pH 8.0 for 20 h at 25°C with gentle rotation. Non-solubilized material was sedimented at 100,000 × g for 1 h at 4°C to yield a supernatant containing PR-SMALP.

Native gel electrophoresis and Western Blotting

Blue native polyacrylamide gel electrophoresis (BN-PAGE) was performed using an XCell SureLock® Mini-Cell apparatus with NativePAGE™ Bis-Tris Protein Gels having a 3-12% acrylamide gradient (ThermoFisher). PR sample preparation and gel electrophoresis were performed according to the instructions provided by the manufacturer. The destained gel was then imaged with a ChemiDoc MP imaging system (Bio-Rad) using the default protocol for Coomassie blue dyes. Western blotting of BN-PAGE was performed using an XCell II™ Blot Module by following the instructions for Western blotting of NativePAGE™ Gels provided by the manufacturer. The blotted PVDF membrane was rinsed with deionized

water and blocked in a TBST buffer containing 5% (w/v) dry milk. The immunodetection was then done by applying HRP conjugated Anti-6X His tag® antibody (Abcam, Cambridge, MA, USA; ab1187) targeted to the six-histidine tag at the N-terminus of PR at 1:5000 in a TBST buffer containing 0.5% (w/v) milk. The membrane was then imaged with a ChemiDoc MP imaging system (Bio-Rad) using the default protocol for chemifluorescence dyes.

SDS-PAGE and PR crosslinking

Crosslinking of inter-PR lysines using the chemical crosslinkers DSG, DSS, or BSOCOES were performed similarly to as reported in the literature[39]. A small volume of crosslinker in a freshly made 150 mM DMSO solution was added in large molar excess (20-100 times) relative to the amount of PR in the base phosphate buffer, quantified by optical absorption, such that the final DSS concentration was 2 mM. After incubation for one hour at room temperature with gently mixing, the crosslinking reaction was quenched by addition of Tris to a final concentration of 50 mM. The same procedure was used to crosslink purified PR and PR in *E. coli* membranes extracted by ultracentrifugation (220,000 g) after cell lysis.

SDS-PAGE was performed using a Bio-Rad electrophoresis apparatus with Criterion TGX Stain-Free gels having an 8-16% acrylamide gradient (Bio-Rad). Samples containing ~3 μg PR were incubated at 37^{o}C for 30 minutes to 1 hour with Laemmli buffer (final SDS concentration of 1%), and then centrifuged to remove the unsolubilized portions. The gel was run at 120 V for one hour and imaged with a ChemiDoc MP imaging system (Bio-Rad) using a PR-specific protocol (excitation with green epi light and 695/705 filters to detect emission) based on the fluorescence properties of PR.172 Protein markers (Precision Plus, Bio-Rad) and total proteins were further imaged using the Stain-Free protocol of ChemiDoc MP. Molecular weight estimates were calculated using the ImageLab software (Bio-Rad).

Molecular dynamics simulation on blue-light absorbing PR (BPR) oligomers in lipid bilayers

The X-ray crystal structures of BPR pentamer from HOT75 (PDB: 4KLY) and hexamer from Med12 (PDB: 4JQ6) were used as the starting structure. Each oligomer was inserted into a 1-palmitoyl-2-oleoyl-sn-glycero-3-phosphoethanolamine/1-palmitoyl-2-oleoyl-sn-glycero-3-phosphoglycerol (POPE:POPG) (3:1 molar ratio) bilayer using the replacement method of the CHARMM-GUI server[40–42], with a total of 827 and 808 lipids, respectively. After addition of water molecules and solvent ions (100 mM NaCl), the BPR lipid bilayer system had a total of 244,212 and 289,929 atoms for pentamer and hexamer, respectively. Two copies were generated for each oligomeric system for a total of four trajectories. All systems were equilibrated for > 100 ns using a 2 fs timestep in the *NPT* ensemble (P = 1 atm, T = 310 K with the Nosé-Hoover barostat and thermostat) with NAMD 2.13[43] based on CHARMM-GUI protocol with the CHARMM c36 force field for lipids, PR, and the retinal chromophore[44–48]. After equilibration and estimation of the requisite boost potentials, Gaussian accelerated MD (GaMD) in NAMD[49] was run for > 300 ns for the pentamer systems and > 1000 ns for the hexamer systems. Analysis of GaMD results was carried out in VMD[50] and LOOS[51].

Continuous wave (cw) EPR measurement on spin labeled PR

The EPR probe, or MTSL spin label, was covalently linked to PR mutants with selected cysteine mutation sites as was introduced in a previous study[10,11]. Briefly, PR with selected cysteine mutation sites were treated with 10x molar excess of MTSL spin label when it was bind on the Ni-NTA resin (Thermo Scientific). The unlabeled MTSL was then removed in later purification steps by either desalting or SEC processes. The prepared PR liposome sample with spin labels were studied with X-band (0.35 T) EPR measurements at

room temperature using a Bruker EMXplus spectrometer. The cw EPR spectra were taken under a setting of 20 mW microwave power, 1 G modulation amplitude, and 150 G total sweep width.

Optical absorption measurements and analyses

The UV-visible absorption spectra of PR under different conditions were taken by a Shimadzu UV-1800 spectrophotometer. All samples were prepared to have an optical density above 0.3 at 520 nm and an initial volume of 750 μL by diluting the PR sample stocks with the HEPES buffer mentioned above for lipid samples. For each PR sample, the optical absorbance between a wavelength range of 400-750 nm in increments of 0.5 nm were recorded under at least 20 different pHs that spread equally between pH 4 and 10. The pH of each sample was adjusted by titrating with 1 M NaOH (aq.) and 1 M HCl (aq.), and the pH was then measured by Orion Star™ A111 pH benchtop meter (Thermo Fisher Scientific) equipped with an Orion ROSS® Micro pH electrode before each optical absorption measurement. The pKa of PR D97 residue was determined by analyzing the pH-dependent optical absorption transition. The obtained optical absorption spectra under various pH conditions were processed by subtracting each absorption spectrum from the most basic one (pH~10). The differential absorbance at 570 nm, which supposed to be the wavelength that showed the greatest differential absorbance change, was normalized and fitted by the Henderson-Hasselbalch equation. The fitting was done by MATLAB (Mathworks, MA) using home-built codes. The detail of the fitting algorithm and codes was published in our previous study[21].

The time-resolved UV-visible measurements were done by a SpectraPhysics Nd:YAG laser with a monochromator. PR samples were excited by a 532 nm pulse laser with

10 ns duration, and the PR transient absorbance under various wavelengths were monitored over a time span of 10 μs to 0.5 s by an oscilloscope. The fitting analyses on the transient spectra at 410 nm was done by MATLAB (Mathworks, MA) using home-built codes. The differential absorbance at 410 nm were assumed to be mainly contributed by the blue-shifted M intermediates, both M_1 and M_2 combined, as the absorbance of the other intermediates (e.g. *K*, *N*, *PR*, *PR'*) is significantly lower at this wavelength[28]. With this assumption, the growth and decay of the difference spectra at 410 nm represented the accumulation and decay of the M intermediates, respectively. A simplification was made by considering the reverse reactions of the K-M and M-N transitions to be negligible. As a result, a biexponential model for a simple 1st-order two-step consecutive reaction model (Figure 2.3C) could be used to fit the differential absorbance at 410 nm:

$$\Delta Abs_{410nm} = a\frac{k_1}{k_2 - k_1}(e^{-k_1 t} - e^{-k_2 t}),$$

where *a* was a parameter that reflected the magnitude of the differential absorbance, k_1 represented the rate constant of the K–M transition step, and k_2 represented the rate constant of the M–N transition step. The difference absorbance data at 410 nm from Figure 2.3A and 2.3B (purple lines) were fitted using the above reaction model (smooth black curves).

Cryo-EM sample preparation and data acquisition

For grid preparation, copper Quantifoil R2/1 300 grids with a carbon foil were first glow-discharged for 30 s at 25 mA in the residual atmosphere using a GloQube® Plus Glow Discharge System. 2 μL of purified 101 μM WT PR in DDM micelles were subsequently applied and incubated for 10 s at 4 °C and 100 % humidity before blotting for 3 s with a blot

force of 0 and plunge frozen into liquid ethane using an FEI Vitrobot MkIV. During the entire freezing process the Vitrobot was covered in aluminum foil and a resting time of 10 s (compared to the ~0.5 s photocycle of WT PR in DDM micelles) prior to blotting was added in order to prevent PR excitation and to limit the range of photocycle conformations in the sample. Micrographs were collected using a Titan Krios operated at 300 kV equipped with a Gatan BioQuantum energy filter operating over a calculated defocus range of -0.2 um to -3.3 um. A K3 detector operating in electron counting mode was used to record 27,398 micrographs at a pixel size of 0.68 $Å^2$ px^{-1} (corresponding to a nominal magnification of 165,000x) over a 4 second exposure at a 15 e px^{-1} s^{-1} flux yielding a total fluence of 60 e px^{-1}, fractioned into 45 dose fractions.

Cryo-EM data processing

Pre-processing steps were performed with cryoSPARC Live v3.1.0[52]. First, motion-correction and dose-weighting was accomplished using MotionCor2 v2.1.1[53]. Contrast transfer function (CTF) estimates for the motion-corrected micrographs were then calculated with CTFFIND4 v4.1.13[54]. Poor-quality micrographs were discarded. Following several rounds of 2D classification, 67,997 remaining particles were used for 3D classification.

2.4 Results

PR exists as both hexamers and pentamers in E. coli membrane and synthetic liposomes

Although both hexameric and pentameric PR have been reported in various surfactant and reconstituted lipid environments[7,10,12,55–58], only hexamers have previously been observed in *E. coli* membranes[11], while Hirschi *et. al.* reported on PR being primarily pentamers upon

crystalization and when solubilized in cymal-5 micelles,[57] and Maciejko *et. al.* reported mainly on the pentamer population in DMPC/DMPA (9:1) liposomes[36]. We performed BN-PAGE and Western Blot analyses of *E. coli* cell lysates containing PR-WT and found that both PR hexamers and pentamers are present but unresolved (Figure S2.1). Since these two oligomeric species have slightly different spacing among the subunits, crosslinkers of various sizes were applied to PR-containing *E. coli* membranes to stabilize both species separately, with the goal to resolve the coexisting two oligomer populations. The proteins were crosslinked with either DSG, DSS, or BSOCOES, three lysine-specific crosslinkers presented in order of increasing length, followed by SDS-PAGE analysis. The spacer arm lengths[59] and the average attainable distances[60] of these crosslinkers are given in Table S2.1. As shown in Figure 2.1, only PR hexamers were crosslinked by DSG and DSS, whereas BSOCOES stabilized both the hexameric and pentameric forms of PR. These results suggest that PR exists as both hexamers and pentamers in the native-like *E. coli* membrane. The pentamers were stabilized by only BSOCOES, likely because they possess a unique K125–K244 distance (21.2–21.9 Å according to molecular dynamics (MD) simulations with Xwalk[61]), consistent with the accessible length of BSOCOES (average attainable distance: 21.6 Å) (see Supplement 1 and Table S2.2). The K125–K244 crosslink is not present in the hexamer structures according to our MD simulations, hence no comparison could be made about the compactness in the overall structure of these two oligomeric states of PR.

Next, the oligomeric distribution of PR in synthetic liposomes was evaluated. POPC/POPG liposomes (4:1, mol/mol) were selected, as the anionic PG headgroup renders the membrane surface negatively charged, similar to that of the native bacterial membrane. PR in this composition has also been shown to be more uniformly oriented than in neutral

bilayers,[6] and to have increased active population as measured by a lower intrinsic pKa_{D97} (calculated from apparent pKa_{D97} by considering the local pH near the membrane surface according to the Gouy-Chapman model) compared to in POPC/DOTAP liposomes[20].

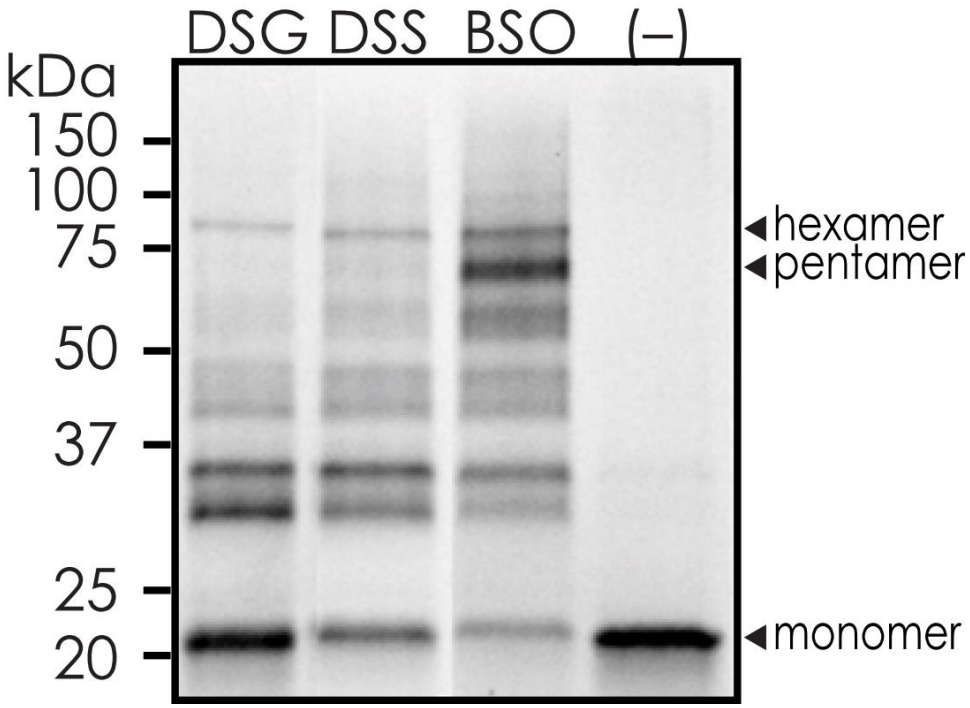

Figure 2.1. SDS-PAGE of WT PR crosslinked in extracted *E. coli* membranes using the three crosslinkers (lanes 1-3) and in membranes that have not been treated with crosslinker (lane 4). These crosslinked SDS-PAGE gels show monomer, dimer, trimer, tetramer, pentamer, and hexamer. The emphasized monomer, pentamer, and hexamer species are labeled.

BN-PAGE analysis again verified the coexistence of PR pentamers and hexamers in the POPC/POPG liposomes, as well as in DDM micelles (Figure S2.2A). This time, despite crosslinking of WT-PR with BSOCOES in POPC/POPG liposomes, SDS-PAGE could not resolve whether one or both oligomeric forms were present, unlike with crosslinked WT-PR in *E. coli* membrane (Figure 2.1) or in DDM micelles[11]. Interestingly, cross-linked PR

oligomers were observed only at high protein:lipid ratios (Figure S2.2B), suggesting that the crosslinking reaction was unfavorable for PR oligomers in liposomes[62,63]. The limited accessibility of the crosslinkers to the PR surface may be owing to the significantly greater thickness of the POPC/POPG membrane compared to the E. coli membranes, which would limit the accessible surface of PR to the solvent.

MD simulations were next used to evaluate the stability of the pentamer and hexamer bundles of PR in different membrane environments. Systems with blue-light absorbing PR (BPR) crystal structures placed in a POPE/POPG (4:1, mol/mol) lipid bilayer in both the pentameric (PDB: 4KLY) and hexameric forms (PDB: 4JQ6) were equilibrated up to 100 ns, followed by several hundred ns of Gaussian accelerated molecular dynamics (GaMD) simulations[49]. The stability of both oligomeric species was assessed via calculation of a packing score at each protomer-protomer interface (Figure 2.2), defined as the relative degree of contact at a given interface. Higher packing scores correlate with greater interactions between monomers. Although both oligomeric forms of PR remained intact in the lipid bilayer environment during the GaMD simulations, different behaviors were observed between the hexamers and pentamers. The hexamer had much higher packing scores at four of the six interfaces compared with the pentamer, but the interfaces between protomers 3-4 and 6-1 were significantly less packed (Figure 2.2B, top). These two interfaces lie opposite one another, indicating that the hexamer could be formed via a dimer of trimers. In contrast, the interfaces of the pentamer had a much broader distribution of packing scores. Overall, these computational results suggested that a synthetic lipid bilayer environment facilitates assembly of stable PR in either oligomeric state, but that subtle differences exist between hexamers and pentamers.

We know that there are key oligomer interfacial contacts defined by specific interactions: the W34 to H75 hydrogen bond is maintained in both the pentameric and hexameric states, whereas the E50-R51-D52 salt bridge exists solely in the pentameric form, illustrated in Figure 2.2A. In addition, PR oligomers are further stabilized by non-specific interactions. This is supported by the coexistence of multiple PR oligomer populations, including dimers, trimers, pentamers and hexamers, and by the observation that the PR oligomer population is modulated by liposome composition and high salt concentrations that tend to alter non-specific molecular interactions. Interestingly, a recently reported cryo-EM study of PR solubilized in Cymal-5 detergent micelles yielded a BN-PAGE analysis that revealed the presence of only pentamers of PR construct without a His-tag, and suggested that PR hexamers are formed only due to the presence of the His-tag added for purification purposes[57]. In contrast, our BN-PAGE analysis of PR WT, upon removal of His-tag, revealed both pentamer and hexamer species in DDM micelles, in E. coli membranes, as well as in POPC/POPG liposomes (Figure S2.3A), ruling out a dominant contribution by the His-tag. We have also performed a preliminary cryo-EM study of PR WT in DDM micelles (experimental details in Materials and Methods) and observe clear 2D and 3D classifications (Figure S2.4) of the PR pentamer. Interestingly, we did not observe hexameric species of PR by cryo-EM. However, this does not mean that hexameric species do not exist. The PR sample consists of a heterogeneous population of oligomers (dimer, trimer etc. besides pentamer) that likely is owing to contributions from non-specific interactions to stabilizing the oligomer interface. This heterogeneity makes PR oligomers inherently difficult to fully characterize by cryo-EM. The observed results still can mean that no stable hexamers are

present, or that the hexamer makes up a more dynamics and heterogenous assembly, and that the pentamer is the most stable and/or homogeneous population.

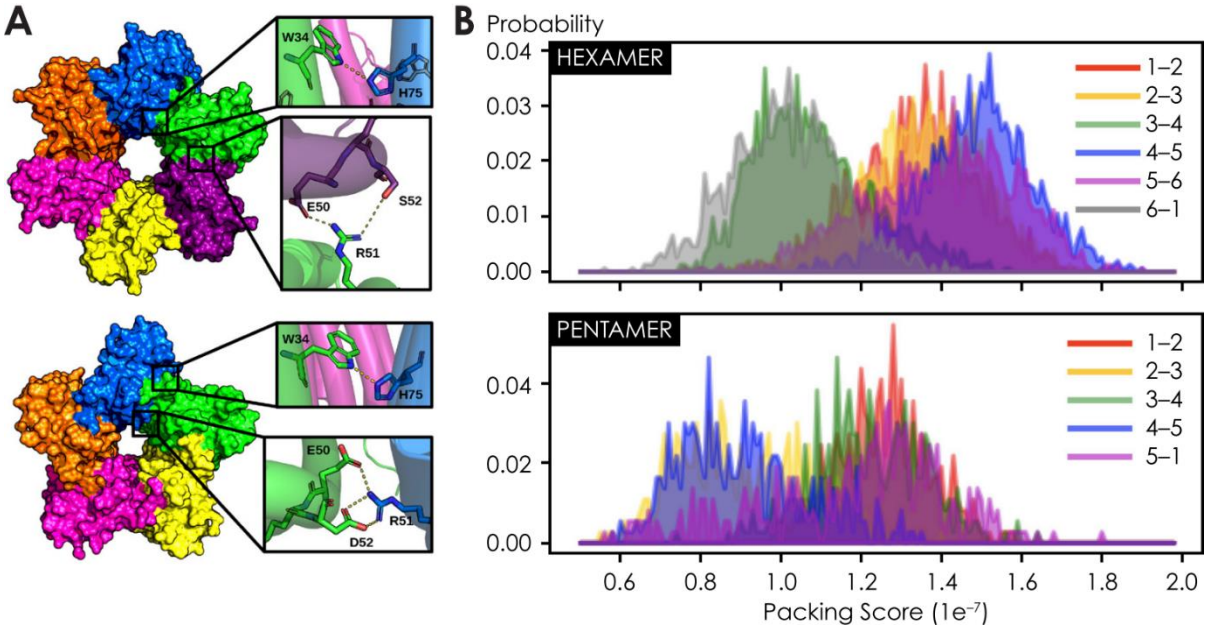

Figure 2.2. Molecular dynamics (MD) simulation on BPR crystal structures placed in a POPE/POPG (4:1, mol/mol) lipid bilayer. **(A)** PR hexamer and pentamer structures with numbering on each subunit to indicate the interface or inter-subunit distances assessed by simulation. **(B)** Histogram of packing scores of BPR hexamer and pentamer at different oligomeric interfaces from GaMD simulations.

We next investigated whether PR oligomers are the product of non-specific associations of PR molecules tightly packed in a lipid membrane by decreasing the protein:lipid ratios, effectively diluting PR density in the proteoliposomes, and evaluating specific intermolecular interactions among PR oligomers by electron paramagnetic resonance (EPR) lineshape analysis. In particular, the cross-protomer distance between residues 55 of PR has been known to be <16 Å, resulting in characteristic and distinct EPR line

broadening.[11] Our results showed that at protein:lipid ratios of both 1:30 and 1:100, the EPR spectra of PR spin-labeled at residue 55 exhibited the characteristic dipolar broadening seen in PR oligomers solubilized with DDM micelles (Figure S2.3B). This indicates that residues 55 are consistently near the cross-protomer interface of PR oligomers, and that PR oligomer formation is partially driven by specific cross-protomer interactions intrinsic to PR. Our results also suggest that non-specific interactions from the His-tag or among PR molecules in close proximity are not a dominant factor in the formation of PR oligomers in synthetic liposomes, but that non-specific interactions still do play a role in PR oligomer formation, giving rise to the heterogeneity of PR oligomer populations.

Oligomerization slows down the photocycle of PR in liposomes

We next sought to understand how oligomerization affects the proton transport function of PR in synthetic liposomes compared with in detergent micelles by evaluating the rate of proton transport. In detergent micelles, oligomerization has been demonstrated to slow down PR's proton transport 2–3 fold[11,21]. To observe this process in POPC/POPG liposomes, we characterized the photocycle of the oligomer-dominant PR WT and of the monomer-enriched E50Q mutant[36]. Compared with PR E50Q, the WT form exhibited differential absorbances that peaked at longer timescales at 410 nm (WT: ~500 μs; E50Q: ~200 μs) and at 590 nm (WT: ~4 ms; E50Q: ~2 ms) (Figure 2.3). This result establishes that oligomerization slows down PR's accumulation of the *M* and *N* intermediates[28] in the liposome environments, as it did in the detergent micelle environment[11,21]. Similar differences were also observed at 470 nm, 500 nm, 550 nm, and 630 nm (Figure S2.5A and 2.5B), although the growth and decay of the transient absorbances at these wavelengths could not be attributed to individual photointermediate, due to overlap of different intermediates

and low signal-to-noise ratio, particularly at 630 nm. Overall, the results reveal that oligomerization slows the kinetics of PR's photocycle in the liposome environment.

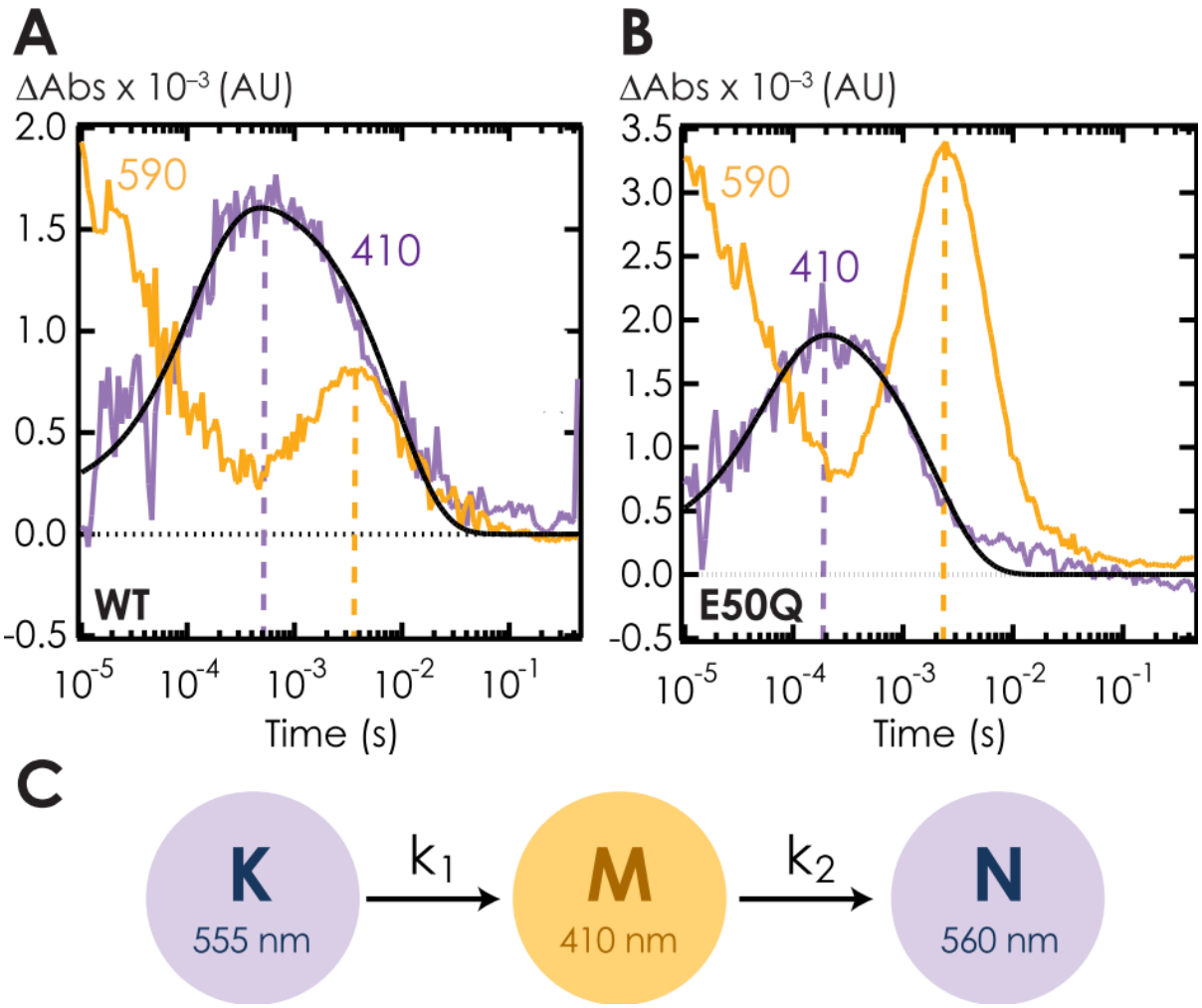

Figure 2.3. Transient difference absorbance data of **(A)** WT PR and **(B)** E50Q PR reconstituted in POPC/POPG (80/20, mol/mol) liposomes. Measurements were performed at pH 8.5 and ~293 K. The transient absorbance changes at 410 nm (purple) and 590 nm (orange) were collected after PR is photoactivated by a green-light pulse laser. The dashed vertical lines indicate the approximate timings for the transient absorbance at 410 nm and 590 nm to reach local maximum. Dark solid curves in (A) and (B) are the fitting curves of the 410 nm transient absorbance (purple) from oligomeric WT PR and monomer-enriched PR E50Q, respectively, using a first-order two-step consecutive reaction model illustrated in **(C)** to describe the accumulation and the decay of M intermediates in PR's photocycle.

To quantify the extent to which oligomerization decreases the kinetics of the PR photocycle in liposomes compared with in detergent micelles, we performed a quantitative analysis of the transient absorbance data for WT PR and the E50Q mutant. The 410 nm traces, associated with the accumulation and decay of the *M* photo-intermediate, were fitted with a biexponential model[64] (see Materials and Methods). The results indicated that in liposomes, the *K–M* transition rate coefficient k_1 for the oligomer-dominant WT PR is ~2 times smaller than that for the monomer-enriched E50Q PR (WT: 8.7 ms^{-1}; E50Q: 16.9 ms^{-1}), while the *M–N* transition rate coefficient k_2 was ~4.5 times smaller (WT: 0.11 ms^{-1}; E50Q: 0.5 ms^{-1}). A very similar result was observed in the DDM detergent environment: the k_1 coefficient for oligomer WT PR was ~2 times smaller than that for E50Q PR (WT: 10.1 ms^{-1}; E50Q: 21.7 ms^{-1}), while the k_2 coefficient was ~4.5 times smaller (WT: 0.16 ms^{-1}; E50Q: 0.77 ms^{-1})[11,21] (Figures S5C and D and Table 2.1). Taken together, these results revealed that oligomerization, in both liposomes and detergent environments, slows PR photocycle kinetics in a significant and remarkably consistent manner, independent of the biomimetic host environments in which PR is embedded.

Table 2.1. Rate coefficients of both the *K-M* transition (k_1) and the *M-N* transition (k_2) for PR in liposome vs. micellar environments from first-order two-step consecutive reaction model fitting

	WT		**E50Q**	
	k_1 (ms^{-1})	**k_2 (ms^{-1})**	**k_1 (ms^{-1})**	**k_2 (ms^{-1})**
POPC/POPG	8.7	0.11	16.9	0.5
DDM[11,21]	10.1	0.16	21.7	0.77

Effects of the liposome environments on PR's active population

In addition to the rate of the photocycle, the proton transport efficiency of PR is also affected by the population of active proteins, which can be assessed by measuring the apparent pKa of the key proton acceptor D97 (pKa_{D97}).[29–32] In the detergent micelle environment, oligomerization was observed to raise PR's pKa_{D97} by almost one pH unit (oligomers: 6.5–6.7; monomers: 7.4–7.8; Figure 2.4A and Table 2.2), indicating a significant decrease in active protein population at neutral pH.[11] To elucidate how oligomerization affects PR's pKa_{D97} in liposomes, we disrupted the critical cross-protomer W34–H75 interaction, which results in the destabilization of the protonated form of D97[34–37], by the two mutations W34D[34] and E50Q.[36] We afterwards used SEC to isolate the WT dimers from the oligomeric population. We then compared the pKa_{D97} of the mutants, W34D and E50Q, and of the isolated WT dimers with that of PR WT oligomers. The E50Q mutation destabilized the PR oligomers and populated a mixture of smaller oligomers (Figure S2.6A), while W34D did not destabilize the PR oligomers, as expected (Figure S2.6A). Unlike in detergent micelles[11], it was difficult to enrich just the monomers in liposomes, thus a mixture of PR dimer and monomer was characterized. Our studies of PR in DDM showed that the pKa_{D97} values of the mutants (E50Q: 7.2; W34D: 7.3; Figure 2.4A) were similar to that of the monomer population of PR WT (7.4), and much higher than the oligomeric population of PR WT (6.7),[11] as expected. However, for PR embedded in POPC/POPG liposomes, the pKa_{D97} values of these mutants (E50Q: 6.4; W34D: 6.6; Figure 2.4B) were comparable to that of PR WT oligomers (6.4) (Figure 2.4B). Likewise, PR WT dimers in POPC/POPG liposomes exhibited a similarly low pKa_{D97} value of 6.2 (Figure 2.4B). We also varied the protein:lipid ratio between 1:10, 1:30, and 1:100 to test whether the cross-protomer interactions stabilizing

PR oligomers could be diluted in the presence of excess lipids; however, we found negligible changes in the pKa_{D97} (6.5–6.6) (Figure S2.6B). These results indicate that the liposome environment itself is sufficient to maintain an active population of PR independent of the cross-protomer modulation of D97.

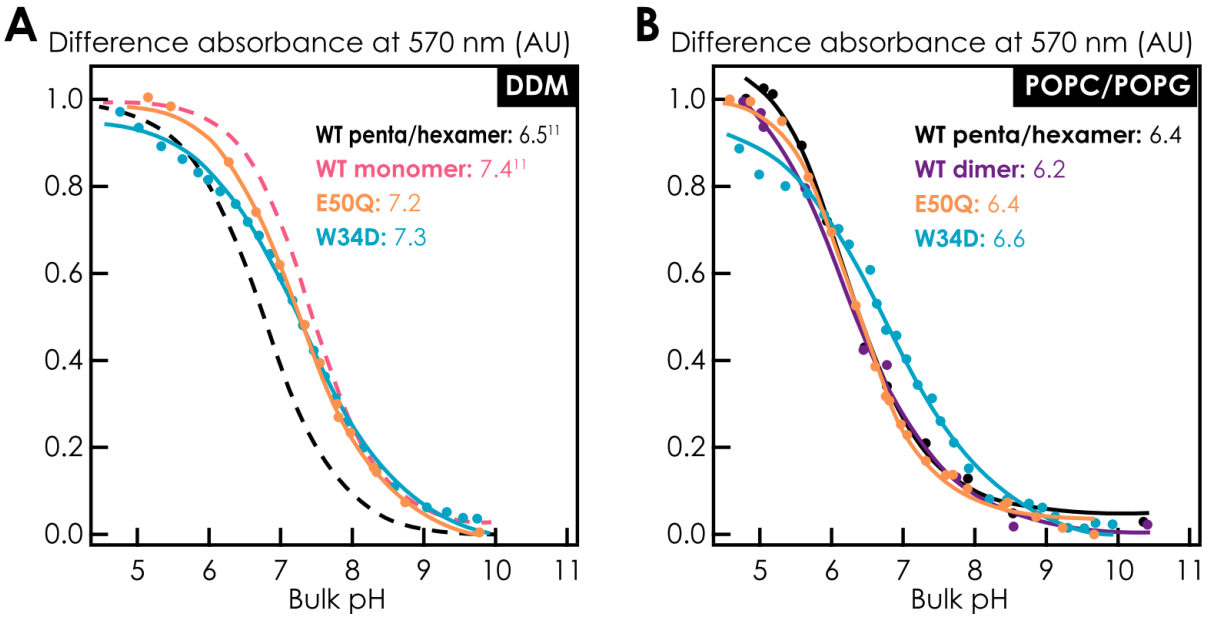

Figure 2.4. pH-dependent absorbance transitions at 570 nm and pKa_{D97} values for PR WT, E50Q, and W34D solubilized in **(A)** DDM detergent micelles and **(B)** POPC/POPG (4:1, mol/mol) liposomes. Previously published results are represented by dashed lines.

Table 2.2. The pKa_{D97} of PR variants in DDM detergent and POPC/POPG (4:1, mol/mol)

	WT penta-/hexamer	WT dimer	WT monomer	E50Q	W34D
DDM	6.5[11]	--	7.4[11]	7.2	7.3
POPC/POPG	6.4	6.2	--	6.4	6.6

SMALPs retain PR's native-like membrane environment but disrupt proton transport function

We have shown that the different lipid membrane mimetic environments of liposomes and detergent micelles significantly impact the proton transport function properties of PR. Next, we explored the functional impact of extracting PR directly from *E. coli* membrane by using styrene maleic acid lipid particles (SMALPs), a nanodisc system that has recently emerged to be a highly efficient lipid membrane mimetic. The use of SMALPs enables detergent-free isolation of transmembrane proteins and retention of their native lipid environment. As a result, SMA has been suggested to be superior to other membrane mimetics in maintaining protein function[16,65,66]. Herein, the protein transport function of PR solubilized with SMALPs was characterized via pKa_{D97} measurements and photochemical reaction cycle experiments. The monomer-enriched E50Q mutant was used, as the oligomer-dominant PR WT could not be captured, possibly due to the limited size of the nanodiscs (see Supplement 2). Our results showed that PR E50Q in SMALPs exhibited a remarkably high pKa_{D97} of 8.9 (Figure 2.5A). This is 1.5–2.5 pKa units higher than those of PR E50Q reconstituted in DDM (7.2) or in POPC/POPG (6.4) (Figure 2.4), indicating that the majority of PR monomers are incapable of proton transport at neutral pHs in SMALPs. Note that the fitting was poor for the data at pH < 6 due to the instability of SMALPs at this pH range,[67] which is in contrast to the high quality pKa_{D97} data of PR reconstituted in other membrane mimetics.

Next, time-resolved UV-visible light spectroscopy was used to evaluate the photocycle kinetics of PR E50Q in SMA at pH 8.0. We found that the photocycle kinetics were severely disrupted compared with PR in DDM micelles, exhibiting absorbance that rapidly diminished over time at all wavelengths examined (Figure 2.5B). The lack of

movement at 410 nm indicates that the M-intermediate, characteristic of proton transport, is not observed. The gradual absorption decay observed at 550 nm and 590 nm is also non-native as both wavelengths exhibit a complex photocycle in DDM micelles and liposomes. Such disruption of the PR photocycle could be explained by the very high pKa_{D97} of 8.9 for PR E50Q in SMALPs estimated above (Figure 2.5A). This indicates that the D97 residue is predominantly protonated, thereby interrupting the native *M-N* transition in the PR and effectively rendering most of the PR molecules inactive. This observation however persisted at pH 10.0 (Figure 2.5B), where the D97 residue should be deprotonated, indicating that the polymer nanodisc platform interferes with PR's photocycle kinetics beyond affecting the protonation state of D97. Taken together, SMALPs appear unable to maintain the proton transport capacity of PR, severely reduce its active population and disrupt its photocycle properties.

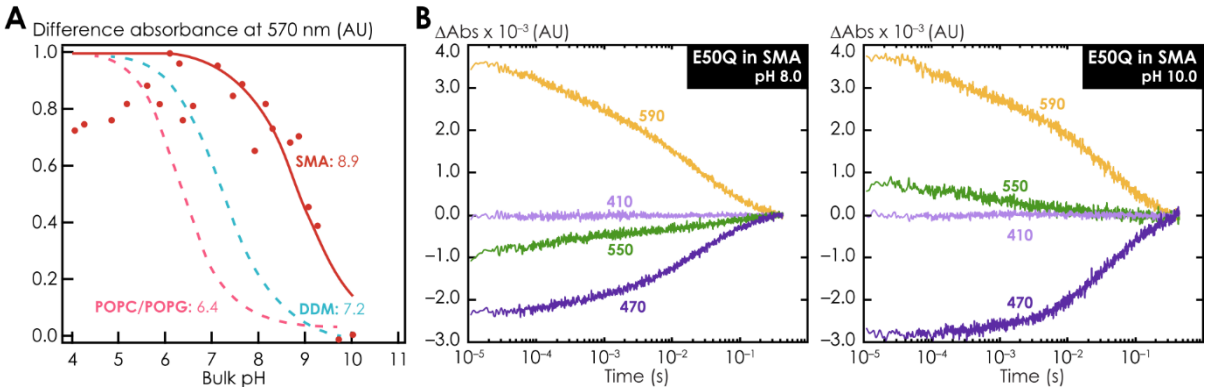

Figure 2.5. (A) pH-dependent absorbance transitions of PR E50Q in SMALPs (solid red line) at 570 nm, compared with those of PR E50Q in DDM detergent (dashed blue line) and in POPC/POPG liposomes (dashed pink line). **(B)** Transient absorbance data of PR E50Q extracted with SMALPs directly from *E. coli* membrane. Measurements were performed at pH 8.0 and 10.0 at ~293 K. The transient absorbance changes at 410, 470, 550, and 590 nm were collected after PR is photoactivated by a green-light pulse laser.

2.5 Discussion

The key finding of this study is that oligomerization is a dominant factor that significantly decreases the kinetics of the PR photocycle. The oligomeric state of PR in *E. coli* membrane and synthetic liposomes are found to include both hexamers and pentamers (Figures 1 and 2). In all cases, this study determined that oligomerization significantly slows down PR's photocycle in liposomes (Figure 2.3) to a similar extent as previously shown for PR in micellar environments. This effect of oligomerization on the photocycle kinetics is likely owing to mechanical inhibition of key conformational changes.

At the same time we know from previous studies that the lipid-based membrane mimetic composition, regardless of the oligomeric state, exerts profound impacts on the active population of the receptor.[20] This is further verified by the observation that disrupting the cross-protomer interaction that modulates the key proton acceptor D97 of PR did not decrease the active population of PR in liposomes (Figure 2.4). In contrast to PR in the detergent micelle environment, PR in liposomes was shown to maintain the active protein population harboring deprotonated D97 even in the absence of the critical cross-protomer W34–H75 contact (Figure 2.4 and Table 2.2). This cross-protomer hydrogen bond serves to increase the tautomerization efficiency of H75[34,36], such that H75 can form a hydrogen bond that stabilizes the deprotonated form of D97.[35] Therefore, there must exist a mechanism by which liposomes can keep D97 deprotonated without the hydrogen bond with H75. These observations are unique to PR embedded in liposomes, and have been proposed to arise from long-range stabilizing electrostatic interaction between lipid headgroups and internal PR residues across the liposomes bilayer, further modulated by the presence of salt in the buffer solution (150 mM NaCl).[20] PR embedded in a bilayer membrane environment composed of

charged and zwitterionic lipids can create a much stronger surface potential that could modulate key electrostatic interactions that may keep D97 deprotonated when PR is reconstituted in liposomes, effectively compensating for the disruption of the cross-protomer W34–H75 interaction.

Strikingly, solubilizing PR from its native *E. coli* using SMA nanodiscs does not preserve the pKa_{D97} of PR reconstituted in liposomes. Rather, the SMA nanodisc environment leads to a drastic increase in pKa_{D97} of PR E50Q compared to that in liposomes or micelles, and a severe disruption of PR's photocycle properties (Figure 2.5). As the nanodiscs are formed, the maleic acid moiety must be deprotonated[68], which could cause an increase in the local proton concentration around residue D97. As a result, residue D97 could become dominantly protonated, leading to the accelerated decay in photocycle (Figure 2.5B). Indeed, a similar trend has been observed with other membrane proteins embedded in SMALPs. In the *Rubrobacter xylanophilus* rhodopsin RxR, the pKa of K209 has been shown to increase by 1.8 pH units in SMALPs compared with that in DDM[69]. Additionally, in the photoreceptor sensory rhodopsin II *Np*SRII of *Natronomonas pharaonic*, an accelerated decay of the *M* photointermediate was found due to the high local proton concentration induced by the maleic acid group of the SMA polymer[70]. Taken together, these results suggest that the charged functional groups of SMALPs can have a dramatic, and potentially adverse, effect on the membrane protein function via adverse local electrostatic interactions. Hence, it is not a given that SMALP-reconstituted membrane proteins display more native-like function, even though PR is lifted out of its native E.coli lipid membrane environment.

Although appearing unimportant in maintaining PR's low pKa_{D97} in liposome environment, oligomerization exerts a substantial impact on PR's rates of proton transport in

both detergent micelle and liposome environments (Figure 2.3 and Table 2.1). This indicates that during the photochemical reaction, PR undergoes structural changes that can be modulated by oligomerization, yet unconnected to the protonation state of D97. Such structural changes may not be limited to any specific region of PR, as movements induced by the photocycle (shown to involve helices D–G[10,12,57,71–74]) occur in regions distinct from the oligomeric interfaces (constituted by helices A–C[10,12,57]). Indeed, by using MD simulations, a recent study has demonstrated that PR pentamers, compared with the monomeric form, exhibited increased rigidity of the overall structure of PR in a POPE/POPG lipid membrane[75]. Increased overall rigidity of PR oligomers might be the structural basis of why PR's photocycle overall is slightly faster in liposomes than in detergent micelles, specifically the rate coefficients associated with the accumulation and decay of the *M* intermediate (Table 2.1). Additionally, different rigidity might render PR pentamers and hexamers functionally dissimilar, as we have shown that PR hexamers have slightly stronger cross-protomer associations and are more compact compared with the pentamers (see Figure 2.2 and Supplement 3). Our study demonstrates that both oligomeric distribution and biomimetic composition can impact PR's functional properties via mechanisms beyond the protonation state of residue D97, underscoring the importance of resolving the structural evolution of PR in different membrane mimetics during activation in the future.

2.6 Conclusions

This study distinguishes and emphasizes the extensive impacts of biomimetic composition and oligomeric distribution on the functional properties of PR. The evidence supports the role(s) of electrostatic interactions from lipid-based membrane mimetics in

maintaining the deprotonated state of PR's primary proton acceptor D97. In addition, oligomerization significantly and consistently slows PR's photocycle kinetics, highlighting the prominent functional role of oligomerization. The task remaining is to investigate the molecular mechanism by which various membrane mimetics modulate the composition-dependent pKa_{D97} of PR and the associated structural changes and their rates that are pertinent to PR's photochemical reaction induced by oligomerization. Also, the functional differences between the pentameric and hexameric forms of PR remain to be explored. This study focuses on PR, but the findings are expected to be broadly applicable to other transmembrane proteins, reinforcing the importance of selecting the appropriate biomimetic platform for structure-function studies of these vital biomolecules.

2.7 Future Directions

These new formulations of lipid surfactants represent significant functional mediation of proteorhodopsin (PR). Further investigation into other charged lipids may reveal even greater changes in the pKa of the D97 residue of PR. Additionally, investigation into larger protein-compatible surfactants with greater hydrophobic-hydrophilic contrast between the head and tail groups may enable the formation of mesostructured protein-host materials with greater extents of mesostructural order (discussed in greater detail in Chapter 3). Furthermore, investigations into asymmetric lipid bilayers (lipids with varied properties contribute to a range of characteristics on each side of the membrane) may better replicate native-like environments and create varied electrostatic environments that are tuned for different regions of the protein.[76] Similarly, amphiphilic block copolymer systems have been shown to orient PR based on charge interactions.[77] My goal to harness the functions of

membrane proteins in non-native materials for incorporation into devices is highly dependent on achieving anisotropic orientational alignment of PR, and optimizations of these interactions may play an important role in this.

Further optimization of PR nanodiscs is another research direction of interest, representing an opportunity to study the functions of this membrane protein in a planar biomimetic environment that closely resembles the curvature of a native lipid bilayer. As shown in Figure 2.5B, SMA nanodiscs interfere with the photocycle of PR, likely due to influencing the local electrostatic environment around key function-dependent residues.[78] However, these electrostatic interactions can be altered by using nanodiscs formed from polymer chains with different charges. Negatively charged styrene maleic acid-ethanol amine (SMA-EA) and positively charged styrene maleimide quaternary ammonium (SMA-QA) are low molecular weight SMA derivatives, and are alternative polymers that can be used to form nanodiscs under more flexible conditions.[79] Unlike SMA, which precipitates out of solution at pH conditions <6, SMA-EA is stable at acidic pH conditions greater than 3.3,[80] and SMA-QA is stable from pH 2.5-10 conditions. Importantly, this means that these nanodiscs are stable at the pH 4.1 conditions I use to formulate DDM+POPC+DOTAP-structure-directed mesostructured silica films. It would be interesting to experiment with SMA-EA and SMA-QA nanodiscs as guests within these materials.

Larger SMA-EA and SMA-QA nanodiscs can solubilize larger PR oligomers, and are also more easily oriented within a magnetic field regardless of protein oligomerization.[78,80] While larger nanodiscs may disrupt the co-assembly of PR-containing nanodiscs, DDM, POPC, DOTAP, and silica into well-ordered mesochannels, replacing the structure-directing surfactants with molecules that contain longer hydrophobic chains (thus larger mesochannel

diameters) may make these two systems compatible. Although not necessary for solubilization, it would be interesting to probe the photocycle kinetics of monomeric PR when solubilized in large lipid nanodiscs in order to test if the protein being a greater distance from the disrupting charges of the polymer nanodisc would enable native-like photocycle kinetics to be observed. These proposed experiments will hopefully provide greater context and understanding to membrane protein-host interactions, and enable the manipulation of lipid bilayer and surfactant environments to mediate PR co-assembly and function.

2.8 References

(1) Lefkowitz, R. J. Historical Review: A Brief History and Personal Retrospective of Seven-Transmembrane Receptors. *Trends in Pharmacological Sciences* **2004**, *25* (8), 413–422. https://doi.org/10.1016/j.tips.2004.06.006.

(2) Kaplan, J. H. Biochemistry of Na,K-ATPase. *Annu. Rev. Biochem.* **2002**, *71* (1), 511–535. https://doi.org/10.1146/annurev.biochem.71.102201.141218.

(3) Bragin, P. E.; Mineev, K. S.; Bocharova, O. V.; Volynsky, P. E.; Bocharov, E. V.; Arseniev, A. S. HER2 Transmembrane Domain Dimerization Coupled with Self-Association of Membrane-Embedded Cytoplasmic Juxtamembrane Regions. *Journal of Molecular Biology* **2016**, *428* (1), 52–61. https://doi.org/10.1016/j.jmb.2015.11.007.

(4) Yan, N. A Glimpse of Membrane Transport through Structures—Advances in the Structural Biology of the GLUT Glucose Transporters. *Journal of Molecular Biology* **2017**, *429* (17), 2710–2725. https://doi.org/10.1016/j.jmb.2017.07.009.

(5) Berndt, A.; Lee, S. Y.; Wietek, J.; Ramakrishnan, C.; Steinberg, E. E.; Rashid, A. J.; Kim, H.; Park, S.; Santoro, A.; Frankland, P. W.; Iyer, S. M.; Pak, S.; Ährlund-Richter, S.; Delp, S. L.; Malenka, R. C.; Josselyn, S. A.; Carlén, M.; Hegemann, P.; Deisseroth,

K. Structural Foundations of Optogenetics: Determinants of Channelrhodopsin Ion Selectivity. *Proc Natl Acad Sci USA* **2016**, *113* (4), 822–829. https://doi.org/10.1073/pnas.1523341113.

(6) Wang, J.; Albers, T.; Grewer, C. Energy Landscape of the Substrate Translocation Equilibrium of Plasma-Membrane Glutamate Transporters. *J. Phys. Chem. B* **2018**, *122* (1), 28–39. https://doi.org/10.1021/acs.jpcb.7b09059.

(7) Klyszejko, A. L.; Shastri, S.; Mari, S. A.; Grubmüller, H.; Muller, D. J.; Glaubitz, C. Folding and Assembly of Proteorhodopsin. *Journal of Molecular Biology* **2008**, *376* (1), 35–41. https://doi.org/10.1016/j.jmb.2007.11.030.

(8) Schonenbach, N. S.; Rieth, M. D.; Han, S.; O'Malley, M. A. Adenosine A2a Receptors Form Distinct Oligomers in Protein Detergent Complexes. *FEBS Letters* **2016**, *590* (18), 3295–3306. https://doi.org/10.1002/1873-3468.12367.

(9) Ferré, S.; Casadó, V.; Devi, L. A.; Filizola, M.; Jockers, R.; Lohse, M. J.; Milligan, G.; Pin, J.-P.; Guitart, X. G Protein–Coupled Receptor Oligomerization Revisited: Functional and Pharmacological Perspectives. *Pharmacological Reviews* **2014**, *66* (2), 413–434. https://doi.org/10.1124/pr.113.008052.

(10) Stone, K. M.; Voska, J.; Kinnebrew, M.; Pavlova, A.; Junk, M. J. N.; Han, S. Structural Insight into Proteorhodopsin Oligomers. *Biophysical Journal* **2013**, *104* (2), 472–481. https://doi.org/10.1016/j.bpj.2012.11.3831.

(11) Hussain, S.; Kinnebrew, M.; Schonenbach, N. S.; Aye, E.; Han, S. Functional Consequences of the Oligomeric Assembly of Proteorhodopsin. *J Mol Biol* **2015**, *427* (6 0 0), 1278–1290. https://doi.org/10.1016/j.jmb.2015.01.004.

(12) Edwards, D. T.; Huber, T.; Hussain, S.; Stone, K. M.; Kinnebrew, M.; Kaminker, I.; Matalon, E.; Sherwin, M. S.; Goldfarb, D.; Han, S. Determining the Oligomeric Structure of Proteorhodopsin by Gd3+-Based Pulsed Dipolar Spectroscopy of Multiple Distances. *Structure* **2014**, *22* (11), 1677–1686. https://doi.org/10.1016/j.str.2014.09.008.

(13) Jastrzebska, B.; Maeda, T.; Zhu, L.; Fotiadis, D.; Filipek, S.; Engel, A.; Stenkamp, R. E.; Palczewski, K. Functional Characterization of Rhodopsin Monomers and Dimers in Detergents. *Journal of Biological Chemistry* **2004**, *279* (52), 54663–54675. https://doi.org/10.1074/jbc.M408691200.

(14) Rietveld, A. W. M.; Ferreira, S. T. Kinetics and Energetics of Subunit Dissociation/Unfolding of TIM: The Importance of Oligomerization for Conformational Persistence and Chemical Stability of Proteins †. *Biochemistry* **1998**, *37* (3), 933–937. https://doi.org/10.1021/bi9721593.

(15) Schonenbach, N. S.; Hussain, S.; O'Malley, M. A. Structure and Function of G Protein-Coupled Receptor Oligomers: Implications for Drug Discovery: Studying GPCR Oligomer Function. *Wiley Interdisciplinary Reviews: Nanomedicine and Nanobiotechnology* **2015**, *7* (3), 408–427. https://doi.org/10.1002/wnan.1319.

(16) Gulati, S.; Jamshad, M.; Knowles, T. J.; Morrison, K. A.; Downing, R.; Cant, N.; Collins, R.; Koenderink, J. B.; Ford, R. C.; Overduin, M.; Kerr, I. D.; Dafforn, T. R.; Rothnie, A. J. Detergent-Free Purification of ABC (ATP-Binding-Cassette) Transporters. *Biochemical Journal* **2014**, *461* (2), 269–278. https://doi.org/10.1042/BJ20131477.

(17) Veatch, W. The Dimeric Nature of the Gramicidin A Transmembrane Cbannel : Conductance and Fluorescence Energy Transfer Stu of Hybrid Channels. *Journal of Molecular Biology* **1977**, *113*, 89–102.

(18) Tunuguntla, R.; Bangar, M.; Kim, K.; Stroeve, P.; Ajo-Franklin, C. M.; Noy, A. Lipid Bilayer Composition Can Influence the Orientation of Proteorhodopsin in Artificial Membranes. *Biophysical Journal* **2013**, *105* (6), 1388–1396. https://doi.org/10.1016/j.bpj.2013.07.043.

(19) Lindholm, L.; Ariöz, C.; Jawurek, M.; Liebau, J.; Mäler, L.; Wieslander, Å.; von Ballmoos, C.; Barth, A. Effect of Lipid Bilayer Properties on the Photocycle of Green Proteorhodopsin. *Biochimica et Biophysica Acta (BBA) - Bioenergetics* **2015**, *1847* (8), 698–708. https://doi.org/10.1016/j.bbabio.2015.04.011.

(20) Han, C.-T.; Song, J.; Chan, T.; Pruett, C.; Han, S. Electrostatic Environment of Proteorhodopsin Affects the PKa of Its Buried Primary Proton Acceptor. *Biophysical Journal* **2020**, *118* (8), 1838–1849. https://doi.org/10.1016/j.bpj.2020.02.027.

(21) Idso, M. N.; Baxter, N. R.; Narayanan, S.; Chang, E.; Fisher, J.; Chmelka, B. F.; Han, S. Proteorhodopsin Function Is Primarily Mediated by Oligomerization in Different Micellar Surfactant Solutions. *The Journal of Physical Chemistry B* **2019**, *123* (19), 4180–4192. https://doi.org/10.1021/acs.jpcb.9b00922.

(22) Lund, S.; Orlowski, S.; de Foresta, B.; Champeil, P.; le Maire, M.; Møller, J. V. Detergent Structure and Associated Lipid as Determinants in the Stabilization of Solubilized Ca2+-ATPase from Sarcoplasmic Reticulum. *Journal of Biological Chemistry* **1989**, *264* (9), 4907–4915. https://doi.org/10.1016/S0021-9258(18)83677-8.

(23) Rosevear, P.; VanAken, T.; Baxter, J.; Ferguson-Miller, S. Alkyl Glycoside Detergents: A Simpler Synthesis and Their Effects on Kinetic and Physical Properties of Cytochrome c Oxidase. *Biochemistry* **1980**, *19* (17), 4108–4115. https://doi.org/10.1021/bi00558a032.

(24) Chawla, U.; Jiang, Y.; Zheng, W.; Kuang, L.; Perera, S. M. D. C.; Pitman, M. C.; Brown, M. F.; Liang, H. A Usual G-Protein-Coupled Receptor in Unusual Membranes. *Angew. Chem. Int. Ed.* **2016**, *55* (2), 588–592. https://doi.org/10.1002/anie.201508648.

(25) Brown, M. F. Soft Matter in Lipid–Protein Interactions. *Annu. Rev. Biophys.* **2017**, *46* (1), 379–410. https://doi.org/10.1146/annurev-biophys-070816-033843.

(26) Ranaghan, M. J.; Schwall, C. T.; Alder, N. N.; Birge, R. R. Green Proteorhodopsin Reconstituted into Nanoscale Phospholipid Bilayers (Nanodiscs) as Photoactive Monomers. *J. Am. Chem. Soc.* **2011**, *133* (45), 18318–18327. https://doi.org/10.1021/ja2070957.

(27) Váró, G.; Lanyi, J. K. Distortions in the Photocycle of Bacteriorhodopsin at Moderate Dehydration. *Biophysical Journal* **1991**, *59* (2), 313–322. https://doi.org/10.1016/S0006-3495(91)82225-1.

(28) Váró, G.; Brown, L. S.; Lakatos, M.; Lanyi, J. K. Characterization of the Photochemical Reaction Cycle of Proteorhodopsin. *Biophysical Journal* **2003**, *84* (2), 1202–1207. https://doi.org/10.1016/S0006-3495(03)74934-0.

(29) Dioumaev, A. K.; Brown, L. S.; Shih, J.; Spudich, E. N.; Spudich, J. L.; Lanyi, J. K. Proton Transfers in the Photochemical Reaction Cycle of Proteorhodopsin. *Biochemistry* **2002**, *41* (17), 5348–5358. https://doi.org/10.1021/bi025563x.

(30) Beja, O. Bacterial Rhodopsin: Evidence for a New Type of Phototrophy in the Sea. *Science* **2000**, *289* (5486), 1902–1906. https://doi.org/10.1126/science.289.5486.1902.

(31) Dioumaev, A. K.; Wang, J. M.; Bálint, Z.; Váró, G.; Lanyi, J. K. Proton Transport by Proteorhodopsin Requires That the Retinal Schiff Base Counterion Asp-97 Be Anionic †. *Biochemistry* **2003**, *42* (21), 6582–6587. https://doi.org/10.1021/bi034253r.

(32) Wang, W.-W.; Sineshchekov, O. A.; Spudich, E. N.; Spudich, J. L. Spectroscopic and Photochemical Characterization of a Deep Ocean Proteorhodopsin. *Journal of Biological Chemistry* **2003**, *278* (36), 33985–33991. https://doi.org/10.1074/jbc.M305716200.

(33) Ikeda, D.; Furutani, Y.; Kandori, H. FTIR Study of the Retinal Schiff Base and Internal Water Molecules of Proteorhodopsin. *Biochemistry* **2007**, *46* (18), 5365–5373. https://doi.org/10.1021/bi700143g.

(34) Ran, T.; Ozorowski, G.; Gao, Y.; Sineshchekov, O. A.; Wang, W.; Spudich, J. L.; Luecke, H. Cross-Protomer Interaction with the Photoactive Site in Oligomeric Proteorhodopsin Complexes. *Acta Crystallogr D Biol Crystallogr* **2013**, *69* (10), 1965–1980. https://doi.org/10.1107/S0907444913017575.

(35) Hempelmann, F.; Hölper, S.; Verhoefen, M.-K.; Woerner, A. C.; Köhler, T.; Fiedler, S.-A.; Pfleger, N.; Wachtveitl, J.; Glaubitz, C. His75−Asp97 Cluster in Green Proteorhodopsin. *J. Am. Chem. Soc.* **2011**, *133* (12), 4645–4654. https://doi.org/10.1021/ja111116a.

(36) Maciejko, J.; Mehler, M.; Kaur, J.; Lieblein, T.; Morgner, N.; Ouari, O.; Tordo, P.; Becker-Baldus, J.; Glaubitz, C. Visualizing Specific Cross-Protomer Interactions in the Homo-Oligomeric Membrane Protein Proteorhodopsin by Dynamic-Nuclear-Polarization-Enhanced Solid-State NMR. *J. Am. Chem. Soc.* **2015**, *137* (28), 9032–9043. https://doi.org/10.1021/jacs.5b03606.

(37) Maciejko, J.; Kaur, J.; Becker-Baldus, J.; Glaubitz, C. Photocycle-Dependent Conformational Changes in the Proteorhodopsin Cross-Protomer Asp–His–Trp Triad Revealed by DNP-Enhanced MAS-NMR. *Proc Natl Acad Sci USA* **2019**, *116* (17), 8342–8349. https://doi.org/10.1073/pnas.1817665116.

(38) Wang, W.; Malcolm, B. A. Two-Stage PCR Protocol Allowing Introduction of Multiple Mutations, Deletions and Insertions Using QuikChangeTM Site-Directed Mutagenesis. *BioTechniques* **1999**, *26*, 680–682.

(39) Mattson, G.; Conklin, E.; Desai, S.; Nielander, G.; Savage, M. D.; Morgensen, S. A Practical Approach to Crosslinking. *Molecular Biology Reports* **1993**, *17* (3), 167–183. https://doi.org/10.1007/BF00986726.

(40) Jo, S.; Kim, T.; Im, W. Automated Builder and Database of Protein/Membrane Complexes for Molecular Dynamics Simulations. *PLoS ONE* **2007**, *2* (9), e880. https://doi.org/10.1371/journal.pone.0000880.

(41) Jo, S.; Lim, J. B.; Klauda, J. B.; Im, W. CHARMM-GUI Membrane Builder for Mixed Bilayers and Its Application to Yeast Membranes. *Biophysical Journal* **2009**, *97* (1), 50–58. https://doi.org/10.1016/j.bpj.2009.04.013.

(42) Jo, S.; Kim, T.; Iyer, V. G.; Im, W. CHARMM-GUI: A Web-Based Graphical User Interface for CHARMM. *J. Comput. Chem.* **2008**, *29* (11), 1859–1865. https://doi.org/10.1002/jcc.20945.

(43) Phillips, J. C.; Braun, R.; Wang, W.; Gumbart, J.; Tajkhorshid, E.; Villa, E.; Chipot, C.; Skeel, R. D.; Kalé, L.; Schulten, K. Scalable Molecular Dynamics with NAMD. *J. Comput. Chem.* **2005**, *26* (16), 1781–1802. https://doi.org/10.1002/jcc.20289.

(44) Vanommeslaeghe, K.; Hatcher, E.; Acharya, C.; Kundu, S.; Zhong, S.; Shim, J.; Darian, E.; Guvench, O.; Lopes, P.; Vorobyov, I.; Mackerell, A. D. CHARMM General Force Field: A Force Field for Drug-like Molecules Compatible with the CHARMM All-Atom Additive Biological Force Fields. *J. Comput. Chem.* **2009**, NA-NA. https://doi.org/10.1002/jcc.21367.

(45) Zhu, S.; Brown, M. F.; Feller, S. E. Retinal Conformation Governs p K_a of Protonated Schiff Base in Rhodopsin Activation. *J. Am. Chem. Soc.* **2013**, *135* (25), 9391–9398. https://doi.org/10.1021/ja4002986.

(46) Mertz, B.; Lu, M.; Brown, M. F.; Feller, S. E. Steric and Electronic Influences on the Torsional Energy Landscape of Retinal. *Biophysical Journal* **2011**, *101* (3), L17–L19. https://doi.org/10.1016/j.bpj.2011.06.020.

(47) Klauda, J. B.; Venable, R. M.; Freites, J. A.; O'Connor, J. W.; Tobias, D. J.; Mondragon-Ramirez, C.; Vorobyov, I.; MacKerell, A. D.; Pastor, R. W. Update of the CHARMM All-Atom Additive Force Field for Lipids: Validation on Six Lipid Types. *J. Phys. Chem. B* **2010**, *114* (23), 7830–7843. https://doi.org/10.1021/jp101759q.

(48) Nina, M.; Roux, B.; Smith, J. C. Functional Interactions in Bacteriorhodopsin: A Theoretical Analysis of Retinal Hydrogen Bonding with Water. *Biophysical Journal* **1995**, *68* (1), 25–39. https://doi.org/10.1016/S0006-3495(95)80184-0.

(49) Pang, Y. T.; Miao, Y.; Wang, Y.; McCammon, J. A. Gaussian Accelerated Molecular Dynamics in NAMD. *J. Chem. Theory Comput.* **2017**, *13* (1), 9–19. https://doi.org/10.1021/acs.jctc.6b00931.

(50) Humphrey, W.; Dalke, A.; Schulten, K. VMD: Visual Molecular Dynamics. *J. Mol. Graph.* **1996**, *14* (1), 33–38.

(51) Romo, T. D.; Leioatts, N.; Grossfield, A. Lightweight Object Oriented Structure Analysis: Tools for Building Tools to Analyze Molecular Dynamics Simulations. *J. Comput. Chem.* **2014**, *35* (32), 2305–2318. https://doi.org/10.1002/jcc.23753.

(52) Punjani, A.; Zhang, H.; Fleet, D. J. Non-Uniform Refinement: Adaptive Regularization Improves Single-Particle Cryo-EM Reconstruction. *Nat Methods* **2020**, *17* (12), 1214–1221. https://doi.org/10.1038/s41592-020-00990-8.

(53) Zheng, S. Q.; Palovcak, E.; Armache, J.-P.; Verba, K. A.; Cheng, Y.; Agard, D. A. MotionCor2: Anisotropic Correction of Beam-Induced Motion for Improved Cryo-Electron Microscopy. *Nat Methods* **2017**, *14* (4), 331–332. https://doi.org/10.1038/nmeth.4193.

(54) Grant, T.; Rohou, A.; Grigorieff, N. CisTEM, User-Friendly Software for Single-Particle Image Processing. *eLife* **2018**, *7*, e35383. https://doi.org/10.7554/eLife.35383.

(55) Hoffmann, J.; Aslimovska, L.; Bamann, C.; Glaubitz, C.; Bamberg, E.; Brutschy, B. Studying the Stoichiometries of Membrane Proteins by Mass Spectrometry: Microbial Rhodopsins and a Potassium Ion Channel. *Phys. Chem. Chem. Phys.* **2010**, *12* (14), 3480. https://doi.org/10.1039/b924630d.

(56) Shastri, S.; Vonck, J.; Pfleger, N.; Haase, W.; Kuehlbrandt, W.; Glaubitz, C. Proteorhodopsin: Characterisation of 2D Crystals by Electron Microscopy and Solid State NMR. *Biochimica et Biophysica Acta (BBA) - Biomembranes* **2007**, *1768* (12), 3012–3019. https://doi.org/10.1016/j.bbamem.2007.10.001.

(57) Hirschi, S.; Kalbermatter, D.; Ucurum, Z.; Fotiadis, D. Cryo-Electron Microscopic and X-Ray Crystallographic Analysis of the Light-Driven Proton Pump Proteorhodopsin Reveals a Pentameric Assembly. *Journal of Structural Biology: X* **2020**, *4*, 100024. https://doi.org/10.1016/j.yjsbx.2020.100024.

(58) Shibata, M.; Inoue, K.; Ikeda, K.; Konno, M.; Singh, M.; Kataoka, C.; Abe-Yoshizumi, R.; Kandori, H.; Uchihashi, T. Oligomeric States of Microbial Rhodopsins Determined by High-Speed Atomic Force Microscopy and Circular Dichroic Spectroscopy. *Sci Rep* **2018**, *8* (1), 8262. https://doi.org/10.1038/s41598-018-26606-y.

(59) Double Agents Cross-Linking Reagents Selection Guide, 1999.

(60) Green, N. S.; Reisler, E.; Houk, K. N. Quantitative Evaluation of the Lengths of Homobifunctional Protein Cross-Linking Reagents Used as Molecular Rulers. *Protein Science* **2008**, *10* (7), 1293–1304. https://doi.org/10.1110/ps.51201.

(61) Kahraman, A.; Malmström, L.; Aebersold, R. Xwalk: Computing and Visualizing Distances in Cross-Linking Experiments. *Bioinformatics* **2011**, *27* (15), 2163–2164. https://doi.org/10.1093/bioinformatics/btr348.

(62) Simons, K.; Ikonen, E. Functional Rafts in Cell Membranes. **1997**, *387*, 4.

(63) Zeev-Ben-Mordehai, T.; Vasishtan, D.; Siebert, C. A.; Whittle, C.; Grünewald, K. Extracellular Vesicles: A Platform for the Structure Determination of Membrane Proteins by Cryo-EM. *Structure* **2014**, *22* (11), 1687–1692. https://doi.org/10.1016/j.str.2014.09.005.

(64) Tamogami, J.; Sato, K.; Kurokawa, S.; Yamada, T.; Nara, T.; Demura, M.; Miyauchi, S.; Kikukawa, T.; Muneyuki, E.; Kamo, N. Formation of M-Like Intermediates in Proteorhodopsin in Alkali Solutions (PH ≥ ∼8.5) Where the Proton Release Occurs First in Contrast to the Sequence at Lower PH. *Biochemistry* **2016**, *55* (7), 1036–1048. https://doi.org/10.1021/acs.biochem.5b01196.

(65) Knowles, T. J.; Finka, R.; Smith, C.; Lin, Y.-P.; Dafforn, T.; Overduin, M. Membrane Proteins Solubilized Intact in Lipid Containing Nanoparticles Bounded by Styrene Maleic Acid Copolymer. *Journal of the American Chemical Society* **2009**, *131* (22), 7484–7485. https://doi.org/10.1021/ja810046q.

(66) Jamshad, M.; Lin, Y.-P.; Knowles, T. J.; Parslow, R. A.; Harris, C.; Wheatley, M.; Poyner, D. R.; Bill, R. M.; Thomas, O. R. T.; Overduin, M.; Dafforn, T. R. Surfactant-Free Purification of Membrane Proteins with Intact Native Membrane Environment. *Biochemical Society Transactions* **2011**, *39* (3), 813–818. https://doi.org/10.1042/BST0390813.

(67) Scheidelaar, S.; Koorengevel, M. C.; van Walree, C. A.; Dominguez, J. J.; Dörr, J. M.; Killian, J. A. Effect of Polymer Composition and PH on Membrane Solubilization by

Styrene-Maleic Acid Copolymers. *Biophysical Journal* **2016**, *111* (9), 1974–1986. https://doi.org/10.1016/j.bpj.2016.09.025.

(68) Tonge, S. R.; Tighe, B. J. Responsive Hydrophobically Associating Polymers: A Review of Structure and Properties. *Advanced Drug Delivery Reviews* **2001**, *53* (1), 109–122. https://doi.org/10.1016/S0169-409X(01)00223-X.

(69) Ueta, T.; Kojima, K.; Hino, T.; Shibata, M.; Nagano, S.; Sudo, Y. Applicability of Styrene-Maleic Acid Copolymer for Two Microbial Rhodopsins, RxR and HsSRI. *Biophysical Journal* **2020**, *119* (9), 1760–1770. https://doi.org/10.1016/j.bpj.2020.09.026.

(70) Mosslehy, W.; Voskoboynikova, N.; Colbasevici, A.; Ricke, A.; Klose, D.; Klare, J. P.; Mulkidjanian, A. Y.; Steinhoff, H. Conformational Dynamics of Sensory Rhodopsin II in Nanolipoprotein and Styrene–Maleic Acid Lipid Particles. *Photochem Photobiol* **2019**, *95* (5), 1195–1204. https://doi.org/10.1111/php.13096.

(71) Hirai, T.; Subramaniam, S. Protein Conformational Changes in the Bacteriorhodopsin Photocycle: Comparison of Findings from Electron and X-Ray Crystallographic Analyses. *PLoS ONE* **2009**, *4* (6), e5769. https://doi.org/10.1371/journal.pone.0005769.

(72) Hussain, S.; Franck, J. M.; Han, S. Transmembrane Protein Activation Refined by Site-Specific Hydration Dynamics. *Angewandte Chemie International Edition* **2013**, *52* (7), 1953–1958. https://doi.org/10.1002/anie.201206147.

(73) Andersson, M.; Malmerberg, E.; Westenhoff, S.; Katona, G.; Cammarata, M.; Wöhri, A. B.; Johansson, L. C.; Ewald, F.; Eklund, M.; Wulff, M.; Davidsson, J.; Neutze, R. Structural Dynamics of Light-Driven Proton Pumps. *Structure* **2009**, *17* (9), 1265–1275. https://doi.org/10.1016/j.str.2009.07.007.

(74) Farrens, D. L.; Altenbach, C.; Ke, Y.; Hubbell, W. L.; Khorana, H. G. Requirement of Rigid-Body Motion of Transmembrane Helices for Light Activation of Rhodopsin. *Science* **1996**, *274*, 768–770.

(75) Hirschi, S.; Kalbermatter, D.; Ucurum, Z.; Lemmin, T.; Fotiadis, D. Cryo-EM Structure and Dynamics of the Green-Light Absorbing Proteorhodopsin. *Nat Commun* **2021**, *12* (1), 4107. https://doi.org/10.1038/s41467-021-24429-6.

(76) Peyret, A.; Zhao, H.; Lecommandoux, S. Preparation and Properties of Asymmetric Synthetic Membranes Based on Lipid and Polymer Self-Assembly. *Langmuir* **2018**, *34* (11), 3376–3385. https://doi.org/10.1021/acs.langmuir.7b04233.

(77) Hua, D.; Kuang, L.; Liang, H. Self-Directed Reconstitution of Proteorhodopsin with Amphiphilic Block Copolymers Induces the Formation of Hierarchically Ordered Proteopolymer Membrane Arrays. *J. Am. Chem. Soc.* **2011**, *133* (8), 2354–2357. https://doi.org/10.1021/ja109796x.

(78) Ravula, T.; Hardin, N. Z.; Ramadugu, S. K.; Cox, S. J.; Ramamoorthy, A. Formation of PH-Resistant Monodispersed Polymer-Lipid Nanodiscs. *Angew. Chem. Int. Ed.* **2018**, *57* (5), 1342–1345. https://doi.org/10.1002/anie.201712017.

(79) Ravula, T.; Hardin, N. Z.; Bai, J.; Im, S.-C.; Waskell, L.; Ramamoorthy, A. Effect of Polymer Charge on Functional Reconstitution of Membrane Proteins in Polymer Nanodiscs. *Chem. Commun.* **2018**, *54* (69), 9615–9618. https://doi.org/10.1039/C8CC04184A.

(80) Ravula, T.; Ramadugu, S. K.; Di Mauro, G.; Ramamoorthy, A. Bioinspired, Size-Tunable Self-Assembly of Polymer-Lipid Bilayer Nanodiscs. *Angew. Chem.* **2017**, *129* (38), 11624–11628. https://doi.org/10.1002/ange.201705569.

(81) Lis, M.; Wizert, A.; Przybylo, M.; Langner, M.; Swiatek, J.; Jungwirth, P.; Cwiklik, L. The Effect of Lipid Oxidation on the Water Permeability of Phospholipids Bilayers. *Phys. Chem. Chem. Phys.* **2011**, *13* (39), 17555. https://doi.org/10.1039/c1cp21009b.

2.9 Supporting Information

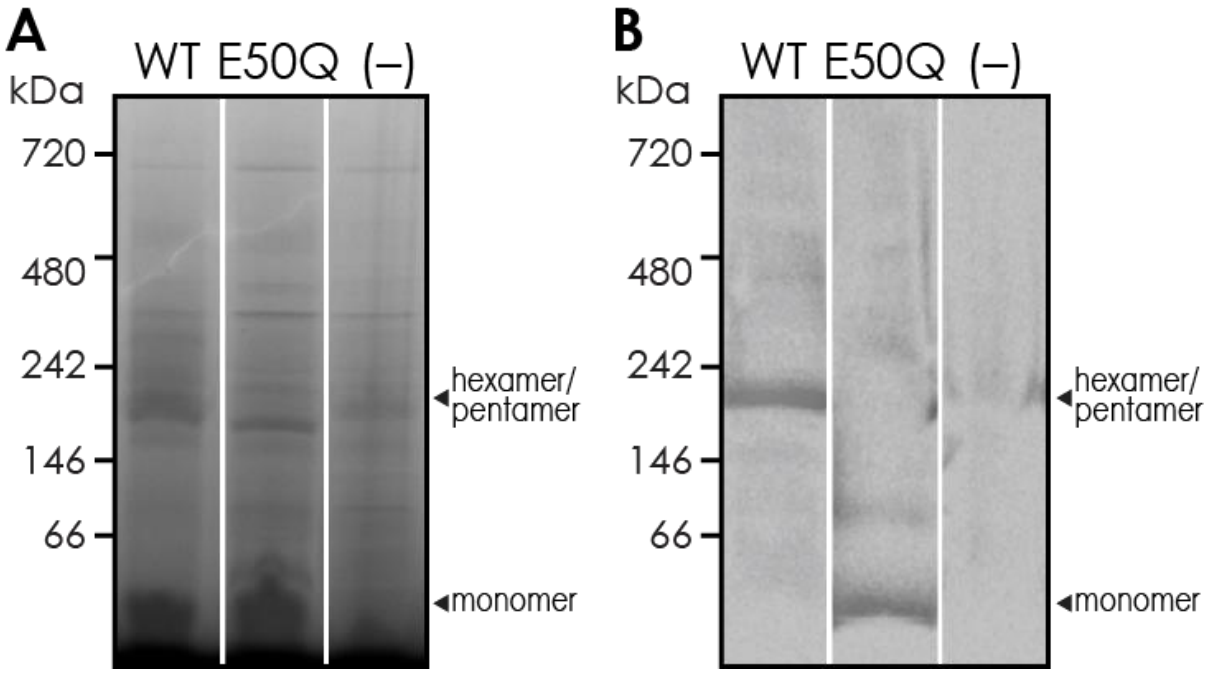

Figure S2.1. (A) BN-PAGE of cell lysates from *E. coli* overexpressing WT PR (lane 1), PR E50Q (lane 2), and a negative control (NC) from lysates without overexpressing PR (lane 3). **(B)** Western Blot analysis of proteins transferred from a BN-PAGE of cell lysates from *E. coli* overexpressing WT PR (lane 1), PR E50Q (lane 2), and a negative control (NC) from lysates without overexpressing PR (lane 3).

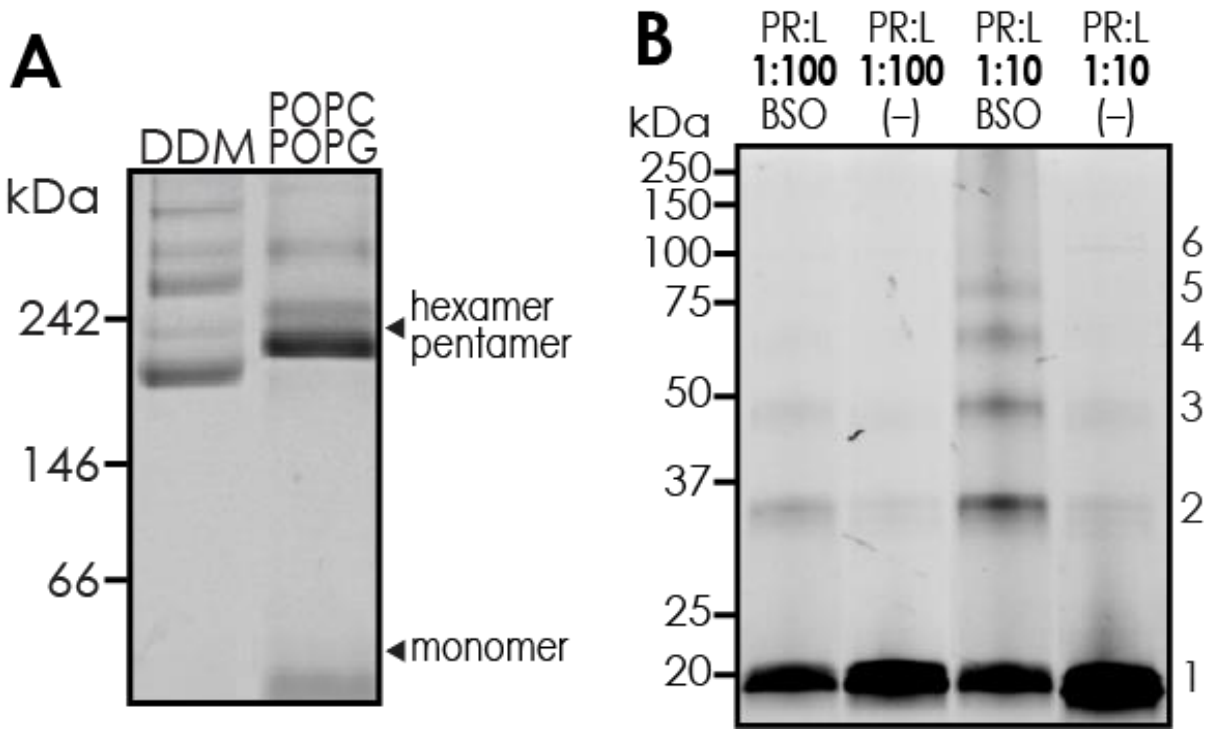

Figure S2.2. (A) BN-PAGE of purified PR in DDM surfactant micelles (lane 1) and reconstituted into POPC/POPG (4:1, mol/mol) (lane 2). **(B)** SDS-PAGE of BSOCOES-crosslinked WT PR after reconstituted in POPC/POPG (4:1, mol/mol) liposomes at different protein-to-lipid ratios (1:10 vs. 1:100 w/w). The negative controls are without application of the BSOCOES crosslinker.

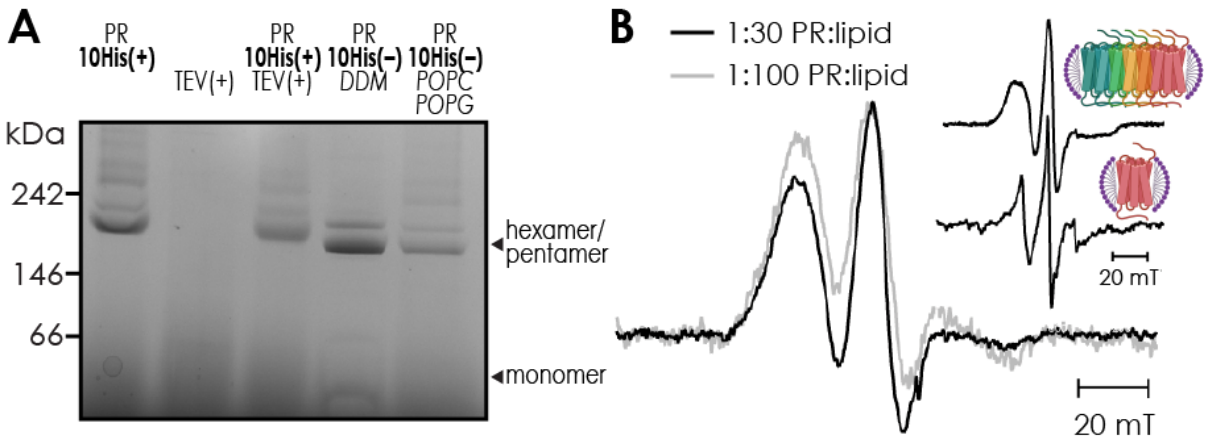

Figure S2.3. Evidence showing PR oligomers are not artifact from nonspecific interactions. **(A)** BN-PAGE of WT PR before the His-tag removal (lane 1), during the His-tag removal process by adding TEV protease (lane 3), after the His-tag removal process reconstituted in a buffer supplemented with 0.05 wt% DDM detergent (lane 4), and after the His-tag removal but reconstituted in POPC/PG liposomes. No bands can be observed from pure TEV protease (lane 2) in the range displayed because of its smaller molecule weight (~25 kDa). **(B)** EPR of PR spin-labeled at site 55 and reconstituted into POPC/POPG (4:1, mol/mol) liposomes at two different protein-to-lipid ratios (1:30 and 1:100). The inset shows characteristic EPR spectral broadening due to the oligomerization of the same PR with a spin label at site 55 in DDM detergent micelles and loss of broadening in the monomeric form of PR separated by SEC.

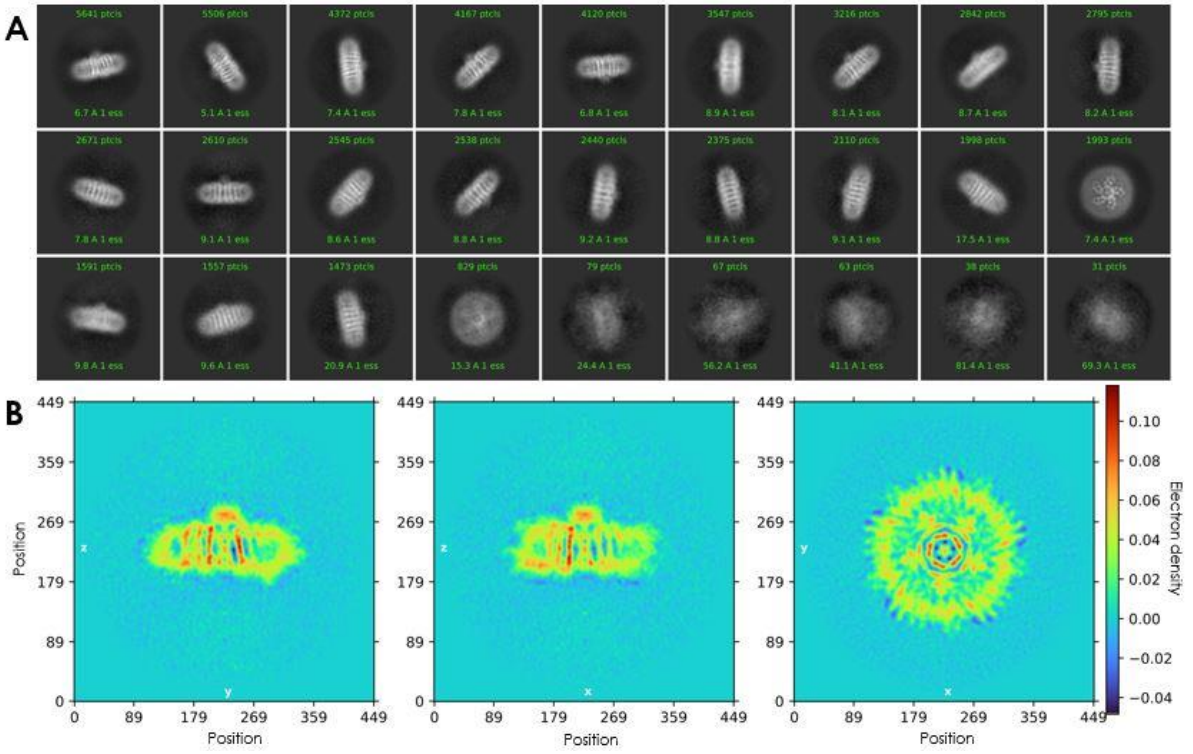

Figure S2.4. (A) 2D classifications of PR WT **(B)** 3D classifications of PR WT. 27,398 micrgraphs were collected on a Titan Krios operating at 300 kV and a sub-selection of 67,997 particles were used.

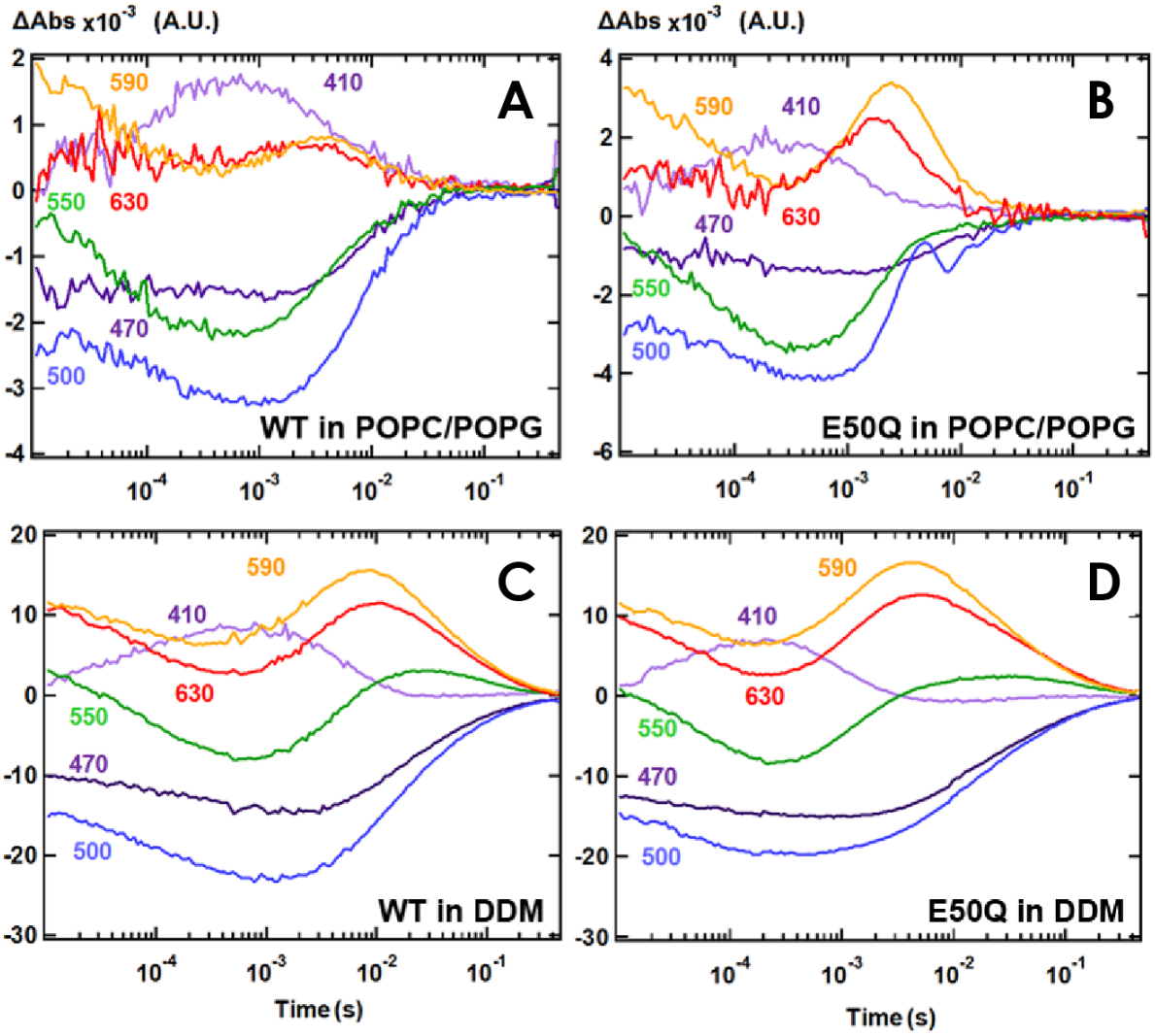

Figure S2.5. Transient difference absorbance data of **(A)** WT PR and **(B)** PR E50Q in POPC/POPG (4:1, mol/mol) liposomes and of **(C)** WT PR (Data published in Idso et al.) and **(D)** PR E50Q in DDM detergent micelles. Measurements were performed at pH 8.5 and ~293 K. The transient absorbance changes at 410 (light purple line), 470 (deep purple line), 500 (blue line), 550 (green line), 590 (orange line), and 630 (red line) nm were collected after PR is photoactivated by a green-light pulse laser.

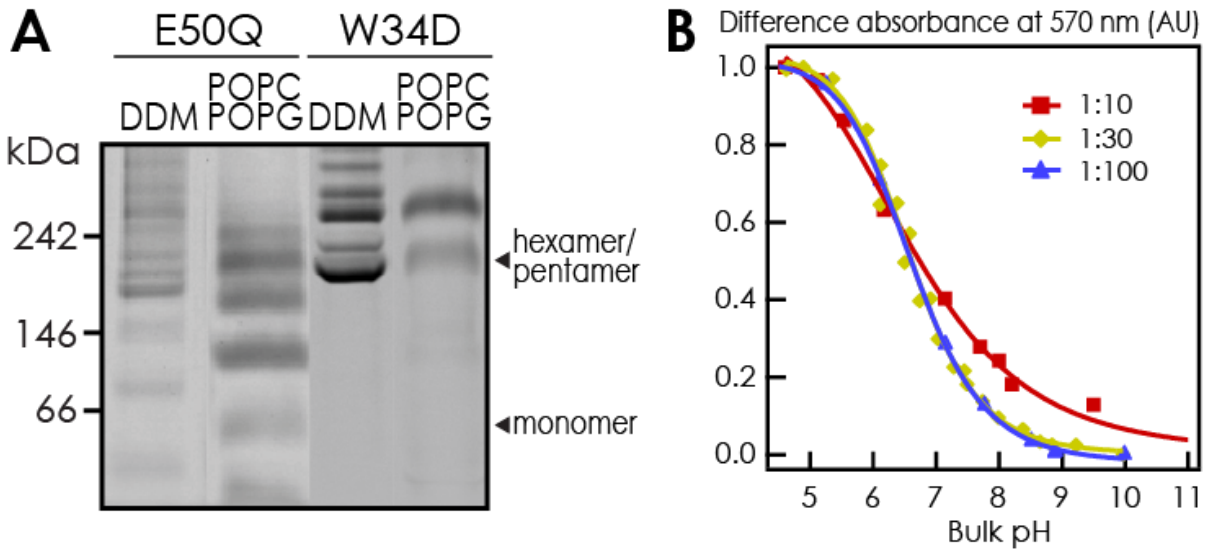

Figure S2.6. (A) BN-PAGE of PR E50Q and W34D in DDM detergent micelles and reconstituted into POPC/POPG (4:1, mol/mol) liposomes. **(B)** pH-dependent absorbance transition at 570 nm for WT PR reconstituted into POPC/POPG (4:1, mol/mol) liposomes at three different protein-to-lipid ratios (1:10, 1:30, and 1:100).

Supplement 1 – PR pentamers could only be observed with the longer crosslinker BSOCOES

The observation that only the longer crosslinker BSOCOES can stabilize PR pentamers (Figure 2.1A) means that a lysine-lysine distance exists between adjacent PR subunits that is only accessible to BSOCOES. To confirm this hypothesis, we analyzed the available BPR oligomer crystal structures (hexamer vs. pentamer) with Xwalk, an existing computational tool used for predicting intermolecular crosslinking[61]. The method relies on the estimated shortest path between two lysine residues in adjacent PR subunits, where the path leads through solvent without penetrating the protein surface. We analyzed lysine-lysine distances in the range of 13–23 Å, which covers all distances attainable with the three crosslinkers DSG, DSS, and BSOCOES (see Table S2.1). Among the possible crosslinks

identified using these constraints, K125–K244 was unique to the pentameric structures (Table S2.2), possibly because it penetrated the protein surface of the hexameric structures. This crosslink falls within a 21–22 Å distance range (Table S2.2), which is closest to the average attainable distance of BSOCOES (21.6 Å; Table S2.1). This result explains why only BSOCOES can stabilize PR pentamers, as shown by our experimental result (Figure 2.1A).

Table S2.1. Cited spacer arm lengths[59] and calculated average attainable distances[60] of the crosslinkers DSG, DSS, and BSOCOES. The average attainable distances include the average N-N distances and the sidechain length of lysine (2 × 5 Å)

	Cited N-N Distance	**Average N-N Distance**	**Average Attainable Distance**	**Range of N-N Distances**	**Range of Attainable Distances**
DSG	7.7	6.2	16.2	3.1–7.5	13.1–17.5
DSS	11.4	8.9	18.9	5.6–11.4	15.6–21.4
BSOCOES	13.0	11.6	21.6	6.8–12.4	16.8–22.4

Table S2.2. Predicted inter-PR crosslinks from three oligomeric BPR crystal structures[34], with calculated solvent-accessible distances[60] given in Å. Note that the K125–K244 crosslink is found only in pentameric structures and is the long distance consistent with reactivity with BSOCOES alone.

Predicted Inter-PR Crosslink	**BPR Hexamer (PDB: 4JQ6)**	**BPR Pentamer (PDB: 4KLY)**	**BPR Pentamer (PDB: 4KNF)**
K59–K59	21.3	21.2	20.6
K59–K244	20.1	--	21.4
K57–K244	14.9	15.0	16.6
K125–K244	--	21.9	21.2

Supplement 2 – SMALPs can extract PR from *E. coli* membranes in the monomeric form

E. coli membranes containing PR-WT and PR-E50Q were tested, as the significant difference in size between the hexameric and the monomeric forms of PR could affect the solubilization efficiency. Western Blot analysis on SDS-PAGE of the final SMA-solubilized samples indicate that only the monomeric form of PR is solubilized in both cases, and that the hexameric form of PR-WT is not (Figure S2.7A). Furthermore, UV absorption measurements at 520 nm are used to determine the protein yield for both cases. The results indicate that 1 L of *E. coli* overexpressing PR solubilized with SMALPs yields 4.0 mg of PR-WT and 72.0 mg of PR-E50Q (Figure S2.7B). Clearly, SMA is very effective at encapsulating the monomer-enrich PR-E50Q mutant but does not solubilize the hexamer-dominant PR-WT. This is observed evidently in after SMA solubilization when comparing PR-E50Q and PR-WT samples (Figure S2.7C). The primarily monomeric PR-E50Q is easily solubilized from *E. coli* membranes by SMA making the supernatant appear pink and the pellet white. In contrast, the primarily oligomeric PR-WT undergoes minimal solubilization by SMA leading to a clear supernatant and pink membrane pellet.

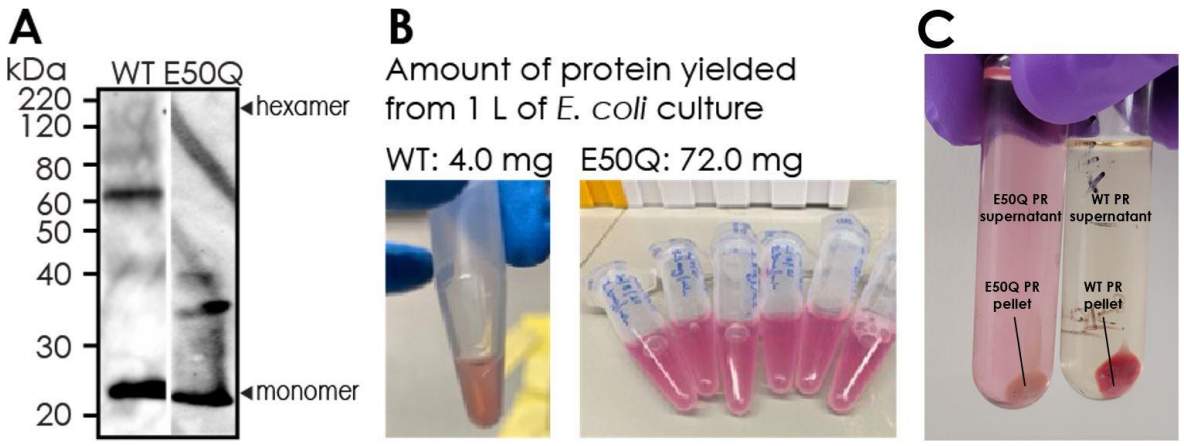

Figure S2.7. SMALPs only solubilizes the monomeric form of PR. **(A)** Western Blot showing the dominant presence of PR-WT and E50Q mutant in SMALPs. MagicMark protein ladder (LC5602) is used as the molecular standard weight. **(B)** The amount of protein yielded from 1 L of *E. coli* culture expressing oligomer-dominant PR-WT and monomer-enriched PR-E50Q. **(C)** Harvested membrane pellet for PR-E50Q and PR-WT after SMA solubilization.

The oligomeric form of PR could not be encapsulated with SMA, perhaps because of the limited size of the nanodiscs formed by this polymer. According to a crystal structure of the hexameric form of blue light-absorbing proteorhodopsin (PDB ID: 4JQ6), the diameter of hexameric PR is ~92 Å, while that of a monomeric PR is ~27.2 Å (Figure S2.8). Although the typical size of a SMALP is also ~100 Å, its mean core diameter is only ~76 ± 4 Å76, which renders it difficult to fit a PR hexamer into a SMALP, while a PR monomer can easily be captured and stabilized.

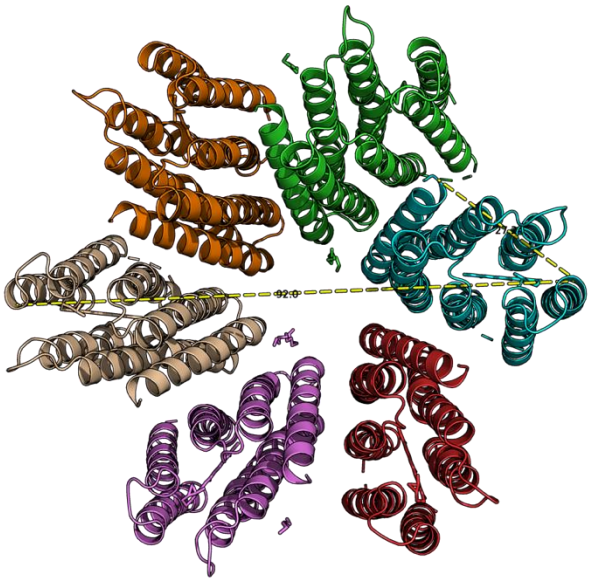

Figure S2.8. Measurements of the diameters of PR hexamer and monomer using PyMOL. Measurements are done on the crystal structure of blue light-absorbing proteorhodopsin (PDB ID: 4JQ6).

Supplement 3 – Packing of PR oligomers is tighter in the hexameric state

We compared the compactness of the hexameric and the pentameric structures through the distance between the center masses of the adjacent protomers during GaMD simulations. PR hexamers exhibited significantly shorter distances compared with the pentamers (hexamers: ~28 Å; pentamers: ~32 Å; Figure S2.9A). These results agreed with the packing score analysis, which showed that PR hexamers exhibited a higher overall packing score than the pentamers (Figure 2.2B), indicating stronger cross-protomer association. Together, these MD simulation results demonstrated that the hexameric form of PR is more tightly packed than the pentameric counterpart.

By replacing 30 mol% of POPG with POVPC, which has the same zwitterionic headgroup but a reoriented sn-2 hydrocarbon chain to make the lipid bilayer leakier[81], we observed from BN-PAGE analysis that the pentamers are the dominant species (Figure S2.9B). This indicates that a leakier surrounding environment could populate PR pentamers, which are less tightly packed compared with the hexamers, as suggested by the lower packing score (Figure 2.2B) and the longer cross-protomer distances from our MD simulations (Figure S2.9A).

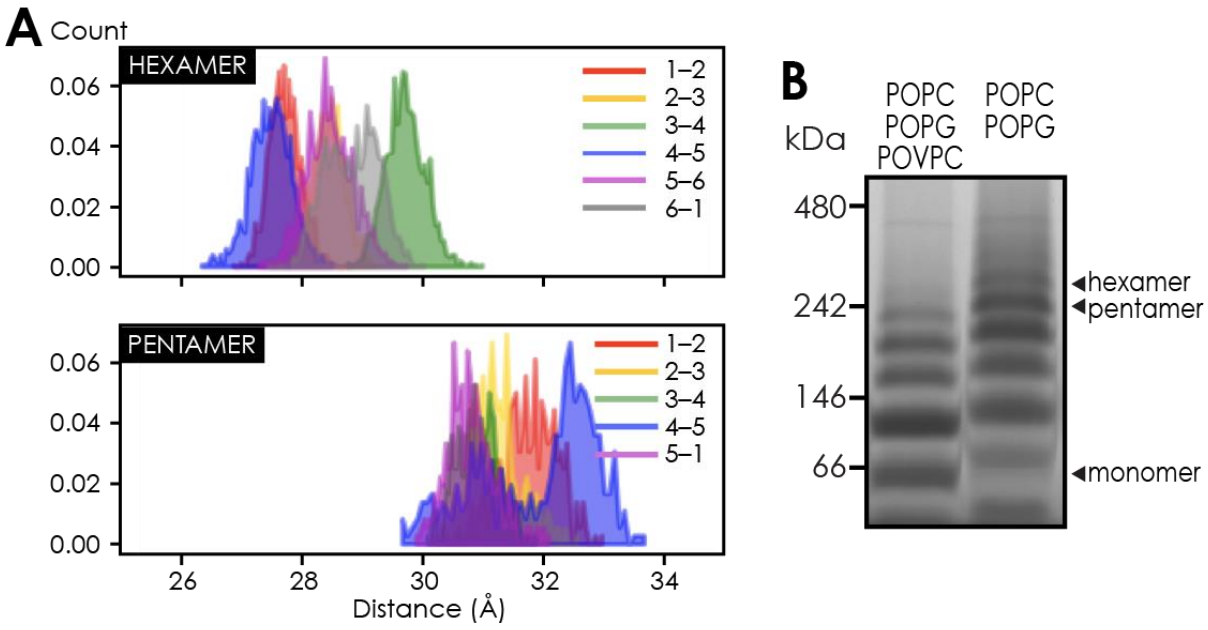

Figure S2.9. (A) The inter-subunit distances between the closest neighboring subunits in BPR hexamer and pentamer were also listed and compared. **(B)** BN-PAGE of PR E50Q reconstituted into POPC/POPG/POVPC (50/20/30, mol/mol/mol) (lane 1) and POPC/POPG (80/20, mol/mol).

Chapter 3. Co-assembly of functionally-active proteorhodopsin membrane protein molecules in mesostructured silica-surfactant films

---

This chapter is adapted from a paper submitted to *Chemistry of Materials*, which is currently under review. I am first author on this paper and my contributions include experimental design, conducting experiments, analyses, and writing/editing.

Journal: *Chemistry of Materials*

Authors: Maxwell W. Berkow, Hosu Gwak, Matthew N. Idso, Michael B. Schmithorst, Bailey Rhodes, Brad D. Price, Daniel S. Gianola, Songi Han, and Bradley F. Chmelka

3.1 Abstract

A combination of non-ionic, cationic, and zwitterionic surfactants are shown both to stabilize the transmembrane protein proteorhodopsin, as well as to direct co-assembly into robust transparent mesostructured silica-surfactant films containing high loadings of functionally-active protein guests. Proteorhodopsin is a transmembrane protein that exhibits light-activated H^+ transport properties, the photocycle kinetics of which are quantified by time-resolved UV-visible spectroscopy and demonstrated to be similar for proteorhodopsin in the abiotic mesostructured films compared to native-like lipids. The surfactants mediate the pKa of a key ion-channel residue, leading to an expanded pH functional range for proteorhodopsin in mesostructured silica-surfactant host materials. Small-angle X-ray diffraction results for 100-μm films show high extents of mesoscale order with protein loadings up to 25 wt% and worm-like mesostructural order for 44 wt% proteorhodopsin. Solid-state ^{1}H, ^{13}C, and ^{29}Si NMR analyses provide atomic-scale insights on the compositions and interactions at the mesochannel surfaces, which account for the structure-directing roles of surfactant species. Nanoindentation measurements reveal the mechanical robustness of the films, which interestingly increases with proteorhodopsin loading for the compositions examined. Heat treatment analyses show improved thermal stability for proteorhodopsin to 110℃ within mesostructurally-ordered films. The results establish closely-correlated relationships between the compositions, nano- and mesoscale structures, proteorhodopsin dynamics, and macroscopic mechanical properties of the silica-surfactant-protein films, providing key biomimetic design criteria.

3.2 Introduction

Membrane proteins perform, within cellular environments, a variety of transport, sensing, and catalytic functions that are attractive for technological applications. For example, the transmembrane protein proteorhodopsin transports H^+ ions in response to light, thus converting solar energy into a chemical (pH) gradient.[1–3] Protein engineering strategies are improving the stabilities and enhancing and diversifying the properties of membrane proteins beyond their native functions.[4] Protein guest molecules can be incorporated into non-native abiotic hosts, such as polymers, glasses, and mesostructured hybrid materials, with diverse macroscopic morphologies, including particles, fibers, films, or monoliths to improve the mechanical or thermal stabilities of the protein-host system.[5] For example, globular proteins can be post-synthetically adsorbed onto the surface of porous materials[6] through hydrogen bonding, electrostatic forces, or hydrophobic effects; however, these interactions are often or transient weak and leaching of the catalyst can lead to a loss in activity.[7] Alternatively, biologically-enabled materials can be made through the co-assembly and subsequent cross-linking of polymeric or inorganic oxide matrices around protein moieties, producing uniform distributions of stable and functionally-active guest molecules. Incorporation of functionally-active protein during syntheses of many of these materials has been challenging, due in part to the often countervailing chemical compositions or conditions required to maintain protein stability, compared with those typically used to synthesize or process polymeric or inorganic host materials.

As a host material for proteins, silica is a good candidate, because it is mechanically and thermally robust and can be synthesized under relatively mild conditions. While many mesostructured silica materials have been synthesized under conditions that typically denature

proteins, such as very high or low pH or with high concentrations of organic solvents, extensive previous work has demonstrated that silica can be synthesized in aqueous sol-gel mixtures at pH values in the range of 5–8.[8] These relatively benign conditions make sol-gel-derived materials suitable for protein incorporation, whereby hydrolyzed siloxane precursors cross-link around typically globular proteins that are occluded into robust inorganic host matrices.[8] Such protein-silica materials are processable into monoliths or thin films, though typically with low protein loadings and often unfavorable or transient interactions between the protein guests and the silica matrix that alter protein function and reduce stability.

Compared to globular proteins, transmembrane proteins are particularly challenging to incorporate into non-native host environments, due in part to their heterogeneous amphiphilic character. While useful for relatively hydrophilic globular proteins,[9] hydrophilic host environments such as silica are generally incompatible with the highly hydrophobic transmembrane regions of membrane proteins. Most transmembrane proteins are made up of hydrophobic α-helices that span the lipid bilayer of cell membranes, with hydrophilic loops that are exposed to aqueous environments at the intra- and extra-cellular sides of the bilayer. Such amphiphilicity can be exploited by using surfactants to simulate native-like cell membrane conditions in abiotic host environments, such as liposomes or micelles.[10–12] In fatty-acid-based lipid bilayers of liposomes, hydrophobic lipid chains stabilize the α-helices of the membrane protein, whereas the charged and hydrophilic lipid headgroups at the cytoplasmic and extracellular interfaces stabilize the protein.[13] However, these bilayers, native or synthetic, exhibit poor mechanical and thermal stabilities and also are not easily processable into macroscopic material morphologies. Amphiphilic block copolymers similarly provide both hydrophilic and hydrophobic regions that offer suitable synthetic environments to stabilize

membrane proteins with better mechanical and chemical stabilities, as well as local orientational order.[14–16] These wholly organic-amphiphile-based synthetic hosts accommodate modest bulk amounts of membrane proteins, with still relatively poor mechanical properties.[14-16]

For optically responsive molecules like proteorhodopsin, it is additionally necessary for the host materials to be optically transparent. Previously, highly hydrophobic photo-responsive conjugated polymers have been incorporated into transparent surfactant-directed silica and titania matrices with significant extents of mesostructural order.[17,18] Similar mesostructured materials have been used to accommodate other molecular guests, such as low-molecular-weight dyes[19–23] and nanoparticles,[24] although these hosts have generally been synthesized using non-aqueous solvents that are incompatible with proteins.

Here, we report novel transparent and robust silica-surfactant films with high extents of mesostructural order and that incorporate high loadings of functionally-active transmembrane protein proteorhodopsin guests. This novel combination of properties is enabled by the judicious selection of three types of surfactants and synthesis conditions, which both stabilize the membrane protein and direct its co-assembly into the hydrophobic regions of the mesostructured silica-surfactant host materials, which can be processed into films up to 1 mm thick with arbitrary lateral dimensions. Small-angle X-ray scattering analyses elucidate the protein-stabilizing and structure-directing roles of the surfactants, while solid-state NMR resolves molecular-level interactions between the surfactants and mesochannel silica surfaces. Notably, time-resolved UV-visible absorption spectra quantify the photocycle kinetics of the proteorhodopsin guests, which retain their native-like light-activated conformational dynamics within the mesostructured silica-surfactant materials, even at high protein loadings.

3.3 Materials and Methods

Proteorhodopsin expression and purification

The monomer-enriched proteorhodopsin mutant E50Q (Figure 3.1a) was cloned into a pET26b (+) vector (Novagen) as described previously.[25] For expression, 10 mL cultures of BL21(DE3) *E. coli* (Thermo Fisher), transformed with the above plasmid, were made in LB broth with 50 µg/mL kanamycin and orbitally shook at 180 rpm for 16 h at 37 ℃. These cultures were diluted into 1 L of LB with 50 µg/mL kanamycin and grown at 37 ℃ with 180 rpm orbital shaking until OD_{600}=0.6, at which point PR expression was induced with 1 mM isopropyl *β-D*-1-thiogalactopyranoside (IPTG, Thermo Fisher) and 1 µM *trans*-retinal (Sigma Aldrich). *Trans*-retinal is essential for PR function and the cells cannot produce it on their own. After 18 h, each liter of cell culture was spun down at 5000 rcf, resuspended in 30 mL of 50 mM K_2HPO_4 (Sigma Aldrich) and 150 mM KCl (Sigma Aldrich) (PR buffer) at pH 8.7, and then lysed for 1 h with incubation in lysis buffer (20 mg/mL lysozyme, DNAse and 20 mM $MgCl_2$). Lysed cells were then centrifuged at 1000 rcf for 10 min to remove large debris in the pellet. The supernatant was then spun down at 10,000 rcf to harvest PR-containing membranes in the new pellet. The supernatant was removed and the membranes were flash frozen as pellets in liquid nitrogen and stored at -80℃ until needed for experiments. Purification of PR began with homogenization of the membrane pellet in 2 wt% *n*-dodecyl-*β-D*-maltoside (DDM, Anatrace) PR buffer with a glass tissue grinder, and then mixed for 1 h. The homogenized solution was spun down at 100,000 rcf and the supernatant collected to obtain PR E50Q in DDM micellar solution. Next, PR was further purified using a 5 mL Ni-NTA resin column (ThermoFisher) with a binding buffer (0.01 wt% DDM and 30 mM imidazole) and eluting buffer (0.01 wt% DDM and 500 mM imidazole). Prior to incorporation

into materials, the ionic strength of the PR-containing solutions was lowered by using a PD-10 desalting column (Millipore) and then concentrating the eluate as desired by centrifugal concentration (50 kDa MWCO, Amicon Ultra), generally >100 µM. Protein concentration was determined using the absorbance at 520 nm using an extinction coefficient of 49,000 M^{-1}•cm and a molecular weight of 29,000 g/mol.

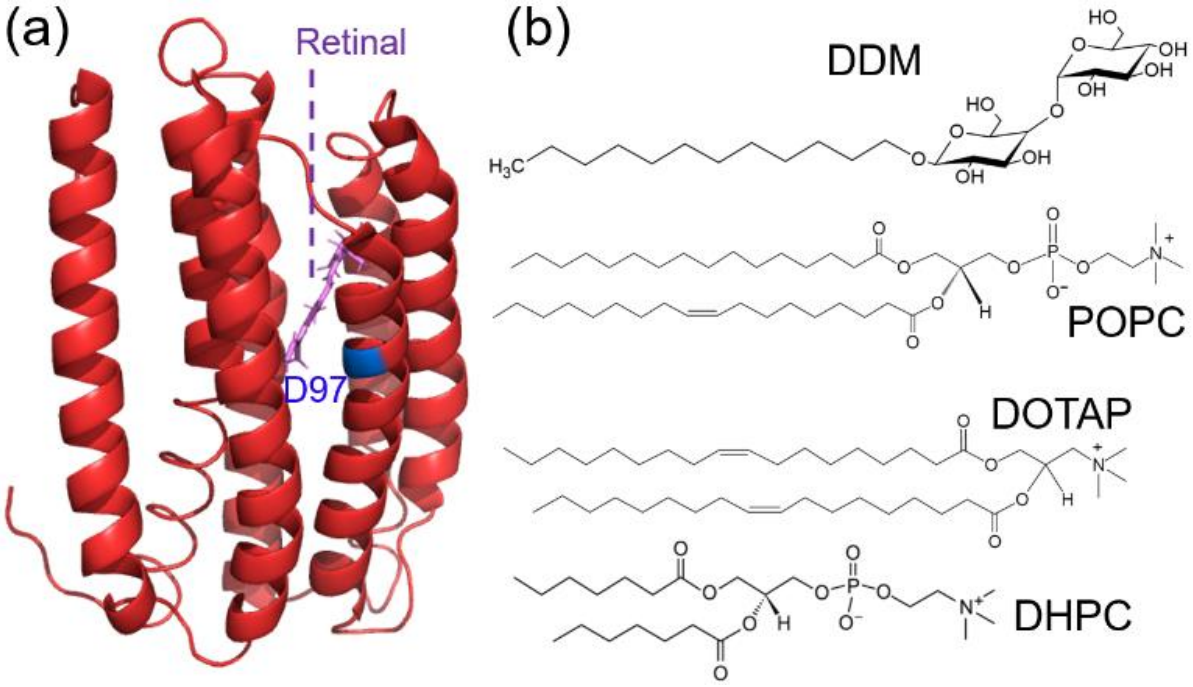

Figure 3.1. Schematic diagrams of **(a)** the E50Q mutant form of the transmembrane protein proteorhodopsin (PR) with 7 α-helices, light-responsive retinal moiety, and key ion-channel aspartic acid residue D97; **(b)** non-ionic C_{12}-maltoside *n*-dodecyl-*β,D*-maltoside (DDM) surfactant, zwitterionic 1-palmitoyl-2-oleoyl-glycero-3-phosphocholine (POPC) lipid, cationic 1,2-dioleoyl-3-trimethylammonium-propane (DOTAP) lipid, and zwitterionic 1,2-diheptanoyl-*sn*-glycero-3-phosphocholine (DHPC) lipid.

Preparation of proteorhodopsin-containing silica-surfactant films

Mesostructured silica materials were prepared by mixing a 3:1 ratio by weight of 262.5 mg tetraethoxysilane (TEOS, Acros Organics) and 87.5 mg *n*-propyltriethoxysilane (PTEOS, 97%, Alfa Aesar) with 1.5 g of H_2O and 10 μL of 400 mM HCl. The solution was stirred vigorously for 3 h, at which point the solution was transparent. 200 mg of this solution was removed and mixed with an appropriate amount of DDM, *n*-decyl-*β,D*-maltoside (DM, Anatrace), or *n*-hexadecyl-*β,D*-maltoside (HDM, Anatrace). Another solution was created by mixing a desalted PR-containing DDM micellar solution with a 9.1 wt% solution of 1-palmitoyl-2-oleoyl-glycero-3-phosphocholine (POPC, Avanti Polar Lipids) and 1,2-dioleoyl-3-trimethylammonium-propane (DOTAP, Avanti Polar Lipids) in 4:1 molar ratio or, for comparative pKa measurements, with 1,2-diheptanoyl-s*n*-glycero-3-phosphocholine (DHPC, Anatrace); the molecular structures are shown in Figure 3.1b. The two solutions were then mixed and quickly titrated to a pH of 4.1 using 50 mM HCl or 50 mM NaOH. The final concentration of species in this mixed solution depended on the desired PR loading, however, ratios of the other components were kept fixed at 62.5 maltoside surfactant : 6.1 POPC : 1.4 DOTAP : 22.5 SiO_2 : 7.5 *n*-propyl-$SiO_{1.5}$ by weight. The amount of maltoside surfactant added to the silica precursor solution (as discussed above) is dependent on the concentration of maltoside surfactant in the protein-stabilizing micelles, measured via 1D solution-state ^{1}H NMR, which varies for different expressions. Final solutions were cast onto PDMS stamps (~2 cm x 2 cm) or Si wafers with a fluoro-monolayer (for mechanical property testing) under ambient temperature and 58% relative humidity conditions for films with rectangular and cubic mesostructural ordering and at 98% relative humidity for films with worm-like mesostructural order. Solvent evaporation was allowed to proceed for 4 days before the materials were

characterized. Synthesized films had thicknesses >100 μm. Films made with predominantly DM- and HDM-structure-directed surfactants still contained small concentrations of DDM, which was used in the expression and purification of PR.

Materials characterization

Small-angle X-ray scattering (SAXS) was used to assess the impact of synthesis conditions on the long-range mesostructural ordering of the silica-surfactant-proteorhodopsin films. SAXS records the pattern of a continuously scattered beam of X-rays incident on a sample. With knowledge of the distance between the sample and the detector, angles of reflection of the X-ray path due to interactions with the material can be calculated. Well-ordered samples will cause the scattered X-rays to be concentrated at certain positions and angles, whereas disordered samples will scatter X-rays in all directions, leading to a broad distribution of X-rays across the detector. The positions and intensities of the SAXS reflections show high extents of mesostructural order that can be analyzed to calculate *d*-spacings that correspond to characteristic scattering distances, such as the mean center-to-center dimensions between surfactant-directed silica mesochannels. SAXS measurements were conducted on a custom instrument using a XENOCS Genix 50W X-ray microsource with Cu Kα radiation (λ = 1.542 Å, voltage 50 keV, current 1 mA), a focus size of 50 microns, a XENOCS FOX2D multilayer optics for SAXS monochomator, and a Dectris EIGER R 1M detector (77.2 mm x 79.9 mm sensitive area, 1030 x 1065 32 bit image) located 1.7 m behind the sample. SAXS patterns were recorded over a range of 1–2.7 q (nm^{-1}).

A two-dimensional (2D) $^{29}Si\{^{1}H\}$ HETCOR NMR analysis of 5 wt% PR, 59.4 wt% DDM, 5.8 wt% POPC, 1.3 wt% DOTAP, 21.4 wt% SiO_2, and 7.1 wt% *n*-propyl-$SiO_{1.5}$ was performed at 11.7 T on a Bruker Avance NMR spectrometer equipped with a double-resonance

4 mm NMR probehead operating at frequencies of 500.2 MHz for ^{1}H and 99.4 MHz for ^{29}Si.[26] The experiment was performed at a magic-angle-spinning frequency of 12.5 kHz and room temperature. For the experiment, 48 increments of 512 scans with a t_1 increment of 96 μs were acquired. The recycle delay between scans was set to 1.2 s to correspond to 1.4T_1, where the ^{1}H T_1 was measured by a saturation recovery experiment. A 50 kHz 90^{o} radiofrequency (r.f.) pulse was used for initial excitation of ^{1}H nuclei, and a 1 ms cross-polarization contact pulse was used to transfer polarization from ^{1}H to ^{29}Si nuclei. The ^{1}H and ^{29}Si contact pulse frequencies were optimized to maximize signal. During the t_1 evolution period, eDUMBO-1$_{22}$ homonuclear decoupling was applied to the ^{1}H channel to enhance resolution of the ^{1}H dimension.[27] SPINAL-64 heteronuclear decoupling was applied to ^{1}H nuclei during acquisition.[28] Solution-state 2D ^{1}H-^{13}C HSQC NMR spectra of POPC and DOTAP were acquired at 300 K on a Bruker Avance NMR spectrometer at a field of 18.8 T equipped with a 5 mm PABBO BB ^{1}H/D Z-GRD probehead operating at frequencies of 800.2 MHz for ^{1}H and 201.2 MHz for ^{13}C (Figures S3.1, S3.2). The high-resolution solution-state 2D ^{1}H-^{13}C NMR spectra were used to assign the ^{1}H signals in the solid-state 2D ^{29}Si{^{1}H} HETCOR NMR analysis. The 2D spectra were acquired using a phase-sensitive gradient HSQC experiment with echo/anti-echo detection (hsqcetgp pulse program in the Bruker library) with 256 increments of 16 scans and a recycle delay of 1.5 s between scans. The ^{13}C and ^{1}H spectral widths were 166 ppm and 13 ppm centered at 94 ppm and 6 ppm, respectively. GARP decoupling was used to decouple ^{13}C spins from detected ^{1}H spins during acquisition. A two-fold linear forward prediction with 32 linear prediction coefficients was applied to the indirect dimension when processing the data. The samples were prepared as follows: stock solutions of POPC and DOTAP in chloroform (25 mg/ml) were blow-dried under a stream of N_2 gas and

further dried under vacuum overnight to remove residual chloroform. Then samples were redissolved in $CDCl_3$ to final concentrations of 33 mM for NMR experiments. Solution-state 2D ^{1}H-^{13}C HSQC NMR spectra of DDM in D_2O were acquired at 300 K on a Varian VNMRS NMR spectrometer at a field of 14.1 T, equipped with a 5 mm AutoXDB PFG probehead operating at frequencies of 599.7 MHz for ^{1}H and 150.8 MHz for ^{13}C (Figure S3.3). Specifically, the 2D spectra were acquired using a gHSQCAD pulse program in the Varian library with 256 increments of 16 scans and a recycle delay of 1.5 s between scans. The ^{13}C and ^{1}H spectral widths were 220 ppm and 16 ppm centered at 90 ppm and 6 ppm, respectively.

Static visible absorption spectroscopy was conducted on a Shimadzu UV-1800 spectrophotometer. For measurement of the pKa of D97, free-standing films of mesostructured silica were inserted into a home-built sample holder that fit into a transparent plastic cuvette. The sample was incubated initially in a solution containing 50 mM K_2HPO_4 and 150 mM KCl (pH ~8.7) for 15 min before UV-vis absorbance measurements were taken. Subsequently, the solution in the cuvette was removed and replaced with 2 mL of new buffered solution that had been titrated to the desired pH, one minute was allowed for incubation, the pH of the solution was measured, and the UV-visible absorbance of the film was taken. To determine the amount of time required for soaked films to equilibrate with the buffered solution, we monitored the visible absorbance of PR in the mesostructured silica after exposure to different buffered solutions; these measurements indicated that soaking as-synthesized films for 15 min and, following this initial soak, incubation times of 1 min in a new buffer were sufficient to allow equilibrium among PR species in the synthetic host and the buffered solution. Using an initial incubation time of 15 min and allowing 1 min of exposure to a new buffered solution between

pH changes, this process was repeated using at least 11 buffered solutions that were at different pH values.

The absorbance data acquired from films soaked in different buffered solutions was analyzed using a home-written MATLAB script to yield the acid dissociation constant for residue D97. In short, the program adjusts each spectrum such that the absorbance intensity at 700 nm is zero, then normalizes each absorption spectrum such that the absorbance maximum between 500-550 nm has an absorbance intensity of unity. Subsequently, the wavelength of maximum absorbance intensity is extracted and plotted as a function of pH. The resulting data is then fit to the Henderson-Hasselbalch equation using a non-linear fitting algorithm with two fitting constants, the pKa value and the Hill coefficient.

Static UV-visible light absorbance measurements at 520 nm were conducted on 5 wt% PR-containing films before and after heat treatment for 24 h at various temperatures to determine the effect of the host matrix on the stability of guest proteorhodopsin. Films with rectangular mesostructural ordering were subjected to heat treatment at 70 ℃, 80 ℃, 90 ℃, 100 ℃, 110 ℃, 120 ℃, 130 ℃, 140 ℃, and 150 ℃. Films with worm-like mesostructural ordering were tested up to 120 ℃, at which point all of the guest PR molecules had been denatured. All measurements were taken through the center of each film, aligned visually. The experimental uncertainties in these analyses are 5–10%, due in part to heterogeneity in the thickness of the sample and limitations of sample alignment.

Transient UV-visible absorption data was acquired using a SpectraPro-500 Triple Grating Monochromator (Acton Research Corporation). Mesostructured silica films that incorporate proteorhodopsin were placed into borosilicate capillaries and either measured as-synthesized or after hydration at pH 9 in PR buffer for 1 week. During measurements, samples

were illuminated using a white-light-emitting halogen lamp; the transient response of proteorhodopsin, as well as the monochromator, was triggered using a SpectraPhysics Quanta-Ray Nd:YAG GCR-150 series 532 nm laser (pulse length ~5 ns, pulse power ~10 mJ). The absorbance intensities at 400, 410, 500, 510, 540, 570, 590, 620, and 630 nm were recorded over timescales ranging from 1 µs to 0.45 s (Figure S3.4**)**. The absorption data at each wavelength were compiled together from 512 scans in which 500,000 absorbance datum were measured over a linear timescale. The absorbance data at each wavelength was averaged over 200 equally spaced bins on a logarithmic scale and truncated at short times to remove artifacts from the laser. Global fitting analyses were performed with a home-build MATLAB code first reported by Idso *et al*.[29] These analyses were performed with two to seven exponential terms and the sum of squared residuals decreased with each added term. However, global fit analyses performed with greater than three exponential terms for as-synthesized films in pH 4.1 environments, or greater than five exponential terms for films hydrated to pH 9, showed significantly diminished improvements as well as the introduction of time constant values that were either repeated or outside the time range of collected data. These artifacts of the analyses indicate that the data for monomeric proteorhodopsin in DDM+POPC+DOTAP-structure-directed films is best fit with five exponential time constants.

Nanoindentation measurements were performed to provide a rapid assessment of the indentation hardness and elastic modulus of mesostructured silica membranes, as a function of their concentration of PR and silica. The films were cast on the fluorinated surface of a Si wafer to diminish adhesion to the substrate and thereby prevent strains, as the mesostructured PR-silica-surfactant films formed. Small diameter films were used to minimize their surface curvatures, enabling accurate determination of the tip area function and consistency in

mechanical measurements between specimens. Nanoindentation measurements were performed using a Nanomechanics iMicro Nanoindenter equipped with a 1 N load cell and diamond Berkovich tip indenter, using load control at a constant strain rate of 0.2 s^{-1}, defined as $\frac{\dot{P}}{P}$. All data were collected using a continuous stiffness method, where dynamic periodic oscillations were superimposed on the loading profile at a frequency of 100 Hz and amplitude of 2.0 nm to enable the continuous measurement of properties as a function of the depth of the indent. In these experiments, indentations were performed to a maximum depth of 1 μm, and with a spacing of 20 μm between neighboring indents to avoid overlap of plastic zones. Each measurement of hardness and modulus reported herein reflects the average (and standard deviation) of between 10 and 20 indents, quantified at depths between 300 nm and 1000 nm to exclude the effects of surface roughness. Measurements of force, indent depth, and contact stiffness were converted to elastic modulus using the Oliver and Pharr method.[30] Nanoindentation measurements enable the direct determination of the reduced elastic modulus E_r of the film, which were used to calculate the elastic modulus, E, of the film, using $\frac{1}{E_r} = \frac{1-\nu^2}{E}$ and an estimated Poisson's ratio, υ, of 0.2.[31]

3.4 Results and Discussion

Syntheses of proteorhodopsin-containing silica-surfactant films

The co-assembly of functional membrane proteins into mesostructured silica films is a transient multicomponent process that requires judicious selection of synthesis compositions and conditions to achieve high degrees of mesostructural order and retention of proteorhodopsin function. Key design objectives are to incorporate high loadings of

functionally-active membrane proteins into robust abiotic host matrices that are processable into films with macroscopically uniform properties. Achieving these objectives simultaneously is challenging and requires trade-offs between countervailing synthesis considerations that often promote either protein stability or the formation of a mechanically stable host matrix, but not both. We hypothesized that membrane-protein-stabilizing and structure-directing amphiphilic surfactants could be used to incorporate high loadings of functionally-active guest proteins into mesostructurally well-ordered silica-surfactant host matrices that also impart strong mechanical properties onto the host film. Syntheses of these materials are governed by (*i*) the thermodynamics of co-assembly and interactions between the protein, surfactant, solvent, and silica species, and *(ii)* the kinetic processes associated with the rates of solvent evaporation, co-assembly of the component species, and polymerization of the silica into a robust cross-linked matrix. A slow rate of solvent evaporation is typically desirable to promote co-assembly of protein-silica-surfactant films with high extents of mesostructural order before the silica polymerizes into a rigid matrix. Key factors that influence these processes and thus the properties of the film, include pH, solvent, humidity, types and relative concentrations of surfactant species, silica precursors, and protein guest molecules. Screening across these conditions leads to an optimized combination of surfactants and hydrolyzed silica precursors in aqueous solution that enable the formation of robust, crack-free, and free-standing mesostructured films with high loadings of the functionally-active membrane protein proteorhodopsin.

Many syntheses of mesostructured silica-surfactant materials have relied on extremes of acidic or alkaline conditions, e.g., pH>10 or pH<2, to slow the rate of silica polymerization. For highly alkaline conditions greater than pH 10, strong electrostatic interactions between

cationic surfactant moieties and hydrolyzed silica anions promote their co-assembly into well-ordered hybrid materials.[32] By comparison, for highly acidic conditions below pH 2 (the isoelectric point of silica), hydrogen-bonding interactions between hydrophilic moieties of non-ionic surfactants with hydrolyzed silica cations similarly lead to well-ordered hybrid materials.[33] Such conditions, however, are incompatible with many proteins and result in their denaturation. In particular, native proteorhodopsin has evolved in marine environments to function at pH ~8.2, although it retains its general structure and behavior over a broad range of pH 4–10.[34,35] It can irreversibly denature at pH conditions outside of this range, due in part to ionization of protein sidechains or backbone moieties. These trade-offs are summarized in Figure 3.2a. Nevertheless, robust, well-ordered, and homogeneous films can be synthesized at pH 4.1, balancing the pH-dependent synthesis near the acidic limit of proteorhodopsin stability where comparatively slower silica polymerization rates can be achieved (Figure S3.5).[36]

Co-assembly of proteorhodopsin into mesostructured silica-surfactant host materials thus requires that the composition of the synthesis mixture be carefully balanced with respect to solvents, acidity, amphiphilicity and ionicity of the surfactants, and silica precursor species. With respect to hydrolyzed, network-forming silica precursors, organosiloxane species have been shown to increase the hydrophobicity of the mesochannel surfaces, and at moderate concentrations yield surfactant-templated silica materials with high extents of mesostructural order.[37,38] Here, tetraethoxysilane (TEOS) was combined with *n*-propyltriethoxysilane (PTEOS) in a 3:1 ratio by weight, with the hydrophobic propyl moieties promoting interactions with the hydrophobic moieties of the structure-directing surfactants. Organic cosolvents, including ethanol produced by the hydrolysis of TEOS and PTEOS silica precursors, aid hydrolysis by solubilizing water-insoluble alkoxide precursors,[39]

though tend to denature proteorhodopsin in the presence of moderate concentrations of organic cosolvents.[40] Aqueous solutions also present challenges, due to the highly hydrophobic transmembrane regions of membrane proteins, which require stabilizing surfactants to promote their solubility in solution.

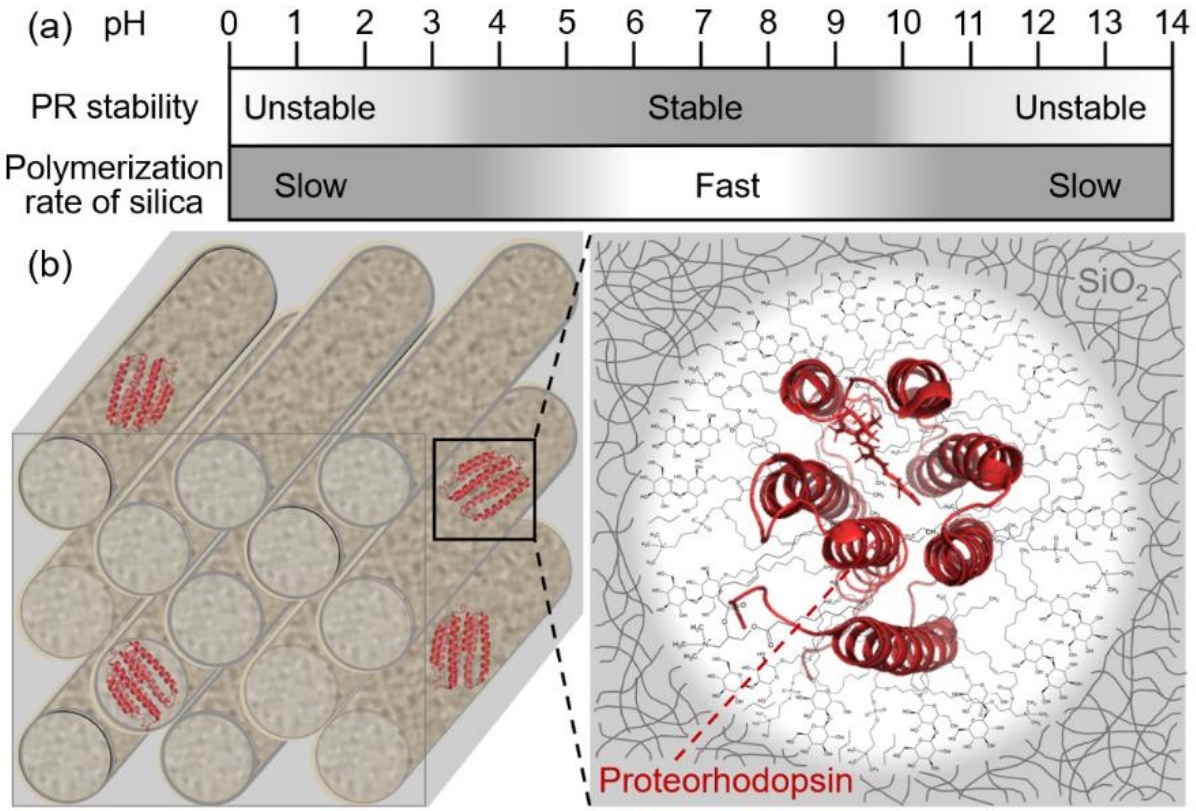

Figure 3.2. (a) Approximate pH ranges over which proteorhodopsin (PR) is stable in solution and corresponding relative ranges of silica polymerization rates.[34–36] **(b)** Schematic diagram of a rectangular array of mesostructured silica-surfactant channels containing proteorhodopsin guests (red) and an enlarged region of a single proteorhodopsin molecule in a silica-surfactant mesochannel.

The judicious selection of surfactants with specific hydrophobic, hydrophilic, or charged moieties is also important to the incorporation of proteorhodopsin in silica-surfactant

films. For example, the length of hydrophobic alkyl chains and the type and size of hydrophilic headgroups of surfactant species have been shown to increase both the stability of functionally-active membrane proteins in aqueous solutions and promote greater extents of mesostructural order in silica.[40] Charged surfactant headgroups are also used to promote mesostructural order by increasing interactions between the surfactant and inorganic species.[41] However, charged headgroups can also lead to protein denaturation, necessitating careful selection of structure-directing surfactants for synthesis of mesostructured silica-surfactant host materials with functionally-active proteorhodopsin. Conversely, neutral surfactants, both non-ionic and zwitterionic, are often used to stabilize membrane proteins in micellar solutions and rarely destabilize the protein. We hypothesized that favorable structure-directing features of the surfactants, such as relatively long alkyl chains and hydrophilic nonionic or charged headgroups, could be selected from amphiphilic surfactants known to stabilize membrane proteins and thereby used to incorporate high-loadings of proteorhodopsin into a robust silica-surfactant film, as depicted in Figure 3.2b. Optimized synthesis conditions promote the formation of well-ordered mesostructured silica-surfactant host materials with significantly greater loadings of proteorhodopsin and mechanical robustness than previously reported.[5]

Surfactant and protein influences on mesoscale order

A mixture of neutral and charged surfactants were identified to stabilize proteorhodopsin and direct its assembly into a silica-surfactant host materials with high extents of mesostructural order. Non-ionic alkyl-saccharide surfactants, specifically alkyl-glucosides and alkyl-maltosides, were identified as promising candidates because of their extensively studied protein-stabilizing properties in solution[40] and their separate propensity to direct the structures (without protein) of crack-free mesoporous films.[42] Alkyl-saccharide surfactants

with varied chain lengths enable the dimensions of the mesochannel diameters to be adjusted to a characteristic length that is conducive for the incorporation of monomeric proteorhodopsin (PR, ~4 nm in length x ~3 nm in diameter). The lipids 1-palmitoyl-2-oleoyl-glycero-3-phosphocholine (POPC) and 1,2-dioleoyl-3-trimethylammonium-propane (DOTAP) were selected as co-surfactants to have a combination of protein-stabilizing and structure-directing properties. Specifically, a 4:1 molar ratio of POPC and DOTAP form liposomes that stabilize PR and also favorably lower the apparent pKa of the key function-dependent D97 residue in proteorhodopsin,[43] enabling native-like photo-activation of PR at neutral pH. Individually, POPC is a zwitterionic lipid with a phosphocholine headgroup, which has been found to enrich monomeric fraction of proteorhodopsin by disrupting protein-protein interactions. By comparison, DOTAP is a cationic surfactant that contributes to the lower pKa_{D97} and favorably promotes interactions with the anionic silica precursors. In addition, POPC and DOTAP each have two relatively long hydrophobic carbon chains that can be expected to promote high extents of mesostructural ordering.

The ratio of the protein-stabilizing and structure-directing surfactant species to silica was selected to produce mesostructural order, either hexagonal or rectangular, based on the binary phase diagrams of these or similar surfactants in water. Furthermore, as water evaporates during synthesis, mesostructural order develops, according to precepts that have previously been reported.[44,45] The binary phase diagram of protein-stabilizing *n*-octyl-*β*-*D*-glucoside (OG) reveals a small synthesis space for the formation of a cylindrical hexagonal mesophase below 22℃ for 60–70 wt% OG, and preferentially forming cubic or lamellar mesophases at higher temperatures or higher concentrations of surfactant.[46] In contrast, the binary phase diagram of *n*-dodecyl-*β*-*D*-maltoside (DDM) in water reveals that hexagonal or

rectangular mesophases are favored at 20℃ over the range 45–80 wt% DDM, above which a multi-phase mixture, including crystallized surfactant, results.[47] Thus, the larger disaccharide headgroup of DDM is expected to be preferred over glucoside surfactants for forming mesostructured PR-containing silica-surfactant materials. The composition of non-protein molecules in PR-containing mesostructured silica-surfactant films was selected to be 70 wt% surfactant and 30 wt% silica, in the center of the hexagonal/rectangular synthesis-space of the DDM-water binary phase diagram. The ratios of surfactants were further refined to balance the structure-directing and protein-stabilizing properties of DDM, POPC, and DOTAP, in particular to overcome the poor solubility of the lipids in aqueous solutions. The optimized composition of non-protein components in the mesostructured PR-silica-surfactant films investigated here was determined to be 62.5 wt% DDM, 7.5 wt% POPC/DOTAP (80/20, mol/mol), and 22.5 wt% SiO_2, and 7.5 wt% *n*-propyl-$SiO_{1.5}$. This balances the chain lengths, charges, and solubilities of surfactants with the anionic silica precursors in aqueous solution at pH 4.1 to produce well-ordered mesostructured PR-host film.

The structure-directing properties of different alkyl-chain-length maltoside surfactants were optimized experimentally. Small-angle X-ray scattering (SAXS) was used to probe the mesostructural ordering of 5 wt% PR-containing silica-surfactant films synthesized under identical conditions, except for the use of maltoside surfactants with different hydrophobic alkyl chain lengths: *n*-decyl-*β,D*-maltoside (C_{10}-maltoside, DM), *n*-dodecyl-*β,D*-maltoside maltoside (C_{12}-maltoside, DDM), and *n*-hexadecyl-*β,D*-maltoside (C_{16}-maltoside, HDM) (Figure 3.3). For example, 5 wt% PR-containing silica-surfactant films synthesized with 5.8 wt% POPC, 1.3 wt% DOTAP, 21.4 wt% SiO_2, 7.1 wt% *n*-propyl-$SiO_{1.5}$, 9.5 wt% DDM, and 49.9 wt% of the structure-directing C_{10}-maltoside DM yield a single broad SAXS reflection at

1.57 nm^{-1} (Figure 3.3a), corresponding to a *d*-spacing of 4.0 nm that is characteristic of worm-like mesostructural ordering. By comparison, the SAXS pattern in Figure 3.3b acquired for a film containing 5 wt% PR synthesized under identical conditions except with the C_{12}-maltoside DDM shows two intense, narrow, and well-resolved reflections at 1.18 nm^{-1} and 1.542 nm^{-1}, as well as weak higher-order reflections at 2.23 nm^{-1} and 2.31 nm^{-1}. These are indexable as the (*20*), (*11*), (*31*), and (*40*) reflections of a rectangular mesophase with *d*-spacings of 5.3 nm, 4.07 nm, 2.8 nm, and 2.7 nm respectively, which manifest a high extent of mesostructural ordering that is corroborated by electron microscopy images in Figure S3.6 of the Supporting Information. For a 5 wt% PR-silica-surfactant film synthesized with a longer C_{16}-maltoside HDM surfactant, the SAXS pattern in Figure 3.3c exhibits a similar (*11*) reflection at 1.518 nm^{-1}, corresponding to a *d*-spacing of 4.14 nm, and a partially resolved (*20*) reflection at 1.43 nm^{-1} (4.4 nm *d*-spacing). These are also consistent with rectangular mesostructural order and a modestly larger center-to-center distance separating the larger cylindrical C_{16}-maltoside surfactant aggregates. The differences in the lengths of the alkyl chains of the C_{10}-, C_{12}-, and C_{16}-maltoside surfactants thus lead to significant differences in mesostructural order of the PR-silica-surfactant films, manifesting the importance of hydrophobic chain length on the co-assembly and structures of these materials. As the C_{12}-maltoside surfactant DDM led to highest extent of rectangular mesostructural order, it was used to synthesize all of the PR-containing silica-surfactant films investigated here, unless otherwise specified.

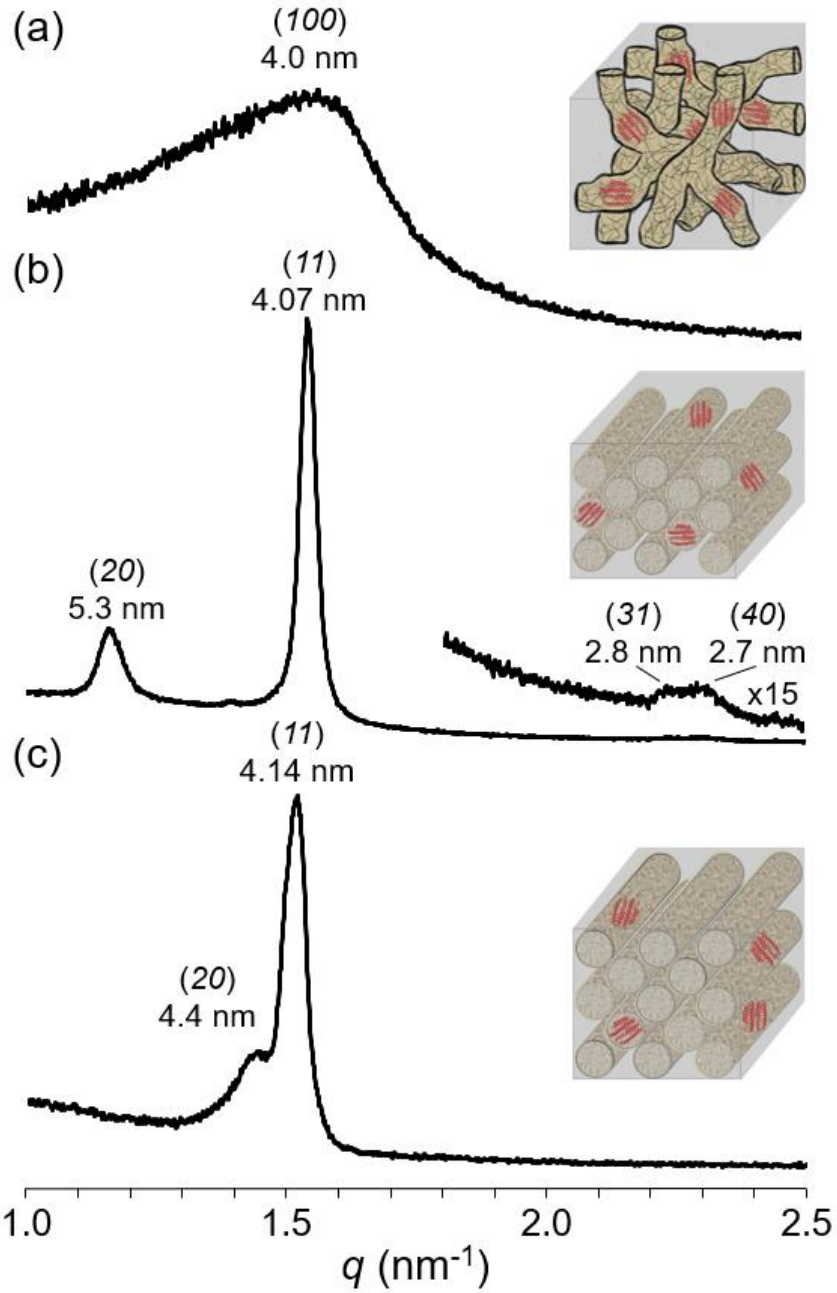

Figure 3.3. Small-angle X-ray scattering (SAXS) patterns for 200-μm-thick mesostructured PR-surfactant-silica films synthesized using structure-directing maltoside surfactants with different alkyl chain lengths and overall compositions of 5.0 wt% PR, 5.8 wt% POPC, 1.3 wt% DOTAP, 21.4 wt% SiO_2, 7.1 wt% *n*-propyl-$SiO_{1.5}$, 9.5 wt% DDM from the expression and purification of PR, and 49.9 wt% additional structure-directing maltoside: **(a)** decylmaltoside (C_{10}-alkyl chain), **(b)** dodecylmaltoside (C_{12}-alkyl chain), and **(c)** hexadecylmaltoside (C_{16}-alkyl chain) surfactant. Each SAXS pattern is accompanied by a schematic diagram showing PR monomers (red) dispersed within mesostructured surfactant channels in silica (grey).

The incorporation of proteorhodopsin guest molecules into the hydrophobic mesochannels of PR-silica-surfactant films serves to swell their local dimensions, with the overall effect on mesostructural order depending on protein loading. For example, Figure 3.4 shows SAXS patterns acquired for mesostructured silica-surfactant films containing 0 wt%, 5 wt%, 15 wt%, 25 wt%, and 44 wt% proteorhodopsin, which were synthesized with the same 62.5 DDM (C_{12}-maltoside) : 6.2 POPC : 1.3 DOTAP : 22.5 SiO_2 : 7.5 *n*-propyl-$SiO_{1.5}$ mass ratios by weight of non-biological components under otherwise identical conditions. Each film exhibited a high degree of transparency and macroscopically uniform distributions of PR across the 1 cm diameter films. Nevertheless, significant differences are observed in the SAXS patterns of the respective films. For example, for mesostructured silica-surfactant films without PR, Figure 3.4a shows three resolved reflections at 1.30 nm^{-1}, 1.44 nm^{-1}, and 1.60 nm^{-1} (full-width-half-maximum, fwhm, values of 0.035 nm^{-1}, 0.049 nm^{-1}, and 0.032 nm^{-1}, respectively), with *d*-spacings of 4.8 nm, 4.4 nm, and 3.9 nm, that are indexed to the (*200*), (*210*), and (*211*) planes of a *Pm*3*n* cubic mesophase. Interestingly, the inclusion of 5 wt% PR results in a silica-surfactant material with a well-ordered rectangular mesophase structure, as evidenced by narrow (*20*) and (*11*) reflections at 1.18 nm^{-1} and 1.542 nm^{-1} (0.049 nm^{-1} and 0.036 nm^{-1} fwhm, respectively) and also higher-order (*31*) and (*40*) Bragg reflections at 2.23 nm^{-1} and 2.31 nm^{-1}, corresponding to *d*-spacings of 5.3 nm, 4.07 nm, 2.8 nm, and 2.7 nm, respectively (Figures 3.3b, 3.4b). The displacements of the (*20*) and (*11*) reflections to higher *d*-spacings are consistent with PR swelling the hydrophobic regions of the mesostructured silica-surfactant films. The effect of increased protein loading is observed in the SAXS pattern of a 15 wt% PR-silica-surfactant film shown in Figure 3.4c, for which a single narrow reflection is observed at 1.536 nm^{-1} (0.052 nm^{-1} fwhm), corresponding to a *d*-spacing of 4.09 nm, similar to but slightly

broader than the (*11*) reflection of the 5 wt% PR-containing film. This reflection is also observed at 1.518 nm^{-1} (4.14 nm *d*-spacing, Figure 3.4d) for a film with 25 wt% PR, which additionally yields another broader overlapping reflection centered at 1.33 nm^{-1} (4.7 nm *d*-spacing). The relatively narrow (*11*) displaced reflections observed for 15 wt% and 25 wt% PR-containing silica-surfactant films suggest moderate degrees of rectangular mesostructural ordering at these high protein loadings, although the absence of resolvable higher-order Bragg reflections prevents indexing to a specific phase. The broad reflection observed at 1.33 nm^{-1} is consistent with increased swelling of the silica-surfactant mesochannels and the presence of worm-like mesostructural order. PR-containing silica-surfactant films have been synthesized with up to 44 wt% functionally-active PR, yielding a single broad SAXS reflection at 1.39 nm^{-1} (Figure 3.4e), corresponding to a *d*-spacing of 4.5 nm, with the absence of higher order Bragg reflections indicative of worm-like mesostructural order. The worm-like mesostructural order exhibited by this film is due in part to the relatively low concentration of structure-directing surfactants (39.2 wt% DDM+POPC+DOTAP), below the 1:1 mass ratio of DDM:PR required for the hydrophobic membrane protein PR to remain soluble during synthesis.[48]

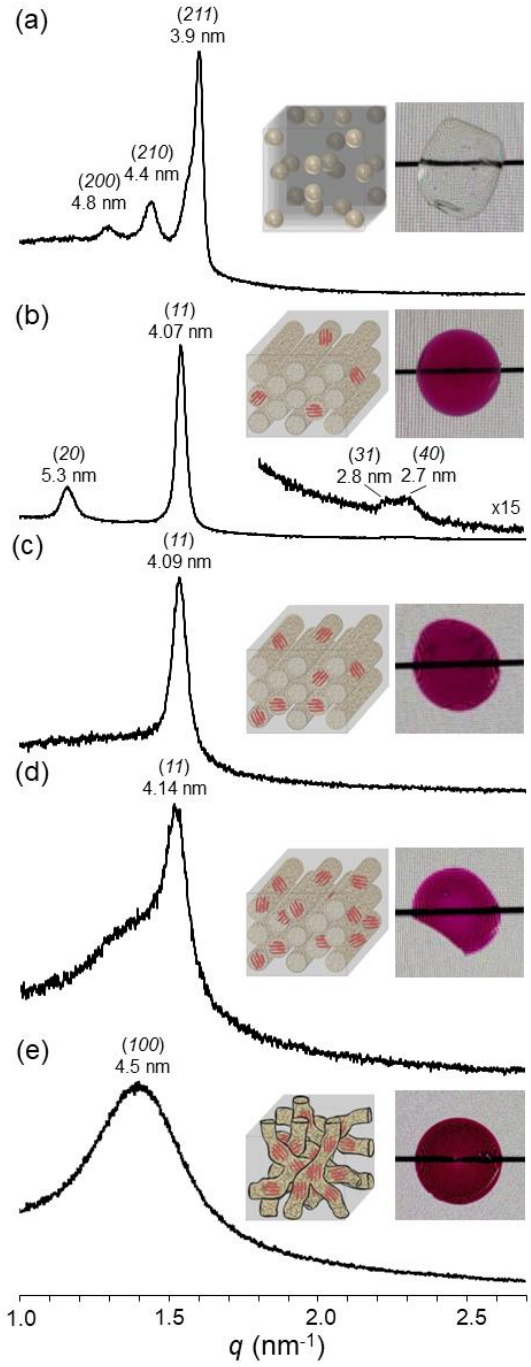

Figure 3.4. Small-angle X-ray scattering (SAXS) reflections of 200-µm-thick mesostructured proteorhodopsin (PR)-surfactant-silica films containing different protein loadings: **(a)** 0 wt% PR, 62.5 wt% DDM, 6.2 wt% POPC, 1.3 wt% DOTAP, 22.5 wt% SiO_2, 7.5 wt% *n*-propyl $SiO_{1.5}$, **(b)** 5 wt% PR, 59.4 wt% DDM, 5.8 wt% POPC, 1.3 wt% DOTAP, 21.4 wt% SiO_2, 7.1 wt% *n*-propyl $SiO_{1.5}$, **(c)** 15 wt% PR, 53.1 wt% DDM, 5.3 wt% POPC, 1.1 wt% DOTAP, 19.1 wt% SiO_2, 6.4 wt% *n*-propyl $SiO_{1.5}$, **(d)** 25 wt% PR, 46.9 wt% DDM, 4.6 wt% POPC, 1.0 wt% DOTAP, 16.9 wt% SiO_2, 5.6 wt% *n*-propyl $SiO_{1.5}$, and **(e)** 44 wt% PR, 35.0 wt% DDM, 3.4 wt% POPC, 0.8 wt% DOTAP, 12.6 wt% SiO_2, 4.2 wt% *n*-propyl $SiO_{1.5}$. Each SAXS pattern is accompanied by an optical image of the film and a schematic diagram showing PR monomers (red) dispersed within the mesostructured surfactant channels in silica (grey).

The maximum loading of proteorhodopsin into these films is limited by its solubility in water, which may be increased by increasing the relative concentration of lipid surfactants (POPC and DOTAP). Careful tuning of composition and synthesis conditions for PR-containing silica-surfactant films with 62.5 DDM : 6.2 POPC : 1.3 DOTAP : 22.5 SiO_2 : 7.5 *n*-propyl-$SiO_{1.5}$ by weight has enabled high PR loadings to be obtained, although with reduced extents of mesostructural order at higher PR contents. Further improvements in mesostructural ordering of the films with high protein loadings may require higher concentrations of structure-directing surfactants at the expense of lower silica contents or careful manipulation of external influences, such as material-substrate interactions or directed nucleation sites.

Local compositions and interactions at mesochannel surfaces

At the atomic scale, complicated interactions between organosiloxanes, silica precursors, surfactants, and proteins govern the assembly of mesostructured silica-surfactant-protein composites. In particular, the interactions of the surfactant species at the mesostructured silica walls are expected to provide insights on the local compositional features that are key to balancing the combined protein-stability and structure-directing functions of the different surfactants. Conventional one-dimensional (1D) solid-state ^{1}H, ^{13}C, and ^{29}Si NMR analyses are sensitive to differences in local bonding environments, which can lead to differences in the isotropic chemical shifts of these NMR-active nuclei that enable different types of chemical species in a material to be identified. To establish the relative proximities or interactions of different moieties with each other, two-dimensional (2D) heteronuclear correlation (HETCOR) NMR techniques are used to correlate the isotropic chemical shifts of nearby (<1 nm) dipole-dipole-coupled nuclei. Such 2D HETCOR analyses provide detailed

atomic-scale insights on the interactions of the co-assembled surfactant and silica species, including at the mesochannel surfaces. For example, a 2D $^{29}Si\{^{1}H\}$ HETCOR NMR spectrum in Figure 3.5a of the same 5 wt% PR-containing film as previously discussed (Figures 3.3b, 3.4b), reveals correlated ^{29}Si and ^{1}H signal intensity that can be assigned to specific moieties that are within nanoscale proximities of one another. Five distinct ^{29}Si NMR signals are observed and can be assigned to ^{29}Si moieties in different bonding environments. Fully crosslinked four-coordinate ^{29}Si Q^4 silica species are assigned to the signal at -110 ppm, and partially-crosslinked Q^3 silica species with a silanol group are assigned to the ^{29}Si NMR signal at -101 ppm.[49] Organosiloxane T^1, T^2, and T^3 ^{29}Si moieties are associated with ^{29}Si NMR signals at -46, -56, and -65 ppm, respectively, where $T^{3\text{-}n}$ represents a tetrahedrally-coordinated ^{29}Si atom with one Si-C covalent bond, $3–n$ Si-O-Si linkages, and n silanol groups.[49] These ^{29}Si organosiloxane moieties originate from the hydrolysis of *n*-propyltriethoxysilane (PTEOS) silica precursor molecules and contribute to increased mesostructural order of the films.

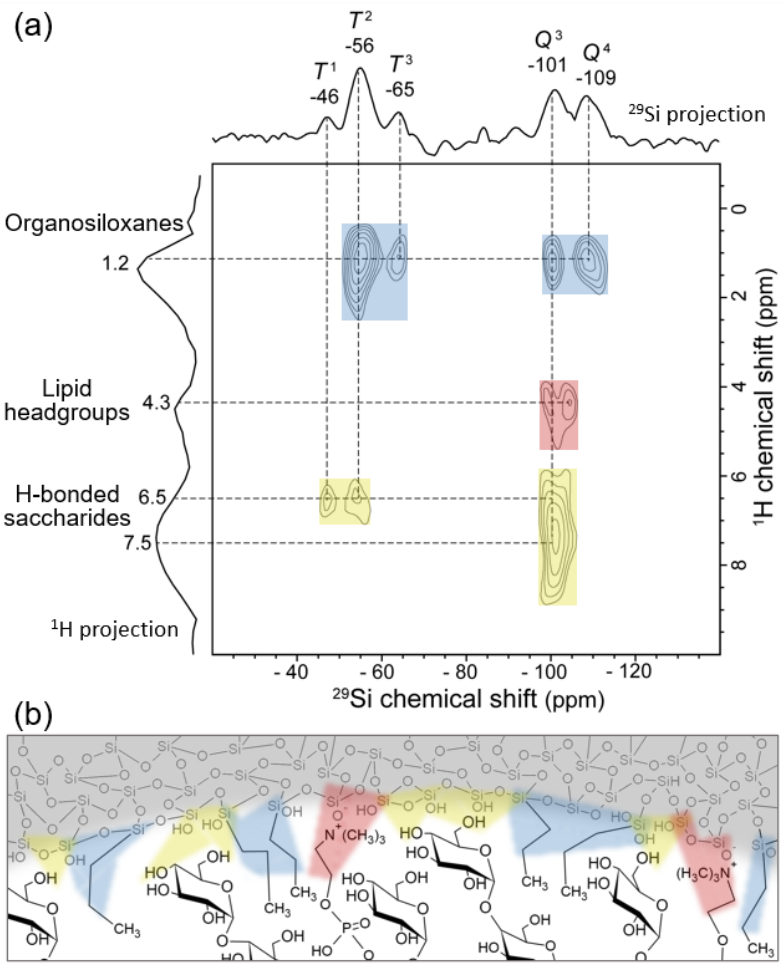

Figure 3.5. (a) Solid-state 2D ^{29}Si{^{1}H} HETCOR NMR spectrum for the same mesostructured 5 wt% PR, 59.4 wt% DDM, 5.8 wt% POPC, 1.3 wt% DOTAP, 21.4 wt% SiO_2, and 7.1 wt% *n*-propyl $SiO_{1.5}$ film for which the SAXS patterns in Figures 3.3b and 3.4b were obtained. The spectrum was acquired at 298 K, 11.7 T and 12.5 kHz MAS with a short 1.0 ms cross-polarization contact time used to excite strong ^{29}Si-^{1}H dipole couplings between ^{29}Si and ^{1}H moieties in sub-nanoscale proximity. 1D projections of correlated ^{29}Si and ^{1}H intensities are shown on the horizontal and vertical axes, respectively. **(b)** Schematic diagram of molecular moieties at the mesochannel walls, which are consistent with the 2D NMR results. Proximate silica-organosiloxane (blue) and silica-surfactant (red) interactions are highlighted.

Five distinct regions of correlated ^{29}Si and ^{1}H intensity are observed in the 2D ^{29}Si{^{1}H} HETCOR NMR spectrum of Figure 3.5a, which reveal distinct types of dipole-dipole-coupled

silica moieties that are in nanoscale proximities to various organosiloxane, adsorbed water, and surfactant ^{1}H species. Specifically, the ^{1}H NMR signal at 1.2 ppm from alkyl moieties on the organosiloxanes and surfactants is correlated with ^{29}Si NMR intensity at -56, -65, -101, and -109 ppm associated with T^2, T^3, Q^3, and Q^4 silica species, respectively, as highlighted in blue. The majority of correlated signal intensity between ^{1}H at 1.2 ppm and the ^{29}Si T^n moieties is due to their strong dipolar interactions with the covalently bonded organosiloxane propyl groups (Figure 3.5b). The ^{1}H signal at 4.3 ppm is attributed to the cationic lipid headgroups of the DOTAP and POPC, which is consistent with solution-state 2D ^{13}C-^{1}H NMR correlation spectra of these lipids (Figures S3.1, S3.2) and literature reports,[50] and which exhibits correlated intensity with the ^{29}Si signal centered at -101 ppm (red) from hydrophilic Q^3 silica moieties. Importantly, the ^{1}H signals in the region of 6.5–7.5 ppm manifest hydrogen-bonded moieties associated with the DDM surfactant species, which are strongly correlated with the ^{29}Si signal centered at -101 ppm (yellow) from partially cross-linked Q^3 moieties and more weakly correlated with ^{29}Si signals at -46 and -56 ppm (yellow) from partially cross-linked T^1 and T^2 moieties, all of which have pendant silanol groups. These results provide evidence for the nanoscale proximity of the DDM species near the mesochannel walls and their role in directing the co-assembly of the mesostructured silica-surfactant matrix. There are no correlated signals that would suggest strong direct interactions between the proteorhodopsin guests and the silica matrix, which is consistent with the conformational freedom of the protein discussed below. The 2D ^{29}Si{^{1}H} HETCOR NMR analyses thus establish strong interactions between the silica mesochannel surfaces and both the saccharide headgroups of the DDM surfactant species and the cationic headgroups of the DOTAP or POPC lipid species. The

results corroborate the schematic diagrams in Figure 3.2b, which depict proteorhodopsin in the mesochannel centers of the PR-containing silica-surfactant films.

Effects of non-native host environments on proteorhodopsin photocycle kinetics

Under native conditions, photoactivation of proteorhodopsin induces a series of cyclical conformational changes that transport H^+ cations along its associated ion channel and across the cell membranes of marine bacteria. This photocycle is dependent, in particular, on the D97 residue of proteorhodopsin (Figure 3.1a), which is a key H^+ acceptor that if already protonated, discourages net H^+ transport.[51] The protonation state of the D97 residue and its pKa (the pH value at which half of these residues are protonated) are therefore integral to the function of proteorhodopsin. Importantly, the pKa of the D97 residue of proteorhodopsin is significantly influenced by its local environment. For example, in similar DDM micellar solutions, the pKa_{D97} is 6.5 for wild-type oligomeric proteorhodopsin and 7.2 for the monomer-enriched E50Q mutant of proteorhodopsin.[25,52] Similarly, the co-assembled surfactants and silica species in the mesostructured films influence the local chemical environments of the PR guest molecules, including the D97 residue and, importantly, the light-responsive retinal group. The latter can be probed by using UV-visible spectroscopy to measure the pH-dependent optical absorbance transition of the retinal group. Doing so, reveals a pKa_{D97} of 6.2 for monomeric PR in the DDM+POPC+DOTAP-directed silica films, a value that is higher than previously reported (pKa_{D97} 5.6) for PR in POPC+DOTAP liposomes without DDM,[43] and significantly lower than the pKa_{D97} of 8.2 observed for PR in DDM+DHPC-directed silica films. The 2-unit lower pKa_{D97} value for PR in DDM+POPC+DOTAP-directed silica films results in a significantly larger percentage (86%) of H^+-transporting PR monomers with a deprotonated D97 residue, compared to DDM+DHPC-silica films for which only 6% of the

D97 residues are deprotonated at pH 7. These large differences in pKa_{D97} appear to arise from differences in ion distributions near function-dependent residues along the PR ion channel, which are sensitively influenced by the compositions and architectures of the cationic and zwitterionic lipid components in mesostructured PR-silica-surfactant films with otherwise identical compositions.

That the proteorhodopsin-stabilizing lipid components so strongly affect protonation of the interior D97 residue suggests extensive non-local conformational changes of the PR guests that are expected to influence their light-activated photocycle kinetics as well. Such effects can be probed by time-resolved UV-visible light spectroscopy, which measures the relative absorbance of light by PR molecules as they undergo photo-activated conformational changes during their photocycle. The retinal chromophore of PR (which absorbs green light, giving the protein its distinct purple-pink color) is sensitive to changes in its local environment, which are manifested by differences in the wavelength of light that the retinal absorbs. As a consequence, the relative absorbance of light by the retinal is a function of both the wavelength of the incident light and the illumination time, as the photocycle proceeds. Time-resolved UV-visible absorbance spectra of PR in different chemical environments can therefore be compared to elucidate the effects that different hosts or conditions have on the photocycle kinetics of PR. In particular, it is possible to monitor the photocycle of monomeric PR with time steps that are sufficiently short so that both the accumulation and depletion of photo-intermediates are observed. This is demonstrated in the time-resolved UV-visible light spectra in Figure 3.6 for 5 wt% PR-containing DDM+POPC+DOTAP-directed silica films at different pH conditions at wavelengths of 410 nm, 500 nm, 570 nm, and 630 nm. For an as-synthesized 5 wt% PR-silica-surfactant film at pH 4.1 (chosen to balance mesophase co-assembly and PR stability

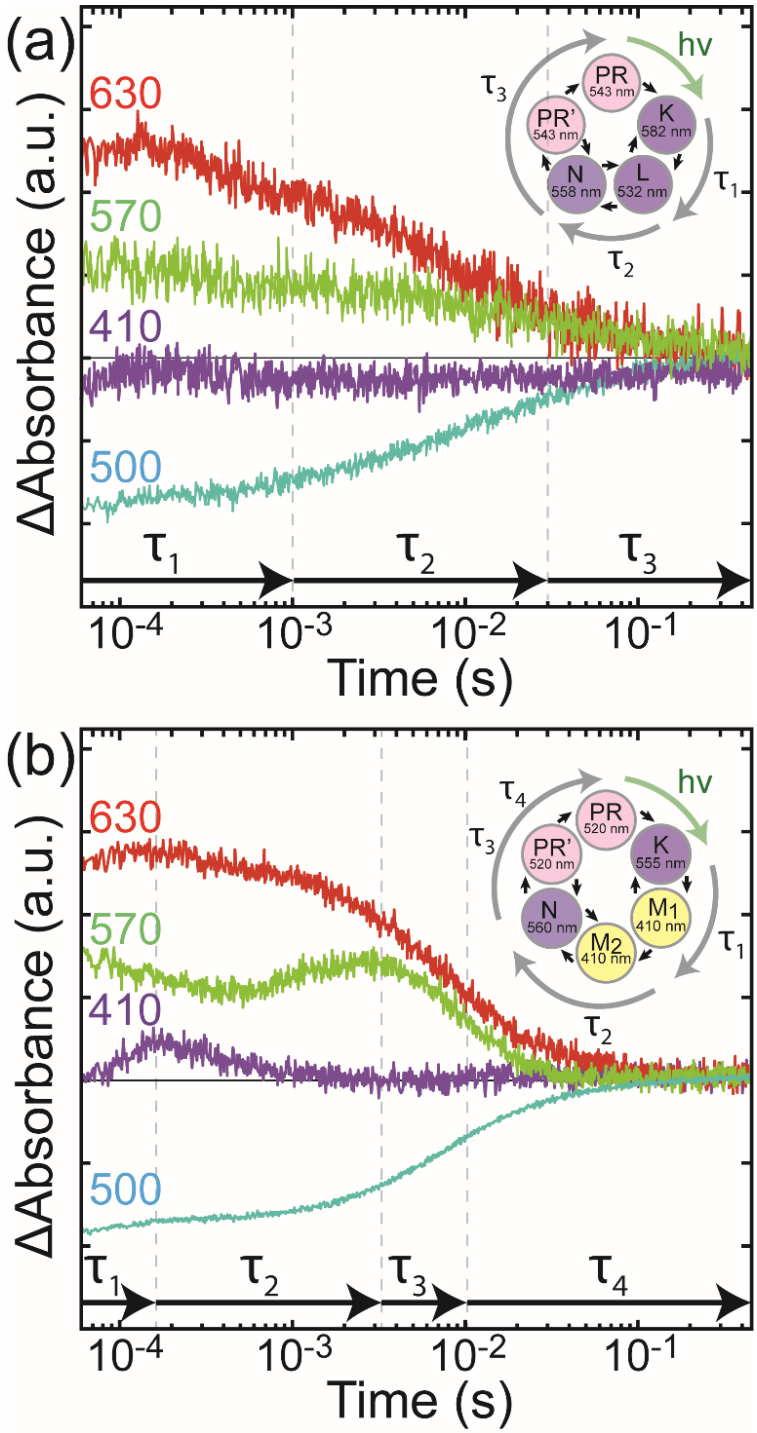

Figure 3.6. Time-resolved UV-visible light spectra showing transient absorbance traces at wavelengths of 410 nm, 500 nm, 570 nm, and 630 nm for monomeric proteorhodopsin (PR) in PR-containing silica-surfactant films under varying pH conditions: **(a)** as-synthesized at pH 4.1 and **(b)** hydrated for 1 week at pH 9. Schematic diagrams are provided for the (a) acidic and (b) alkaline photocycles of proteorhodopsin.

considerations during synthesis, as discussed above), the low pH conditions result in less than 1% of the D97 residues of monomeric PR guests being deprotonated. Under these conditions a distinct photocycle with three spectrally resolved intermediates (*K*, *L*, and *N*) and one spectrally silent intermediate (*PR'*) are observed, as shown in the Figure 3.6a.[51]

The UV-visible light spectra of PR in as-synthesized DDM+POPC+DOTAP-directed silica-surfactant films (Figure 3.6a) show no absorbance changes at 410 nm throughout the PR photocycle, which is characteristic of proteorhodopsin with a dominating fraction of protonated (i.e., inactive) D97.[51] At early times following green laser excitation, mesostructured silica-surfactant films with PR show a positive difference absorbance intensity at 570 nm and 630 nm, and a negative intensity at 500 nm. The intensities at each of these wavelengths decay monotonically towards zero at long times, similar to spectra observed for PR in DDM micellar solutions and in *E. coli* lipids under aqueous acidic conditions, which also show positive difference intensities at 570 nm and 630 nm and negative intensities for 500 nm immediately after light-excitation.[51] To evaluate these differences quantitatively, the spectra were fit by approximating the absorbance intensities at each wavelength as a sum of mono-exponential decays with wavelength-specific pre-exponential factors and mutual (wavelength-non-specific) time constants. These time constants are shared across the set of linear equations and represent the characteristic time scales for the serial light-activated interconversions of PR between two or more down-cycle photo-intermediates. For the spectra in Figure 3.6a, three exponentials corresponding to time constants τ_1=1 ms, τ_2=19 ms, and τ_3=165 ms were used to produce accurate fits. By comparison with other photocycle analyses of PR in *E. coli* lipids,[51] these characteristic times (the reciprocals of which represent apparent rate coefficients) are associated with the rates of interconversion between specific PR photo-

intermediates: τ_1 to the conformational change that occurs as the *K* conformer isomerizes into the *L* intermediate, τ_2 to conversion of the *L* conformer into the *N* intermediate, and τ_3 to the rate-limiting conversions of the *N* conformer into the *PR'* intermediate and the subsequent isomerization of *PR'* back to the original *PR* conformation, whereupon the cycle can repeat. Or the proteorhodopsin-containing mesostructured silica-surfactant films investigated here, acidic conditions are not suitable for selective H^+ transport.

By comparison, moderately alkaline pH conditions lead to substantial deprotonation of the key D97 residue of proteorhodopsin in DDM+POPC+DOTAP-directed silica films, which is required for H^+ transport. Previously, photo-activation of proteorhodopsin at pH 9.5 in membrane-fragments encased in polyacrylamide was shown to produce a spectrally distinct photocycle that transported a H^+ cation through the PR ion channel.[53] To observe this photocycle in 5 wt% PR-containing DDM+POPC+DOTAP-directed silica materials, the films were hydrated for one week in pH 9 buffer containing 50 mM K_2HPO_4 and 150 mM HCl. Importantly, due to the low pKa_{D97} value of 6.2 of this material, these conditions result in deprotonated D97 residues in 99.8% of PR monomers in the film. The effect of alkaline hydration on this film can be observed macroscopically as a displacement of the maximum absorbance of the retinal of PR to shorter wavelengths, causing the film to change from pink to red. The photocycle of proteorhodopsin under these pH conditions has been previously reported and involves conformational changes into six photocycle intermediates (*PR*, *K*, M_1, M_2, *N*, and *PR'*, as shown in the inset of Figure 3.6b).[54]

In fact, the complicated photocycle kinetics of PR-containing silica-surfactant films at pH 9 resemble the light absorbance properties of native-like PR. Specifically, the accumulation and decay of the 410 nm trace, which is not observed for as-synthesized acidic PR-silica-

surfactant films (Figure 3.6a), is attributable solely to the populations of the *M* intermediates and indicates that proteorhodopsin undergoes a native-like photocycle.[51] Interestingly, this 410 nm trace rises to a maximum at ~500 μs, significantly slower than monomeric PR in DDM micellar solutions, which peak at ~60 μs for a similar alkaline pH value,[29] and is instead more similar to the absorbance spectra observed for wild-type proteorhodopsin in POPC bicelles.[55] This is notable because the 5 wt% PR-silica-surfactant films analyzed in Figure 3.6 contain 59.4 wt% DDM and only 7.1 wt% POPC+DOTAP, suggesting that interactions between the protein, POPC, and DOTAP significantly impact the PR photocycle. While the accumulation and depletion of the *M* intermediate of PR, which maximally absorbs at 410 nm, can be observed on its own, the absorbance spectra of the *PR*, *K*, *N*, and *PR'* photo-intermediates overlap, absorbing maximally at approximately 520 nm, 555 nm, 560 nm, and 520 nm, respectively.[54] The absorbance-difference data at 570 nm show initially positive intensity, which is attributable to accumulation of the *K* intermediate conformer, and decays until ~300 μs, at which point a second increase in intensity is observed, corresponding to an increase in the *N* intermediate. These results correlate well with the accumulation and decay of the *M* intermediates, characterized by the 410 nm spectral data, which are between the *K* and *N* intermediates in the PR photocycle. Although not directly attributable to the populations of specific photocycle intermediates, the absorbance-difference data at 500 nm and 630 nm show distinct decreases in intensity at ~3 ms, which are similar to the behavior of monomeric proteorhodopsin in DDM micelles at similar wavelengths.[29] Importantly, the similar UV-visible light spectral behavior of proteorhodopsin in alkaline-hydrated mesostructured silica-surfactant films, compared to PR in native-like micellar solutions and lipid bicelles,

demonstrates that functionally-active PR guest species can be obtained by rehydrating the films from pH 4.1 to alkaline conditions, such as pH 9.

Based on global fit analyses of transient UV-visible spectroscopy results in Figure 3.6b, four exponentials accurately described the photocycle kinetics of PR in DDM+POPC+DOTAP-directed silica materials under alkaline conditions at pH 9. Specifically, the absorbance-difference spectra lead to distinct time constants of τ_1=95 μs, τ_2=2 ms, τ_3=8 ms, and τ_4=60 ms. Following the analyses of Idso *et al*. for monomeric PR in DDM micellar solutions,[29] τ_1 is attributed to the conversion of the *K* conformer into the M_1 intermediate, τ_2 is associated with sequential conversions between the M_1, M_2, and *N* intermediates, and τ_3 and τ_4 correspond to serial conversions between the *N*, *PR*', and *PR* intermediates. Notably, the longest time constant (τ_4=60 ms) observed for monomeric PR in DDM+POPC+DOTAP-directed silica-surfactant films is significantly shorter than the corresponding time constant of 82 ms for PR in DDM micelles, as reported by Idso *et al*.[29] Comparison of these analyses suggests that the time constants τ_3 and τ_4 correspond to the rate-limiting steps *N* to *PR'* and *PR'* to *PR* associated with H^+ transport of PR in the mesostructured silica-surfactant host film, which are dependent on and can be mediated by interactions between PR molecules and the structure-directing and stabilizing DDM surfactant species and POPC and DOTAP lipids.

Mechanical and thermal-stability properties of proteorhodopsin-containing silica films

The composition-structure relationships of protein-host materials influence their mechanical properties. Specifically, the elastic moduli and hardnesses of mesostructured PR-

containing silica-surfactant films are dependent on the extents of mesostructural ordering and PR loading of the films. This is evident in Figure 3.7, which shows nanoindentation analyses

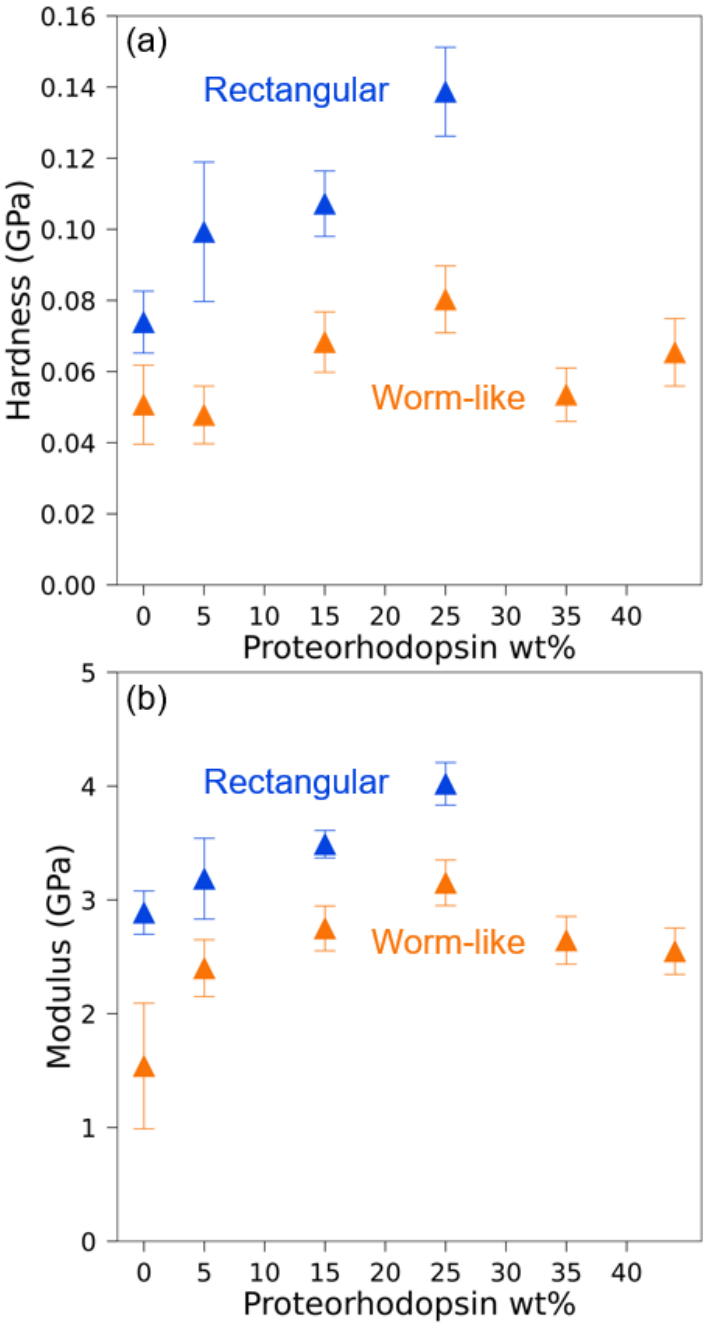

Figure 3.7. Nanoindentation analyses of the **(a)** hardness and **(b)** elastic moduli of mesostructured silica- DDM+POPC+DOTAP films with different monomeric proteorhodopsin loadings: 0 wt%, 5 wt%, 15 wt%, 25 wt%, 35 wt%, and 44 wt% PR with rectangular (blue) or worm-like (orange) mesostructural order.

of PR-containing mesostructured silica-surfactant films as a function of proteorhodopsin content over the range 0–25 wt% PR. Previously, relatively poor mechanical properties (0.005 GPa mean hardness, 0.260 GPa mean modulus) were reported for a 5 wt% PR-containing silica-surfactant film with worm-like mesostructural order that was synthesized using DDM, 1,2-diheptanoyl-*sn*-glycero-3-phosphocholine (DHPC), and sodium perfluorooctanoate.[5]

Here, for comparison, 5 wt% PR-containing DDM+POPC+DOTAP-directed mesostructured silica-surfactant films with worm-like or rectangular mesostructural ordering were synthesized and their mechanical properties compared. The worm-like material exhibited a hardness of 0.05 ± 0.01 GPa (Figure 3.7a) and modulus of 2.40 ± 0.26 GPa (Figure 3.7b), while the rectangular mesostructured PR-silica-surfactant material was measured to have a hardness of 0.10 ± 0.02 GPa (Figure 3.7a) and a modulus of 3.19 ± 0.35 GPa (Figure 3.7b), values of which are at least an order of magnitude greater than previous PR-containing films. For PR-containing DDM+POPC+DOTAP-directed mesostructured silica-surfactant films over the range 0–25 wt% PR loading, rectangular mesostructural ordering exhibits on average a 0.04 GPa higher hardness and 0.94 GPa higher modulus, compared to similar films with worm-like mesostructural ordering. The increased hardnesses and moduli of PR-containing silica-surfactant films with rectangular, compared to worm-like, mesostructural ordering is attributed in part to the periodic organization and thickness of silica walls between the mesochannels over which stresses are relatively evenly distributed.[56]

PR loading is also observed to have a significant effect on the mechanical properties of the films. PR-containing silica-surfactant films with worm-like mesostructural ordering exhibit hardnesses of 0.05 ± 0.01 GPa without PR and up to 0.08 ± 0.01 GPa for a 25 wt% PR film

(Figure 3.7a), while compositionally similar films with rectangular mesostructural ordering (the same films as in Figures 3.4a-d) exhibit hardnesses of 0.07 ± 0.01 GPa without PR and up to 0.14 ± 0.01 GPa for a 25 wt% PR-containing film (Figure 3.7b). The moduli of the respective films similarly increase from 1.54 ± 0.55 GPa to 3.2 ±1.6 GPa for films with worm-like mesostructural order and from 2.9 ± 0.19 GPa to 4.0 ± 0.19 GPa for films with rectangular mesostructural order. Interestingly, the hardnesses and moduli of the films increase, even though the silica contents are lower in films with higher PR contents (with the ratios of all other species held constant). This is consistent with the relatively stiff properties of the seven aligned α-helices that constitute much of each PR monomer and is supported by recent investigations that have reported similar moduli and trends for other α-helix-containing proteins.[57] However, otherwise identical mesostructured-containing silica-surfactant films with higher PR loadings of 35 wt% and 44 wt% PR and reduced extents of worm-like mesostructural order (Figure 3.4) exhibited less robust mechanical properties, with hardnesses of 0.05 ± 0.01 GPa and 0.07 ± 0.01 GPa, and moduli of 2.64 ± 0.21 GPa and 2.55 ± 0.2 GPa respectively. These hardness and modulus values are significantly lower than those measured for the mesostructured 25 wt% PR films with similar worm-like mesostructural order. This is due in part to the lower silica contents of the 35 wt% and 44 wt% PR-containing films (19.5 wt% and 16.8 wt% silica, respectively), compared to the 25 wt% PR film (22.5 wt% silica), which provides the most robust host matrix for the film compositions and conditions examined. These results demonstrate that, for the compositions and conditions investigated, high mesostructural order and 25 wt% PR loading correlate with increased film hardness and modulus, observations that are supported by trends in other materials in which high-modulus guest molecules have been incorporated to increase the bulk modulus of composite materials.[58]

The moduli and hardnesses of rectangular PR-containing silica-surfactant films are significantly greater than previous formulations of similar materials[5] and comparable with non-protein-containing mesostructured silica materials.[31,59]

Similarly, the thermal stability of proteorhodopsin guest molecules in silica-surfactant host matrices also depends on the composition of the films and their extents of mesostructural order. Previously, DDM+DHPC+PFO-directed host films were shown to exhibit higher thermal stability of PR (up to approximately 97 ^{o}C), compared to PR in P123 triblock-copolymer-directed films or PR in native-like phospholipid membranes.[5] Figure 3.8 shows the results of normalized static UV-visible light absorbance measurements, as functions of temperature, for 5 wt% PR incorporated into DDM+POPC+DOTAP-directed rectangular and worm-like mesostructured silica films. Interestingly, proteorhodopsin guest molecules exhibited significantly greater thermal stabilities, up to approximately 110 ^{o}C after 2 h in well-ordered rectangular mesostructured silica-surfactant materials, compared to compositionally identical host matrices with worm-like structures. For PR in the rectangular mesostructured host, 85% normalized intensity at 520 nm was retained at 110℃ and 48% at 130℃, which represents a significant increase in the thermal stability of PR, compared to other previously reported synthetic host materials.[5] The retention of PR stability up to 110℃ and the gradual loss in absorbance at 520 nm (attributed to denaturation of PR) can be observed visually as loss in the purple color of the film (Figure S3.7). Significant and essentially complete denaturation of the PR guest molecules, at 140℃ and 150 ℃ respectively, can be observed visually as a transition to a yellow film, the color associated with denatured PR.

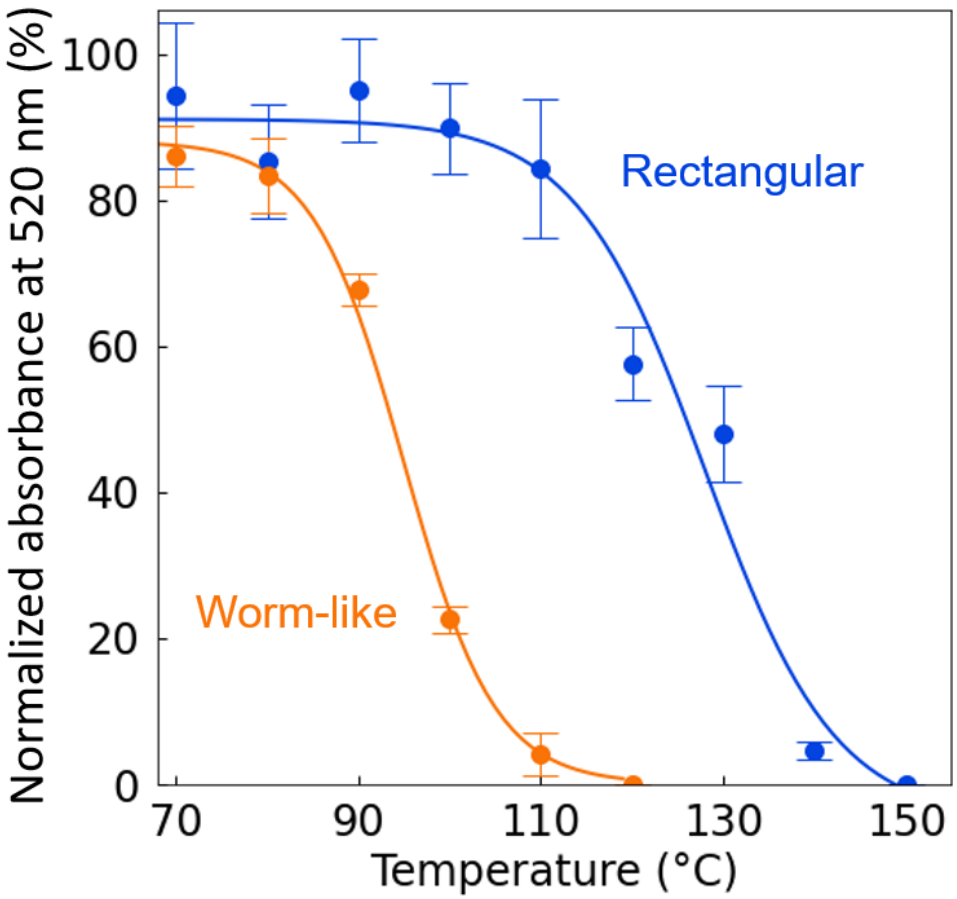

Figure 3.8. Normalized UV-visible light absorbance intensities at 520 nm for mesostructured 5 wt% PR, 59.4 wt% DDM, 5.8 wt% POPC, 1.3 wt% DOTAP, 21.4 wt% SiO_2, and 7.1 wt% *n*-propyl $SiO_{1.5}$ films with rectangular (blue) and worm-like (orange) mesostructural ordering after heat treatment for 24 h. The absorbance at 520 nm was measured for the center of each sample following heat treatment and normalized against a similar measurement taken prior to heat treatment.

For comparison, heat treatment analyses were conducted on films with identical compositions but with worm-like mesostructural order. As shown by the orange data points in Figure 3.8, PR guest molecules in films with worm-like structures exhibited significantly lower normalized absorbances at 520 nm following heat treatment over the range 70–120 °C. More

specifically, PR in DDM+POPC+DOTAP-directed silica films with worm-like mesostructural order retained approximately 80% absorbance at 520 nm up to 80 ℃, similar to PR in phospholipid membranes.[5] However, PR in such films exhibited significantly diminished absorbance above 90 ^{o}C, temperatures at which PR in phospholipid bilayers are also fully denatured. The different thermal stabilities of PR in DDM+POPC+DOTAP-directed mesostructured silica films with rectangular versus worm-like mesostructural order is thought to be due, in part, to differences in the local hydration environments of hydrophilic moieties at the extracellular and cytoplasmic ends of PR.[60,61] Such moieties are expected to be influenced by interactions with the structure-directing surfactant species that will depend on the extent of mesostructural order. Hydrophilic protein loops can exchange protons with surrounding water molecules, and environment-induced changes in hydration have been shown to have significant effects on the photocycle kinetics of PR.[62] The normalized absorbance data in Figure 3.8 suggests that lower extents of mesoscale order perturb the hydration of these hydrophilic moieties and their interactions with surrounding water molecules, resulting in unfavorable distributions of PR hydration that reduces their hydrothermal stability compared to similar host matrices with more ordered mesoscale structures.

3.5 Conclusions

Mesostructured silica-surfactant materials have emerged as promising hosts to harness the unique and diverse functionalities of transmembrane proteins in macroscopic material morphologies, such as thin films. The mesostructured PR-containing silica-surfactant materials reported here are well-ordered and have high membrane protein contents that exhibit native-like photocycle kinetics in transparent and mechanically and thermally robust films.

Complementary multiscale characterization techniques provide detailed insights on the protein-stabilizing and structure-directing roles of surfactant species that promote co-assembly of membrane proteins into mesostructured silica-surfactant hosts, along with the effects of different abiotic environments on the photocycle kinetics of the proteorhodopsin guests. SAXS analyses establish the alkyl chain lengths necessary to achieve high extents of rectangular mesostructural order in DDM+POPC+DOTAP-structure-directed films. Furthermore, this technique elucidates the effects of guest PR loading (up to 44 wt%) on the mesostructural ordering of silica-surfactant host films. Solid-state NMR corroborates that hydrophilic surfactant and charged lipid headgroups associate with hydrophilic moieties of the silica mesochannel wall by hydrogen-bonding and electrostatic interactions, respectively. The results demonstrate the importance of film composition, particularly the types and relative fractions of non-ionic, zwitterionic, and cationic surfactants that contribute towards significantly improved mesostructural ordering, protein loadings, and mechanical properties, when compared to polymer, gel, glass, or previously reported mesostructured silica protein-host materials. Nanoindentation analyses quantify the bulk mechanical properties of the films and showed that the hardness and modulus of a silica-surfactant film increased with PR loading or mesostructural order. Additionally, thermal testing analyses reveal improved stability for PR guest moieties within well-ordered host materials. Complementary pKa measurements and time-resolved UV-visible absorption spectroscopy established that the inclusion of zwitterionic POPC and cationic DOTAP lipids significantly lowered the pKa of a key function-dependent residue of PR, thereby increasing the active populations of PR. Global fit analyses of the time-resolved UV-visible light spectra quantify influences of local chemical environments on the photocycle of proteorhodopsin, revealing that the kinetics of the rate-

limiting step in the photocycle of PR are dependent on and can be mediated by the host material composition and structure. Such insights enable the selective incorporation of monomeric proteorhodopsin molecules into mesostructured silica-surfactant materials, with the tertiary structure of the protein largely unperturbed during the co-assembly process. The high protein loading, mechanical robustness, and thermal stability demonstrated by these DDM+POPC+DOTAP-silica-surfactant protein-host films opens opportunities for harnessing transmembrane proteins in non-native environments. The results provide improved understanding of the complicated interactions that mediate PR functionality in non-biological environments and provide criteria and guidance for selecting and optimizing the compositions and conditions that enhance PR performance. Given the archetypical seven α-helical structure of proteorhodopsin, the insights are expected to apply to other transmembrane membrane proteins and provide general guidance for synthesizing abiotic host materials for incorporating proteins with diverse functions.

3.6 Future Directions

Following the formulation of mesostructured silica-surfactant films with high extents of protein loading and mesostructural order, the next objective is to achieve orientational alignment of the cylindrical mesochannels within the robust host matrix. Chapter 5 details what has been accomplished regarding the orientational alignment of these silica-surfactant mesochannels, as well as future directions for this work. Here, I will suggest paths to continue this research by optimizing of the composition of protein-containing films, and increase understanding of these materials via additional characterization techniques. During the revision of my paper, I received recommendations from interested reviewers for environmental

ellipsoporosimetry (to investigate ellipsoidal pore diameters, porous volume, and surface area, and Young moduli of films in the direction perpendicular to the substrates),[63] and computational modeling. I agree with this reviewer that environmental ellipsoporosimetry would complement the data presented in this chapter well, potentially elucidating more information of the topology of mesostructure.[64]

Computational modeling can investigate a variety of highly complex interactions, providing additional information regarding the self-assembly and silica polymerization processes that occur during synthesis, which are not well understood. (There is a comprehensive understanding of molecules and their concentrations within the self-assembling solution, and also after synthesis, when the fully polymerized material has been well-characterized.) As this is an extremely complex system with many different molecules co-assembling based on many interactions, such as electrostatic and hydrophobic/hydrophilic, and van der Waals forces, the scope of investigation must be targeted to limit computational cost. Modeling the co-assembly of a mesochannel, both around a proteorhodopsin monomer and without a protein guest, can provide information at intermediate length-scales inaccessible by mesoscale SAXS and atomic-scale NMR techniques. Greater understanding of protein-surfactant and surfactant-surfactant interactions within these mesochannels may elucidate the intermolecular interactions that lead to the greatly improved thermal stability exhibited by PR in these materials, and inform the selection of new surfactants to better accommodate PR or other membrane protein guests. Additionally, comparison of the two systems, specifically with regards to the packing density of surfactants within the channel and the distribution of surfactants around the channel, may direct future improvements to these host materials. It would also be valuable to analyze preferred orientations of proteorhodopsin monomers within

the channel. NMR experiments have validated the location of PR within the mesochannels, and α-helices are hypothesized to prefer orientation along the axis of the mesochannel cylinder due to hydrophobic interactions; however, this has not been corroborated with analyses. Separate models of the interactions that the co-assembling solution has with varied or patterned substrates would also be interesting, and potentially inform future experiments and designs of substrates to achieve higher extents of mesostructural and orientational order (This concept is discussed in more detail in Chapter 5).

Similar to these proposed models, *in situ* experiments probe the development of mesostructural ordering in silica-surfactant films during synthesis. I have previously conducted *in situ* SAXS experiments of PR-containing liquid crystals, with varied surfactant concentrations and as a function of temperature, to see which mesostructures are thermodynamically preferred at equilibrium. These results showed a phase change as a function of temperature, the formation of an emerging body-centered cubic phase was observed along with the rectangular and hexagonal phases that existed at lower temperatures; however, this data could not be reliably used to direct the synthesis of silica-surfactant films because the presence of polymerizing silica significantly altered resulting mesostructures, and also because increased temperatures sped up silica polymerization. However, if silica polymerization can be significantly slowed or postponed during the co-assembly of silica-DDM+POPC+DOTAP films, temperature-dependent experiments could result in higher mesostructural ordering either through optimization or annealing techniques.[65] *In situ* ^{29}Si NMR experiments are another method of proving mesostructural formation during synthesis. These experiments would investigate the extent of crosslinking during synthesis and could be done as a function of various synthesis conditions, potentially revealing methods of making silica polymerization

less disruptive, and thus enabling the previously discussed temperature-dependent synthesis techniques.

In addition to experiments meant to gain a better understanding of the synthesis of silica-DDM+POPC+DOTAP films, new compositions of materials should be developed and optimized based on this platform. The interactions used to stabilize proteorhodopsin are applicable to similarly structured proteins, and have a wide application across other membrane proteins regardless of function. Efforts in the Chmelka group are planned to continue with aquaporin, a transmembrane protein that passively facilitates water transport across a cell membrane, for the important application of light-weight water purification. Optimization of an aquaporin-containing silica-surfactant film pursues many of the same desired characteristics of proteorhodopsin-containing materials, namely high extents of mesostructural and orientational order of the mesochannels, high protein loading, and orientational alignment of the aquaporin molecules. This is important to pursue as silica-DDM+POPC+DOTAP films provide an opportunity to produce a general platform for macroscopic molecular and ion transport, which has previously never been done. In addition, I think that the incorporation of enzymatic membrane proteins is an interesting target for these materials. Harnessing the functions of these proteins will not require the same significant extent of orientational ordering of the mesochannels or proteins required for anisotropic (molecular or ion) transport proteins, meaning that the high protein loadings already achieved may be enough to see significant biocatalytic results.

2.7 References

(1) Béjà, O.; Spudich, E. N.; Spudich, J. L.; Leclerc, M.; DeLong, E. F. Proteorhodopsin Phototrophy in the Ocean. *Nature* **2001**, *411* (6839), 786–789. https://doi.org/10.1038/35081051.

(2) Sabehi, G.; Massana, R.; Bielawski, J. P.; Rosenberg, M.; Delong, E. F.; Beja, O. Novel Proteorhodopsin Variants from the Mediterranean and Red Seas. *Environ. Microbiol.* **2003**, *5* (10), 842–849. https://doi.org/10.1046/j.1462-2920.2003.00493.x.

(3) Béjà, O.; Aravind, L.; Koonin, E. V.; Suzuki, M. T.; Hadd, A.; Nguyen, L. P.; Jovanovich, S. B.; Gates, C. M.; Feldman, R. A.; Spudich, J. L.; Spudich, E. N.; DeLong, E. F. Bacterial Rhodopsin: Evidence for a New Type of Phototrophy in the Sea. *Science* **2000**, *289* (5486), 1902–1906. https://doi.org/10.1126/science.289.5486.1902.

(4) Engqvist, M. K. M.; McIsaac, R. S.; Dollinger, P.; Flytzanis, N. C.; Abrams, M.; Schor, S.; Arnold, F. H. Directed Evolution of Gloeobacter Violaceus Rhodopsin Spectral Properties. *J. Mol. Biol.* **2015**, *427* (1), 205–220. https://doi.org/10.1016/j.jmb.2014.06.015.

(5) Jahnke, J. P.; Idso, M. N.; Hussain, S.; Junk, M. J. N.; Fisher, J. M.; Phan, D. D.; Han, S.; Chmelka, B. F. Functionally Active Membrane Proteins Incorporated in Mesostructured Silica Films. *J. Am. Chem. Soc.* **2018**, *140* (11), 3892–3906. https://doi.org/10.1021/jacs.7b06863.

(6) Kalantari, M.; Yu, M.; Yang, Y.; Strounina, E.; Gu, Z.; Huang, X.; Zhang, J.; Song, H.; Yu, C. Tailoring Mesoporous-Silica Nanoparticles for Robust Immobilization of Lipase and Biocatalysis. *Nano Res.* **2017**, *10* (2), 605–617. https://doi.org/10.1007/s12274-016-1320-6.

(7) Califano, V.; Costantini, A. Immobilization of Cellulolytic Enzymes in Mesostructured Silica Materials. *Catalysts* **2020**, *10* (6), 706. https://doi.org/10.3390/catal10060706.

(8) Gupta, R.; Chaudhury, N. K. Entrapment of Biomolecules in Sol–Gel Matrix for Applications in Biosensors: Problems and Future Prospects. *Biosens. Bioelectron.* **2007**, *22* (11), 2387–2399. https://doi.org/10.1016/j.bios.2006.12.025.

(9) Blin, J. L.; Gérardin, C.; Carteret, C.; Rodehüser, L.; Selve, C.; Stébé, M. J. Direct One-Step Immobilization of Glucose Oxidase in Well-Ordered Mesostructured Silica Using a Nonionic Fluorinated Surfactant. *Chem. Mater.* **2005**, *17* (6), 1479–1486. https://doi.org/10.1021/cm048033r.

(10) Nordlund, G.; Sing Ng, J. B.; Bergström, L.; Brzezinski, P. A Membrane-Reconstituted Multisubunit Functional Proton Pump on Mesoporous Silica Particles. *ACS Nano* **2009**, *3* (9), 2639–2646. https://doi.org/10.1021/nn9005413.

(11) Janshoff, A.; Steinem, C. Transport across Artificial Membranes–an Analytical Perspective. *Anal. Bioanal. Chem.* **2006**, *385* (3), 433–451. https://doi.org/10.1007/s00216-006-0305-9.

(12) Petkova, V.; Benattar, J.-J.; Zoonens, M.; Zito, F.; Popot, J.-L.; Polidori, A.; Jasseron, S.; Pucci, B. Free-Standing Films of Fluorinated Surfactants as 2D Matrices for Organizing Detergent-Solubilized Membrane Proteins. *Langmuir* **2007**, *23* (8), 4303–4309. https://doi.org/10.1021/la063249o.

(13) Bogdanov, M.; Dowhan, W.; Vitrac, H. Lipids and Topological Rules Governing Membrane Protein Assembly. *Biochim. Biophys. Acta BBA - Mol. Cell Res.* **2014**, *1843* (8), 1475–1488. https://doi.org/10.1016/j.bbamcr.2013.12.007.

(14) Liang, H.; Whited, G.; Nguyen, C.; Stucky, G. D. The Directed Cooperative Assembly of Proteorhodopsin into 2D and 3D Polarized Arrays. *Proc. Natl. Acad. Sci.* **2007**, *104* (20), 8212–8217. https://doi.org/10.1073/pnas.0702336104.

(15) Liang, H.; Whited, G.; Nguyen, C.; Okerlund, A.; Stucky, G. D. Inherently Tunable Electrostatic Assembly of Membrane Proteins. *Nano Lett.* **2008**, *8* (1), 333–339. https://doi.org/10.1021/nl0729173.

(16) Hua, D.; Kuang, L.; Liang, H. Self-Directed Reconstitution of Proteorhodopsin with Amphiphilic Block Copolymers Induces the Formation of Hierarchically Ordered Proteopolymer Membrane Arrays. *J. Am. Chem. Soc.* **2011**, *133* (8), 2354–2357. https://doi.org/10.1021/ja109796x.

(17) Neyshtadt, S.; Jahnke, J. P.; Messinger, R. J.; Rawal, A.; Segal Peretz, T.; Huppert, D.; Chmelka, B. F.; Frey, G. L. Understanding and Controlling Organic–Inorganic Interfaces in Mesostructured Hybrid Photovoltaic Materials. *J. Am. Chem. Soc.* **2011**, *133* (26), 10119–10133. https://doi.org/10.1021/ja200054z.

(18) Kirmayer, S.; Dovgolevsky, E.; Kalina, M.; Lakin, E.; Cadars, S.; Epping, J. D.; Fernández-Arteaga, A.; Rodríguez-Abreu, C.; Chmelka, B. F.; Frey, G. L. Syntheses of Mesostructured Silica Films Containing Conjugated Polymers from Tetrahydrofuran−Water Solutions. *Chem. Mater.* **2008**, *20* (11), 3745–3756. https://doi.org/10.1021/cm703478g.

(19) Melosh, N. A.; Steinbeck, C. A.; Scott, B. J.; Hayward, R. C.; Davidson, P.; Stucky, G. D.; Chmelka, B. F. Mesostructured Silica/Block Copolymer Composites as Hosts for Optically Limiting Tetraphenylporphyrin Dye Molecules. *J. Phys. Chem. B* **2004**, *108* (32), 11909–11914. https://doi.org/10.1021/jp040064m.

(20) Segal-Peretz, T.; Jahnke, J. P.; Berenson, A.; Neeman, L.; Oron, D.; Rossini, A. J.; Chmelka, B. F.; Frey, G. L. Understanding and Promoting Molecular Interactions and Charge Transfer in Dye-Mediated Hybrid Photovoltaic Materials. *J. Phys. Chem. C* **2014**, *118* (44), 25374–25391. https://doi.org/10.1021/jp508819w.

(21) Phan, H.; Jahnke, J. P.; Chmelka, B. F.; Nguyen, T.-Q. Structural and Optoelectronic Properties of Hybrid Bulk-Heterojunction Materials Based on Conjugated Small Molecules and Mesostructured TiO_2. *Appl. Phys. Lett.* **2014**, *104* (23), 233305. https://doi.org/10.1063/1.4883001.

(22) Ramírez, M. G.; Jahnke, J. P.; Junk, M. J. N.; Villalvilla, J. M.; Boj, P. G.; Quintana, J. A.; Calzado, E. M.; Chmelka, B. F.; Díaz-García, M. A. Improved Amplified Spontaneous Emission of Dye-Doped Functionalized Mesostructured Silica Waveguide

Films. *Adv. Opt. Mater.* **2015**, *3* (10), 1454–1461. https://doi.org/10.1002/adom.201500297.

(23) Steinbeck, C. A.; Ernst, M.; Meier, B. H.; Chmelka, B. F. Anisotropic Optical Properties and Structures of Block Copolymer/Silica Thin Films Containing Aligned Porphyrin *J* -Aggregates. *J. Phys. Chem. C* **2008**, *112* (7), 2565–2573. https://doi.org/10.1021/jp075310j.

(24) Granja, L. P.; Martínez, E. D.; Troiani, H.; Sanchez, C.; Soler Illia, G. J. A. A. Magnetic Gold Confined in Ordered Mesoporous Titania Thin Films: A Noble Approach for Magnetic Devices. *ACS Appl. Mater. Interfaces* **2017**, *9* (1), 965–971. https://doi.org/10.1021/acsami.6b15189.

(25) Han, C.-T.; Nguyen, K. D. Q.; Berkow, M. W.; Hussain, S.; Kiani, A.; Kinnebrew, M.; Idso, M. N.; Baxter, N.; Chang, E.; Aye, E.; Winslow, E.; Rahman, M.; Seppälä, S.; O'Malley, M. A.; Chmelka, B. F.; Mertz, B.; Han, S. Lipid Membrane Mimetics and Oligomerization Tune Functional Properties of Proteorhodopsin. *Biophys. J.* **2023**, *122* (1), 168–179. https://doi.org/10.1016/j.bpj.2022.11.012.

(26) Ernst, R. R.; Bodenhausen, G.; Wokaun, A. *Principles of Nuclear Magnetic Resonance in One and Two Dimensions*; The International series of monographs on chemistry; Clarendon Press ; Oxford University Press: New York, NY, 1987.

(27) Elena, B.; De Paëpe, G.; Emsley, L. Direct Spectral Optimisation of Proton–Proton Homonuclear Dipolar Decoupling in Solid-State NMR. *Chem. Phys. Lett.* **2004**, *398* (4–6), 532–538. https://doi.org/10.1016/j.cplett.2004.09.122.

(28) Fung, B. M.; Khitrin, A. K.; Ermolaev, K. An Improved Broadband Decoupling Sequence for Liquid Crystals and Solids. *J. Magn. Reson.* **2000**, *142* (1), 97–101. https://doi.org/10.1006/jmre.1999.1896.

(29) Idso, M. N.; Baxter, N. R.; Narayanan, S.; Chang, E.; Fisher, J.; Chmelka, B. F.; Han, S. Proteorhodopsin Function Is Primarily Mediated by Oligomerization in Different

Micellar Surfactant Solutions. *J. Phys. Chem. B* **2019**, *123* (19), 4180–4192. https://doi.org/10.1021/acs.jpcb.9b00922.

(30) Oliver, W. C.; Pharr, G. M. An Improved Technique for Determining Hardness and Elastic Modulus Using Load and Displacement Sensing Indentation Experiments. *J. Mater. Res.* **1992**, *7* (6), 1564–1583. https://doi.org/10.1557/JMR.1992.1564.

(31) Chemin, N.; Klotz, M.; Rouessac, V.; Ayral, A.; Barthel, E. Mechanical Properties of Mesoporous Silica Thin Films: Effect of the Surfactant Removal Processes. *Thin Solid Films* **2006**, *495* (1–2), 210–213. https://doi.org/10.1016/j.tsf.2005.08.260.

(32) Gross, A. F.; Ruiz, E. J.; Tolbert, S. H. Effect of Framework Polymerization on the Phase Stability of Periodic Silica/Surfactant Nanostructured Composites. *J. Phys. Chem. B* **2000**, *104* (23), 5448–5461. https://doi.org/10.1021/jp9944379.

(33) Zhao, D.; Feng, J.; Huo, Q.; Melosh, N.; Fredrickson, G. H.; Chmelka, B. F.; Stucky, G. D. Triblock Copolymer Syntheses of Mesoporous Silica with Periodic 50 to 300 Angstrom Pores. *Science* **1998**, *279* (5350), 548–552. https://doi.org/10.1126/science.279.5350.548.

(34) Partha, R.; Krebs, R.; Caterino, T. L.; Braiman, M. S. Weakened Coupling of Conserved Arginine to the Proteorhodopsin Chromophore and Its Counterion Implies Structural Differences from Bacteriorhodopsin. *Biochim. Biophys. Acta BBA - Bioenerg.* **2005**, *1708* (1), 6–12. https://doi.org/10.1016/j.bbabio.2004.12.009.

(35) Albarracín, V. H.; Kraiselburd, I.; Bamann, C.; Wood, P. G.; Bamberg, E.; Farias, M. E.; Gärtner, W. Functional Green-Tuned Proteorhodopsin from Modern Stromatolites. *PLOS ONE* **2016**, *11* (5), e0154962. https://doi.org/10.1371/journal.pone.0154962.

(36) Brinker, C. J.; Sehgal, R.; Hietala, S. L.; Deshpande, R.; Smith, D. M.; Loy, D.; Ashley, C. S. Sol-Gel Strategies for Controlled Porosity Inorganic Materials. *J. Membr. Sci.* **1994**, *94* (1), 85–102. https://doi.org/10.1016/0376-7388(93)E0129-8.

(37) Guillemin, Y.; Etienne, M.; Aubert, E.; Walcarius, A. Electrogeneration of Highly Methylated Mesoporous Silica Thin Films with Vertically-Aligned Mesochannels and

Electrochemical Monitoring of Mass Transport Issues. *J. Mater. Chem.* **2010**, *20* (32), 6799. https://doi.org/10.1039/c0jm00305k.

(38) Despas, C.; Vodolazkaya, N. A.; Ghanbaja, J.; Walcarius, A. Preparation of Ordered and Oriented Mesoporous Silica Thin Films Bearing Octyl or Hexadecyl Groups by Electrochemically Assisted Self-Assembly and Evaluation of Their Transport Properties. *J. Solid State Electrochem.* **2015**, *19* (7), 2075–2085. https://doi.org/10.1007/s10008-014-2726-2.

(39) ALOthman, Z. A Review: Fundamental Aspects of Silicate Mesoporous Materials. *Materials* **2012**, *5* (12), 2874–2902. https://doi.org/10.3390/ma5122874.

(40) Otzen, D. Protein–Surfactant Interactions: A Tale of Many States. *Biochim. Biophys. Acta BBA - Proteins Proteomics* **2011**, *1814* (5), 562–591. https://doi.org/10.1016/j.bbapap.2011.03.003.

(41) Wu, S.-H.; Mou, C.-Y.; Lin, H.-P. Synthesis of Mesoporous Silica Nanoparticles. *Chem. Soc. Rev.* **2013**, *42* (9), 3862. https://doi.org/10.1039/c3cs35405a.

(42) Štangar, U. L.; Hüsing, N. Alkyl-Glycoside Surfactants in the Synthesis of Mesoporous Silica Films. *Silicon Chem.* **2003**, *2* (3/4), 157–165. https://doi.org/10.1023/B:SILC.0000046724.80191.21.

(43) Han, C.-T.; Song, J.; Chan, T.; Pruett, C.; Han, S. Electrostatic Environment of Proteorhodopsin Affects the PKa of Its Buried Primary Proton Acceptor. *Biophys. J.* **2020**, *118* (8), 1838–1849. https://doi.org/10.1016/j.bpj.2020.02.027.

(44) Lu, Y.; Fan, H.; Doke, N.; Loy, D. A.; Assink, R. A.; LaVan, D. A.; Brinker, C. J. Evaporation-Induced Self-Assembly of Hybrid Bridged Silsesquioxane Film and Particulate Mesophases with Integral Organic Functionality. *J. Am. Chem. Soc.* **2000**, *122* (22), 5258–5261. https://doi.org/10.1021/ja9935862.

(45) Alberius, P. C. A.; Frindell, K. L.; Hayward, R. C.; Kramer, E. J.; Stucky, G. D.; Chmelka, B. F. General Predictive Syntheses of Cubic, Hexagonal, and Lamellar Silica

and Titania Mesostructured Thin Films. *Chem. Mater.* **2002**, *14* (8), 3284–3294. https://doi.org/10.1021/cm011209u.

(46) Nilsson, F.; Söderman, O.; Johansson, I. Physical−Chemical Properties of the *n* -Octyl β-D -Glucoside/Water System. A Phase Diagram, Self-Diffusion NMR, and SAXS Study. *Langmuir* **1996**, *12* (4), 902–908. https://doi.org/10.1021/la950602+.

(47) Auvray, X.; Petipas, C.; Anthore, R.; Ricolattes, I.; Lattes, A. X-Ray-Diffraction Study of the Ordered Lyotropic Phases Formed by Sugar-Based Surfactants. *Langmuir* **1995**, *11*, 433–439. https://doi.org/10.1021/la00002a012.

(48) Idso, M. N. Understanding and Optimizing the Interactions of Functional Species in Mesostructured Materials with Diverse Transport Properties. Ph.D. Thesis, University of California, Santa Barbara, 2017.

(49) Lesaint, C.; Lebeau, B.; Marichal, C.; Patarin, J. Synthesis of Mesoporous Silica Materials Functionalized with N-Propyl Groups. *Microporous Mesoporous Mater.* **2005**, *83* (1–3), 76–84. https://doi.org/10.1016/j.micromeso.2005.01.012.

(50) Cruciani, O.; Mannina, L.; Sobolev, A.; Cametti, C.; Segre, A. An Improved NMR Study of Liposomes Using 1-Palmitoyl-2-Oleoyl-Sn-Glycero-3-Phospatidylcholine as Model. *Molecules* **2006**, *11* (5), 334–344. https://doi.org/10.3390/11050334.

(51) Lakatos, M.; Lanyi, J. K.; Szakács, J.; Váró, G. The Photochemical Reaction Cycle of Proteorhodopsin at Low PH. *Biophys. J.* **2003**, *84* (5), 3252–3256. https://doi.org/10.1016/S0006-3495(03)70049-6.

(52) Hussain, S.; Kinnebrew, M.; Schonenbach, N. S.; Aye, E.; Han, S. Functional Consequences of the Oligomeric Assembly of Proteorhodopsin. *J. Mol. Biol.* **2015**, *427* (6), 1278–1290. https://doi.org/10.1016/j.jmb.2015.01.004.

(53) Dioumaev, A. K.; Wang, J. M.; Bálint, Z.; Váró, G.; Lanyi, J. K. Proton Transport by Proteorhodopsin Requires That the Retinal Schiff Base Counterion Asp-97 Be Anionic. *Biochemistry* **2003**, *42* (21), 6582–6587. https://doi.org/10.1021/bi034253r.

(54) Váró, G.; Brown, L. S.; Lakatos, M.; Lanyi, J. K. Characterization of the Photochemical Reaction Cycle of Proteorhodopsin. *Biophys. J.* **2003**, *84* (2), 1202–1207. https://doi.org/10.1016/S0006-3495(03)74934-0.

(55) Lindholm, L.; Ariöz, C.; Jawurek, M.; Liebau, J.; Mäler, L.; Wieslander, Å.; Von Ballmoos, C.; Barth, A. Effect of Lipid Bilayer Properties on the Photocycle of Green Proteorhodopsin. *Biochim. Biophys. Acta BBA - Bioenerg.* **2015**, *1847* (8), 698–708. https://doi.org/10.1016/j.bbabio.2015.04.011.

(56) Miyoshi, H.; Matsuo, H.; Oku, Y.; Tanaka, H.; Yamada, K.; Mikami, N.; Takada, S.; Hata, N.; Kikkawa, T. Theoretical Analysis of Elastic Modulus and Dielectric Constant for Low- *k* Two-Dimensional Periodic Porous Silica Films. *Jpn. J. Appl. Phys.* **2004**, *43* (2), 498–503. https://doi.org/10.1143/JJAP.43.498.

(57) Perticaroli, S.; Nickels, J. D.; Ehlers, G.; O'Neill, H.; Zhang, Q.; Sokolov, A. P. Secondary Structure and Rigidity in Model Proteins. *Soft Matter* **2013**, *9* (40), 9548. https://doi.org/10.1039/c3sm50807b.

(58) Reynaud, E.; Jouen, T.; Gauthier, C.; Vigier, G.; Varlet, J. Nanofillers in Polymeric Matrix: A Study on Silica Reinforced PA6. *Polymer* **2001**, *42* (21), 8759–8768. https://doi.org/10.1016/S0032-3861(01)00446-3.

(59) Williford, R. E.; Li, X. S.; Addleman, R. S.; Fryxell, G. E.; Baskaran, S.; Birnbaum, J. C.; Coyle, C.; Zemanian, T. S.; Wang, C.; Courtney, A. R. Mechanical Stability of Templated Mesoporous Silica Thin Films. *Microporous Mesoporous Mater.* **2005**, *85* (3), 260–266. https://doi.org/10.1016/j.micromeso.2005.06.024.

(60) Feng, J.; Mertz, B. Proteorhodopsin Activation Is Modulated by Dynamic Changes in Internal Hydration. *Biochemistry* **2015**, *54* (48), 7132–7141. https://doi.org/10.1021/acs.biochem.5b00932.

(61) Hirschi, S.; Kalbermatter, D.; Ucurum, Z.; Lemmin, T.; Fotiadis, D. Cryo-EM Structure and Dynamics of the Green-Light Absorbing Proteorhodopsin. *Nat. Commun.* **2021**, *12* (1), 4107. https://doi.org/10.1038/s41467-021-24429-6.

(62) Hussain, S.; Franck, J. M.; Han, S. Transmembrane Protein Activation Refined by Site-Specific Hydration Dynamics. *Angew. Chem. Int. Ed.* **2013**, *52* (7), 1953–1958. https://doi.org/10.1002/anie.201206147.

(63) Boissiere, C.; Grosso, D.; Lepoutre, S.; Nicole, L.; Bruneau, A. B.; Sanchez, C. Porosity and Mechanical Properties of Mesoporous Thin Films Assessed by Environmental Ellipsometric Porosimetry. *Langmuir* **2005**, *21* (26), 12362–12371. https://doi.org/10.1021/la050981z.

(64) Vayer, M.; Nguyen, T. H.; Grosso, D.; Boissiere, C.; Hillmyer, M. A.; Sinturel, C. Characterization of Nanoporous Polystyrene Thin Films by Environmental Ellipsometric Porosimetry. *Macromolecules* **2011**, *44* (22), 8892–8897. https://doi.org/10.1021/ma201497z.

(65) Firouzi, A.; Atef, F.; Oertli, A. G.; Stucky, G. D.; Chmelka, B. F. Alkaline Lyotropic Silicate−Surfactant Liquid Crystals. *J. Am. Chem. Soc.* **1997**, *119* (15), 3596–3610. https://doi.org/10.1021/ja963007i.

3.8 Supporting Information

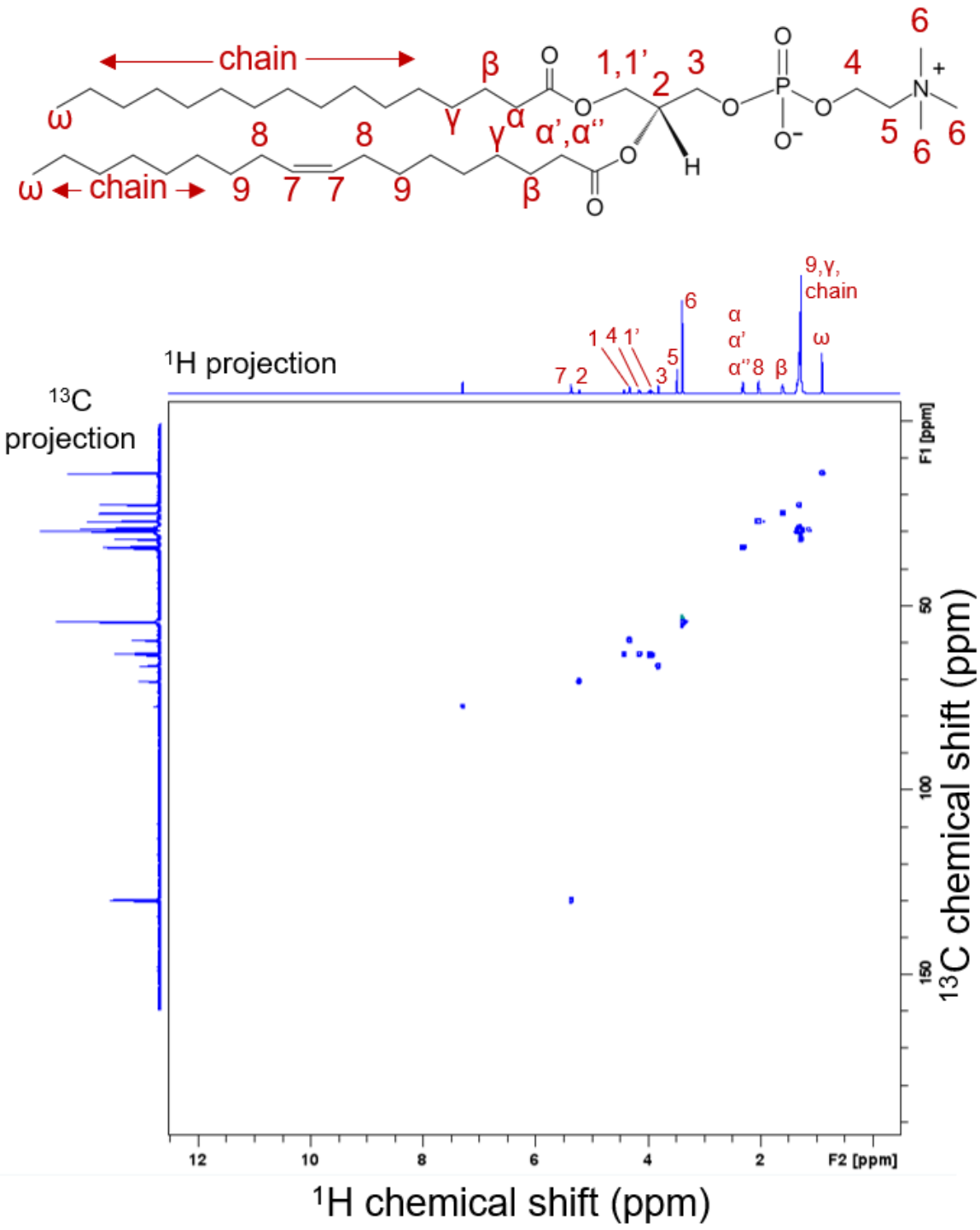

Figure S3.1. Solution-state 2D ^{1}H–^{13}C HSQC NMR spectra and atomic structure of POPC with ^{1}H assignments acquired at 18.8 T and 298 K. 1D projections of correlated ^{1}H and ^{13}C intensities are shown on the horizontal and vertical axes, respectively.

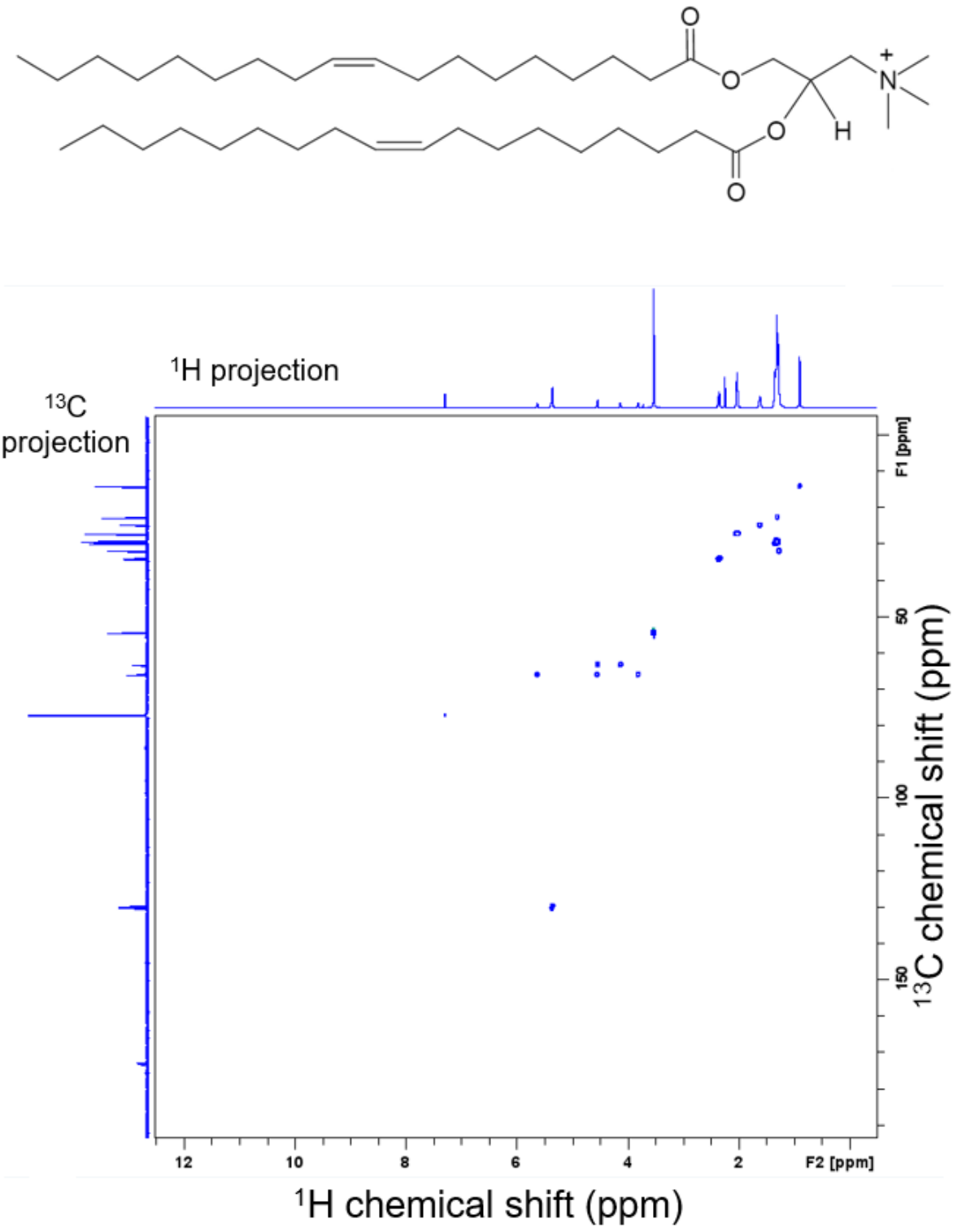

Figure S3.2. Solution-state 2D ^{1}H–^{13}C HSQC NMR spectra and atomic structure of DOTAP acquired at 18.8 T and 298 K. 1D projections of correlated ^{1}H and ^{13}C intensities are shown on the horizontal and vertical axes, respectively.

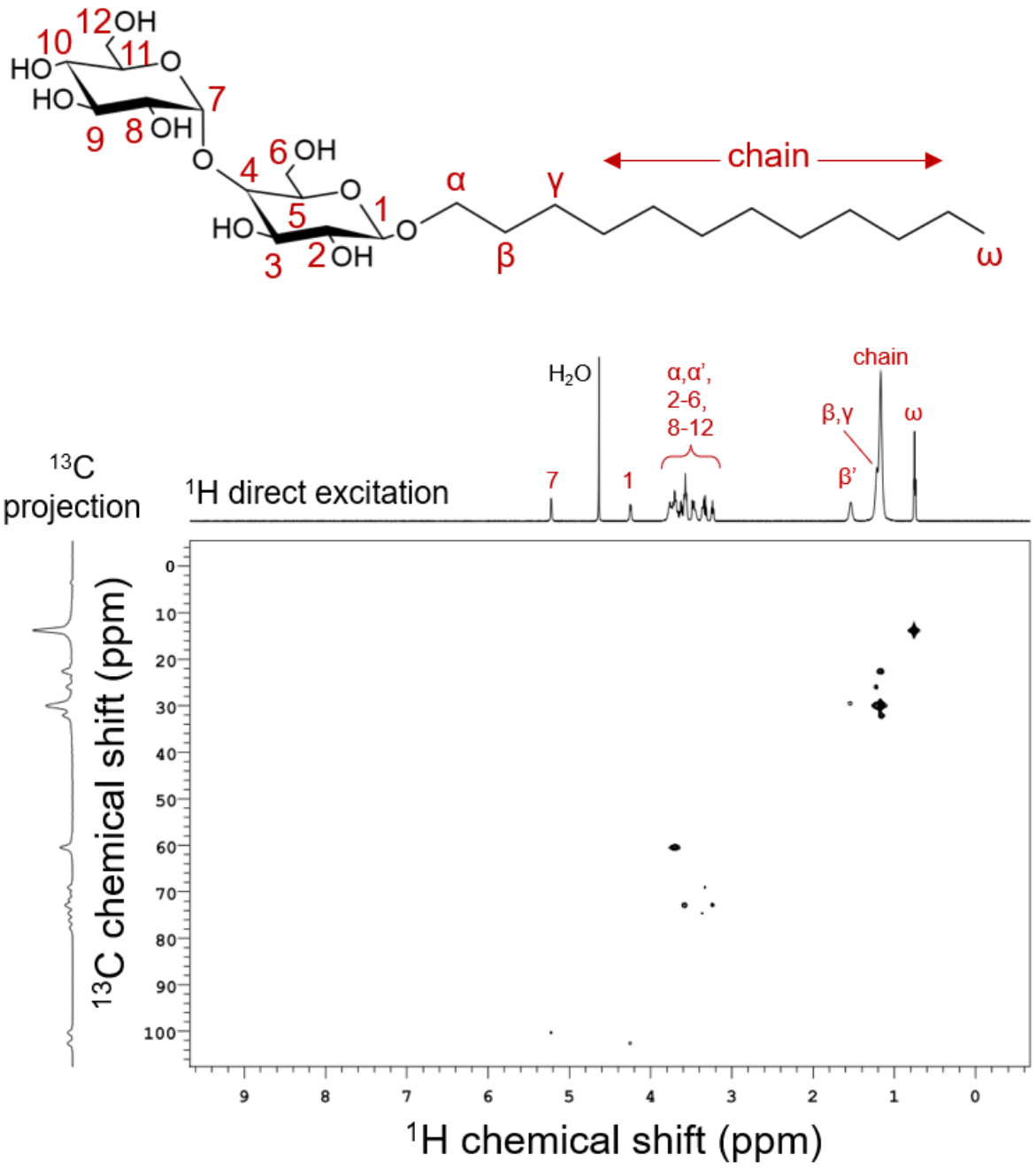

Figure S3.3. Solution-state 2D ^{1}H–^{13}C HSQC NMR spectra of DDM with ^{1}H assignments acquired at 14.1 T and 298 K. 1D projections of correlated ^{1}H and ^{13}C intensities are shown on the horizontal and vertical axes, respectively.

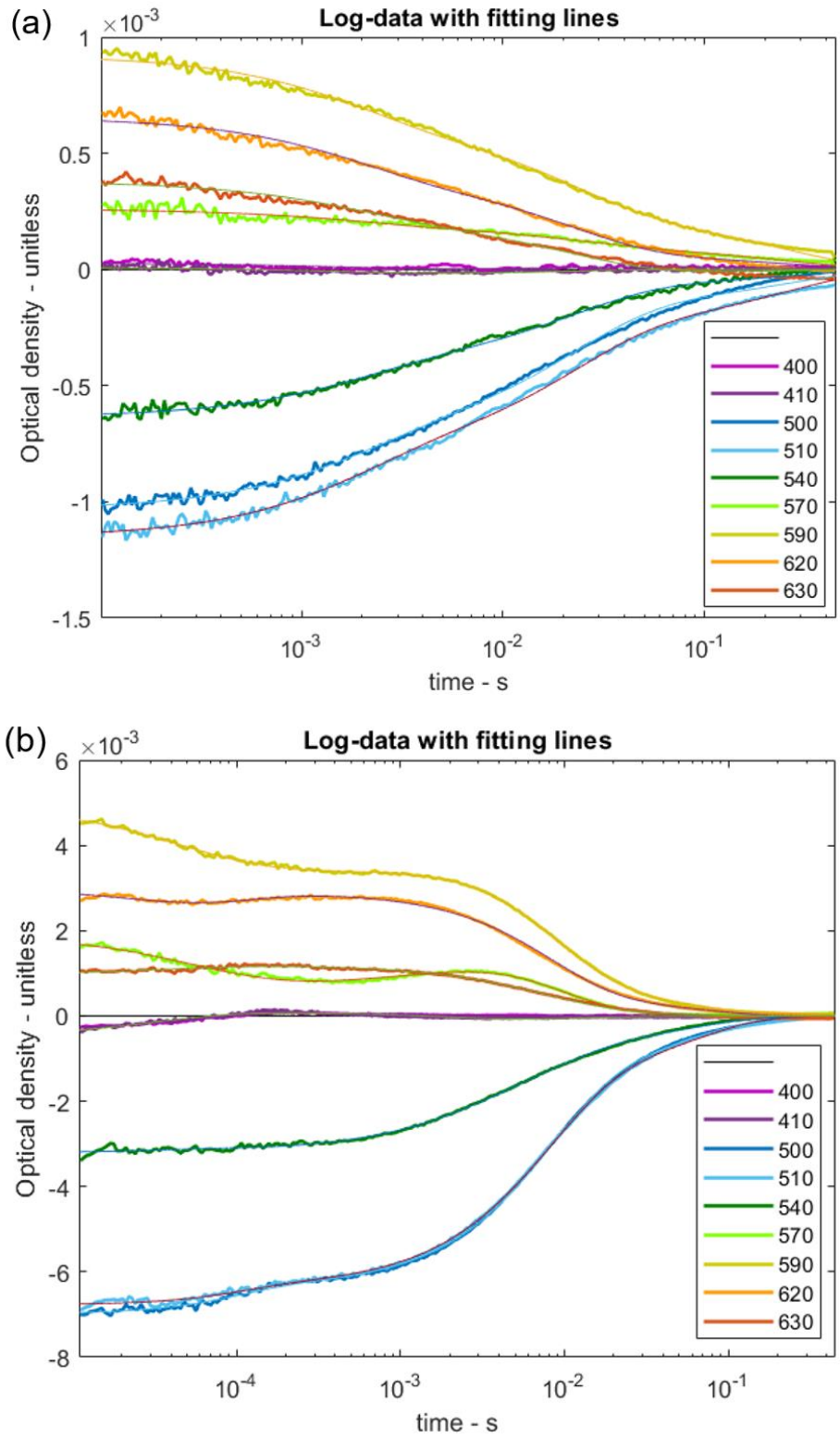

Figure S3.4. Time-resolved UV-visible light spectra showing transient absorbance traces at wavelengths of at 400, 410, 500, 510, 540, 570, 590, 620, and 630 nm for monomeric PR in mesostructured silica-surfactant films under varying pH conditions: **(a)** as-synthesized film at pH 4.1 and **(b)** hydrated for 1 week at pH 9 in 50 mM K_2HPO_4 and 150 mM KCl.

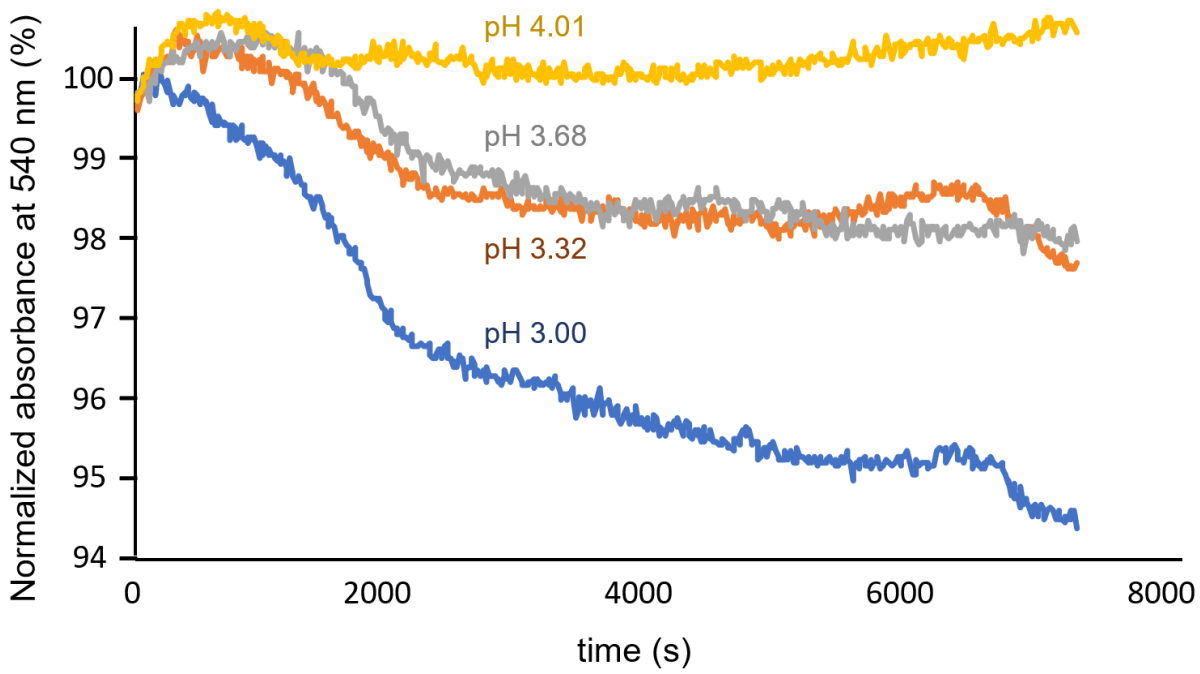

Figure S3.5. Transient UV-visible light absorbance intensities at 540 nm for wild-type proteorhodopsin at pH 3.00, 3.32, 3.68, and 4.01 for 2 h, normalized against the first collected 540-nm absorbance intensity at 0 s.

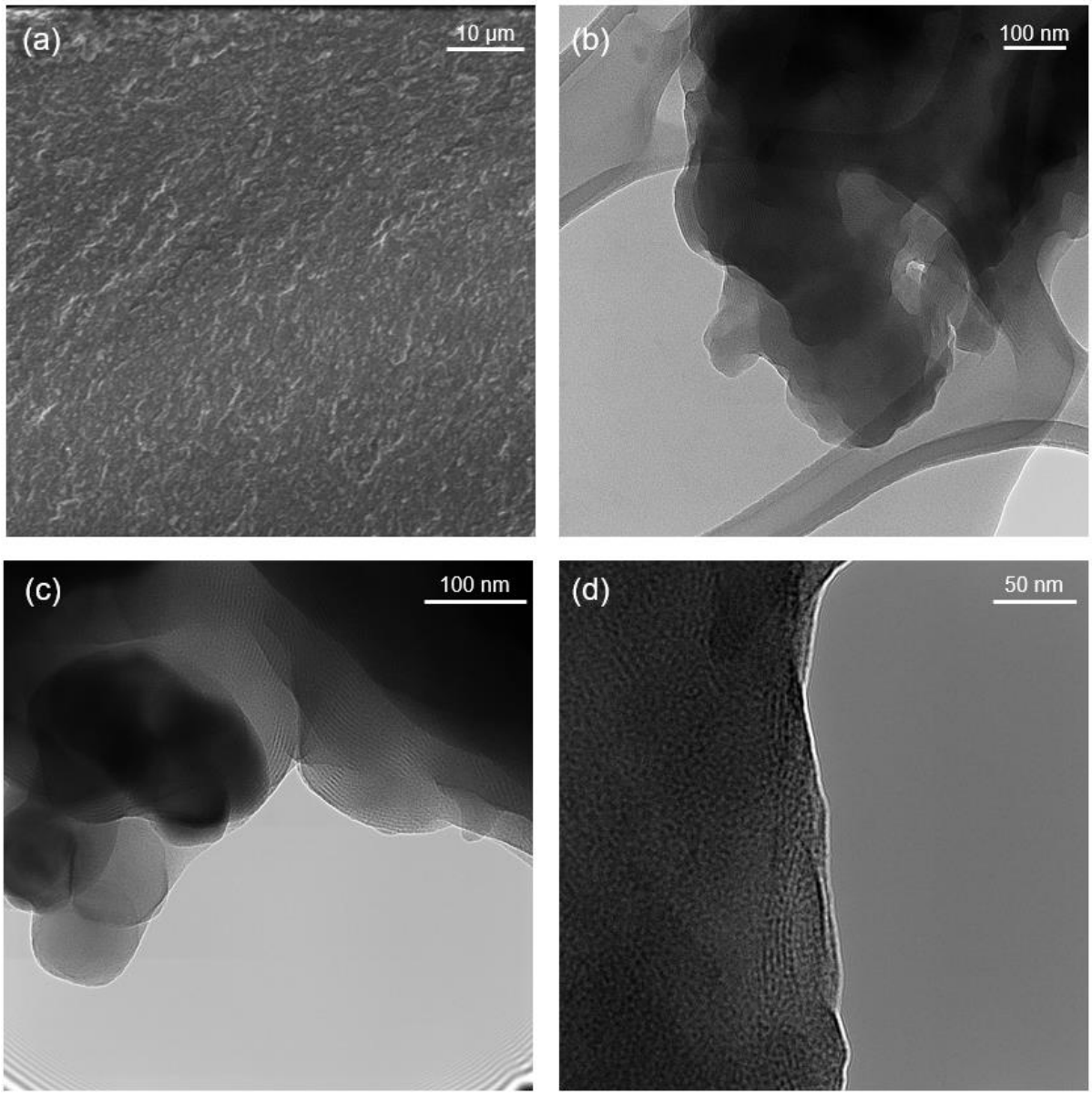

Figure S3.6. Representative electron microscopy images of a mesostructured silica-surfactant films with 5 wt% PR, 59.4 wt% DDM, 5.8 wt% POPC, 1.3 wt% DOTAP, 21.4 wt% SiO_2, and 7.1 wt% *n*-propyl $SiO_{1.5}$ obtained by **(a)** SEM at 2000x magnification, and TEM at **(b)** 58000x, **(c)** 94000x, and **(d)** 150000x magnifications.

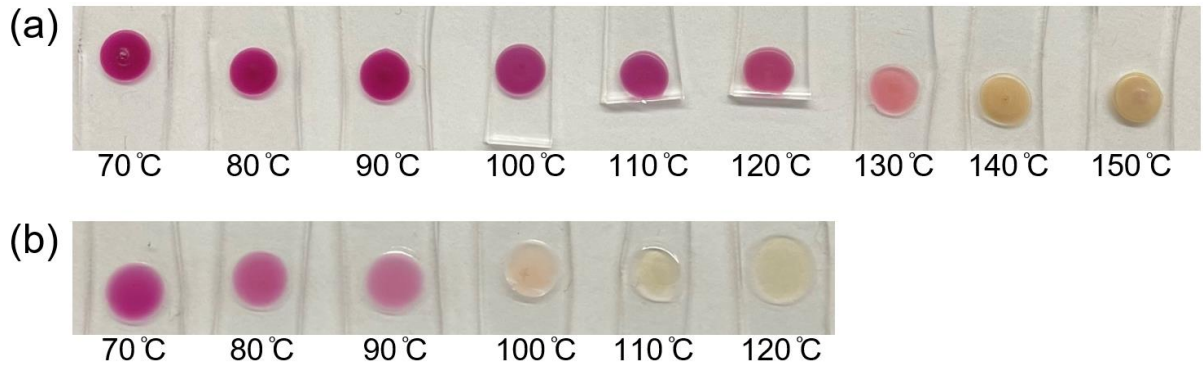

Figure S3.7. Optical images of mesostructured silica-surfactant films containing 5 wt% PR, 59.4 wt% DDM, 5.8 wt% POPC, 1.3 wt% DOTAP, 21.4 wt% SiO_2, and 7.1 wt% *n*-propyl $SiO_{1.5}$ with **(a)** rectangular and **(b)** worm-like mesostructural ordering after heat treatment at different temperatures for 24 h.

Chapter 4. Cryogenic electron microscopy analyses of oligomeric proteorhodopsin in micellar DDM solutions

4.1 Abstract

Structure-determination of transmembrane proteins is a complex and difficult pursuit, for which only a select few have been solved. Currently, membrane proteins make up less than 6% of solved three-dimensional structures of proteins, due in part to poor solubility, reliance on stabilizing surfactants and lipid membranes to maintain structure and function, and physiochemical properties of the stabilizing environment making analyses challenging. Following a number of recent improvements to instrumentation such as computing power and electron diffraction cameras, often referred to as the "resolution revolution," cryogenic electron (cryo-EM) microscopy has become a primary technique of structural biology, often even utilized prior to X-ray crystallography or NMR, the traditional methods of protein structure determination. In this chapter, cryo-EM analyses reveal a pentameric oligomeric structure for wild-type proteorhodopsin in flat *n*-dodecyl-β-D-maltopyranoside (DDM) surfactant micelles. However, a high resolution structure did not converge from the data, likely due to local heterogeneities of the protein due to flexibility within the large DDM micelle. Although not of interest in structural biology, this knowledge is extremely valuable when trying to understand how host environments impact the structure of proteorhodopsin, and how structural changes and dynamics are related to function. Additional results correlate sample preparation protocols and compositions to higher-purity homogeneous oligomers and represent advances in the synthesis of well-ordered co-assembled mesostructured proteorhodopsin-silica-surfactant hosts (highlighted in Chapter 3). Potential future experiments are presented which would build

upon these cryo-EM results and utilize orthogonal techniques to understand the interactions between host and protein that influence function. These results contribute to the goal of producing non-native host materials capable of harnessing the diverse functions of membrane proteins.

4.2 Introduction

Proteorhodopsin structure and function

Integral membrane proteins, proteins that are permanently attached to a cell membrane lipid bilayer, are important targets for characterization as they make up roughly 30% of the mammalian proteome and 50-60% of all drug targets.[1–3] Additionally, some of these membranes have industrially relevant functions in biocatalysis,[4] biosensing,[5] and ion/molecular transport.[6–8] The biological membrane stabilizes significant hydrophobic regions of membrane proteins, effectively performing multiple roles as a substrate, solvent, and regulatory co-factor for protein function. Many pharmaceutical drugs target the interface between protein and lipids as a method to reach important protein binding sites, however, the complex interactions here are poorly understood.[3] Currently, membrane proteins make up less than 1% of solved three-dimensional (3D) structures of proteins,[9] due in part to poor solubility, reliance on stabilizing surfactants and lipid membranes to maintain structure and function, and physiochemical properties of the stabilizing environment making analyses challenging.[10] Structural biology methods such as X-ray crystallography, nuclear magnetic resonance spectroscopy, and cryogenic electron microscopy require purified and homogeneous protein samples, which for membrane proteins in most cases entails expression and purification into synthetic lipid bilayer or micellar environments. Selection of the composition of these

membrane mimetic environments can significantly impact the function of membrane proteins, creating debate around the question of which constitutes a more native-like membrane.[11–14]

Proteorhodopsin (PR) is a membrane protein found ubiquitously in marine bacteria that acts as a light-activated proton pump, assisting in the supply of ATP to organisms such as picoplankton. These organisms are found in the ocean and therefore have native functionality at a pH around 8.2. This functionality involves undergoing a series of conformational changes resulting in the transport of an H^+ ion across the transmembrane region of PR. Under native pH conditions, the D97 residue of PR is deprotonated, which is necessary for the native photocycle to proceed. Under pH conditions lower than the pKa (the pH value at which half of these residues are protonated) of the D97 residue, it can become protonated, restricting transition through the native photocycle and forcing an alternate series of conformational states that discourages net H^+ transport.[15] The protonation state of the D97 residue and its pKa are therefore integral to the function of PR. Importantly, the pKa of the D97 residue of PR is significantly influenced by its oligomerization and local environment. For example, in similar DDM micellar solutions, the pKa_{D97} is 6.5 for wild-type oligomeric PR and 7.2 for the monomer-enriched E50Q mutant of proteorhodopsin.[11,16]

Understanding the structure of proteorhodopsin (as well as other medically and industrially relevant membrane proteins) is important because it may lead to the tuning of function-dependent properties (such as the pKa of its D97 residue) through the manipulation of protein environments.[17,18] A 2.9 Å resolution structure for the pentameric assembly of wild-type proteorhodopsin in cymal-4 surfactant micelles was recently published that reveals the position and orientation of functionally-important residues within this environment.[19] This data can be analyzed individually, but also together with the published structures of monomeric

PR,[20] which shows differences in the orientation of the D97 residue, and protein homologs[21,22] to provide further context to the complex structure-function relationships of membrane protein proton pumps. Expanding this library of protein structures, and specifically the structures of PR or PR mutants in different biomimetic environments, can provide the information necessary to find answers in the multifaceted pursuit of understanding and tuning protein function.

Structure-determination techniques

Protein structure determination techniques such has X-ray crystallography, nuclear magnetic resonance (NMR), computational modeling, and cryogenic electron microscopy (Cryo-EM) present different methods to achieve high-resolution structural models of proteins, each accompanied by unique combinations of advantages and disadvantages. X-ray crystallography utilizes diffracted X-ray photon irradiation of crystalline proteins and a detector to achieve scattering data (called reflections) in two dimensions that can be converted into a three-dimensional molecular structure with high resolution. While photons diffracted at greater angles, producing reflections further from the beam center, produce reflections that represent increasing resolution, these reflections also display lower signal intensities. The highest resolution protein structure ever resolved is for crambin, reconstructed at 0.48 Å by X-ray crystallography.[23] X-ray crystallography is a powerful and often-used technique, making up approximately 85% of structures in the protein data bank (an online repository of protein structures); however, it relies on the preparation of highly ordered protein crystals, which can often be extremely difficult and labor-intensive, restricting the structures that can be solved.[9,24]

Solution-state NMR is another method used extensively in the structure determination of biological molecules and does not require protein crystallization. NMR utilizes strong magnets to align nuclei in a magnetic field, which are knocked out of thermodynamic

equilibrium by radio frequency pulses. Differences in the rate of procession back to equilibrium with the magnetic field are measured and characteristic of specific atomic environments. Instead of directly detecting locations of protein residues by diffracted X-rays or electrons, NMR provides information on bulk atomic environments and proximate species that other methods cannot. Although this produces important structural information, this technique is often limited to comparatively poor resolution compared to X-ray crystallography because of the complexity of the molecule and lack of constraints that can be applied to resolve the data.[24] Because of this, structure determination by NMR is also limited by the size of the protein; the largest protein structure solved by NMR is the 81.4 kDa enzyme malate synthase G (MSG).[25,26] Proteins greater than 50 kDa are difficult to evaluate by solution-state NMR because slow molecular tumbling leads to low detecting sensitivity.

Increasingly powerful protein structure modeling software continues to be released as improvements are made to available computational power (for example, GPUs with significantly greater processing capability) and methods improve. Recently, the deep neural network algorithm of AlphaFold has displayed significant improvements over previously-standard homology and *ab-initio* methods—in one blind test, AlphaFold exhibited modeling accuracy of the protein backbone to 0.96 Å root mean squared deviation (rmsd), compared to 2.80 Å rmsd of the prior best performing model.[27] An important advantage of modeling protein structure is that it avoids labor and the challenges of sample preparation and data collection, evidenced by modeled coordinates for 98.5% proteins in the human proteome compared to the less than 10% that have been found experimentally.[27] However, current limitations of this algorithm, such as predicting the relative positions of disordered protein domains as well as those linked by short and flexible amino acid chains, mean that only 58% of the residues in the

human proteome are modeled with high confidence. Importantly, the varied advantages and challenges of modeling and experimental methods mean that both techniques can be used symbiotically to solve future questions in structural biology.

Similar to computational modeling, Cryo-EM has improved significantly in recent years due to improvements in computational methods, but also due to the invention of new sample preparation techniques and technologies such as direct electron detectors. These developments have been named the "resolution revolution" and have spurred an increase in published cryo-EM maps, even surpassing those published using X-ray crystallography and NMR during the same time period.[28,29] This growth of scientific interest in cryo-EM coincided with leaps in the quality of published cryo-EM protein maps, reconstructing 3D maps of proteins with near 1.2 Å resolution that enable the positions of individual atoms to be determined by single-particle electron microscopy for the first time.[30,31] Scattering data for these analyses is collected as micrographs which, at high quality, typically contain many homogenous particles. Algorithms select and center these particles within a defined frame so that signal from thousands of alike particles can be averaged to produce higher resolution classifications. Because protein molecules may be oriented in multiple directions, analyses sort similarly-oriented particles together so that the averaging process constructively results in higher resolution rather than averaging out to nothing. This is done repeatedly in series and each time the scattering data of particles in poorly resolved two-dimensional (2D) classifications is removed from the overall data set. These poor classifications are likely due to low quality scattering data resulting from aggregated proteins and other impurities that were improperly selected in the sample. A similar process is repeated to take this data from two to three dimensions, reconstructing a 3D electron density map from the cleaned high quality

electron scattering data that can be fit to specific orientations of amino acid residues (using the amino acid sequence of the protein) to produce a high-resolution structure.

However, structure-determination via cryo-EM is limited to large proteins because small proteins (less than 100 kDa) often lack prominent features that can be used at low resolution early in the refinement process to center and align the particles.[32] Roughly 50% of all known proteins are smaller than 50 kDa, including many that are medically relevant, highlighting the importance to make progress against this restriction. Methods being researched to address this limitation include (1) the use of micrograph-contrast-increasing phase plates, and (2) attaching proteins to larger and more easily identifiable structures (in a way that does not disturb the protein's structure) which has resulted in relatively modest resolution structural maps approaching 3 Å, for 23 kDa and 52 kDa proteins respectively.[32,33] Another approach utilizes the different length-scales, complementary protein size constraints, and varied types of structural information gained via cryo-EM and NMR to achieve protein structure maps currently unobtainable by each methods individually. A 4.1 Å resolution cryo-EM map of the 468 kDa protein TET2 was complemented by secondary structure information (H-bonding in the protein polypeptide backbone) of smaller sub-units of TET2 probed by solution-state NMR, to achieve sub-1 Å resolution structure determination at the peptide backbone.[24] This represents a symbiotic relationship between these collaborative techniques, which when also combined with the different advantages of X-ray crystallography and computational modeling may result in continued significant improvements in structural biology.

4.3 Materials and Methods

Expression and purification of wild-type proteorhodopsin

Wild-type proteorhodopsin (WT PR) was cloned into a pET26b (+) vector (Novagen) as described previously.[17] For expression, 10 mL cultures of BL21(DE3) *E. coli* (Thermo Fisher), transformed with the above plasmid, were made in LB broth with 50 µg/mL kanamycin and orbitally shook at 180 rpm for 16 h at 37 ℃. These cultures were diluted into 1 L of LB with 50 µg/mL kanamycin and grown at 37 ℃ with 180 rpm orbital shaking until OD_{600}=0.6, at which point WT PR expression was induced with 1 mM isopropyl *β-D*-1-thiogalactopyranoside (IPTG, Thermo Fisher) and 1 µM *trans*-retinal (Sigma Aldrich). *Trans*-retinal is essential for PR function and the cells cannot produce it on their own. After 18 h, each liter of cell culture was spun down at 5000 rcf, re-suspended in 30 mL of 50 mM K_2HPO_4 (Sigma Aldrich) and 150 mM KCl (Sigma Aldrich) (PR buffer) at pH 8.7, and then lysed for 1 h with incubation in lysis buffer (20 mg/mL lysozyme, DNAse and 20 mM $MgCl_2$). Lysed cells were then centrifuged at 1000 rcf for 10 min to remove large debris in the pellet. The supernatant was then spun down at 10,000 rcf to harvest WT PR-containing membranes in the new pellet. The supernatant was removed and the membranes were flash frozen as pellets in liquid nitrogen and stored at -80℃ until needed for experiments. Purification of WT PR began with homogenization of the membrane pellet in 2 wt% *n*-dodecyl-*β-D*-maltoside (DDM, Anatrace) PR buffer with a glass tissue grinder, and then mixed for 1 h. The homogenized solution was spun down at 100,000 rcf and the supernatant collected to obtain WT PR in DDM micellar solution. Next, WT PR was further purified using a 5 mL Ni-NTA resin column (ThermoFisher) with a binding buffer (0.01 wt% DDM and 30 mM imidazole) and eluting buffer (0.01 wt% DDM and 500 mM imidazole). High-performance liquid chromatography

was performed with a Sucrose 6 Increase 3.2/300 column equilibrated in PR buffer. Purified WT PR was loaded and 50 µL were aliquots were collected. In between the Ni-NTA resin and Sucrose 6 Increase 3.2/300 columns, WT PR was concentrated to ~4000 µM so that diluted aliquots collected from the HPLC could be loaded directly onto a cryo-EM grid without concentration, which was identified to add impurities to the sample. Protein concentration was determined using the absorbance at 520 nm using an extinction coefficient of 49,000 M^{-1}•cm and a molecular weight of 29,000 g/mol.

Cryo-EM sample preparation and data collection

For grid preparation, copper Quantifoil R2/1 300 grids with a carbon foil were first glow-discharged for 30 s at 25 mA in the residual atmosphere using a GloQube® Plus Glow Discharge System. 2 µL of purified 101 µM WT PR in DDM micelles were subsequently applied and incubated for 10 s at 4 °C and 100 % humidity before blotting for 3 s with a blot force of 0 and plunge frozen into liquid ethane using an FEI Vitrobot MkIV. During the entire freezing process the Vitrobot was covered in aluminum foil and a resting time of 10 s (compared to the ~0.5 s photocycle of WT PR in DDM micelles) prior to blotting was added in order to prevent PR excitation and to limit the range of photocycle conformations in the sample. Micrographs were collected using a Titan Krios operated at 300 kV equipped with a Gatan BioQuantum energy filter operating over a calculated defocus range of -0.2 um to -3.3 um. A K3 detector operating in electron counting mode was used to record 27,398 micrographs at a pixel size of 0.68 $Å^2$ px^{-1} (corresponding to a nominal magnification of 165,000x) over a 4 second exposure at a 15 e px^{-1} s^{-1} flux yielding a total fluence of 60 e px^{-1}, fractioned into 45 dose fractions.

Cryo-EM data analyses

Pre-processing steps were performed with cryoSPARC Live v3.1.0.[34] First, motion-correction and dose-weighting was accomplished using MotionCor2 v2.1.1.[35] Contrast transfer function (CTF) estimates for the motion-corrected micrographs were then calculated with CTFFIND4 v4.1.13.[36] Poor-quality micrographs were discarded. Following several rounds of 2D classification, 67,997 remaining particles were used for 3D classification.

4.4 Results and Discussion

Co-assembly of proteorhodopsin oligomers

The structure-function relationship of the transmembrane protein proteorhodopsin (PR) and its native proton pumping function is highly complex and dependent on the local environment around specific amino acid residues, intramolecular interactions between residues, and intermolecular contacts between protein molecules. Specifically, the pH and ionic strength of the protein-containing solution significantly influence the assembly and function of PR molecules. PR can undergo either of two distinct photocycles, dependent on the protonation state of its D97 residue; at native alkaline pH conditions, the function-dependent D97 residue is deprotonated, and photoactivated PR will transport a proton via a six-step photocycle; however, if the D97 residue is protonated during photoactivation, a five-step photocycle is instead observed that pumps a proton in the opposite direction.[37,38] In addition to the D97 residue, pH influences the protonation state of a collection of amino acid residues with electrically charged side chains, which can lead to a net electric dipole moment across each PR monomer. Positively charged side chains of histidine, arginine, and lysine residues, as well as negatively charged side chains of aspartic acid and glutamic acid residues, contribute to this

electric dipole moment. Significant quantities of the later four residues, with sample-relevant pKa values of approximately 9.04, 8.95, 9.60, and 9.67 respectively, are located at ends of each PR monomer and (under native-like pH 8 conditions) produce a -7 net negative charge at the extracellular side and a +3 net positive charge at the intracellular side of each monomer.

Using cryogenic electron microscopy, a technique that measures electron diffraction patterns through proteins in vitrified water to produce micrographs of the sample, the effect of the electric dipole moment of PR on the protein's co-assembly can be observed (Figure 4.1a). In Figure 4.1, a series of micrographs are presented featuring vitrified solutions of wild-type (WT) PR at pH 8 with varied concentrations of WT PR, buffer salts, and protein-stabilizing DDM surfactant. Figure 4.1a reveals that WT PR in a solution of 1 wt% DDM, 50 mM K_2HPO_4, and 150 mM KCl at pH 8 will co-assemble in relatively long head-to-tail structures based on each oligomer's electric dipole moment. The distribution in number of co-assembled oligomers per structure is varied and likely due to the concentration of PR and specifics of sample preparation such as vortex mixing, time between solution preparation and sample preparation, time between cryo-EM grid blotting and sample vitrification, and the thickness of the vitrified sample. In comparison, a sample under identical conditions except for an additional 100 mM KCl (up to a total of 250 mM KCl) exhibits a distribution of singlets and doublets of WT PR oligomers (Figure 4.1b). The additional buffer salt concentration screens the charges of the charged residues of PR, leading to the greater dispersion of molecules. Interestingly, a significantly greater concentration of 208 μM WT PR in a solution containing just 150 mM KCl is observed with relatively concentrated monodispersed WT PR oligomers (Figure 4.1c) due to a lower 0.3 wt% DDM. This distribution is due to the interactions between DDM and buffer salts, where hydroxides of the maltoside headgroup of

DDM associate with anions in solution, preventing them from screening the charges of PR oligomers. Assuming strong interactions between these surfactant and salt moieties, the 150 mM KCl difference between samples observed in Figure 4.1b and 5.1c would associate with 0.714 wt% DDM, similar to the difference between samples. This ratio of associating DDM and Cl^- anions is observed in the micrograph shown in Figure S4.1a, in which a sample of 104 μM WT PR, 0.8 wt% DDM, 50 mM K_2HPO_4, and 150 mM KCl at pH 8 co-assembles as singlets and doublets of oligomers similar to those observed in Figure 4.1b. This phenomena is advantageous to PR sample preparation because desired homogeneous monodispersed samples can be achieved by removing electron-scattering excess DDM (which would have reduced the contrast of the micrograph) without adding extra salts that can influence intramolecular electrostatics interactions.[39] In Figure 4.1d, a lower concentration 153 μM WT PR sample with 0.27 wt% DDM and 500 mM KCl displays similar monodispersed protein oligomers, showing that there are not significant improvements made in sample preparation through increasing buffer salt concentrations when excess DDM is already removed. It should be noted that these micrographs are being used to optimize protein homogeneity and dispersion in sample preparation, and not themselves used for high resolution structure determination analyses, meaning that the differences in contrast and resolution due to using different acquisition instruments is not significant. From these results we observe trends in the co-assembly of PR oligomers as a function of solution composition that inform future experiments. For example, the co-assembly of anisotropic films designed to harness the functions of membrane proteins require orientationally-aligned proteins similar to the proteins observed in Figure 4.1a. However, conducting structure determination analyses on these head-to-tail assemblies of proteins is challenging because the electron scattering signals from each

oligomer may be conflated with adjacent proteins, thereby disrupting the important particle-centering process. Therefore, we conclude that samples made for high resolution structure determination experiments via cryo-EM should contain highly concentrated and homogeneous monodispersed molecules that can be easily identified during analysis.

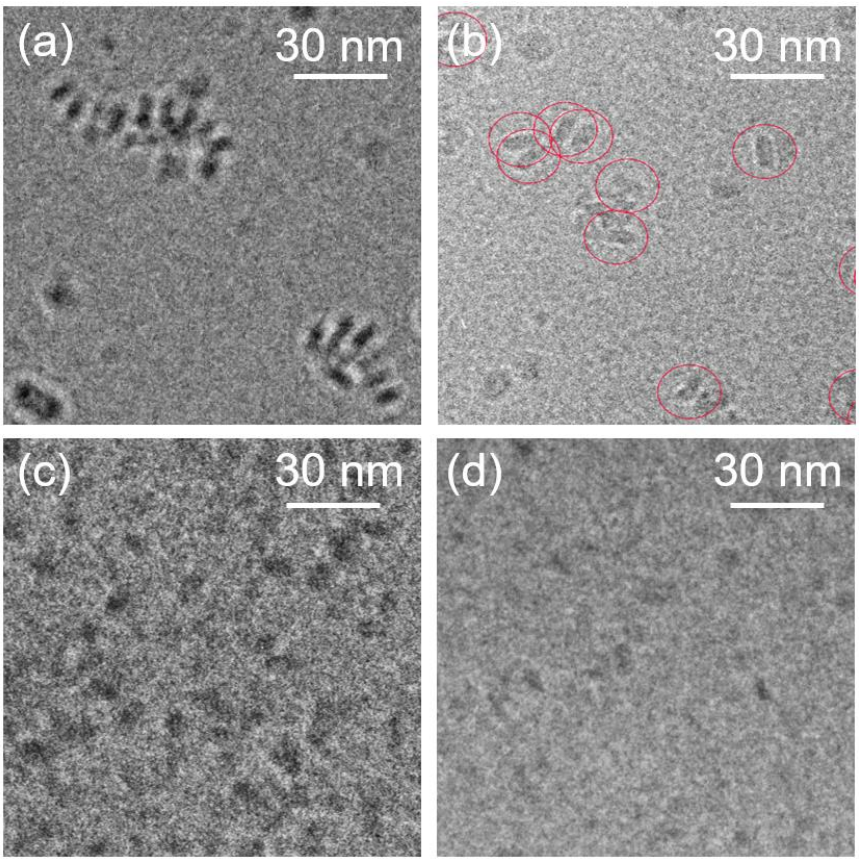

Figure 4.1. Cryo-electron micrographs of wild-type proteorhodopsin in vitrified solutions of *n*-dodecyl-β-D-maltopyranoside (DDM), K_2HPO_4, and KCl: **(a)** 75 μM WT PR, 1 wt% DDM, 50 mM K_2HPO_4, and 150 mM KCl, **(b)** 75 μM WT PR, 1 wt% DDM, 50 mM K_2HPO_4, and 250 mM KCl, **(c)** 208 μM WT PR, 0.3 wt% DDM, 50 mM K_2HPO_4, and 150 mM KCl, and **(d)** 153 μM WT PR, 0.27 wt% DDM, 50 mM K_2HPO_4, and 500 mM KCl. Micrographs were collected on different instruments, leading to significant differences in micrograph contrast and resolution: (a) Talos Arctica microscope operated at 200 kV equipped with a Falcon III, Gatan K2 camera, (b) Titan Krios microscope operated at 300 kV equipped with a Gatan BioQuantum energy filter and K3 detector, and (c-d) were collected on a FEI Tecnai G2 Sphera microscope operated at 200 kV equipped with a K2 detector.

Optimization of the solubilization protocol for purifying proteorhodopsin

High resolution structure determination benefits from a number of characteristics achievable through proper sample preparation including highly concentrated monodispersed particles, minimal electron scattering of non-protein solution leading to high contrast micrographs, varied orientations of particles, and most importantly a homogeneous sample. This is because the methods utilized to convert relatively low-resolution two-dimensional micrographs into high-resolution 2D and 3D protein structures fundamentally sort and average signals from similar particles until they converge into high resolution structures. Previous WT PR expression and purification protocols used at UCSB were not optimized for these properties and so structure determination was not possible. Figure S4.2a shows a micrograph collected from these old samples, revealing inhomogeneity between electric dipole co-assembled oligomers, larger protein aggregates, broken *E. coli* membranes, and DNA, which together lead to poor analyses. Figure S4.2b-c reveal limited resolution of 2D and 3D classifications obtained from this raw data. New protocols were generated through experiments such as those featured in Figure 4.1, which improve sample composition to produce concentrated monodispersed proteins while reducing detrimental electron scattering of empty surfactant micelles. While sample orientation in the thin vitrified ice samples is not well understood and could not be improved, even limited isotropy of particles is enough to obtain high-resolution structures when other factors are optimized.

During optimization of the WT PR expression and purification protocols, adequate solubilization of the protein into micellar solutions from freeze-fracture *E. coli* membranes was identified as significant in producing a homogeneous sample. Figure 4.2 shows the effects of the solubilization protocol with high-performance liquid chromatography (HPLC) and

cryo-EM microscopy. In Figure 4.2a, based on estimated protocols from other proteins, freeze-fractured WT PR-containing *E. coli* cell membranes were solubilized in a 1.2 wt% DDM solution for 30 min, followed by a centrifugal spin down at 30,000 rcf for 1 h to separate out broken membranes. The HPLC chromatogram in Figure 4.2a reveals that mixing was stopped before the sample was properly solubilized based on the broad distribution of absorbance observed across 1.2-2.0 mL of the eluted sample, while large impurities such as protein aggregates and broken cell membranes (indicative of insufficient centrifugal separation) is evidenced by the strong absorbance signal from 0.0-1.2 mL. Poor solubilization can be seen in the cryo-EM micrograph of Figure 4.2a as a distribution of membranes longer than 15 nm (the approximate width of a PR-containing DDM micelle), while the large PR aggregates observed should be pelleted out of solution during centrifugation. The effects of proper solubilization and separation of PR from *E. coli* membranes is shown through HPLC and cryo-EM in Figure 4.2b which features the purified results of WT PR-containing membranes mixing in a 1.2 wt% DDM solution for 1 h and subsequently centrifuged at 100,000 rcf for 1 h. The chromatograph (left) displays a single significant narrow peak centered at 1.65 mL, corresponding to the desired WT PR oligomer, and minimal signal intensities at low and high quantities volumes eluted where impurities would be represented. These optimizations result in a concentrated sample of homogeneous monodispersed WT PR oligomers in DDM micelles that display high contrast and appear suitable for high resolutions structure determination measurements.

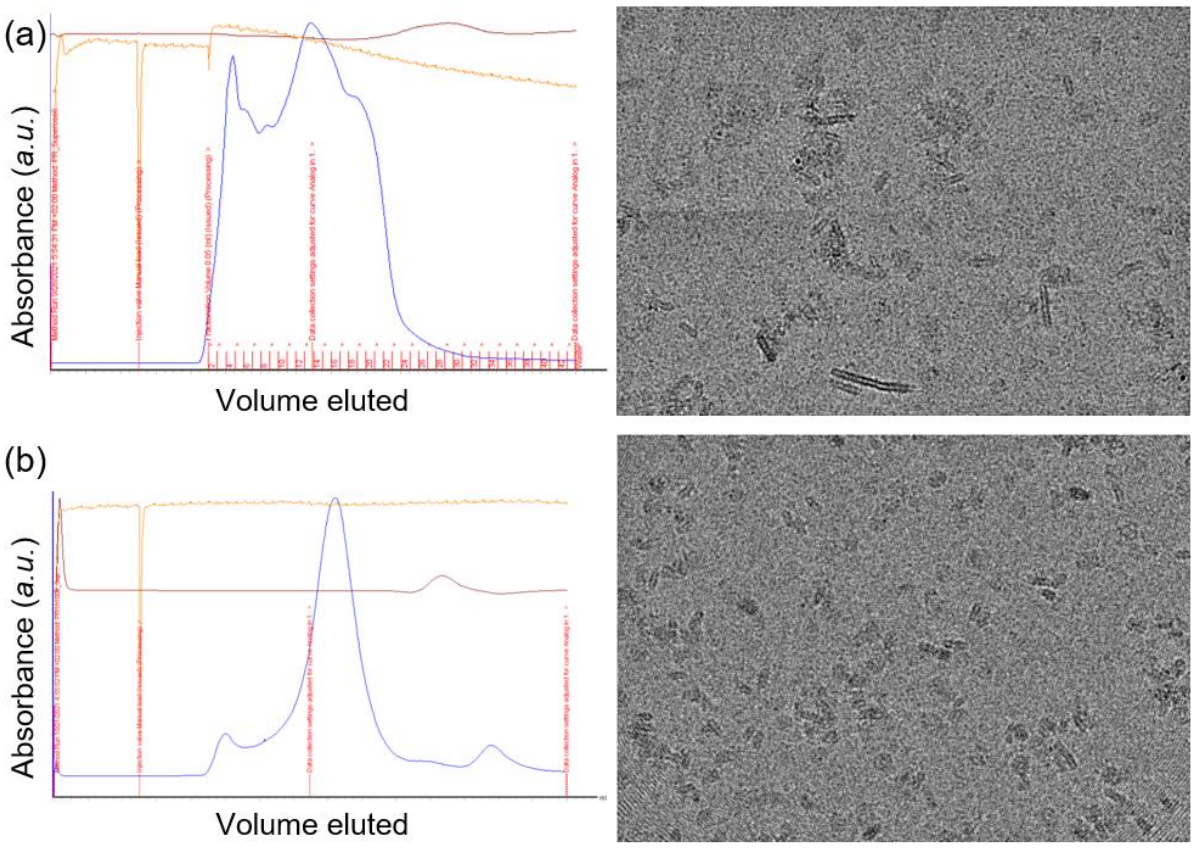

Figure 4.2. During expression and purification, wild-type proteorhodopsin is solubilized into DDM micelles from broken cell membranes, followed by a separation by centrifugal separation. These two steps have a significant effect on the final sample as shown by (left) high-performance liquid chromatography and (right) cryogenic electron microscopy for **(a)** 30 min solubilization and 30,000 rcf spin down for 1 h, and **(b)** 1 h solubilization and 100,000 rcf spin down for 1 h.

Cryo-EM analyses of homogeneous monodispersed proteorhodopsin oligomers

Concentrated and homogeneous monodispersed proteins enable structural analyses with potentially high resolution. Simply put, these analyses procedurally identify single oligomers within each micrograph, center them within a frame with uniform dimensions, and average the signal from thousands of these frames to create 2D classifications. This enables much greater resolution than would be possible from the data a single protein (which quickly

becomes damaged by the high-energy electrons passing through the sample). Since there are different orientations of the protein within these micrographs, they must be sorted appropriately, otherwise, signal values from different amino acids of the protein will average out and structural information will be lost. In Figure 4.3, 2D classifications with high contrast and resolution reveal a clear pentameric oligomeric structure for WT PR in DDM micelles. This is significant because other experiments intended to test this were inconclusive regarding possible distributions of pentameric or hexameric oligomers.[11] Figure 4.3a shows the top down orientations of WT PR for as (left) well-resolved 2D classifications next to (right) a published 3D model in a different surfactant environment (PDB ID: 7B03).[19] The assembly of this oligomer is very clear in the 2D electron diffraction classification: five closely-packed monomers each containing seven well-resolved signals that correspond to individual α-helices (the most electron dense regions), surrounded by a large ~15 nm diameter DDM micelle (mild electron scattering). These transitory α-helices span the width of the DDM micelle as seen in the side view 2D classification (Figure 4.3b). While these results confirm a pentameric structure of WT PR in DDM micelles, they do not exclude potential hexamers at lower concentrations that could not be well resolved by the algorithms used in cryo-EM analyses. In fact, early processing showed evidence of WT PR hexamers with poorly resolved 2D classifications that disappeared after further refining of the data set (Figure S4.4).

These results are similar to the only published structure of wild-type green-light absorbing proteorhodopsin, which models PR as a pentamer in a cymal-4 surfactant micelle.[19] However, unlike that work, the data collected on PR in DDM micelles does not converge to a well-resolved 3D structure despite similar quality micrographs and 2D classifications. We hypothesize that this is due to small movements of protein monomers or individual α-helices

within large DDM micelles of the PR+DDM sample. Since analyses rely on averaging of thousands of particles, even limited local heterogeneities can make the data difficult or impossible to refine. Evidence of this can be inferred from comparisons with the published data of Hirschi et al., which reveals a significantly smaller micelle due to the shorter cymal-4 surfactant used.[19] (Cymal-4 is a maltoside connected to a cyclohexane group by a 4-carbon alkyl chain.) Additionally, electron scattering signals are observed between monomers of the structure that suggests immobile or (consistently exchanging) surfactants appear in the same locations across protein oligomers. This hypothesis is supported by the bent protein and cymal-4 micelle of the resolved 3D structure, which represents rigidity in the sample. For an anisotropic transmembrane transport protein such as PR, we would expect a flat orientation of the monomers of each WT PR oligomer (such as the 2D classification of WT PR in DDM micelles shown in Figure 4.3) because the curvature of a cell is only relevant on much larger-length scales. We hypothesize that the increased sample rigidity and the smaller micelle of cymal-4 prevent local movement of proteorhodopsin and enables a high resolution 3D structure to be resolved.

Further experiments are needed to support these findings, the results of which could inform future sample preparation techniques of transmembrane proteins. The selection of which host environment is most native-like in which to study these proteins is frequently debated in literature and highly relevant in both structure-determination and biochemistry applications.[40] Hopefully, these results lead to a more informed selection of stabilizing surfactants to either promote structure-determination via immobilizing surfactants or native-like studies via cryo-EM analysis of the host-environment. These analytical tools have the

potential to improve understanding of membrane protein host environments and the structure-function relationships of transmembrane proteins.

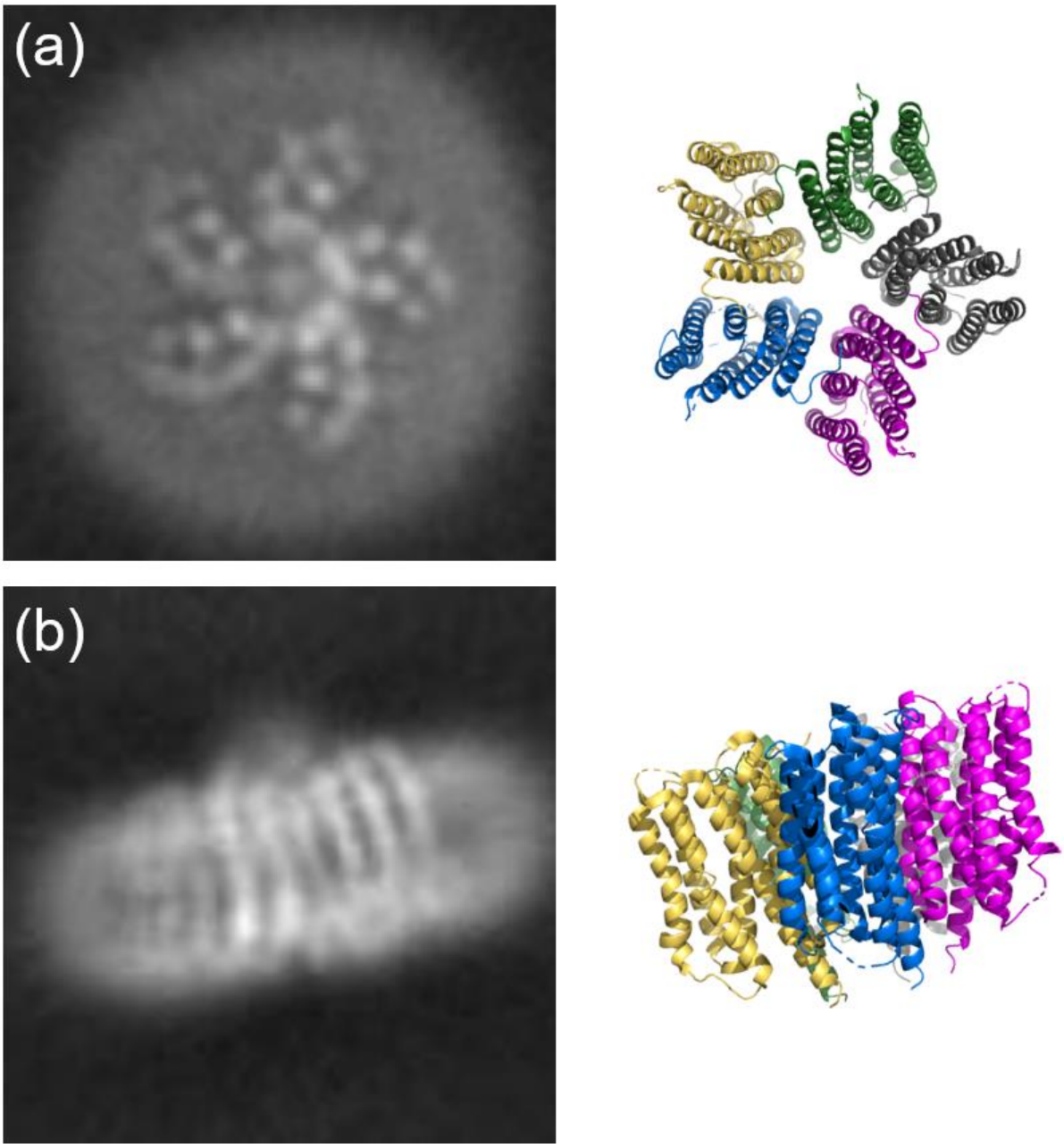

Figure 4.3. (left) Cryo-EM 2D classifications of pentameric wild-type proteorhodopsin in DDM micelles and (right) 3D protein structures (PDB ID: 7B03)[19] from the **(a)** top view and **(b)** side view.

4.5 Conclusions

The confirmation of a pentameric structure of wild-type proteorhodopsin (WT PR) in DDM micelles represents an important result that gives greater context to ambiguous results from size exclusion chromatography and protein gels.[11] Although high resolution structure determination was not possible with this sample, the data collected helps to elucidate the effects of stabilizing surfactants on local dynamics of the protein by comparing it with other published structures within the context of what enables cryo-EM analyses to converge. Follow-up experiments may build on these results to optimize sample preparation and identify important host-structure and structure-function relationships of WT PR. Through methods like these we see that cryogenic electron microscopy has been shown to be an effective tool for high-resolution structure determination, and also that the collection and analysis of electron scattering data can be used to inform research outside of the more common pursuits of structural biology. The assembly of proteorhodopsin by its electric dipole moment, and its dependence on the concentration of surfactant and buffer salts, has important implications for the design of protein-incorporating host materials and the harnessing of protein function in potential devices. This is also true for the optimization of purified homogeneous protein samples, as even minimal impurities can impede the complex co-assembly of well-ordered materials. These results can be supported and enhanced through combination with direct proton transport measurements, or photocycle analysis techniques such as time-resolved UV-visible light spectroscopy. Gaining improved understanding of highly complex structure-function relationships of membrane proteins and non-native host materials is an important step in harnessing their diverse functions. These results begin to elucidate the structure-function

relationships of WT PR stabilized within DDM micelles, informing experiments on similar systems such as mesostructured silica host materials.

4.6 Future Directions

Extensions of the results presented in this chapter could make significant progress towards understanding the structure-function relationships of membrane proteins and how host-environments can be optimized to promote native-like protein function. In this section, I suggest future paths of investigation to continue and build on this research. Specifically, interrogating the contrasts and similarities between cryo-EM micrographs and 2D classifications of PR in DDM micelles with published data of PR in cymal-4 micelles raises useful and productive questions regarding how host-micelles may interact differently with membrane proteins. Electron scattering data suggests that may restrict movement of cymal-4, facilitating high-resolution structure-determination, but also potentially influencing function; and if so, is this primarily a result of the size of the host micelle or because of the cyclohexane group at the end of the alkyl chain. Hirschi et al. conducted photoactivity assays of WT PR and mutants in cymal-4 micelles, however, these results are normalized to the photoactivity of WT PR, which itself should be corroborated. Directly measuring proton transport from WT PR in varied host environments, such as DDM and cymal-4 micelles, via the observed change of charge across a membrane or by using pH-sensitive electrodes would provide a more rigorous test of PR function.[38] A symbiotic experiment would then evaluate the effects of host environment on the photocycle of WT PR, measuring the build-up and decay of specific photocycle intermediate with time-resolved UV-visible light spectroscopy (UV-vis). I have previously used this method in conjunction with global fit analyses to compare the photocycle

kinetics of PR in different, surfactant, lipid, and silica host environments.[11,18] These results have helped me synthesize new compositions of robust solid protein-host materials that may be further improved by utilizing cryo-EM and tying in the new structure-function experiments I suggest here. If successful, this combination of cryo-EM, time-resolved UV-vis, and direct proton transport analyses could inform the sample preparation of future cryo-EM experiments and provide a new screening method for the design of new materials.

One class of materials recently gaining discussion as a native-like host for biochemistry and structural biology applications are nanodiscs. Nanodiscs primarily utilize either protein or polymer belts to hold together a section of a lipid bilayer that contains a protein. The concept behind the native-like properties of these host materials are that you can isolate individual membrane protein monomers or oligomers in lipid bilayers either from synthetically formed liposomes or even straight from *E. coli* membranes.[11,40] However, despite native-like claims, I have observed significant changes in both the pKa of the function dependent D97 residue and photocycle of PR monomer in styrene-maleic acid (SMA) lipid nanodiscs (as discussed in Chapter 2). I hypothesize that these changes are due to the negative charge of SMA which allows it to penetrate lipid bilayers and remove membrane proteins. Cryo-EM analyses of oligomeric WT PR stabilized within these nanodiscs may reveal if structural differences in the protein (as a result of the different host) also contribute to the observed changes in function. Local structural differences around the affected D97 residue are of interest; additionally, larger scale interactions can be investigated via the comparison of the oligomeric structure of WT PR-containing nanodiscs with the primarily pentameric structure seen in DDM and cymal-4 micelles.

Systematic studies of intra-oligomeric interactions and their effect on proteorhodopsin function support and build upon previous work that has been influential in directing the design of new materials. Based upon the results presented in this chapter, I suggest further investigation of inter-oligomer interactions for PR oligomers in DDM micelles co-assembled due to electric dipole moments. While probing these aligned oligomers through signal averaging cryo-EM analyses, significant intensities of scattered electrons are observed between co-assembled PR oligomers. Scattering data and analyses presented in Figure S4.2 display a representative micrograph of these head-to-tail aligned WT PR doublets as well as 2D and 3D classifications of the processed signals. A similar, but more purified, sample is presented in Figure 4.1b containing 75 μM WT PR, 1 wt% DDM, 50 mM K_2HPO_4, and 250 mM KCl that produces mostly isolated doublets with scattered electrons between mostly single pairs of oligomers. Based on this limited data, we hypothesize that there may be either a salt bridge between oligomers or contacts between loops of each oligomer. To properly probe the interactions between oligomers of WT PR, a concentrated solution of homogeneous doublets is ideal so that analyses can center the analysis frame on these interactions. Hirschi et al. found that the structure of pentameric WT PR in cymal-4 micelles contains a large hydrophilic cavity at the extracellular surface of the protein consistent with the location of the proton release group and a completely blocked off solvent-inaccessible pathway to the proton donor group at the intracellular side of PR.[19] It would be interesting to probe how this may change for both singlets and doublets of WT PR oligomers as it may be influenced by both the different surfactant host environment and electrostatic (or other) interactions between oligomers. In addition, a protruding bump of electron density is observed on a single side of monodispersed WT PR oligomers in DDM, clearly visible in 2D classification shown in Figure 4.3b. This

structural feature may contribute to the interactions observed between oligomers as the observed electron scattering appears in a similar location to the intermolecular protein contacts. These cryo-EM analyses could be supported by parallel functionality measurements such as time-resolved UV-vis where salt concentration can be varied based on the findings from Figure 4.1 to evaluate if interacting oligomers influence the photocycle kinetics of the protein.

Lastly, I would like to suggest future experiments to probe the structures of specific PR photointermediates as it undergoes its photocycle. PR is an active transport transmembrane protein, meaning that it goes through a series of conformational changes necessary to transport a proton. While the function of PR and its photocycle have been closely studied, the structures of these photointermediates are still largely unknown. Cryo-EM analyses enable the probing of these specific structures, but a necessarily homogeneous sample is difficult to prepare because of the short life-cycles of each individual intermediate. Even with a strong (maximally-absorbing) green laser pulse, the sample may contain distributions of multiple photointermediates that would make high-resolution structure determination extremely challenging. Cleaning this scattering data by separating signals from each intermediate would reduce the population of usable proteins in analysis and be computationally expensive. I suggest using the E108Q PR mutant instead, which alters the proton donor E108 residue to extend the photocycle of PR from ~0.5 s to greater than 10 s. This mutation extends the build-up and decay of the *M* photointermediate from milliseconds to seconds, causing it to accumulate to an extent that should enable cryo-EM structure-determination analyses.[41] The *M* intermediate is often used to probe PR functionality because it is only observed in the native-like photocycle of PR when the D97 residue is deprotonated at alkaline conditions, and is not observed when the D97 residue is protonated under acidic conditions upon light excitation.[15]

The *M* intermediate is thought to involve significant structural changes when compared to its intermediate homologue in the similar proton transport protein bacteriorhodopsin.[42] Using a Vitrobot with a dark sample preparation area (to ensure molecules start in the same dark state before light-excitation) with E108Q PR should enable the preparation of the a homogeneous sample of the *M* photointermediate conducive for cryo-EM analyses and high-resolution structure determination. Importantly, the *M* intermediate is also spectrally distinct, and is significantly blue-shifted (from ~520 nm of the equilibrium state to ~410 nm) due to deprotonation of the retinal Schiff base of PR.[16] This enables time-resolved UV-vis experiments to directly observe the buildup and decay of this state. Combining these experiments probes an important photointermediate of proteorhodopsin, establishing key links between protein structure and proton transport, and potentially informing future understanding of the structure-function relationships of membrane proteins.

4.7 References

(1) Overington, J. P.; Al-Lazikani, B.; Hopkins, A. L. How Many Drug Targets Are There? *Nat Rev Drug Discov* **2006**, *5* (12), 993–996. https://doi.org/10.1038/nrd2199.

(2) Newport, T. D.; Sansom, M. S. P.; Stansfeld, P. J. The MemProtMD Database: A Resource for Membrane-Embedded Protein Structures and Their Lipid Interactions. *Nucleic Acids Research* **2019**, *47* (D1), D390–D397. https://doi.org/10.1093/nar/gky1047.

(3) Levental, I.; Lyman, E. Regulation of Membrane Protein Structure and Function by Their Lipid Nano-Environment. *Nat Rev Mol Cell Biol* **2023**, *24* (2), 107–122. https://doi.org/10.1038/s41580-022-00524-4.

(4) Shieh, F.-K.; Wang, S.-C.; Yen, C.-I.; Wu, C.-C.; Dutta, S.; Chou, L.-Y.; Morabito, J. V.; Hu, P.; Hsu, M.-H.; Wu, K. C.-W.; Tsung, C.-K. Imparting Functionality to Biocatalysts via Embedding Enzymes into Nanoporous Materials by a *de Novo* Approach: Size-Selective Sheltering of Catalase in Metal–Organic Framework Microcrystals. *J. Am. Chem. Soc.* **2015**, *137* (13), 4276–4279. https://doi.org/10.1021/ja513058h.

(5) Swift, B. J. F.; Shadish, J. A.; DeForest, C. A.; Baneyx, F. Streamlined Synthesis and Assembly of a Hybrid Sensing Architecture with Solid Binding Proteins and Click Chemistry. *J. Am. Chem. Soc.* **2017**, *139* (11), 3958–3961. https://doi.org/10.1021/jacs.7b00519.

(6) Bamann, C.; Bamberg, E.; Wachtveitl, J.; Glaubitz, C. Proteorhodopsin. *Biochimica et Biophysica Acta (BBA) - Bioenergetics* **2014**, *1837* (5), 614–625. https://doi.org/10.1016/j.bbabio.2013.09.010.

(7) Fane, A. G.; Wang, R.; Hu, M. X. Synthetic Membranes for Water Purification: Status and Future. *Angew. Chem. Int. Ed.* **2015**, *54* (11), 3368–3386. https://doi.org/10.1002/anie.201409783.

(8) Wang, M.; Wang, Z.; Wang, X.; Wang, S.; Ding, W.; Gao, C. Layer-by-Layer Assembly of Aquaporin Z-Incorporated Biomimetic Membranes for Water Purification. *Environ. Sci. Technol.* **2015**, *49* (6), 3761–3768. https://doi.org/10.1021/es5056337.

(9) Berman, H. M. The Protein Data Bank. *Nucleic Acids Research* **2000**, *28* (1), 235–242. https://doi.org/10.1093/nar/28.1.235.

(10) Kroeck, K. G.; Qiu, W.; Catalano, C.; Trinh, T. K. H.; Guo, Y. Native Cell Membrane Nanoparticles System for Membrane Protein-Protein Interaction Analysis. *JoVE* **2020**, No. 161, 61298. https://doi.org/10.3791/61298.

(11) Han, C.-T.; Nguyen, K. D. Q.; Berkow, M. W.; Hussain, S.; Kiani, A.; Kinnebrew, M.; Idso, M. N.; Baxter, N.; Chang, E.; Aye, E.; Winslow, E.; Rahman, M.; Seppälä, S.; O'Malley, M. A.; Chmelka, B. F.; Mertz, B.; Han, S. Lipid Membrane Mimetics and

Oligomerization Tune Functional Properties of Proteorhodopsin. *Biophysical Journal* **2023**, *122* (1), 168–179. https://doi.org/10.1016/j.bpj.2022.11.012.

(12) Han, C.-T.; Song, J.; Chan, T.; Pruett, C.; Han, S. Electrostatic Environment of Proteorhodopsin Affects the PKa of Its Buried Primary Proton Acceptor. *Biophysical Journal* **2020**, *118* (8), 1838–1849. https://doi.org/10.1016/j.bpj.2020.02.027.

(13) Martens, C.; Shekhar, M.; Lau, A. M.; Tajkhorshid, E.; Politis, A. Integrating Hydrogen–Deuterium Exchange Mass Spectrometry with Molecular Dynamics Simulations to Probe Lipid-Modulated Conformational Changes in Membrane Proteins. *Nat Protoc* **2019**, *14* (11), 3183–3204. https://doi.org/10.1038/s41596-019-0219-6.

(14) Hossain, K. R.; Clarke, R. J. General and Specific Interactions of the Phospholipid Bilayer with P-Type ATPases. *Biophys Rev* **2019**, *11* (3), 353–364. https://doi.org/10.1007/s12551-019-00533-2.

(15) Lakatos, M.; Lanyi, J. K.; Szakács, J.; Váró, G. The Photochemical Reaction Cycle of Proteorhodopsin at Low PH. *Biophysical Journal* **2003**, *84* (5), 3252–3256. https://doi.org/10.1016/S0006-3495(03)70049-6.

(16) Hussain, S.; Kinnebrew, M.; Schonenbach, N. S.; Aye, E.; Han, S. Functional Consequences of the Oligomeric Assembly of Proteorhodopsin. *Journal of Molecular Biology* **2015**, *427* (6), 1278–1290. https://doi.org/10.1016/j.jmb.2015.01.004.

(17) Han, C.-T.; Nguyen, K. D. Q.; Berkow, M. W.; Hussain, S.; Kiani, A.; Kinnebrew, M.; Idso, M. N.; Baxter, N.; Chang, E.; Aye, E.; Winslow, E.; Rahman, M.; Seppälä, S.; O'Malley, M. A.; Chmelka, B. F.; Mertz, B.; Han, S. Lipid Membrane Mimetics and Oligomerization Tune Functional Properties of Proteorhodopsin. *Biophysical Journal* **2023**, *122* (1), 168–179. https://doi.org/10.1016/j.bpj.2022.11.012.

(18) Berkow, M. W.; Gwak, H.; Idso, M. N.; Schmithorst, M. B.; Rhodes, B.; Price, B.; Gianola, D. S.; Han, S.; Chmelka, B. F. Co-Assembly of Functionally-Active Proteorhodopsin Membrane Protein Molecules in Mesostructured Silica-Surfactant Films. *Chemistry of Materials* **2023**, under review.

(19) Hirschi, S.; Kalbermatter, D.; Ucurum, Z.; Lemmin, T.; Fotiadis, D. Cryo-EM Structure and Dynamics of the Green-Light Absorbing Proteorhodopsin. *Nat Commun* **2021**, *12* (1), 4107. https://doi.org/10.1038/s41467-021-24429-6.

(20) Reckel, S.; Gottstein, D.; Stehle, J.; Löhr, F.; Verhoefen, M.-K.; Takeda, M.; Silvers, R.; Kainosho, M.; Glaubitz, C.; Wachtveitl, J.; Bernhard, F.; Schwalbe, H.; Güntert, P.; Dötsch, V. Solution NMR Structure of Proteorhodopsin. *Angew. Chem. Int. Ed.* **2011**, *50* (50), 11942–11946. https://doi.org/10.1002/anie.201105648.

(21) Ran, T.; Ozorowski, G.; Gao, Y.; Sineshchekov, O. A.; Wang, W.; Spudich, J. L.; Luecke, H. Cross-Protomer Interaction with the Photoactive Site in Oligomeric Proteorhodopsin Complexes. *Acta Crystallogr D Biol Crystallogr* **2013**, *69* (10), 1965–1980. https://doi.org/10.1107/S0907444913017575.

(22) Morizumi, T.; Ou, W.-L.; Van Eps, N.; Inoue, K.; Kandori, H.; Brown, L. S.; Ernst, O. P. X-Ray Crystallographic Structure and Oligomerization of Gloeobacter Rhodopsin. *Sci Rep* **2019**, *9* (1), 11283. https://doi.org/10.1038/s41598-019-47445-5.

(23) Schmidt, A.; Teeter, M.; Weckert, E.; Lamzin, V. S. Crystal Structure of Small Protein Crambin at 0.48 Å Resolution. *Acta Crystallogr F Struct Biol Cryst Commun* **2011**, *67* (4), 424–428. https://doi.org/10.1107/S1744309110052607.

(24) Gauto, D. F.; Estrozi, L. F.; Schwieters, C. D.; Effantin, G.; Macek, P.; Sounier, R.; Sivertsen, A. C.; Schmidt, E.; Kerfah, R.; Mas, G.; Colletier, J.-P.; Güntert, P.; Favier, A.; Schoehn, G.; Schanda, P.; Boisbouvier, J. Integrated NMR and Cryo-EM Atomic-Resolution Structure Determination of a Half-Megadalton Enzyme Complex. *Nat Commun* **2019**, *10* (1), 2697. https://doi.org/10.1038/s41467-019-10490-9.

(25) Tugarinov, V.; Choy, W.-Y.; Orekhov, V. Yu.; Kay, L. E. Solution NMR-Derived Global Fold of a Monomeric 82-KDa Enzyme. *Proc. Natl. Acad. Sci. U.S.A.* **2005**, *102* (3), 622–627. https://doi.org/10.1073/pnas.0407792102.

(26) Foster, M. P.; McElroy, C. A.; Amero, C. D. Solution NMR of Large Molecules and Assemblies. *Biochemistry* **2007**, *46* (2), 331–340. https://doi.org/10.1021/bi0621314.

(27) David, A.; Islam, S.; Tankhilevich, E.; Sternberg, M. J. E. The AlphaFold Database of Protein Structures: A Biologist's Guide. *Journal of Molecular Biology* **2022**, *434* (2), 167336. https://doi.org/10.1016/j.jmb.2021.167336.

(28) Kühlbrandt, W. The Resolution Revolution. *Science* **2014**, *343* (6178), 1443–1444. https://doi.org/10.1126/science.1251652.

(29) Sorzano, C. O. S.; Carazo, J. M. Cryo-Electron Microscopy: The Field of 1,000+ Methods. *Journal of Structural Biology* **2022**, *214* (3), 107861. https://doi.org/10.1016/j.jsb.2022.107861.

(30) Nakane, T.; Kotecha, A.; Sente, A.; McMullan, G.; Masiulis, S.; Brown, P. M. G. E.; Grigoras, I. T.; Malinauskaite, L.; Malinauskas, T.; Miehling, J.; Uchański, T.; Yu, L.; Karia, D.; Pechnikova, E. V.; De Jong, E.; Keizer, J.; Bischoff, M.; McCormack, J.; Tiemeijer, P.; Hardwick, S. W.; Chirgadze, D. Y.; Murshudov, G.; Aricescu, A. R.; Scheres, S. H. W. Single-Particle Cryo-EM at Atomic Resolution. *Nature* **2020**, *587* (7832), 152–156. https://doi.org/10.1038/s41586-020-2829-0.

(31) Yip, K. M.; Fischer, N.; Paknia, E.; Chari, A.; Stark, H. Atomic-Resolution Protein Structure Determination by Cryo-EM. *Nature* **2020**, *587* (7832), 157–161. https://doi.org/10.1038/s41586-020-2833-4.

(32) Wu, X.; Rapoport, T. A. Cryo-EM Structure Determination of Small Proteins by Nanobody-Binding Scaffolds (Legobodies). *Proc. Natl. Acad. Sci. U.S.A.* **2021**, *118* (41), e2115001118. https://doi.org/10.1073/pnas.2115001118.

(33) Fan, X.; Wang, J.; Zhang, X.; Yang, Z.; Zhang, J.-C.; Zhao, L.; Peng, H.-L.; Lei, J.; Wang, H.-W. Single Particle Cryo-EM Reconstruction of 52 KDa Streptavidin at 3.2 Angstrom Resolution. *Nat Commun* **2019**, *10* (1), 2386. https://doi.org/10.1038/s41467-019-10368-w.

(34) Punjani, A.; Zhang, H.; Fleet, D. J. Non-Uniform Refinement: Adaptive Regularization Improves Single-Particle Cryo-EM Reconstruction. *Nat Methods* **2020**, *17* (12), 1214–1221. https://doi.org/10.1038/s41592-020-00990-8.

(35) Zheng, S. Q.; Palovcak, E.; Armache, J.-P.; Verba, K. A.; Cheng, Y.; Agard, D. A. MotionCor2: Anisotropic Correction of Beam-Induced Motion for Improved Cryo-Electron Microscopy. *Nat Methods* **2017**, *14* (4), 331–332. https://doi.org/10.1038/nmeth.4193.

(36) Grant, T.; Rohou, A.; Grigorieff, N. CisTEM, User-Friendly Software for Single-Particle Image Processing. *eLife* **2018**, *7*, e35383. https://doi.org/10.7554/eLife.35383.

(37) Lakatos, M.; Lanyi, J. K.; Szakács, J.; Váró, G. The Photochemical Reaction Cycle of Proteorhodopsin at Low PH. *Biophysical Journal* **2003**, *84* (5), 3252–3256. https://doi.org/10.1016/S0006-3495(03)70049-6.

(38) Bamann, C.; Bamberg, E.; Wachtveitl, J.; Glaubitz, C. Proteorhodopsin. *Biochimica et Biophysica Acta (BBA) - Bioenergetics* **2014**, *1837* (5), 614–625. https://doi.org/10.1016/j.bbabio.2013.09.010.

(39) Han, C.-T.; Song, J.; Chan, T.; Pruett, C.; Han, S. Electrostatic Environment of Proteorhodopsin Affects the PKa of Its Buried Primary Proton Acceptor. *Biophysical Journal* **2020**, *118* (8), 1838–1849. https://doi.org/10.1016/j.bpj.2020.02.027.

(40) Notti, R. Q.; Walz, T. Native-like Environments Afford Novel Mechanistic Insights into Membrane Proteins. *Trends in Biochemical Sciences* **2022**, *47* (7), 561–569. https://doi.org/10.1016/j.tibs.2022.02.008.

(41) Dioumaev, A. K.; Brown, L. S.; Shih, J.; Spudich, E. N.; Spudich, J. L.; Lanyi, J. K. Proton Transfers in the Photochemical Reaction Cycle of Proteorhodopsin. *Biochemistry* **2002**, *41* (17), 5348–5358. https://doi.org/10.1021/bi025563x.

(42) Hirai, T.; Subramaniam, S. Protein Conformational Changes in the Bacteriorhodopsin Photocycle: Comparison of Findings from Electron and X-Ray Crystallographic Analyses. *PLoS ONE* **2009**, *4* (6), e5769. https://doi.org/10.1371/journal.pone.0005769.

4.8 Supporting Information

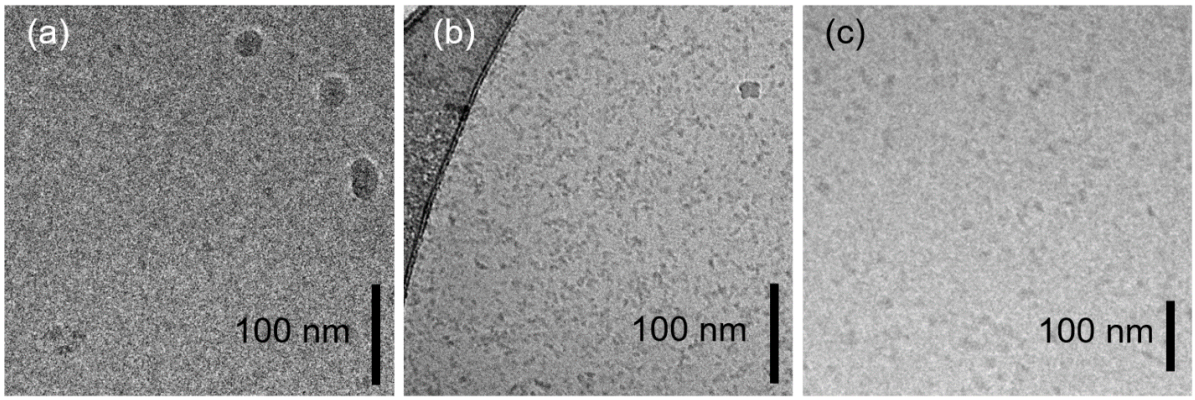

Figure S4.1. Cryo-electron micrographs of wild-type proteorhodopsin in vitrified solutions of *n*-dodecyl-β-D-maltopyranoside (DDM), K_2HPO_4, and KCl: **(a)** 104 μM WT PR, 0.8 wt% DDM, 50 mM K_2HPO_4, and 150 mM KCl, **(b)** 208 μM WT PR, 0.3 wt% DDM, 50 mM K_2HPO_4, and 150 mM KCl, and **(c)** 153 μM WT PR, 0.27 wt% DDM, 50 mM K_2HPO_4, and 500 mM KCl. All micrographs were collected were collected on a FEI Tecnai G2 Sphera microscope operated at 200 kV equipped with a K2 detector.

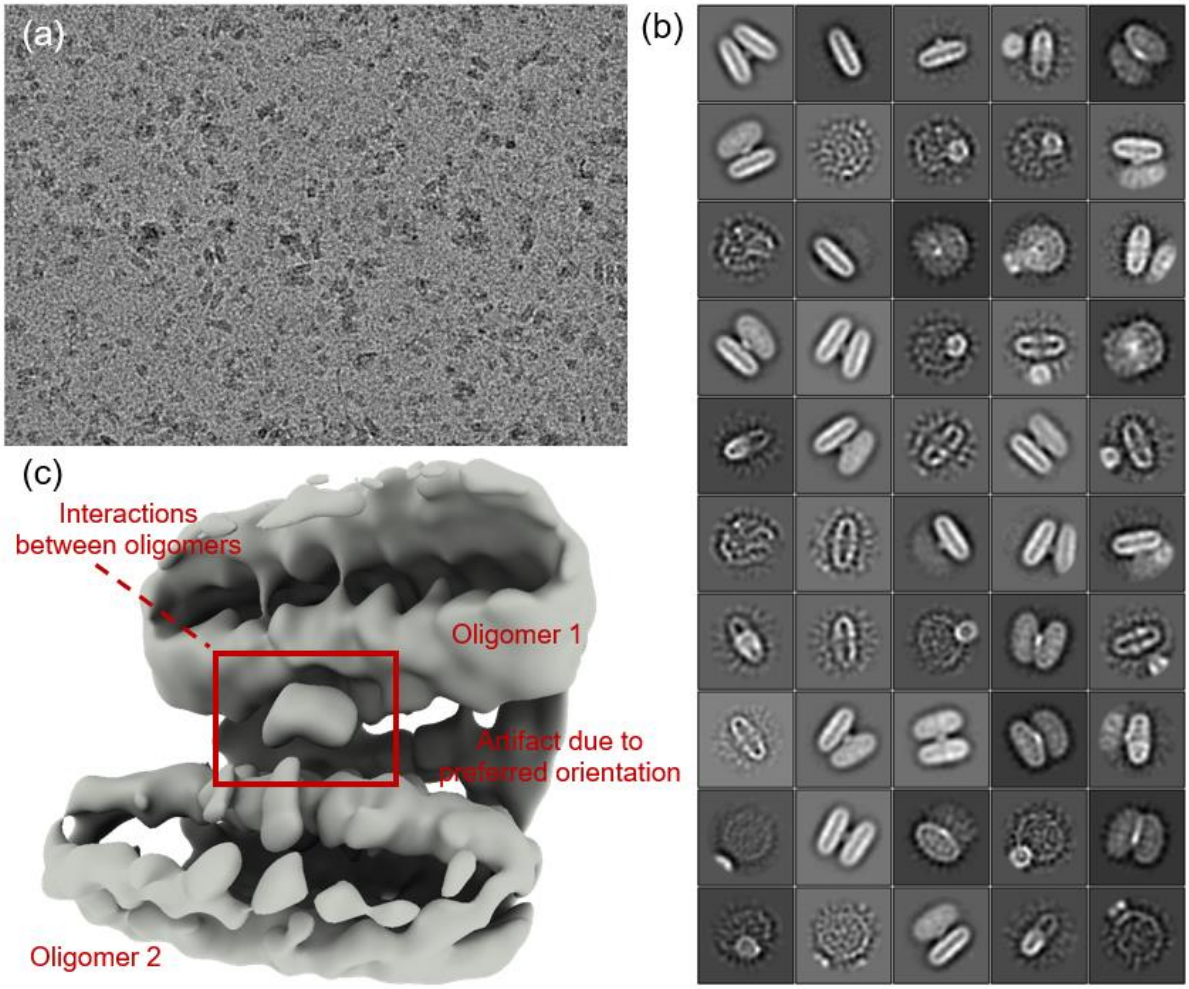

Figure S4.2. Cryo-EM analyses of a 60 µM WT PR, 0.8 wt% DDM, 50 mM K_2HPO_4, 150 mM KCl sample prepared at UCSB, flash-frozen, shipped to the SciLifeLab for measurements. Micrographs were collected on a Titan Krios microscope operated at 300 kV equipped with a Gatan BioQuantum energy filter and K3 detector. **(a)** A representative micrograph from the data set. **(b)** 2D classifications of WT PR from this data set via RELION. **(c)** A low-resolution 3D classification of a doublet of WT PR oligomers revealing interactions between oligomers.

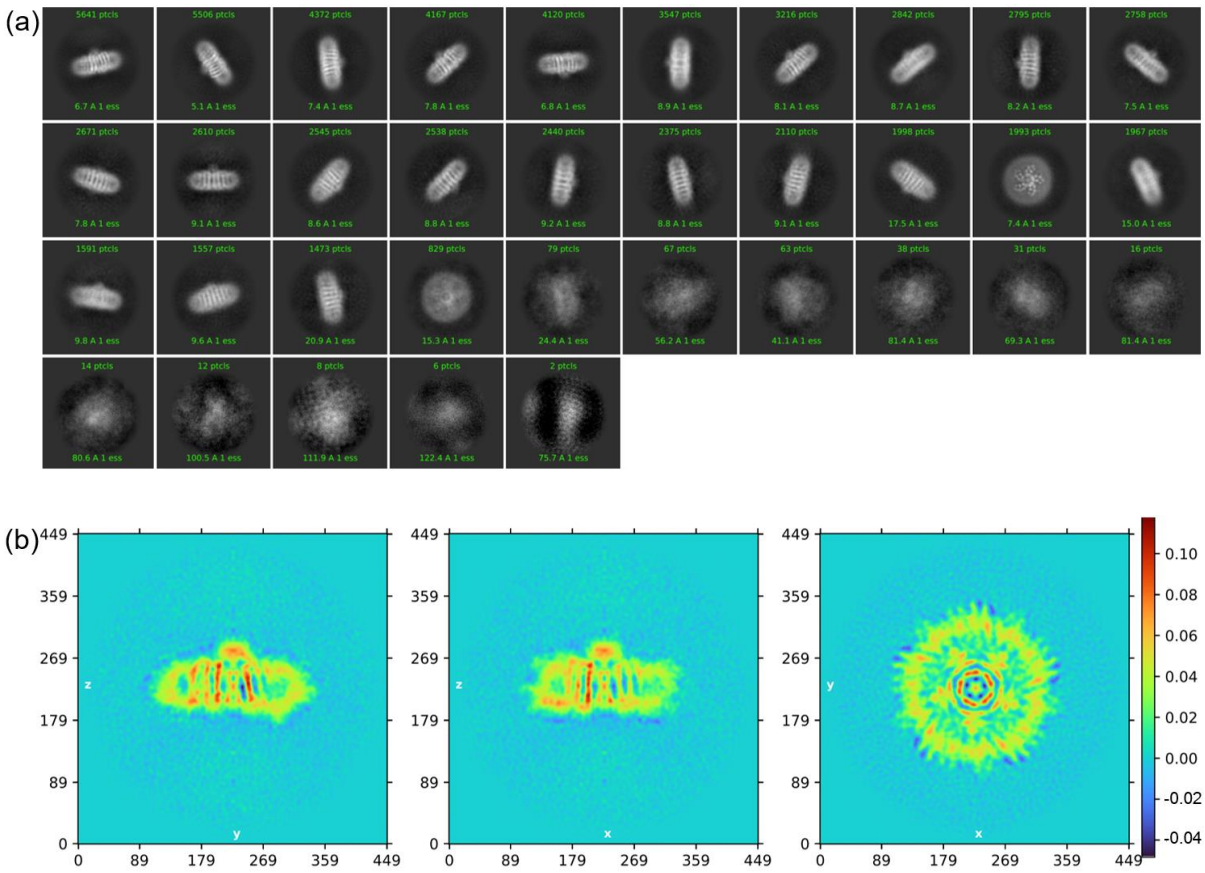

Figure S4.3. Cryo-EM analyses from best wild-type proteorhodopsin sample and micrographs after sample optimization produces **(a)** high-contrast and resolution 2D classifications and **(b)** relatively poorly-resolved 3D classifications.

Figure S4.4. Two-dimensional cryo-EM classification of wild-type proteorhodopsin in DDM micelles that resembles a hexameric structure.

Chapter 5. Orientationally ordered mesostructured silica-surfactant protein-host films

---

This chapter contains sections adapted from a submitted paper that I am a co-author on. My contributions to this paper include writing, editing, and submission to the journal *Advanced Materials*. Some sections of this chapter contain writing adapted from the submitted paper. Any data presented from this paper is labeled throughout the chapter.

Journal submitted to: *Advanced Materials*

Authors: Justin P. Jahnke, Donghun Kim, Doug Wildemuth, Jordi Nolla, Maxwell W. Berkow, Shany Neyshtadt, Tamar Segal-Peretz, Gitti L. Frey, Bradley F. Chmelka

5.1 Abstract

The preparation of nanocomposite or mesostructured materials with high degrees of controllable macroscopic orientational order and anisotropic material properties is difficult to achieve. This is due to the complicated transient and coupled transport, chemical reaction, and surface processes that occur during materials syntheses. By understanding such processes, general criteria are established and used to prepare diverse mesostructured materials with highly aligned channels with uniform nanometer dimensions and controllable directionalities over macroscopic dimensions and thicknesses. This is achieved by using a micropatterned semipermeable poly(dimethylsiloxane) stamp to manage the rates, directions, and surfaces at which self-assembling phases nucleate and the directions that they grow. This, in turn, enables mesostructured surfactant-directed silica composites, including with proteorhodopsin membrane protein guest species, to be prepared with high degrees of hexagonal order, as well as controllable orientational order. Additional challenges, due to working with unstable membrane proteins that are incompatible with many surfactants and synthesis conditions typically used to synthesize well-ordered materials, can be overcome through optimization of film composition and properties of the semipermeable stamp, with consideration of intermolecular interactions and kinetic effects during synthesis. These materials exhibit novel anisotropic and protein stabilizing properties, making them ideal candidates to harness the varied anisotropic functions of membrane proteins for applications in separations, catalysis, and energy conversion.

5.2 Introduction

The inherent anisotropy of hexagonal or lamellar liquid-crystal-like mesophases permits the preparation of orientationally ordered mesostructured materials, although high extents of alignment are challenging to achieve over macroscopic length scales and even harder to control. For example, liquid crystal displays utilize electric fields to control the alignment of regions of liquid crystals, which in conjunction with light polarizers produce images in technical devices such as watches, phones, and televisions.[1] However, this orientational alignment is not preserved outside of the electric field, which is a useful property for image changing displays, but not desired in materials that seek to exploit consistent material properties (electrical, mechanical, or chemical) resulting from anisotropic orientation. Investigations into stable, orientationally ordered mesostructured materials often attempt to impart anisotropic alignment onto an adaptable material before trapping this structure within a more robust environment such as a crosslinked oxide material.[2] Achieving stable orientationally ordered mesostructured materials through this method has been challenging due to the difficulties of managing complex transient phenomena that occur during material syntheses. These include mass transport processes (*e.g.*, diffusive and convective mixing, solvent evaporation), surfactant or block-copolymer self-assembly (*e.g.*, mesophase nucleation and growth), and chemical reaction kinetics (*e.g.*, cross-linking of network-forming inorganic oxides or resins), which are all interdependent. Furthermore, these processes generally need to occur in the sequence listed in order to form mesostructured materials with high degrees of mesoscale order. Additionally, whether and to what extent anisotropic mesophases can be prepared with macroscopic alignment depend on additional interdependent processing variables and conditions, such as film drawing rates, interfacial interactions, solvent

viscosities, concentration gradients, and thermal gradients within the materials. Until now, these have been challenging to balance with respect to the formation of macroscopically aligned inorganic-organic mesophase materials, making it difficult to introduce and control anisotropic properties. As a consequence, the intrinsically anisotropic structures of hexagonal (or lamellar) mesophase materials have been difficult to exploit, in particular in applications[3,4] where directional transport of charges, ions, or molecular species is desirable across semi-permeable barriers. Such applications include heterostructure junctions in photovoltaic devices,[5,6] micro- or nanoelectronics,[7–9] thermoelectric devices,[10,11] ion-exchange membranes,[12,13] and electrocatalysts.[14,15]

Several techniques have been used with limited success to induce macroscopic orientational ordering in inorganic-organic solids. For example, dip-coating of nanostructured inorganic-organic films has yielded aligned domains, albeit with nanochannel alignments that are generally parallel to substrate surfaces.[16,17] The use of specialized substrates during film formation can lead to aligned domains perpendicular to the substrate,[18,19] although the resulting orientational order typically does not persist more than ca. 100 nanometers from the substrate. For certain polymeric materials, modifications of substrate surfaces have been shown to induce partial alignment of hexagonal phases during post-synthesis annealing to yield cylinders that are oriented predominantly perpendicular to the substrate.[20,21] However, relatively modest extents of orientational order have resulted, which have been challenging to control, and the approach is unsuitable for nanocomposite materials with rigid inorganic or highly cross-linked organic frameworks that are not amenable to annealing-induced rearrangements. Strong electric[22,23] or magnetic fields[24,25] have been used to induce orientational order in block copolymer films and in nanostructured inorganic-organic materials. However, applying such

fields is difficult over large areas, and limitations with respect to annealing conditions lead to relatively low degrees of orientational ordering (>50° full-width-half-maximum, FWHM, for magnetic fields).

By understanding the factors that influence nucleation and growth of anisotropic self-assembled domains, the limitations can often be overcome and the extent of macroscopic orientational order improved.[26,27] An example is the orientational ordering that can be induced during surfactant self-assembly at surfaces from lyotropic solutions, due to concentration gradients that arise as a result of solvent removal across an interface. As solvent is removed during syntheses of mesostructured composites, amphiphilic structure-directing agents (SDAs) form micelles, which subsequently self-assemble into close-packed surfactant aggregates as the solvent concentration is reduced by evaporation, diffusion, or other means. Depending on the architecture(s) of the SDA molecules, the relative concentrations of the various solution species, synthesis temperature, and other thermodynamic variables, a variety of liquid-crystal-like mesophases (*e.g.*, lamellar, hexagonal, or cubic) may be formed.[28,29] Of these, the intrinsic anisotropy of the hexagonal phase is of particular interest, because of its uniaxiality and utility for optical device or membrane applications.[30,31] As the solvent is depleted, the hexagonal phase initially forms where the surfactant concentration is highest, specifically at the interface through which the solvent is removed. In conventional casting, spin-coating, or dip-coating processes that synthesize surfactant-directed inorganic or block-copolymeric materials from solution, this occurs at the vapor-solution interface from which evaporation occurs and where self-assembled domains nucleate and grow.[32,33] These coupled processes, however, take place such that the hexagonal-phase domains tend to nucleate with parallel and often transversely isotropic distributions of macroscopic orientational order (if at all). As the solvent continues

to be removed from the interior of the film by diffusion to the evaporation interface, the domains grow perpendicular from the surface into the film and tend to maintain their individual orientations. If cross-linking of the inorganic oxide framework occurs on a comparable timescale, the domains may also adopt a different phase or manifest disorder, as they grow farther from the evaporation surface.[34] Thus, long-range orientational ordering has been challenging to obtain and to control, especially in thick films or monoliths.

5.3 Materials and Methods

Small-angle X-ray scattering

Small-angle X-ray scattering (SAXS) patterns were acquired to establish the degree of mesostructural and orientational ordering in the surfactant-directed silica and titania films. These measurements were conducted with a XENOCS Genix 50W X-ray microsource with Cu K_α radiation (λ = 1.542 Å, voltage 50 keV, current 1 mA) and a MAR345 image plate area detector (located 1.4 m behind the sample) in a transmission geometry. In this geometry, a hexagonal SAXS pattern of 6 spots with equal intensity is indicative of a hexagonal mesophase in which the cylindrical mesochannels are oriented with their axes parallel to the beam and therefore perpendicular to the substrate. By comparison, two SAXS spots of equal intensity that are symmetrically displaced 180^o on opposite sides of the beam center indicate that the cylindrical mesochannels of a hexagonal mesophase are oriented with their axes perpendicular to the beam and therefore are parallel the substrate. Grazing-incidence SAXS (GISAXS), where the X-ray beam is oriented within 5^o of parallel to the substrate, was also used (Figure 5.2) to confirm the high degrees of parallel orientational order in the plane of the substrate.

Transmission Electron Microscopy

Transmission electron microscopy (TEM) measurements were conducted using an FEI Tecnai G2 T20 Sphera microscope operating at 200 keV. TEM samples were prepared using a Gallium Focused ion beam (FIB) integrated in a FEI DB235 Dual-Beam Focus Ion Beam to cut 150 nm thick cross-sectional samples.

Preparation of patterned poly(dimethyl siloxane) stamps

Polydimethylsiloxane (PDMS) is patternable, permeable to many solvents, and relatively hydrophobic, with a Hildebrand solubility parameter of ca. 17 $MPa^{1/2}$.[35] Therefore, the PDMS interacts preferentially with the hydrophobic alkyl or poly(propyleneoxide) segments of the amphiphilic SDAs used here, which have Hildebrand parameters of 14–20 $MPa^{1/2}$ and less favorably with the hydrophilic poly(ethyleneoxide) segments, which have a Hildebrand parameter of ca. 24 $MPa^{1/2}$.[35] The relative orientation of a mesophase domain within a given microchannel depends on the direction of solvent removal and on the relative interactions of the different surfactant blocks at the surface where the mesophase nucleates. The self-assembled phase will nucleate such that the more hydrophobic surfactant blocks can interact maximally with the hydrophobic PDMS surface (within thermodynamic constraints). For the case of a hexagonal mesophase with hydrophobic cylinders, this results in cylindrical aggregates that nucleate with their axes oriented perpendicular to the upper microchannel surface. As the solvent species diffuse through the top of a given microchannel, the surfactant species concentrate and can self-assemble into an array of hexagonally close-packed cylinders that eventually fill the microchannel. For the surfactants and conditions used here, the hydrophobic PDMS surfaces are thus expected to favor interactions with the hydrophobic surfactant moieties of the first hexagonal mesostructured nanocomposite nucleates that form,

allowing alignment of their cylinder axes to be determined by the nucleating surface from which they continue to grow.

Patterned poly(dimethylsiloxane) (PDMS) stamps were prepared from 4-inch silicon [100] wafers (Wafer World Inc., West Palm Beach, Florida, USA) that were patterned by using photolithographic methods. To limit the adhesion of PDMS to the surface of the wafers, the wafers were coated with 1*H*,1*H*,2*H*,2*H*-perfluoro-decyltricholorsilane. The PDMS stamp was cast from a standard commercial curing kit (Sylgard® 184, Ellsworth Adhesives, Wisconsin, USA), with the elastomer mixed with a curing agent in a 10:1 mixture; after mixing it was poured over the patterned silicon master and cured for at least 6 h at 65 °C under vacuum. The thickness of the stamp was determined by the weight of PDMS poured on the silicon wafer and the area of the stamp was established by cutting the stamp into pieces of desired size after curing. The stamps were typically square with 2-cm long sides and were generally 1-mm thick, unless THF was used as a solvent, in which case they were 8-mm thick to limit swelling and prevent de-adhesion of the stamp. Each microchannel was 1-μm high and 7-μm wide, with the third dimension spanning the length of the stamp Other aspects of the patterning protocols used in these experiments are discussed in the Results and Discussion.

Preparation of orientationally ordered mesostructured silica–surfactant films

Typically the casting solutions were prepared by mixing two solutions that consisted of the hydrolyzed silica source and the dissolved surfactant, respectively. Mesostructured silica protein-host materials were prepared by mixing a 3:1 ratio by weight of 262.5 mg tetraethoxysilane (TEOS, Acros Organics) and 87.5 mg *n*-propyltriethoxysilane (PTEOS, 97%, Alfa Aesar) with 1.5 g of H_2O and 10 μL of 400 mM HCl. The TEOS solution was allowed to hydrolyze fully (typically 2-3 h) before the solutions were mixed and the sample

was cast. The solution was stirred vigorously for 3 h, at which point the solution was transparent. 200 mg of this solution was removed and mixed with an appropriate amount of *n*-dodecyl-*β,D*-maltoside (DDM, Anatrace). Another solution was created with a 9.1 wt% solution of 1-palmitoyl-2-oleoyl-glycero-3-phosphocholine (POPC, Avanti Polar Lipids) and 1,2-dioleoyl-3-trimethylammonium-propane (DOTAP, Avanti Polar Lipids) in 4:1 molar ratio. If the materials are being made with guest proteorhodopsin molecules, this second solution would also be mixed with a desalted PR-containing DDM micellar solution. The silica precursor- and surfactant-containing solutions were then mixed and quickly titrated to a pH of 4.1 using 50 mM HCl or 50 mM NaOH, producing a casting solution. To cast the sample, typically 11 μL of the casting solution is placed on a suitable substrate (typically glass or metalized Kapton^{TM}) and then a PDMS stamp, patterned as described above, was placed on top. Thicker films of 1 mm or more can be prepared by increasing the solution volume. Such thicker 1-mm films were used to prepare the mesoporous carbons as detailed below. Once the PDMS stamp was applied, the solution was placed in a controlled relative humidity chamber at a relative humidity determined by a supersaturated salt solution and allowed to dry for one week before characterization.

Other (non-protein-host) silica-surfactant materials were made from a different casting solution: a surfactant solution consisting of 0.7 g of Pluronic^{TM} P123 dissolved in 3.6 g of ethanol, and a hydrolyzed silica solution contained 1.47 g of TEOS dissolved in 3.6 g of ethanol and 0.65 g of 0.07 M HCl. The TEOS solution was allowed to hydrolyze 2 h before the solutions were mixed and the sample was cast.

5.4 Results and Discussion

Mesostructured inorganic-organic materials are generally prepared by precipitation from solution or by solvent evaporation during casting or spin-coating, which usually result in micrometer-size domains with low extents of orientational order over macroscopic length scales. In order to control the mass transport processes, surfactant co-assembly, and silica polymerization kinetics that determine the results of synthesis and encourage the formation of orientationally ordered mesostructured silica-silica surfactant materials, a micropatterned poly(dimethylsiloxane) (PDMS) stamp can be employed that manages the rates, directions, and surfaces at which self-assembling phases nucleate and the directions that they grow. The schematic diagram in Figure 5.1a shows how vertically aligned mesophases are hypothesized to form between these micropatterned stamps and a substrate. Surfactants co-assemble at the top of stamp microchannels where the corners of PDMS surfaces meet and surfactant concentration is greatest. Co-assembly nucleates here where surfactant concentration and solvent removal rates are greatest because solvent leaves/diffuses both vertically and horizontally through the semipermeable PDMS stamp. The effect of directed nucleation imposed by the stamp on the co-assembling mesostructured film is exhibited in the two-dimensional grazing-incidence small angle X-ray scattering (GISAXS) patterns of two films with identical compositions (Figure 5.1b). The narrow spots observed for the film made with a PDMS stamp represent three of six reflections indicative of a hexagonal mesostructure. Figure 5.1c presents transmission electron microscopy (TEM) images of a 0 wt% proteorhodopsin (PR), 62.5 wt% DDM, 6.2 wt% POPC, 1.3 wt% DOTAP, 22.5 wt% SiO_2, 7.5 wt% n-propyl $SiO_{1.5}$ mesostructured film made with a PDMS stamp. While the TEM micrograph confirms the GISAXS results and shows equally spaced cylindrical mesochannels

in a hexagonal arrangement, it reveals that the orientational ordering of these channels is not consistent over length-scales relevant to harness membrane protein functions within devices.

Favorable synthetic characteristics, such as slow silica polymerization rate and strongly interacting surfactants, enable the formation of macroscopically aligned channels from the nucleation sites at the PDMS surface to the substrate below. The substrate has been generally selected as either a deposited titanium or aluminum layer which are robust and adhere to the silica films, meaning that the film is not pulled off when the stamp is removed, however, this does not exclude other substrates that may have similarly favorably properties from future syntheses. Mesostructured silica–Pluronic^{TM} P123 films can been synthesized using these methods to produce films with high extents of both mesostructural and orientational order, and additionally, the direction of orientational ordering can be controlled by mediating the paths of solvent removal (Figure S5.1). However, the low pH and high concentrations of organic co-solvents used to synthesize these films denature most proteins, and so cannot be used to synthesize an orientally ordered protein-host material.

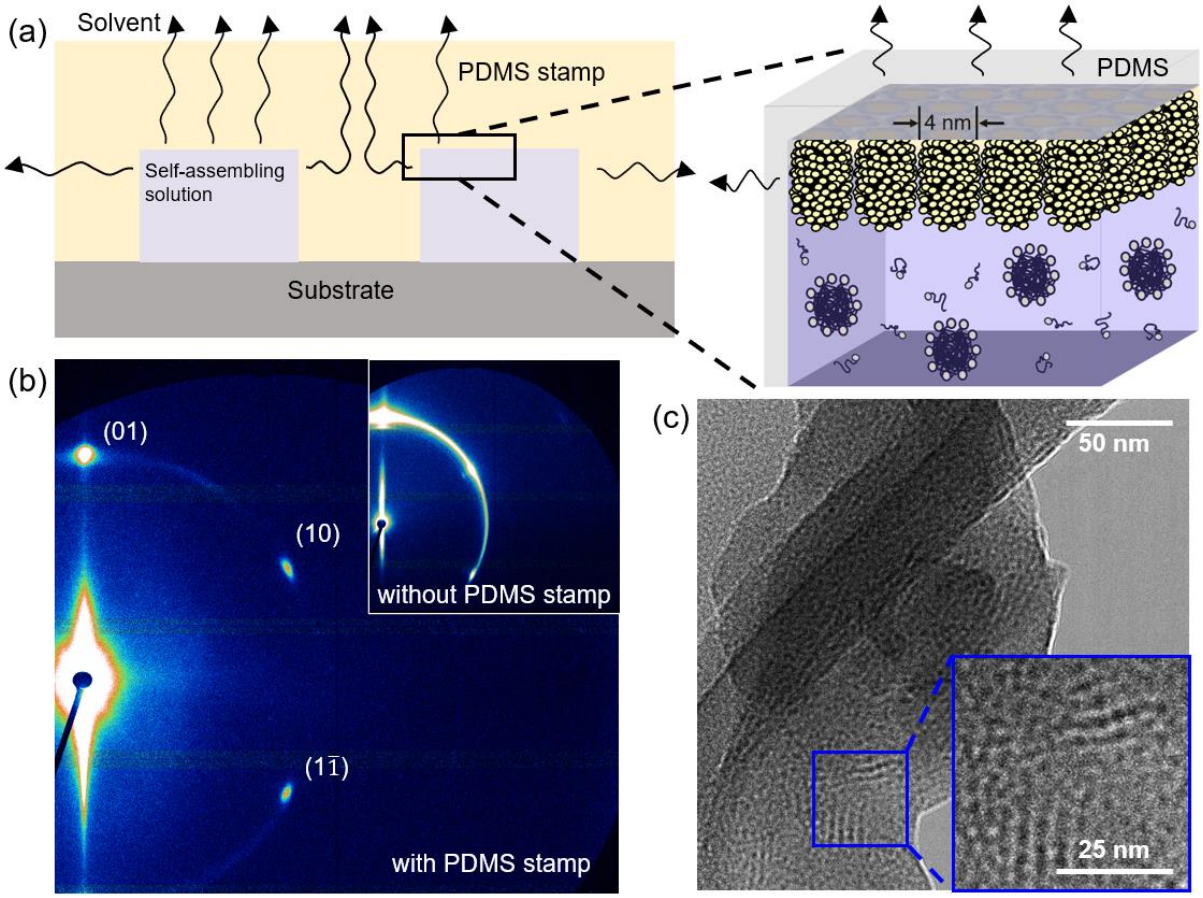

Figure 5.1. (a) Schematic diagram of a mesostructured silica-surfactant film being synthesized within a PDMS stamp, displaying (left) design and solvent removal paths and (right) the formation of cylindrical columns starting from the corner of a PDMS stamp microchannel. **(b)** Two dimensional grazing-incidence small-angle X-ray scattering patterns for films made with and without a PDMS stamp. **(c)** Transmission electron micrograph at two different magnifications depicting the a silica-DDM+DOTAP+POPC mesostructured film made with a PDMS stamp. The films in (b) and (c) are 0 wt% E50Q PR, 62.5 wt% DDM, 6.2 wt% POPC, 1.3 wt% DOTAP, 22.5 wt% SiO_2, and 7.5 wt% n-propyl $SiO_{1.5}$.

Similar to freestanding films, the extent of mesostructural order in films made with a PDMS stamp are primarily dependent on the film composition, however, the different ways that molecules interact at the PDMS-solution versus air-solution interfaces can influence structure even beyond orientational order. In Figure 5.2, two-dimensional X-ray diffraction

data is presented for mesostructured silica films that probes mesostructural ordering and alignment across three orthogonal axes. A combination of transmission SAXS and GISAXS probing the material across the three axes can be used to identify mesostructural ordering (as shown in Figure S5.2). In Figure 5.2a, schematic diagrams show the different directionalities of X-rays used to probe these three axes. Figure 5.2b shows narrow X-ray reflections of a well-ordered hexagonal mesostructure. In addition, this combination of two- and six-spot patterns in orthogonal axes also reveals that the sample is macroscopically oriented horizontally, with parallel mesochannels. While evidence of similarly narrow six-spot patterns are observed in silica-DDM+POPC+DOTAP (Figure 5.2c), six-spot patterns observed in two orthogonal axes is indicative of in-plane alignment. These results reveal domains of highly ordered hexagonal mesostructures that are consistently aligned parallel to the substrate; however, within this plane of alignment, mesochannels are oriented in different directions. This is supported by collected TEM images (Figure 5.1c) and can be confirmed through transmission SAXS; however, the instruments currently available at UCSB in conjunction with the extremely thin sample make this measurement infeasible. These measurements can be done either with a thicker sample or at a synchrotron beam line that would significantly increase the number of scattered X-rays.

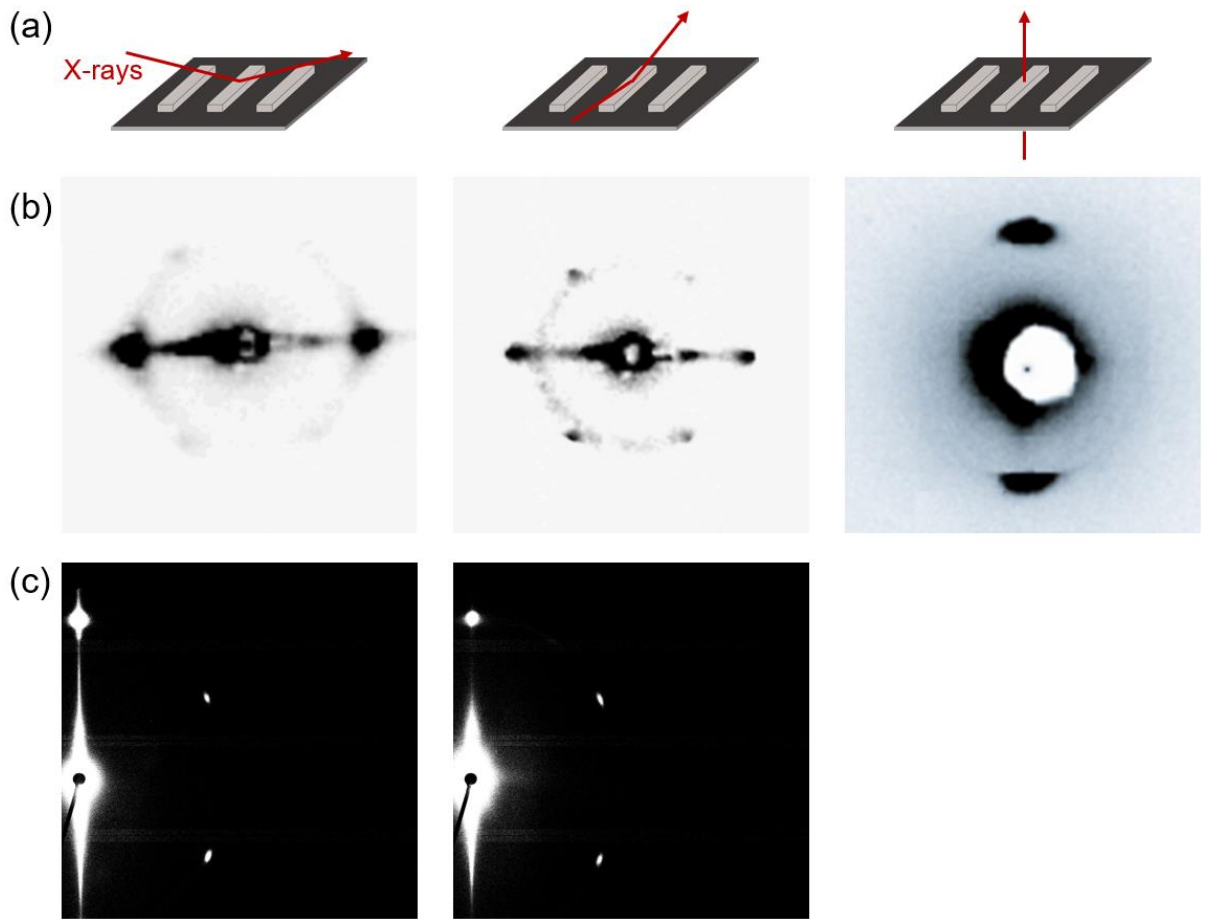

Figure 5.2. (a) Schematic diagram depicting the direction of X-rays used to measure scattering data of mesostructured silica films in the orthogonal (left) x, (middle) y, and (right) z axes. Two dimensional X-ray scattering patterns for **(b)** silica–Pluronic^{TM} P123 and **(c)** silica-DDM+POPC+DOTAP hexagonally ordered films acquired from orthogonal axes.

My goal is to synthesize robust mesostructured silica materials with high extents of mesostructural and orientational ordering in order to accommodate membrane protein guests (as previously discussed in Chapter 3). Macroscopic materials provide a medium for nanoscale proteins to operate in technological applications, in which controllable orientational order enables the harnessing of anisotropic protein function. As previously mentioned, certain mesostructured silica materials (such as silica-Pluronic^{TM} 123 films) that display these favorable properties cannot stabilize guest proteins because of denaturing charges, organic

solvents, and low pH synthesis conditions; however, even materials conducive to the incorporation of membrane protein guest molecules (such as silica-DDM+POPC+DOTAP films) are challenging to work with because even small loadings of protein can significantly disrupt co-assembly or ordered mesochannels. Results of initial syntheses of mesostructured silica-DDM+POPC+DOTAP films containing varied loadings of PR are presented in Figure 5.3 as a series of scanning electron microscopy (SEM) images and step-height profilometer graphs as a function of dilution. Figure 5.3a shows these results for a 0 wt% proteorhodopsin (PR), 62.5 wt% DDM, 6.2 wt% POPC, 1.3 wt% DOTAP, 22.5 wt% SiO_2, 7.5 wt% n-propyl $SiO_{1.5}$ mesostructured film made with a PDMS stamp (the same films as reported in Figure 5.1b-c and Figure 5.2c) revealing relatively uniform micropatterned films with vertical walls and a flat top along with well-ordered six-spot GISAXS pattern. In contrast, Figure 5.3b represents results from a 5.0 wt% PR, 59.4 wt% DDM, 5.8 wt% POPC, 1.3 wt% DOTAP, 21.4 wt% SiO_2, 7.1 wt% *n*-propyl $SiO_{1.5}$ film, which displays inhomogeneity at the surface of the film via SEM, inconsistent sample thickness via profilometry, and poor mesostructural ordering via GISAXS. The addition of only 5 wt% PR to this sample had a much more significant impact on the macroscopic and mesostructural ordering of the film when compared to similar free-standing films (Figure 3.4) that retained film homogeneity and high extents of mesostructural ordering. Similarly, a 25 wt% PR-containing film (25 wt% PR, 46.9 wt% DDM, 4.6 wt% POPC, 1.0 wt% DOTAP, 16.9 wt% SiO_2, 5.6 wt% *n*-propyl $SiO_{1.5}$) exhibits increased film inhomogeneity as well as the complete loss of signal intensity corresponding to mesostructural or orientational order. These differences between the formation of free-standing films and films made within a PDMS stamp despite identical compositions of PR, silica, and surfactants is likely due to new intermolecular or interfacial

interactions with PR or because of other physical constraints the PDMS stamp imposes during co-assembly.

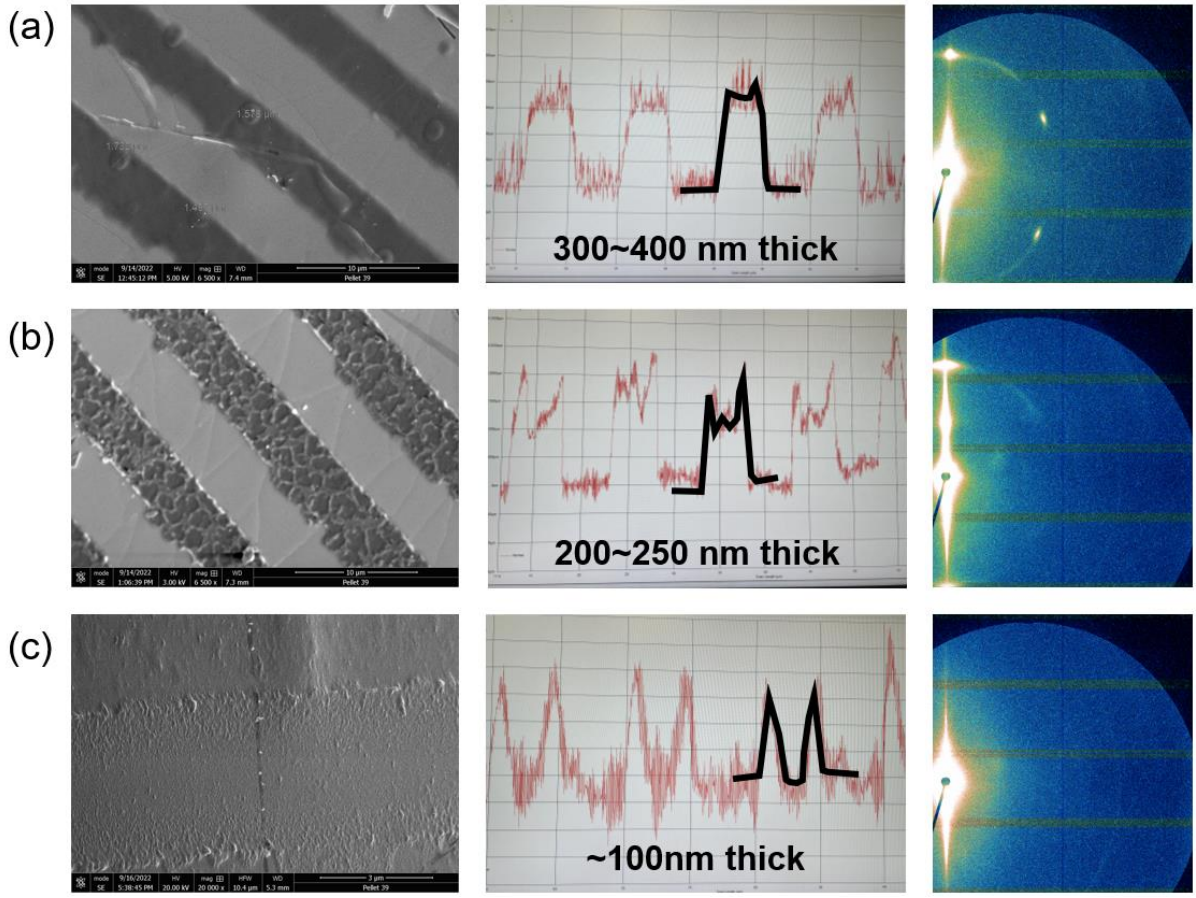

Figure 5.3. (left) Scanning electron micrographs, (middle) profilometry sample height data, and (right) grazing-incidence small angle X-ray scattering patterns for **(a)** 0 wt% E50Q PR, 62.5 wt% DDM, 6.2 wt% POPC, 1.3 wt% DOTAP, 22.5 wt% SiO_2, and 7.5 wt% n-propyl $SiO_{1.5}$, **(b)** 5 wt% E50Q PR, 59.4 wt% DDM, 5.8 wt% POPC, 1.3 wt% DOTAP, 21.4 wt% SiO_2, 7.1 wt% n-propyl $SiO_{1.5}$, **(c)** 25 wt% E50Q PR, 46.9 wt% DDM, 4.6 wt% POPC, 1.0 wt% DOTAP, 16.9 wt% SiO_2, 5.6 wt% n-propyl $SiO_{1.5}$ mesostructured silica films made with a PDMS stamp. The significant results observed are due to the dilution of the co-assembling material solution as a result of using similarly concentrated proteorhodopsin. The PDMS stamp used has linear 0.45 μm x 5 μm x 1.5 cm microchannels.

Similar to freestanding films (discussed in Chapter 3), synthesis conditions such as ambient temperature and humidity impact the mesostructure of a film made within a PDMS stamp (Figure S5.3). However, when synthesizing films within a PDMS stamp, solvent removal rate is considered as two distinct processes, the solvent diffusing through the PDMS stamp and evaporation rate into the atmosphere. Water diffusion through the PDMS stamp can be tuned by controlling the crosslinking of the polymer stamp and through solvent saturation of the stamp prior to synthesis.[36] While the extent of crosslinking in the polymer stamp remains to be optimized for this synthesis, the effect of saturating the PDMS stamp prior to synthesis is shown to affect the orientational order of the resulting film (Figure S5.4). Overall, low temperature (4℃), low humidity (0% relative humidity), and saturated PDMS stamps have resulted in increasing intensity of GISAXS spot patterns, but did not appear to be the driving factors towards achieving macroscopic vertical alignment of mesochannels or the driving factors disrupting the incorporation of PR.

Unlike freestanding films that contract radially as the solvent evaporates, the film area synthesized with a PDMS stamp generally maintains the width of the PDMS channel due to surface tension. As the solvent leaves through the PDMS stamp, a headspace of air fills the vacated volume at the top of the channels, continuing to enable the formation of silica-surfactant mesochannels at the intersection of solution-PDMS and solution-air interfaces. This means that the dilution of the synthesis solution that is placed under the PDMS stamp is important, rather than only the relative concentrations of molecules, which together largely determine the final mesostructure of freestanding silica-surfactant films. Each of the films synthesized for Figure 5.3 were made with 214 μM E50Q PR in water solvent, meaning that the mol/mol ratios of solvent to silica and surfactants is 46, 133, and 508 for 0 wt%, 5 wt%,

and 25 wt% E50Q PR respectively. The consequences of diluting the co-assembling material solution are (1) not enough co-assembling mass to produce homogeneous films that are the size of the microchannel, (2) more solvent leaving through the PDMS will take longer, and results in the silica polymerization occurring before well-ordered channels are formed, and (3) lower overall concentrations of structure-directing surfactants mean well-ordered co-assembled structures are less likely to form. Interestingly, the shape of the film heights (as given by profilometry data in Figure 5.3) at different dilutions support the hypothesis that nucleation of co-assembly in these films first occurs at the corners of the microchannels. This is because the thickness of the co-assembled film is consistently greatest at the edge of the channels. Following nucleation at the corners, co-assembly processes inwards from the channel walls only if permitted by a high enough concentration and quantity of surfactants and silica moieties. Thus, if there is not enough material to make a film with homogeneous thickness (as in Figure 5.3a), the middle of the film is formed thinner than at the walls (as observed in Figure 5.3b-c). For comparison, two films were both synthesized within PDMS microchannels 450 nm tall; the 0 wt% PR film in Figure 5.3a has a thickness of ~350 nm across the channel while the 5 wt% PR film in Figure 5.3b has a thickness of ~200 nm at the walls and only ~100 nm in between. While this is true on average across the width of a channel, the SEM micrograph in Figure 5.3b reveals further local inhomogeneities in the form of amorphously-shaped patches of thinner film formation. The 25 wt% PR sample examined in Figure 5.3c exhibits 100 nm and 10 nm thickness at the channel walls and average thinnest center point respectively. While the thickness of the films are decreasing at the channel walls with increased sample dilution, the ratio of thicknesses between the film at the channel walls and the thinnest point in between is increasing with dilution. This is consistent with our hypotheses that co-

assembly nucleates and forms first at the corners of the microchannel and processes inward from the channel walls when enough water solvent has evaporated or diffused through the stamp that the concentration of surfactants and silica is high enough to enable self-assembly. The results of these experiments reveal the importance of a synthesis parameter not previously optimized for freestanding films and which would enable the formation of a homogeneous film within the PDMS stamp.

Following the interesting but inconclusive results presented in Figure 5.3, mesostructured silica-surfactant films are made from both concentrated and dilute materials with and without protein guests. By isolating each of these variables, the synthesis-relevant parameters can be identified and optimized. Figure 5.4 shows the results of these later experiments, presenting two-dimensional GISAXS for PR-containing and non-PR-containing silica-DDM+POPC+DOTAP films with similar concentrated and dilute starting material co-assembly solutions. For non-PR-containing films, the concentrated solution (Figure 5.1b, 5.2c, 5.3a, 5.4a) exhibits a spot pattern with similar coordinates to the diluted solution sample (Figure 5.3b), however, the film produced from a diluted solution has less intense spot reflections and an observable isotropic ring. Along with GISAXS from the horizontal orthogonal direction, this indicates evidence of both in-plane and three-dimensional isotropic orientational order. The mesostructural ordering of this film synthesized from a diluted co-assembly solution is in significant contrast to the PR-containing film made from similarly dilute material solution (Figure 5.3b, 5.4d), which displays no spot pattern. Interestingly, a 5 wt% PR-containing film made from a more concentrated material solution as in Figure 5.4a, exhibits a weak spot pattern as well as an isotropic ring (Figure 5.4c), better ordered than the diluted sample but more poorly ordered than either sample made without PR. The disorder

observed in Figure 5.3 is due in part to both the initial dilution of the self-assembling solution as well as the co-assembly of PR with surfactants and silica precursors within the PDMS stamp.

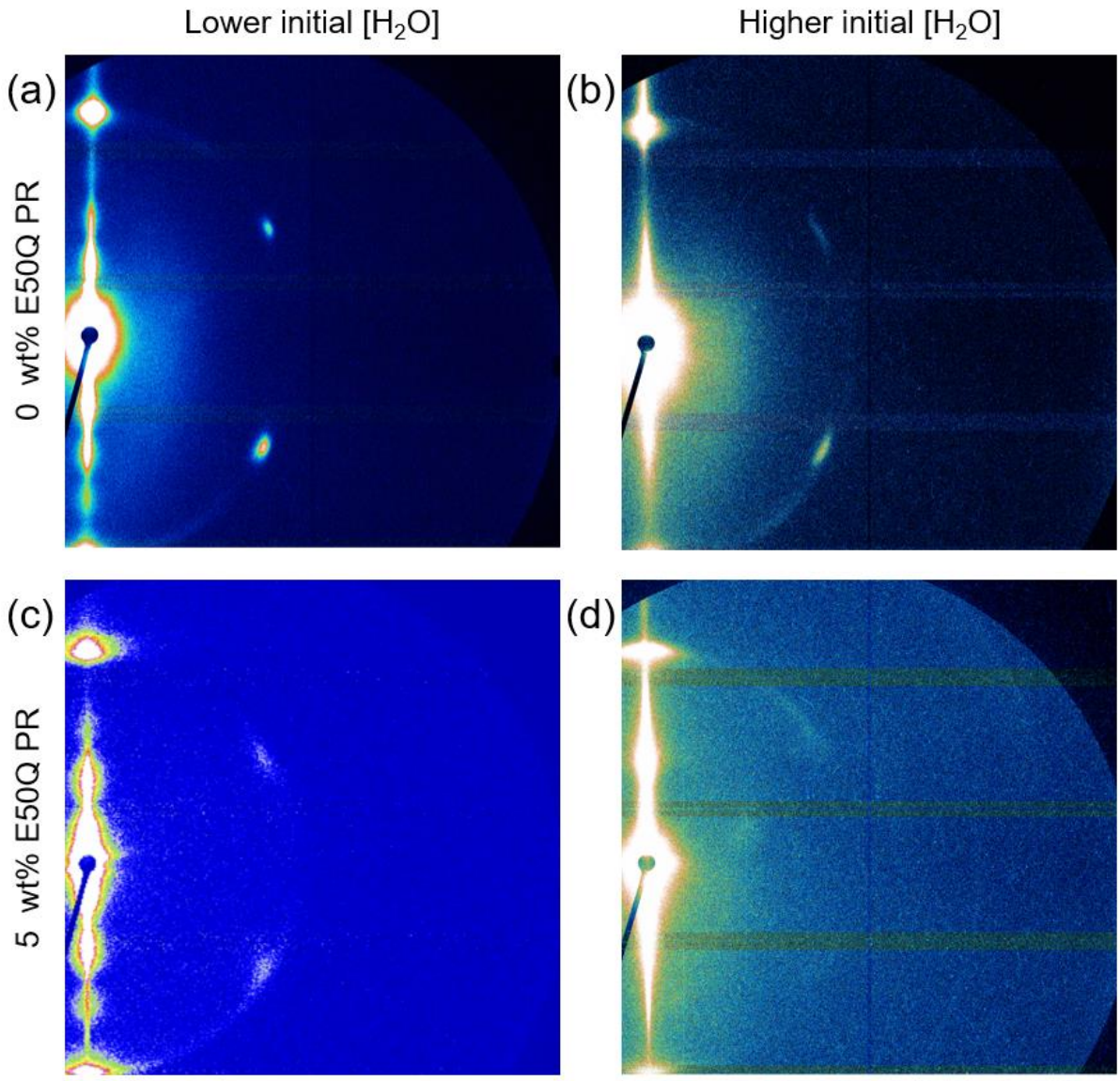

Figure 5.4. Two-dimensional grazing-incidence small angle X-ray scattering patterns depicting mesostructured silica films synthesized within the microchannels of a PDMS stamp. The starting compositions of the material solutions are **(a)** 0 wt% E50Q PR, 9.1 wt% DDM, 0.8 wt% POPC, 0.2 wt% DOTAP, 5.2 wt% TEOS, 2.2 wt% PTEOS, 70 wt% H_2O, 12.5 wt% EtOH, **(b)** 0 wt% E50Q PR, 4.8 wt% DDM, 0.4 wt% POPC, 0.1 wt% DOTAP, 4 wt% silica, 84 wt% H_2O, 6.7 wt% EtOH, **(c)** 0.9 wt% E50Q PR, 8.8 wt% DDM, 0.8 wt% POPC, 0.2 wt% DOTAP, 5.1 wt% TEOS, 1.7 wt% PTEOS, 70 wt% H_2O, 12.5 wt% EtOH, and **(d)** 0.3 wt% E50Q PR, 4.2 wt% DDM, 0.4 wt% POPC, 0.1 wt% DOTAP, 2.5 wt% TEOS, 1.1 wt% PTEOS, 85.5 wt% H_2O, 5.9 wt% EtOH.

These results suggest that influences beyond the dilution effects imposed by the PDMS stamp are significant to the mesostructure of self-assembled silica-surfactant films. While, the inclusion of PR also disrupts the self-assembled mesostructure of free-standing films (Chapter 3), those samples display isotropic orientational order at all protein loadings and so are not directly comparable. Deconvoluting the effects of PR intermolecular or interfacial interactions on the film mesostructure and orientational order is difficult because they depend on many properties such as charge, hydrophobicity/hydrophilicity, and Van der Waals forces. I hypothesize that the differences observed in Figure 5.4 are due significantly to intermolecular interactions between PR and stabilizing DDM surfactants. Proteorhodopsin is a membrane protein and therefore has significant hydrophobic regions that are typically stabilized by a lipid bilayer, or in the case of the co-assembling solution, amphiphilic DDM micelles. When mixing co-assembling solutions containing PR, much of the DDM molecules (especially at high concentrations of PR) are stabilizing the protein rather than floating around as empty micelles ready to reassemble into cylindrical channels. I hypothesize that this effectively reduces the concentration of surfactants that can nucleate at the PDMS surface, preventing the co-assembly of mesochannels before silica polymerization begins, and thereby reducing the mesostructural order of the resulting film. Future directions will have to account for this phenomena, as well as investigate dilution interactions and potential interfacial interactions, in order to synthesize mesostructured silica materials as membrane protein hosts.

5.5 Conclusions

The synthesis of membrane proteins into orientationally-aligned mesostructured silica host materials is an important step in harnessing a varied collection of technologically relevant functions. Silica-surfactant composite materials in conjunction with micropatterned PDMS stamps are one promising method towards this goal, utilizing directed evaporation pathways to nucleate self-assembly and form cylindrical mesochannels over macroscopic length-scales. The results presented in this chapter indicate synthesis conditions beneficial to achieving high extents of mesostructural order and modest control of orientational alignment. Generally, high concentration of surfactants and silica precursor molecules, low temperature, low humidity, and solvent-saturated PDMS stamps prior to synthesis produce the best results. However, complex intramolecular and interfacial interactions make incorporation of membrane protein guests and the control of orientational order difficult. Utilizing optimized synthesis conditions, a 5 wt% E50Q proteorhodopsin film was synthesized with relatively favorable extents of mesostructural ordering and in-plane orientational order. Given time to experiment, the challenges of vertical alignment and high protein loadings can be mediated through the judicious selection of the composition of film and prerequisite self-assembling material solution, as well as functionalization of PDMS and substrate surfaces. Proposed future directions are presented later in this chapter that layout experiments I would continue if I had more time. Hopefully, the results in this chapter and suggested lines of investigation can be used to achieve orientationally ordered mesostructured silica host materials with significant loadings of membrane protein guests.

5.6 Future Directions

Understanding how the complex interactions between molecules of a co-assembling solution and PDMS of the micropatterned stamp dictate the structure of a synthesized material is important in the application of this technique with new film compositions. As presented earlier in this chapter, identical PDMS stamps were used to different levels of success with silica-Pluronic^{TM} 123, silica-DDM+POPC+DOTAP films, and proteorhodopsin-containing silica-DDM+POPC+DOTAP host films. For these protein-host films, the PDMS stamp was used to synthesize a more desired hexagonal mesostructural order with an identical composition to a rectangular ordered free-standing film; the equitable spacing of mesochannels in a hexagonal arrangement is the lowest free energy state of cylindrical channels in most materials and generally corresponds to stronger mechanical properties.[37] However, even just 5 wt% proteorhodopsin (PR) guest molecules in these films has been shown to lower the extent of mesostructural and orientational order of the host film. Additionally, the desired macroscopic vertical alignment of DDM+POPC+DOTAP materials has not yet been achieved with or without PR guest molecules. First, I would like to further probe the extent to which proteorhodopsin incorporation affects the development of mesostructural and orientational order by synthesizing films with PR loadings between 0 wt% and 5 wt% under a PDMS stamp. These experiments are meant to investigate the effect of varying the ratio of surfactants stabilizing PR versus surfactants floating in solution as empty micelles. I hypothesize that high-protein loading solutions may exhibit relatively poor co-assembly because surfactants surrounding and solubilizing proteorhodopsin molecules may be thermodynamically prevented from leaving the protein and nucleating at the solution-PDMS interface. Self-assembly may even occur around the PR molecules because there is already a high concentration of

surfactants there to stabilize the protein in the aqueous solution. If true, this would significantly inhibit nucleation of mesochannels at the solution-PDMS interface (as encouraged by the PDMS stamp), and explain why poorer mesostructural order is achieved with PR-containing samples. These experiments are intended to identify if poor orientational alignment is due to intermolecular interactions between the protein and PDMS/substrate or because of a lack of surfactants capable of nucleating on the surface of PDMS.

I hypothesize that the limitations observed for the application of the PDMS stamp with PR-containing DDM+DOTAP+POPC-structure directed mesostructured silica host films (as presented in this chapter) can be mitigated through surface modifications of the PDMS stamp or metal substrate. Functionalization of substrates is a common technique used to influence orientational alignment of self-assembling material. Chemical treatments can be used to add physical deformations,[38] block copolymers,[39] or ordered substrate layers for epitaxial growth[40] in order to produce interactions at the self-assembling solution-substrate interface that promote vertical alignment. However, it is difficult to make these interactions translate greater than 100 nm from the substrate and produce macroscopically oriented domains. Similarly, electro-induced self-assembly has been utilized to induce vertical alignment at the surface of an electrode.[23,41] While these techniques can be applied to silica-DDM+POPC+DOTAP PR-hosts, success may be limited for film thicknesses greater than 100 nm,[42] which are produced in the presence of extreme pH conditions, high concentrations of organic solvents, or high electric potentials that each can lead to the denaturation of proteins.

In addition to manipulating interactions at the solution-substrate interface, similar treatments and techniques manipulate the thermodynamics of self-assembly at the upper PDMS substrate to mediate nucleation, mesostructural ordering, and alignment.

Functionalization of the surface of the PDMS stamp is an important adjustment tool to mediate nucleation and attractive/repulsive interactions of self-assembly that isn't possible with freestanding films. Nucleation of mesochannel co-assembly in the silica-surfactant films made with a PDMS stamp occurs at the top surface of the microchannel at the solution-PDMS interface, where surfactant concentration is greatest. This suggests that functionalization of this surface may have an important impact towards achieving vertical alignment of mesochannels. Regardless of specific functional groups being added to these surfaces, treating the PDMS either only at the top of the microchannel to nucleate effectively or along the walls to discourage the nucleation of in-plane mesochannels is a significant challenge. Because nucleation first occurs at the corner intersections of the walls and the top of the PDMS microchannel, a PDMS treatment would need to be selectively applied, perhaps by vertical deposition to the top, in order to produce anisotropic impact on the nucleating mesostructure.

Separate from the thermodynamic driving forces that dictate the preferred mesophase at equilibrium, the kinetic effects that interfere with the formation of the thermodynamically preferred mesostructure should be considered. This is especially true for evaporation-induced self-assembly, such as mesostructured silica-surfactant materials within the PDMS stamp, which forms a mesostructure under non-equilibrium conditions. For example, controlling the directions of solvent removal through the PDMS stamp provides control over the direction of macroscopically oriented mesochannels in silica-P123 films.[43] Similar phenomena have been observed using directed evaporation to achieve in-plane orientational alignment of carbon nanotubes[44] and patterned in-plane alignment of colloidal films.[45] Along these lines, increasing vertical removal of solvent through a PDMS stamp, while minimizing horizontal escape, should help induce vertical alignment of mesostructured silica materials. The rate at which

solvent is removed likely requires optimization as too fast of a rate may dominate the formation of a specific mesostructure over the thermodynamic forces of self-assembly that have already been carefully optimized to produced cylindrical rectangular and hexagonal mesostructures. A number of synthesis conditions can affect the direction and rate of solvent evaporation including the extent of polymerization in the PDMS stamp, the dimensions of the PDMS stamp walls and solution-containing microchannels, the thickness of the PDMS stamp, the rate of solvent removal (by relative humidity or vacuum), and things that affect the direction of evaporation (such as non-permeable barriers on the top or sides of the PDMS stamp). I hypothesize that optimizing the rate of vertical evaporation through these synthesis conditions while minimizing lateral evaporation will improve vertical orientational order of mesostructured silica-surfactant films within the PDMS stamp.

Alternatively, the nucleation of self-assembled structures can be directed by changing the geometry of the PDMS stamp. I hypothesized that exhibit heterogeneous nucleation may be occurring because of differences in solvent flux at the corners of the channels (3 solution-PDMS interfaces) and along the 1.5 cm edge length (2 solution-PDMS interfaces). To test this, PDMS stamps were made with 5 μm x 5 μm squares microchannels, increasing the frequency of high solvent flux corners compared to 5 μm x 1.5 cm rectangular microchannels. If the self-assembly of these silica-surfactant films is directed towards competing orientations, vertically oriented mesochannels nucleating at the high flux corners versus in-plane oriented mesochannels nucleating at the (comparatively) lower flux edges, this geometry should increase the overall fraction of vertically. However, no change in mesostructural or orientational ordering was observed as a result of this in mesochannel dimension, indicating either homogeneous self-assembly of in-plane mesochannels, or that 5 μm is still too great of

a distance between microchannel corners to produce homogeneous extents of orientational order. Assuming that the distance between nucleation sites is still too great, I suggest surface modification at the top surface of the PDMS microchannels with small cylindrical domains that would promote the nucleation of vertical surfactant channels. Utilizing known silicon etching processes, sub-40 nm diameter vertical cylinders (up to 1.5 μm tall) can be formed in the micropatterned channels of a silicon wafer.[46] When used as a stencil for a polymerizing PDMS stamp, vacant cylinders would be left at the top surface of microchannels. These cylinders may nucleate the self-assembly of vertical mesochannels, due in part to the vertical solvent flux[43] and the preference of cylindrical mesochannels to form parallel to a curved surface.[47] Once vertically oriented mesochannels are nucleated across the upper surface of the microchannel, a well-ordered and aligned material can self-assemble to the lower substrate.[43] Importantly, the high density and regularity of these nucleating cylinders across the relatively large surface area of PDMS microchannels may allow homogeneous orientational alignment of surfactant mesochannels across macroscopic dimensions. Utilizing cylinders to nucleate

In addition to controlling thermodynamics and kinetic processes related to the nucleation and self-assembly of protein-silica-surfactant mesostructures, external magnetic fields (produced by a superconducting magnet) can be used to align similar materials, orienting rod-like micelles of surfactants whose individual low diamagnetic susceptibilities are combined as an aggregate.[41,48,49] Furthermore, the orientational alignment of bicelles and mesochannels, either parallel or perpendicular to the magnetic field, has been controlled through paramagnetic ion or benzene additives.[2,50] Magnetic fields also present a potential solution for one challenge not yet discussed, alignment of the anisotropic PR monomers. Membrane proteins hosted in bicelles have previously been aligned in magnetic fields under

equilibrium conditions[51,52] by taking advantage of the anisotropic diamagnetic susceptibility tensor of lipid bilayer hosts.[53] The challenge of applying this technique to the current investigation is the weak magnetic dipole moment of the monomeric form of proteorhodopsin being used in these materials and the surfactant channels, which are not as tightly packed as the previously discussed bilayer hosts. Alone, this not a significant obstacle, as similar molecules have been successfully aligned in strong (>10 T) magnetic fields, however, alignment becomes much more difficult under non-equilibrium synthesis conditions, which apply competing influences over orientation and a viscous environment due to silica polymerization. Applying these strategies to channel alignment is most feasible if the starting material solution imitates the bicelle solution; therefore, co-assembly of channel walls must be fast with strong intermolecular interactions and the rate of silica polymerization must be minimized.

Each of these have the potential to orientationally order mesostructured silica-DDM+POPC+DOTAP protein host materials and unlock the ability to harness membrane protein function on macroscopic length scales. As often is the case with this challenging and complex project, determining the method to pursue (and allocation of significant time and labor) is difficult. Optimization of solvent removal rates and pathways, magnetic alignment, and patterned substrate epitaxy are promising techniques to utilize as they do not interfere with the already complex mixture of film components or interfere with intramolecular components. I hypothesize that a combination of techniques may be most resourceful, and make up for the inability to use synthesis conditions generally considered favorable because of instability of protein guests. Vertically aligned mesostructured silica materials have previously been produced from identical self-assembly directing parallel surfaces;[54] however, there is nothing

inherently more disruptive about two separate techniques as long as they both promote the same extents of order. Techniques tuned to promote similar nucleation and self-assembled structures should be synergistic, and be capable of promoting high extents of mesostructural and orientational ordering.

5.7 References

(1) Kumar, P.; Jaggi, C.; Sharma, V.; Raina, K. K. Advancements of Vertically Aligned Liquid Crystal Displays. *Micron* **2016**, *81*, 34–47. https://doi.org/10.1016/j.micron.2015.11.001.

(2) Firouzi, A.; Atef, F.; Oertli, A. G.; Stucky, G. D.; Chmelka, B. F. Alkaline Lyotropic Silicate−Surfactant Liquid Crystals. *J. Am. Chem. Soc.* **1997**, *119* (15), 3596–3610. https://doi.org/10.1021/ja963007i.

(3) Morris, M. A. Directed Self-Assembly of Block Copolymers for Nanocircuitry Fabrication. *Microelectronic Engineering* **2015**, *132*, 207–217. https://doi.org/10.1016/j.mee.2014.08.009.

(4) Mendoza, C.; Nirwan, V. P.; Fahmi, A. Nanofabrication of Hybrid Nanomaterials: Macroscopically Aligned Nanoparticles Pattern via Directed Self-assembly of Block Copolymers. *J of Applied Polymer Sci* **2023**, *140* (5), e53409. https://doi.org/10.1002/app.53409.

(5) Chen, W.; Nikiforov, M. P.; Darling, S. B. Morphology Characterization in Organic and Hybrid Solar Cells. *Energy Environ. Sci.* **2012**, *5* (8), 8045. https://doi.org/10.1039/c2ee22056c.

(6) Lee, M. M.; Teuscher, J.; Miyasaka, T.; Murakami, T. N.; Snaith, H. J. Efficient Hybrid Solar Cells Based on Meso-Superstructured Organometal Halide Perovskites. *Science* **2012**, *338* (6107), 643–647. https://doi.org/10.1126/science.1228604.

(7) Warren, S. C.; Perkins, M. R.; Adams, A. M.; Kamperman, M.; Burns, A. A.; Arora, H.; Herz, E.; Suteewong, T.; Sai, H.; Li, Z.; Werner, J.; Song, J.; Werner-Zwanziger, U.; Zwanziger, J. W.; Grätzel, M.; DiSalvo, F. J.; Wiesner, U. A Silica Sol–Gel Design Strategy for Nanostructured Metallic Materials. *Nature Mater* **2012**, *11* (5), 460–467. https://doi.org/10.1038/nmat3274.

(8) Whittell, G. R.; Hager, M. D.; Schubert, U. S.; Manners, I. Functional Soft Materials from Metallopolymers and Metallosupramolecular Polymers. *Nature Mater* **2011**, *10* (3), 176–188. https://doi.org/10.1038/nmat2966.

(9) Zhang, Y.; Danielsen, S. P. O.; Popere, B. C.; Heitsch, A. T.; Li, M.; Trefonas, P.; Segalman, R. A.; Katsumata, R. Discrete, Shallow Doping of Semiconductors via Cylinder-Forming Block Copolymer Self-Assembly. *Macro Materials & Eng* **2022**, *307* (9), 2200155. https://doi.org/10.1002/mame.202200155.

(10) Ma, Y.; Heijl, R.; Palmqvist, A. E. C. Composite Thermoelectric Materials with Embedded Nanoparticles. *J Mater Sci* **2013**, *48* (7), 2767–2778. https://doi.org/10.1007/s10853-012-6976-z.

(11) Vineis, C. J.; Shakouri, A.; Majumdar, A.; Kanatzidis, M. G. Nanostructured Thermoelectrics: Big Efficiency Gains from Small Features. *Adv. Mater.* **2010**, *22* (36), 3970–3980. https://doi.org/10.1002/adma.201000839.

(12) Varoon, K.; Zhang, X.; Elyassi, B.; Brewer, D. D.; Gettel, M.; Kumar, S.; Lee, J. A.; Maheshwari, S.; Mittal, A.; Sung, C.-Y.; Cococcioni, M.; Francis, L. F.; McCormick, A. V.; Mkhoyan, K. A.; Tsapatsis, M. Dispersible Exfoliated Zeolite Nanosheets and Their Application as a Selective Membrane. *Science* **2011**, *334* (6052), 72–75. https://doi.org/10.1126/science.1208891.

(13) Schmidt-Rohr, K.; Chen, Q. Parallel Cylindrical Water Nanochannels in Nafion Fuel-Cell Membranes. *Nature Mater* **2008**, *7* (1), 75–83. https://doi.org/10.1038/nmat2074.

(14) Wu, G.; More, K. L.; Johnston, C. M.; Zelenay, P. High-Performance Electrocatalysts for Oxygen Reduction Derived from Polyaniline, Iron, and Cobalt. *Science* **2011**, *332* (6028), 443–447. https://doi.org/10.1126/science.1200832.

(15) Van Der Vliet, D. F.; Wang, C.; Tripkovic, D.; Strmcnik, D.; Zhang, X. F.; Debe, M. K.; Atanasoski, R. T.; Markovic, N. M.; Stamenkovic, V. R. Mesostructured Thin Films as Electrocatalysts with Tunable Composition and Surface Morphology. *Nature Mater* **2012**, *11* (12), 1051–1058. https://doi.org/10.1038/nmat3457.

(16) Zhang, B.; Wang, Q.; Zhang, Y.; Gao, W.; Hou, Y.; Zhang, G. A Self-Assembled, Nacre-Mimetic, Nano-Laminar Structure as a Superior Charge Dissipation Coating on Insulators for HVDC Gas-Insulated Systems. *Nanoscale* **2019**, *11* (39), 18046–18051. https://doi.org/10.1039/C9NR06827A.

(17) Fan, R.; Huh, S.; Yan, R.; Arnold, J.; Yang, P. Gated Proton Transport in Aligned Mesoporous Silica Films. *Nature Mater* **2008**, *7* (4), 303–307. https://doi.org/10.1038/nmat2127.

(18) Kim, J. Y.; Liu, P.; Maher, M. J.; Callan, D. H.; Bates, C. M.; Carlson, M. C.; Asano, Y.; Blachut, G.; Rettner, C. T.; Cheng, J. Y.; Sunday, D. F.; Kline, R. J.; Sanders, D. P.; Lynd, N. A.; Ellison, C. J.; Willson, C. G.; Baiz, C. R. Spatial Control of the Self-Assembled Block Copolymer Domain Orientation and Alignment on Photopatterned Surfaces. *ACS Appl. Mater. Interfaces* **2020**, *12* (20), 23399–23409. https://doi.org/10.1021/acsami.0c02997.

(19) Zhang, S.; Pelligra, C. I.; Feng, X.; Osuji, C. O. Directed Assembly of Hybrid Nanomaterials and Nanocomposites. *Adv. Mater.* **2018**, *30* (18), 1705794. https://doi.org/10.1002/adma.201705794.

(20) Freer, E. M.; Krupp, L. E.; Hinsberg, W. D.; Rice, P. M.; Hedrick, J. L.; Cha, J. N.; Miller, R. D.; Kim, H.-C. Oriented Mesoporous Organosilicate Thin Films. *Nano Lett.* **2005**, *5* (10), 2014–2018. https://doi.org/10.1021/nl051517h.

(21) Hosono, N.; Kajitani, T.; Fukushima, T.; Ito, K.; Sasaki, S.; Takata, M.; Aida, T. Large-Area Three-Dimensional Molecular Ordering of a Polymer Brush by One-Step Processing. *Science* **2010**, *330* (6005), 808–811. https://doi.org/10.1126/science.1195302.

(22) Pester, C. W.; Liedel, C.; Ruppel, M.; Böker, A. Block Copolymers in Electric Fields. *Progress in Polymer Science* **2017**, *64*, 182–214. https://doi.org/10.1016/j.progpolymsci.2016.04.005.

(23) Goux, A.; Etienne, M.; Aubert, E.; Lecomte, C.; Ghanbaja, J.; Walcarius, A. Oriented Mesoporous Silica Films Obtained by Electro-Assisted Self-Assembly (EASA). *Chem. Mater.* **2009**, *21* (4), 731–741. https://doi.org/10.1021/cm8029664.

(24) Gopinadhan, M.; Choo, Y.; Kawabata, K.; Kaufman, G.; Feng, X.; Di, X.; Rokhlenko, Y.; Mahajan, L. H.; Ndaya, D.; Kasi, R. M.; Osuji, C. O. Controlling Orientational Order in Block Copolymers Using Low-Intensity Magnetic Fields. *Proc. Natl. Acad. Sci. U.S.A.* **2017**, *114* (45), E9437–E9444. https://doi.org/10.1073/pnas.1712631114.

(25) Pelligra, C. I.; Majewski, P. W.; Osuji, C. O. Large Area Vertical Alignment of ZnO Nanowires in Semiconducting Polymer Thin Films Directed by Magnetic Fields. *Nanoscale* **2013**, *5* (21), 10511. https://doi.org/10.1039/c3nr03119e.

(26) Yu, D. M.; Smith, D. M.; Kim, H.; Mapas, J. K. D.; Rzayev, J.; Russell, T. P. Morphological Evolution of Poly(Solketal Methacrylate)- *Block* -Polystyrene Copolymers in Thin Films. *Macromolecules* **2019**, *52* (10), 3592–3600. https://doi.org/10.1021/acs.macromol.9b00488.

(27) Chmelka, B. F.; Nolla, J.; Steinbeck, C. A.; Athens, G. L.; Wildemuth, D. Mesostructured Inorganic Materials Prepared with Controllable Orientational Ordering. US7837909B2, November 23, 2010.

(28) Bridges, C. R.; Ford, M. J.; Thomas, E. M.; Gomez, C.; Bazan, G. C.; Segalman, R. A. Effects of Side Chain Branch Point on Self Assembly, Structure, and Electronic

Properties of High Mobility Semiconducting Polymers. *Macromolecules* **2018**, *51* (21), 8597–8604. https://doi.org/10.1021/acs.macromol.8b01906.

(29) Liberman, L.; Coughlin, M. L.; Weigand, S.; Bates, F. S.; Lodge, T. P. Phase Behavior of Linear-Bottlebrush Block Polymers. *Macromolecules* **2022**, *55* (7), 2821–2831. https://doi.org/10.1021/acs.macromol.2c00337.

(30) Rodrigues, L. D.; Sunil, D.; Chaithra, D.; Bhagavath, P. 1,2,3/1,2,4-Triazole Containing Liquid Crystalline Materials: An up-to-Date Review of Their Synthetic Design and Mesomorphic Behavior. *Journal of Molecular Liquids* **2020**, *297*, 111909. https://doi.org/10.1016/j.molliq.2019.111909.

(31) Hassan-Aghaei, F.; Mohebi, M. M. Synthesis and Characterization of Novel Multi-Layer Silica Thin Films with Tailored Mesostructure as Anti-Reflective Coatings. *Optical Materials* **2023**, *135*, 113246. https://doi.org/10.1016/j.optmat.2022.113246.

(32) Lu, Y.; Ganguli, R.; Drewien, C. A.; Anderson, M. T.; Brinker, C. J.; Gong, W.; Guo, Y.; Soyez, H.; Dunn, B.; Huang, M. H.; Zink, J. I. Continuous Formation of Supported Cubic and Hexagonal Mesoporous Films by Sol–Gel Dip-Coating. *Nature* **1997**, *389* (6649), 364–368. https://doi.org/10.1038/38699.

(33) Soler-Illia, G. J. D. A. A.; Louis, A.; Sanchez, C. Synthesis and Characterization of Mesostructured Titania-Based Materials through Evaporation-Induced Self-Assembly. *Chem. Mater.* **2002**, *14* (2), 750–759. https://doi.org/10.1021/cm011217a.

(34) Melosh, N. A.; Davidson, P.; Chmelka, B. F. Monolithic Mesophase Silica with Large Ordering Domains. *J. Am. Chem. Soc.* **2000**, *122* (5), 823–829. https://doi.org/10.1021/ja992801b.

(35) Barton, A. F. M. *CRC Handbook of Polymer-Liquid Interaction Parameters and Solubility Parameters*; CRC Press: Boca Raton, 1990.

(36) Donaldson, S. H.; Jahnke, J. P.; Messinger, R. J.; Östlund, Å.; Uhrig, D.; Israelachvili, J. N.; Chmelka, B. F. Correlated Diffusivities, Solubilities, and Hydrophobic Interactions

in Ternary Polydimethylsiloxane–Water–Tetrahydrofuran Mixtures. *Macromolecules* **2016**, *49* (18), 6910–6917. https://doi.org/10.1021/acs.macromol.6b01514.

(37) Miyoshi, H.; Matsuo, H.; Oku, Y.; Tanaka, H.; Yamada, K.; Mikami, N.; Takada, S.; Hata, N.; Kikkawa, T. Theoretical Analysis of Elastic Modulus and Dielectric Constant for Low- *k* Two-Dimensional Periodic Porous Silica Films. *Jpn. J. Appl. Phys.* **2004**, *43* (2), 498–503. https://doi.org/10.1143/JJAP.43.498.

(38) Liu, B.; Yao, Y.; Che, S. Template-Assisted Self-Assembly: Alignment, Placement, and Arrangement of Two-Dimensional Mesostructured DNA-Silica Platelets. *Angew. Chem. Int. Ed.* **2013**, *52* (52), 14186–14190. https://doi.org/10.1002/anie.201307897.

(39) Koganti, V. R.; Dunphy, D.; Gowrishankar, V.; McGehee, M. D.; Li, X.; Wang, J.; Rankin, S. E. Generalized Coating Route to Silica and Titania Films with Orthogonally Tilted Cylindrical Nanopore Arrays. *Nano Lett.* **2006**, *6* (11), 2567–2570. https://doi.org/10.1021/nl061992v.

(40) Richman, E. K.; Brezesinski, T.; Tolbert, S. H. Vertically Oriented Hexagonal Mesoporous Films Formed through Nanometre-Scale Epitaxy. *Nature Mater* **2008**, *7* (9), 712–717. https://doi.org/10.1038/nmat2257.

(41) Urbanova, V.; Walcarius, A. Vertically-Aligned Mesoporous Silica Films: Vertically-Aligned Mesoporous Silica Films. *Z. anorg. allg. Chem.* **2014**, *640* (3–4), 537–546. https://doi.org/10.1002/zaac.201300442.

(42) Sikolenko, T.; Despas, C.; Vilà, N.; Walcarius, A. Thickness Control in Electrogenerated Mesoporous Silica Films by Wet Etching and Electrochemical Monitoring of the Process. *Electrochemistry Communications* **2019**, *100*, 11–15. https://doi.org/10.1016/j.elecom.2019.01.013.

(43) Jahnke, J. P.; Kim, D.; Wildemuth, D.; Nolla, J.; Berkow, M. W.; Neyshtadt, S.; Segal-Peretz, T.; Frey, G. L.; Chmelka, B. F. Mesostructured Materials with Controllable Long-Range Orientational Ordering and Anisotropic Properties. *Advanced Materials* **2023**, under review.

(44) Zhang, D.; Ryu, K.; Liu, X.; Polikarpov, E.; Ly, J.; Tompson, M. E.; Zhou, C. Transparent, Conductive, and Flexible Carbon Nanotube Films and Their Application in Organic Light-Emitting Diodes. *Nano Lett.* **2006**, *6* (9), 1880–1886. https://doi.org/10.1021/nl0608543.

(45) Harris, D. J.; Hu, H.; Conrad, J. C.; Lewis, J. A. Patterning Colloidal Films via Evaporative Lithography. *Phys. Rev. Lett.* **2007**, *98* (14), 148301. https://doi.org/10.1103/PhysRevLett.98.148301.

(46) Morton, K. J.; Nieberg, G.; Bai, S.; Chou, S. Y. Wafer-Scale Patterning of Sub-40 Nm Diameter and High Aspect Ratio (>50:1) Silicon Pillar Arrays by Nanoimprint and Etching. *Nanotechnology* **2008**, *19* (34), 345301. https://doi.org/10.1088/0957-4484/19/34/345301.

(47) Miyata, H.; Takahashi, M. Lithographically Formed Fine Wavy Surface Morphology for Universal Alignment Control of Mesochannels in Mesostructured Silica Films. *Langmuir* **2021**, *37* (6), 2179–2186. https://doi.org/10.1021/acs.langmuir.0c03494.

(48) Tolbert, S. H.; Firouzi, A.; Stucky, G. D.; Chmelka, B. F. Magnetic Field Alignment of Ordered Silicate-Surfactant Composites and Mesoporous Silica. *Science* **1997**, *278* (5336), 264–268. https://doi.org/10.1126/science.278.5336.264.

(49) Yamauchi, Y. Field-Induced Alignment Controls of One-Dimensional Mesochannels in Mesoporous Materials. *J. Ceram. Soc. Japan* **2013**, *121* (1417), 831–840. https://doi.org/10.2109/jcersj2.121.831.

(50) Prestegard, J. H.; Kishore, A. I. Partial Alignment of Biomolecules: An Aid to NMR Characterization. *Current Opinion in Chemical Biology* **2001**, *5* (5), 584–590. https://doi.org/10.1016/S1367-5931(00)00247-7.

(51) Prosser, R. S.; Hunt, S. A.; DiNatale, J. A.; Vold, R. R. Magnetically Aligned Membrane Model Systems with Positive Order Parameter: Switching the Sign of Szz with Paramagnetic Ions. *J. Am. Chem. Soc.* **1996**, *118* (1), 269–270. https://doi.org/10.1021/ja953598x.

(52) De Angelis, A. A.; Nevzorov, A. A.; Park, S. H.; Howell, S. C.; Mrse, A. A.; Opella, S. J. High-Resolution NMR Spectroscopy of Membrane Proteins in Aligned Bicelles. *J. Am. Chem. Soc.* **2004**, *126* (47), 15340–15341. https://doi.org/10.1021/ja045631y.

(53) Sanders, C. R.; Hare, B. J.; Howard, K. P.; Prestegard, J. H. Magnetically-Oriented Phospholipid Micelles as a Tool for the Study of Membrane-Associated Molecules. *Progress in Nuclear Magnetic Resonance Spectroscopy* **1994**, *26*, 421–444. https://doi.org/10.1016/0079-6565(94)80012-X.

(54) Koganti, V. R.; Rankin, S. E. Synthesis of Surfactant-Templated Silica Films with Orthogonally Aligned Hexagonal Mesophase. *J. Phys. Chem. B* **2005**, *109* (8), 3279–3283. https://doi.org/10.1021/jp045037a.

5.8 Supporting Information

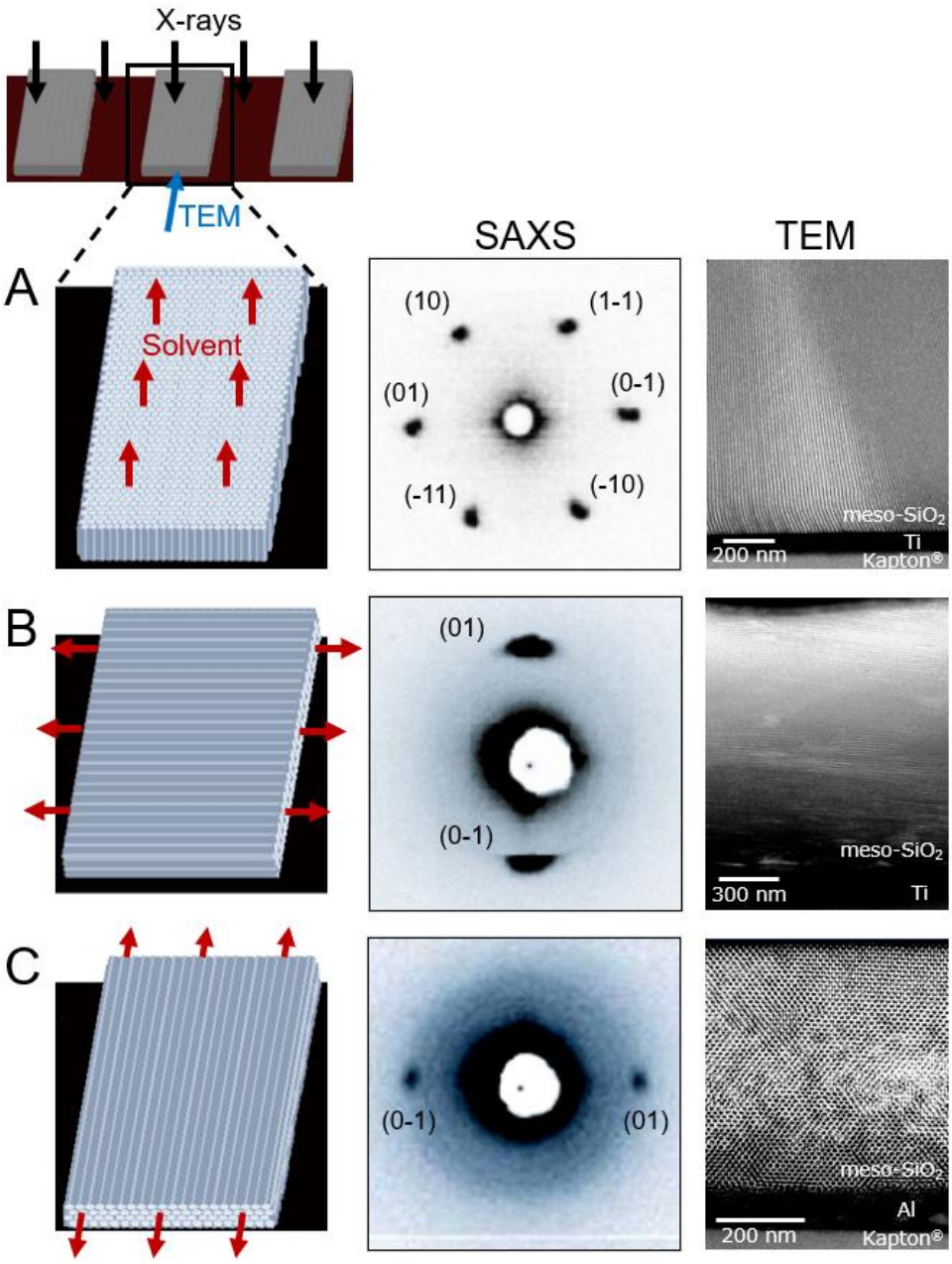

Figure S5.1. Schematic diagrams (left), transmission small-angle X-ray scattering (SAXS) patterns (center), and cross-sectional transmission electron microscopy (TEM) images (right) of three 4-cm^2 patterned hexagonal nanocomposite *silica*–Pluronic^{TM} P123 films that are identical, except for the directions in which their cylindrical channels are macroscopically orientationally ordered: **(A)** vertically, **(B)** laterally, or **(C)** longitudinally, relative to the axes of the 1 μm x 7 μm x 2 cm.

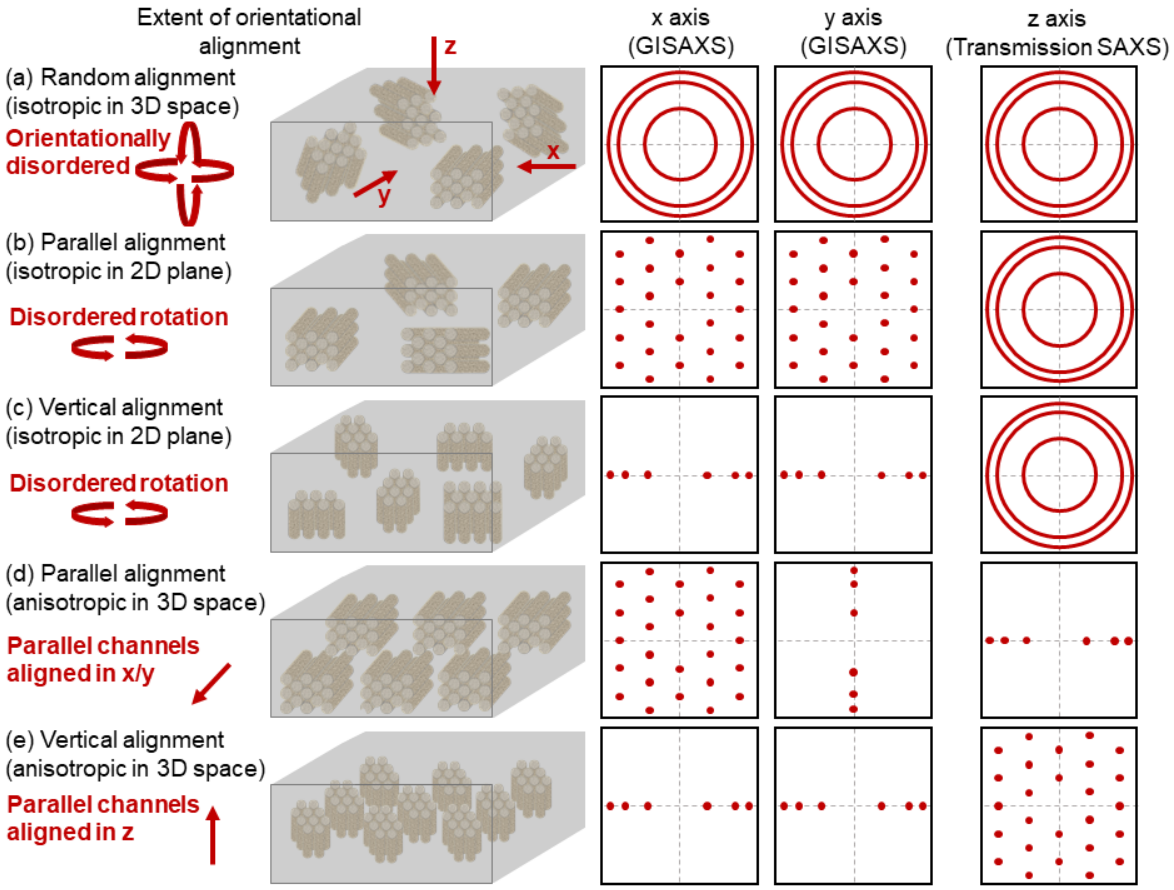

Figure S5.2. X-ray scattering data representative of extent of orientational alignment in a mesostructured film via probing across three axes: **(a)** random alignment, **(b)** parallel alignment in a two-dimensional plane, **(c)** vertical alignment in a two-dimensional plane, **(d)** parallel alignment in three-dimensional space, and **(e)** vertical alignment in three-dimensional space. Schematic diagrams of mesostructured films with each extent of orientational alignment is included on the left.

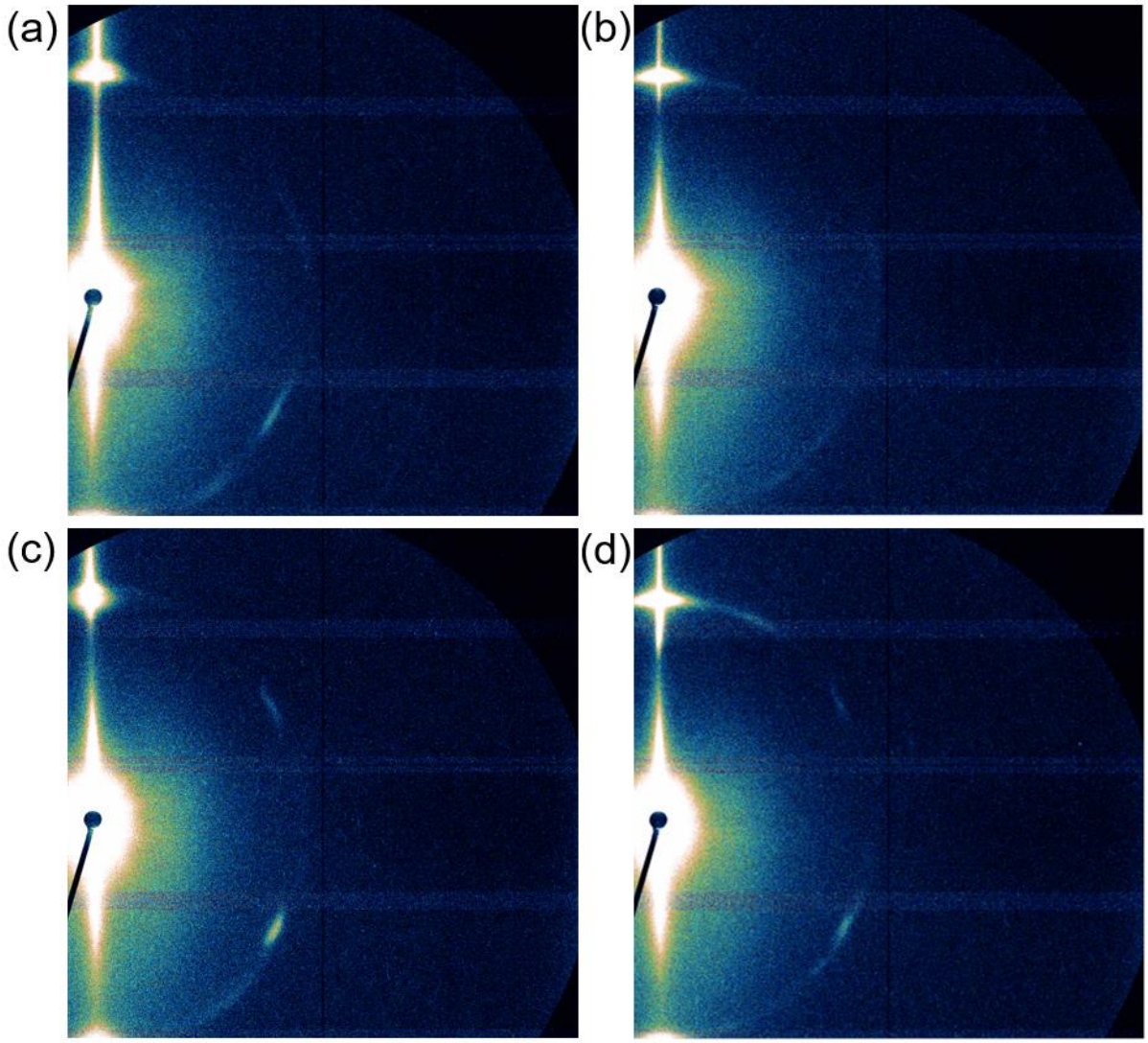

Figure S5.3. Two-dimensional grazing-incidence small angle X-ray scattering patterns of 62.5 wt% DDM, 6.2 wt% POPC, 1.3 wt% DOTAP, and 22.5 wt% SiO_2, and 7.5 wt% n-propyl $SiO_{1.5}$ synthesized at **(a)** 58% relative humidity and 4℃, **(b)** 58% relative humidity and 20℃, **(c)** 0% relative humidity and 4℃, and **(d)** 0% relative humidity and 20℃. The composition of the self-assembling solutions when covered by the PDMS stamps was 9.1 wt% DDM, 0.8 wt% POPC, 0.2 wt% DOTAP, 5.5 wt% TEOS, and 1.9 wt% PTEOS, 70 wt% H_2O, and 12.5 wt% EtOH.

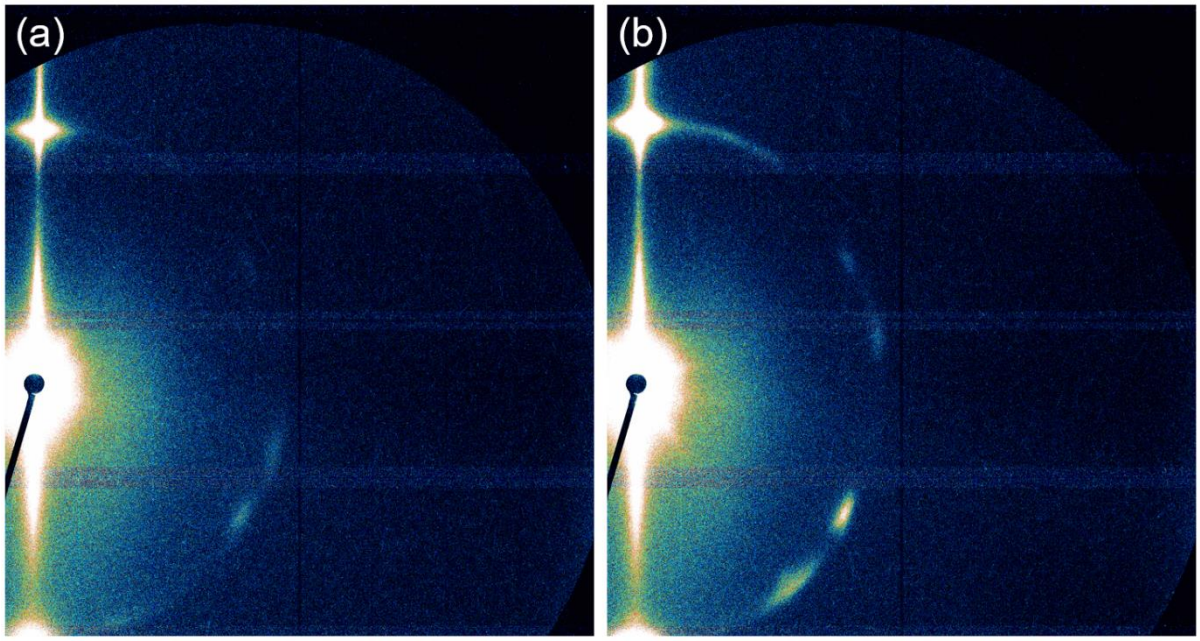

Figure S5.4. Grazing-incidence small angle X-ray scattering patterns of 62.5 wt% DDM, 6.2 wt% POPC, 1.3 wt% DOTAP, and 22.5 wt% SiO_2, and 7.5 wt% n-propyl $SiO_{1.5}$ synthesized with an **(a)** unsaturated and **(b)** saturated PDMS stamp. The composition of the self-assembling solutions when covered by the PDMS stamps was 9.1 wt% DDM, 0.8 wt% POPC, 0.2 wt% DOTAP, 5.5 wt% TEOS, and 1.9 wt% PTEOS, 70 wt% H_2O, and 12.5 wt% EtOH.

Appendix A. Protocols developed and used during my thesis

A.1 Proteorhodopsin expression and purification

In my research to incorporate proteorhodopsin into silica-surfactant host materials, I needed a pure and homogeneous sample. Early methods that I tried did not produce protein solutions with the characteristics that I needed, and so I developed my own, presented below:

Day 0

Transformation of PR-pET vector into E. coli

1. Get cells from -80° C freezer (one 100 μL aliquot for each transformation) and immediately put on ice.
2. Add 1 μL of DNA to cells. Do not pipet aspirate or vortex, but mix gently with pipet tip.
3. Incubate for 10-15 minutes on ice.
4. Turn on heating block to 42° C, or make water bath.
5. Heat shock at 42° C for 45 seconds for the BL21 cells.
6. Immediately put back on ice and rest for at least 2 minutes.
7. Near a flame, transfer 1 mL of autoclaved SOC media (or LB) to each sample.
8. Put cells on a shaker at 37° C and 200 rpm for 30 minutes.
9. Near a flame:
    a. Make a sterile scraper with long glass pipettes and flame.
    b. Add 100 uL of BL21 cells (150 uL if XL1Blue) to a premade LB Agar (2.5 wt% Agar (miller) not Agar w/ broth) plate with Kanamycin.
    c. Spread cells with a cool spreader.
10. Place plates upside down in an incubator at 37°C for 16-18 hours.

NOTE: When autoclaving LB, heat to 121℃ for at least 15 minutes. In the chemistry building use the program “Liquids 3”

Day 1: Prepare little (10mL) culture of E. coli transformant

1. Check cell growth on plate in the morning

    a. Continue to incubate cells that have not grown visible colonies longer

    b. Put plates with cells in fridge to prevent overgrowth

Start here if you are starting from a glycerol stock stored at -80° C

2. In the afternoon (~4 PM onwards), make little cultures to grow near a flame

    a. Pour 10 mL of LB with 10 uL of 50 mg/mL kanamycin into a 50 mL falcon tube

    b. Using a medium-sized autoclaved pipet tip, carefully pick (touch) one colony (or just touch to glycerol stock).

    c. Put pipette tip into falcon tube, and loosely close the lid

    d. Tape the unclosed lid in place

3. Put the little culture in the 37° C shaker @ 180 rpm for 16-18 hours.

4. Autoclave 1 L of LB broth in 2 L Erlenmeyer flasks for each culture planned to be made on day 2

Day 2: Make large (1L) cultures and induce expression of proteorhodopsin

1. If this is a new transformation, make a glycerol stock:

    a. Near the fire, pipet 800 µL of cell culture and 200 µL 80% filter-sterilized glycerol-in-water solution

    b. Store at -80° C

2. Add one mL of a 50 mg/ml Kan solution to 1 L of autoclaved LB

3. Then pour the little culture (there should be growth) into the LB

4. Shake at 200 rpm and 37 °C for about 3 hours and 45 minute. After 3 hours the OD should be around .2, and double every 20 minutes (however, the cells typically grow a little slower)

5. Check cell growth with UV-Vis:

    a. Pipet a 1 mL sample of cells from the 1L culture into disposable cuvette

    b. Blank UV-Vis with autoclaved LB (pipette near a flame)

    c. Check optical density (OD) at 600nm

6. When OD at 600 equals 0.8 to 1.0, induce PR expression by adding:

    a. 1mL 1 M IPTG

    b. 500 uL of 21 mM trans-retinal (in freezer). 2.844 mg trans-retinal/L culture. The final concentration in the LB broth should be about 10 μM trans-retinal. The stock solution is made with a minimal amount of EtOH to dissolve the retinal.

7. Put flasks on ice for ~5+ minutes

8. Put cells back on the shaker at 180 rpm @ 18℃ for 16-18 hours or until pink

Day 3: Cell lysis and extraction of PR from membranes

1. Pour cells back into 3 large centrifuge tubes, balance, and spin down at 5000 g for 5 minutes in the large centrifuge on the first floor of the chemistry building. (You need to get trained before using it.)

2. Pour off LB

3. Add 10 mL of PR buffer (no DDM) to each centrifuge tube to resuspend the cells. Using a serological pipette, pipette up and down to mix well.

4. Recombine in a 50mL falcon tube. Your total volume should be ~40-50mL.

5. To break the cell membrane, add the following to each 50 mL falcon tube:

   a. 500uL lysozyme (20 mg/ml) from enzyme box and shake well

   b. 20uL/mL 1 M MgCl2

   c. DNase (at least 600 U/L cells, about 1 mg DNase, can make a stock 10 mg/mL dissolved in water and add 100 µL)

6. Parafilm lid, and shake for 1 hour-overnight in fridge

7. Transfer lysed cell solution back to 50mL falcon tube and freeze fracture with liquid nitrogen

8. Spin down 50 mL falcon tube in centrifuge at 1000 g for 5-10 minutes, collect supernatant (thus removing broken e coli cells), fraction into 15 mL falcon tubes and spin down at 10,000 g for 25 minutes.

9. Pour out supernatant. If supernatant is clear skip to step 13. If not, proceed to step 10.

10. Resuspend the pellets with 10 mL of PR buffer

11. Fill the 50 mL falcon tube to about 50 mL with PR buffer

12. Repeat four more times or until supernatant is clear

13. Freeze in liquid nitrogen and store at -80℃

Day 4: Purification

1. Homogenize with 10 mL of 2% DDM PR Buffer (Can add more if you think you have more protein than usual). First aspirate then use homogenizer.

2. Parafilm lid, and shake in the fridge 1+ hours.

3. Spin down for 1 h at 100,000 g.

4. Equilibrate 5 mL His-trap resin column with water, then binding buffer (PR buffer with 0.01 wt% DDM with 30 mM imidazole).

5. Trap PR on his-trap column.

6. Wash away impurities with 30mM imidazole binding buffer.

7. Elute PR with PR buffer with 0.01 wt% DDM with 500 mM imidazole.

8. Concentrate as desired.

9. Run gel filtration SEC.

10. Collect sample.

11. Remove buffer salts from sample

    a. Equilibrate PD-10 desalting column with 20 mL total (4x5 mL) MQ water.

    b. Equilibrate PD-10 desalting column with 20 mL total (4x5 mL) desired PR buffer.

    c. Place PR (volume = x) on column, maximum of 2.5 mL.

    d. Run 5mL – x PR buffer w/o salt through.

    e. Collect sample.

12. Check concentration of PR with UV-visible light spectroscopy

13. Check DDM concentration with NMR

Extra notes:

To remove salt from protein solution:

1. Equilibrate PD-10 desalting column with 20 mL total (4x5 mL) MQ water.

2. Equilibrate PD-10 desalting column with 20 mL total (4x5 mL) desired PR buffer.

3. Place PR (volume = x) on column, maximum of 2.5 mL.

4. Run 5mL – x PR buffer w/o salt through.

5. Collect sample.

Check protein concentration with UV-Vis:

1. Blank with 200 uL of .05% DDM PR buffer

2. Take out 4 uL of .05% DDM PR buffer and add 4 uL of protein sample (a 50 fold dilution) to find absorbance at 520 nm

3. Multiply absorbance value at 520 nm by 50 (dilution factor) and then divide by 49000 M-1cm-1 to find the moles/L of PR

4. Multiply by the number of liters you have in your sample to find moles of PR

5. Multiply by the molar mass of PR, 29,000 grams/mole, to find the grams of PR 1mL of Ni-NTA resin binds 20mg of protein, and the resin is diluted in solution by ½, so add 1 mL of well mixed resin per 10 mg PR.

Check DDM concentration with NMR:

1. Make 0.91 wt% DDM standard by dissolving 10 mg DDM in 990 μL D_2O.

2. Make sample by adding 20 μL PR stock sample with 980 μL D_2O.

3. Conduct 1D ^1H solution state NMR measurement.

4. Calculate wt% of DDM in PR sample by comparing ^1H signals around 0.6-1.8 ppm to the standard. This experiment is quantitative so after properly baselining you can compare the areas under the signals. Make sure to account for dilution of sample in step 2.

A.2 Etching micropatterned silicon wafer to make PDMS stamps

In order to make micropatterned PDMS stamps for the orientational alignment of mesostructured silica-surfactant films, a micropattern Si wafer stencil is needed. PDMS is dried on the wafer to impart the geometry of the channels on the polymer. I developed this protocol below to make these wafers.

Photoresist and lithography

1. Clean 4" Si wafer with acetone and IPA, then blow dry with N_2.

2. Place wafer on wafer chuck in photoresist bay.

3. Coat wafer in SPR 220-3.0 positive photoresist, use plastic disposable pipet from glove cabinet.

4. Spin coat wafer at 2.5k rpm for 30 s. This should result in a thickness of ~2.7 μm.

5. Bake wafer at 115℃ for 90 s.

6. Conduct lithography. If using maskless aligner, make gdsii files in KLayout (make sure "gdsii" is lowercase). For SPR 220-3.0 photoresist, use these parameters:

a. Laser: 405 nm.

b. Exposure dose: 325 mJ/cm^2.

c. Defocus: -4

8. Wait 10 min after MLA lithography is done and post-exposure bake the wafer at 115℃ for 90 s.

Develop and clean

1. Develop using AZ 300 MIF developer. Soak in developer and agitate for 60 s. Pull out and rinse down with water immediately. When sufficiently washed, dry with N_2.

2. Use optical microscope to make sure lithography and developing were successful.

3. Plasma clean sample using PEII system running at 300 mT and 100 W for 30 s. When using Ashers (Technics PEII) in UCSB nanofab:

a. Check vac, vent, power, O_2, are in down position.

b. vent up.

c. Load sample.

d. Vent down.

e. Vac up.

f. Once at 300 mT, O_2 up.

g. Wait for 300 mT again, power up for however long needed.

h. Power down.

i. O_2 down.

j. Vac down.

k. Vent up.

l. Unload sample.

m. Vac up until ~200 mT.

n. Vac down.

Etch and remove photoresist

1. Etch using Fluorine ICP Etcher using SiVertHF program. Etch for length of time dependent on desired etch depth.

2. Check depth of etch using profilometry. Make sure to account for thickness of photoresist.

3. Remove photoresist:

    a. Acetone wash.

    b. IPA wash.

    c. Dry with N2.

    d. Deep UV flood expose for 5 min.

    e. Soak and agitate in AZ 300 MIF developer for 2 min.

    f. Plasma clean using PEII at 300 mT and 100 W for 2 min. Can do longer if needed.

4. Check etch depth and verticality of microchannel walls.

Extra notes:

If getting new photoresist, clean bottle first:

1. Rinse brown (photo-protective) bottle (from glove shelf) with acetone.

2. Pour out acetone.

3. Rinse bottle with IPA.

4. Pour out IPA.

5. Bake bottle at 110℃ for 1+ hr (can bake cap too).

6. Let cool for ~5 min before pouring in photoresist (minimize time photoresist stick is outside of the freezer cabinet).

7. Let new bottle of photoresist sit and thaw to room temperature before use (this stock should be good up to one year).

If something goes wrong and you need to remove photoresist from wafer:

a. Acetone wash.

b. IPA wash.

c. Dry with N2.

d. Deep UV flood expose for 5 min.

e. Soak and agitate in AZ 300 MIF developer for 2 min.

f. Plasma clean using PEII at 300 mT and 100 W for 2 min. Can do longer if needed.